Title 40 CFR Part 191
Subparts B and C
Compliance Recertification Application 2019
for the
Waste Isolation Pilot Plant

Appendix GEOCHEM-2019
Implementation of Chemistry Conceptual Models

United States Department of Energy
Waste Isolation Pilot Plant

Carlsbad Field Office
Carlsbad, New Mexico

Compliance Recertification Application 2019
Appendix GEOCHEM-2019
Implementation of Chemistry Conceptual Models

Table of Contents

GEOCHEM-1.0 INTRODUCTION GEOCHEM-1
GEOCHEM-1.1 How Chemistry is Incorporated in Performance Assessment GEOCHEM-1
GEOCHEM-1.1.1 Features, Events, and Processes GEOCHEM-2
GEOCHEM-1.1.2 Conceptual and Process Models GEOCHEM-2
GEOCHEM-1.1.3 Parameterization GEOCHEM-3
GEOCHEM-1.1.4 Quantification of Uncertainty GEOCHEM-3
GEOCHEM-1.2 Initial and Boundary Conditions GEOCHEM-6
GEOCHEM-1.2.1 Geologic Setting GEOCHEM-6
GEOCHEM-1.2.2 Hydrologic Setting GEOCHEM-7
GEOCHEM-1.2.3 Waste Characteristics GEOCHEM-8
GEOCHEM-1.2.4 Emplacement Material Characteristics GEOCHEM-8
GEOCHEM-1.2.5 Repository Conditions ..... GEOCHEM-
GEOCHEM-2.0 GAS GENERATION AND BRINE PRODUCTION GEOCHEM-10
GEOCHEM-2.1 Gas Generation and Brine Production Conceptual Model GEOCHEM-11
GEOCHEM-2.1.1 Homogeneous Gas Generation GEOCHEM-11
GEOCHEM-2.1.2 Oxygen Depletion GEOCHEM-11
GEOCHEM-2.1.3 Corrosion of Ferrous Metals GEOCHEM-12
GEOCHEM-2.1.4 Corrosion of Non-Ferrous Metals GEOCHEM-12
GEOCHEM-2.1.5 Microbial Degradation of CPR Materials GEOCHEM-12
GEOCHEM-2.1.6 Steel Passivation GEOCHEM-13
GEOCHEM-2.1.7 Radiolysis GEOCHEM-13
GEOCHEM-2.2 Gas Generation and Brine Production Process Models GEOCHEM-14
GEOCHEM-2.2.1 Process Model for Corrosion of Ferrous Metals GEOCHEM-19
GEOCHEM-2.2.2 Process Model for Microbial Degradation of CPR Materials GEOCHEM-20
GEOCHEM-2.2.3 Process Model for MgO Hydration and Carbonation GEOCHEM-21
GEOCHEM-2.2.4 Process Model for Hydromagnesite to Magnesite Conversion GEOCHEM-22
GEOCHEM-2.3 Parameterization of Gas Generation and Brine Production Process Models GEOCHEM-23
GEOCHEM-2.3.1 Parameters for Ferrous Metal Corrosion GEOCHEM-23
GEOCHEM-2.3.2 Parameters for Microbial Gas Generation GEOCHEM-23
GEOCHEM-2.3.3 Parameters for MgO Hydration and Carbonation GEOCHEM-23
GEOCHEM-2.3.4 Parameters for Hydromagnesite to Magnesite Conversion GEOCHEM-23
GEOCHEM-2.4 Quantification of Uncertainty in Gas Generation and Brine Production GEOCHEM-24
GEOCHEM-2.4.1 Uncertainty in Corrosion of Steel GEOCHEM-25
GEOCHEM-2.4.2 Uncertainty in Microbial Degradation of CPR Materials GEOCHEM-27
GEOCHEM-2.4.3 Uncertainty in MgO Hydration Rate GEOCHEM-29

GEOCHEM-2.4.4 Uncertainty in the Hydromagnesite Conversion Rate GEOCHEM-29

GEOCHEM-3.0 CHEMICAL CONDITIONS GEOCHEM-30

GEOCHEM-3.1 WIPP Chemical Conditions Conceptual Model GEOCHEM-31
GEOCHEM-3.1.1 Use of the Pitzer Model GEOCHEM-31
GEOCHEM-3.1.2 The Presence of Carbon Dioxide Gas GEOCHEM-31
GEOCHEM-3.1.3 A Well-Mixed Repository at Equilibrium GEOCHEM-31
GEOCHEM-3.1.4 Availability of Minerals GEOCHEM-32
GEOCHEM-3.1.5 Availability of Waste Materials GEOCHEM-32
GEOCHEM-3.1.6 The Use of End Member Brines GEOCHEM-32
GEOCHEM-3.1.7 Reducing Conditions Due to Ferrous Metal Corrosion GEOCHEM-33
GEOCHEM-3.1.8 The Role of Magnesium Oxide GEOCHEM-33

GEOCHEM-3.2 WIPP Chemical Conditions Process Models GEOCHEM-33
GEOCHEM-3.2.1 Ionic Strength, Brine pH, pcH, or pmH and E_h, and Fugacity of CO_2 ..... GEOCHEM-36
GEOCHEM-3.2.2 Salado and Castile Minerals GEOCHEM-38
GEOCHEM-3.2.3 Salado and Castile Brines GEOCHEM-41
GEOCHEM-3.2.4 Magnesium Oxide GEOCHEM-41
GEOCHEM-3.2.5 Organic Ligands GEOCHEM-42
GEOCHEM-3.2.6 Borate GEOCHEM-44
GEOCHEM-3.2.7 Lead GEOCHEM-45
GEOCHEM-3.2.8 Iron GEOCHEM-46

GEOCHEM-3.3 Parameterization of the WIPP Chemical Conditions Process Models GEOCHEM-47
GEOCHEM-3.3.1 Ionic Strength, Brine pcH and Eh, and Fugacity of CO_2 ..... GEOCHEM-47
GEOCHEM-3.3.2 Salado and Castile Minerals GEOCHEM-48
GEOCHEM-3.3.3 Salado and Castile Brines GEOCHEM-49
GEOCHEM-3.3.4 Magnesium Oxide GEOCHEM-55
GEOCHEM-3.3.5 Organic Ligands GEOCHEM-56
GEOCHEM-3.3.6 Borate GEOCHEM-62
GEOCHEM-3.3.7 Lead GEOCHEM-65
GEOCHEM-3.3.8 Iron GEOCHEM-67

GEOCHEM-3.4 Quantification of Uncertainty in WIPP Chemical Conditions GEOCHEM-68
GEOCHEM-3.4.1 Conceptual Model Uncertainty GEOCHEM-69
GEOCHEM-3.4.2 Process Model Uncertainty GEOCHEM-72
GEOCHEM-3.4.3 Parameter Uncertainty GEOCHEM-73

GEOCHEM-3.5 WIPP Chemical Conditions Model Summary for CRA-2019 ..... GEOCHEM-74

GEOCHEM-4.0 DISSOLVED ACTINIDE SOURCE TERM GEOCHEM-75

GEOCHEM-4.1 Dissolved Actinide Source Term Conceptual Model GEOCHEM-75
GEOCHEM-4.1.1 A Well-Mixed Repository at Equilibrium GEOCHEM-75
GEOCHEM-4.1.2 Use of the Pitzer Model GEOCHEM-76
GEOCHEM-4.1.3 The Use of End Member Brines GEOCHEM-76

GEOCHEM-4.1.4 Oxidation-state Analogy GEOCHEM-76
GEOCHEM-4.1.5 Redox Status of the Actinides GEOCHEM-77
GEOCHEM-4.1.6 The Effect of Organic Ligands GEOCHEM-77
GEOCHEM-4.1.7 Immobile Substrates GEOCHEM-77
GEOCHEM-4.1.8 Phase Stability GEOCHEM-77
GEOCHEM-4.1.9 Solubility-Controlling Phases GEOCHEM-78
GEOCHEM-4.2 Dissolved Actinide Source Term Process Models GEOCHEM-78
GEOCHEM-4.2.1 +III Actinides GEOCHEM-79
GEOCHEM-4.2.2 +IV Actinides GEOCHEM-80
GEOCHEM-4.2.3 +V Actinides GEOCHEM-81
GEOCHEM-4.3 Parameterization of Dissolved Actinide Source Term Process Models GEOCHEM-81
GEOCHEM-4.3.1 +III Actinides GEOCHEM-82
GEOCHEM-4.3.2 +IV Actinides GEOCHEM-86
GEOCHEM-4.3.3 +V Actinides GEOCHEM-89
GEOCHEM-4.4 Quantification of Uncertainty in the Dissolved Actinide Source Term GEOCHEM-92
GEOCHEM-4.4.1 Conceptual Model Uncertainty for the Dissolved Actinide Source Term GEOCHEM-93
GEOCHEM-4.4.2 Process Model Uncertainty for the Dissolved Actinide Source Term GEOCHEM-94
GEOCHEM-4.4.3 Parameter Uncertainty for the Dissolved Actinide Source Term Process Model GEOCHEM-96
GEOCHEM-4.4.4 Quantification of Uncertainty Summary for CRA-2019 ..... GEOCHEM-103
GEOCHEM-4.5 WIPP Dissolved Actinide Source Term Model Summary for CRA-2019 ..... GEOCHEM-104
GEOCHEM-5.0 COLLOIDS GEOCHEM-104
GEOCHEM-5.1 Types of Colloids GEOCHEM-105
GEOCHEM-5.2 Colloid Stability GEOCHEM-106
GEOCHEM-5.3 Conceptual WIPP PA Colloid Model GEOCHEM-107
GEOCHEM-5.4 WIPP PA Colloid Model GEOCHEM-108
GEOCHEM-5.4.1 Mineral Fragment Colloids Model GEOCHEM-110
GEOCHEM-5.4.2 Intrinsic Colloids Model GEOCHEM-111
GEOCHEM-5.4.3 Humic Substance Colloids Model GEOCHEM-112
GEOCHEM-5.4.4 Microbial Colloids Model GEOCHEM-115
GEOCHEM-5.5 New WIPP Colloid Model Parameter Analyses GEOCHEM-116
GEOCHEM-5.5.1 Mineral Fragment Colloids GEOCHEM-116
GEOCHEM-5.5.2 Intrinsic Colloids GEOCHEM-122
GEOCHEM-5.5.3 Humic Substance Colloids GEOCHEM-129
GEOCHEM-5.5.4 Microbial Colloids GEOCHEM-139
GEOCHEM-5.6 Summary GEOCHEM-141
GEOCHEM-5.7 References GEOCHEM-142

List of Tables

Table GEOCHEM-1. Iron Corrosion Reactions in the WIPP Gas Generation Process Model GEOCHEM-13

Table GEOCHEM-2. Microbial Gas Generation Reactions in the WIPP Gas Generation Process Model GEOCHEM-20

Table GEOCHEM-3. MgO Hydration and Carbonation Reactions in the WIPP Gas Generation Process Model GEOCHEM-22

Table GEOCHEM-4. Probabilities for Biodegradation of Different Organic Materials in the CRA-2014 PA[A] GEOCHEM-29

Table GEOCHEM-5. Composition of GWB and ERDA-6 Brine Before Reaction with Anhydrite, Brucite and Hydromagnesite GEOCHEM-33

Table GEOCHEM-6. Dissolution Reactions for Salado and Castile Minerals Implemented in the WIPP Chemical Conditions Process Model for CRA-2019[A] .. GEOCHEM-40

Table GEOCHEM-7. Dissociation Reactions for Ions in Salado and Castile Brines Implemented in the WIPP Chemical Conditions Process Model for CRA-2019[A] .. GEOCHEM-41

Table GEOCHEM-8. Dissolution Reactions for MgO Solids Implemented in the WIPP Chemical Conditions Process Model for CRA-2019[A] GEOCHEM-42

Table GEOCHEM-9. Reactions with Organic Ligands Implemented in the WIPP Chemical Conditions Process Model for CRA-2019[A] GEOCHEM-43

Table GEOCHEM-10. Reac with Borate Implemented in the WIPP Chemical Conditions Process Model for CRA-2019[A] GEOCHEM-45

Table GEOCHEM-11. Reactions with Lead Implemented in the WIPP Chemical Conditions Process Model For CRA-2019[A] GEOCHEM-46

Table GEOCHEM-12. Reactions with Iron Implemented in the WIPP Chemical Conditions Process Model for CRA-2019[A] GEOCHEM-47

Table GEOCHEM-13. Equilibrium Constants for Dissolution Reactions for Salado and Castile Minerals Implemented in the WIPP Chemical Conditions Process Model for CRA-2019[A] GEOCHEM-48

Table GEOCHEM-13 (continued). Equilibrium Constants for Dissolution Reactions for Salado and Castile Minerals Implemented in the WIPP Chemical Conditions Process Model for CRA-2019[A] GEOCHEM-49

Table GEOCHEM-14. Equilibrium Constants for Aqueous Dissociation Reactions for Ions in Salado and Castile Brines Implemented in the WIPP Chemical Conditions Process Model for CRA-2019[A] GEOCHEM-50

Table GEOCHEM-15. Pitzer Interaction Coefficients (Cation-Anion Interactions) for Ions in Salado and Castile Brines Implemented in the WIPP Chemical Conditions Process Model for CRA-2019 ..... GEOCHEM-51

Table GEOCHEM-16. Pitzer Interaction Coefficients (Cation-Cation; Anion-Anion Interactions) for Ions in Salado and Castile Brines Implemented in the WIPP Chemical Conditions Process Model for CRA-2019 ..... GEOCHEM-52

Table GEOCHEM-17. Pitzer Interaction Coefficients (Neutral-Cation; Neutral-Anion Interactions) for Ions in Salado and Castile Brines Implemented in the WIPP Chemical Conditions Process Model for CRA-2019 ..... GEOCHEM-53

Table GEOCHEM-18. Pitzer Interaction Coefficients (Cation-Cation-Anion Interactions) for Ions in Salado and Castile Brines Implemented in the WIPP Chemical Conditions Process Model for CRA-2019 ..... GEOCHEM-53

Table GEOCHEM-19. Pitzer Interaction Coefficients (Anion-Anion-Cation Interactions) for Ions in Salado and Castile Brines Implemented in the WIPP Chemical Conditions Process Model for CRA-2019 ..... GEOCHEM-54

Table GEOCHEM-20. Equilibrium Constants for Dissolution Reactions for MgO Solids Implemented in the WIPP Chemical Conditions Process Model for CRA-2019[A] .. GEOCHEM-56

Table GEOCHEM-21. Equilibrium Constants for Reactions with EDTA Implemented in the WIPP Chemical Conditions Process Model[A] GEOCHEM-57

Table GEOCHEM-22. Equilibrium Constants for Reactions with Citrate Implemented in the WIPP Chemical Conditions Process Model for CRA-2019[A] GEOCHEM-58

Table GEOCHEM-23. Equilibrium Constants for Reactions with Oxalate Implemented in the WIPP Chemical Conditions Process Model[A] GEOCHEM-59

Table GEOCHEM-24. Pitzer Interaction Coefficients (Cation-Anion Interactions) for Ions Containing EDTA Implemented in the WIPP Chemical Conditions Process Model[A] GEOCHEM-60

Table GEOCHEM-25. Pitzer Interaction Coefficients (Cation-Anion Interactions) for Ions Containing Citrate Implemented in the WIPP Chemical Conditions Process Model[A] GEOCHEM-61

Table GEOCHEM-26. Pitzer Interaction Coefficients (Cation-Anion Interactions) for Ions Containing Oxalate Implemented in the WIPP Chemical Conditions Process Model for CRA-2019[A] GEOCHEM-61

Table GEOCHEM-27. Pitzer Interaction Coefficients (Neutral-Cation; Neutral-Anion Interactions) for Ions Containing Organic Ligands Implemented in the WIPP Chemical Conditions Process Model for CRA-2019[A] GEOCHEM-62

Table GEOCHEM-28. Equilibrium Constants for Reactions with Borate Implemented in the WIPP Chemical Conditions Process Model for CRA-2019[A] GEOCHEM-63

Table GEOCHEM-29. Pitzer Interaction Coefficients (Cation-Anion Interactions) for Ions Containing Borate Implemented in the WIPP Chemical Conditions Process Model for CRA-2019 ..... GEOCHEM-64

Table GEOCHEM-30. Pitzer Interaction Coefficients (Anion-Anion Interactions) for Ions Containing Borate Implemented in the WIPP Chemical Conditions Process Model for CRA-2019 ..... GEOCHEM-64

Table GEOCHEM-31. Pitzer Interaction Coefficients (Neutral-Cation; Neutral-Anion Interactions) for Ions Containing Borate Implemented in the WIPP Chemical Conditions Process Model for CRA-2019..... GEOCHEM-65

Table GEOCHEM-32. Pitzer Interaction Coefficients (Neutral-Cation-Anion Interactions) for Ions Containing Borate Implemented in the WIPP Chemical Conditions Process Model for CRA-2019..... GEOCHEM-65

Table GEOCHEM-33. Equilibrium Constants for Reactions with Lead Implemented in the WIPP Chemical Conditions Process Model for CRA-2019 ..... GEOCHEM-66

Table GEOCHEM-34. Equilibrium Constants for Reactions with Iron Implemented in the WIPP Chemical Conditions Process Model for CRA-2019 ..... GEOCHEM-67

Table GEOCHEM-35. Pitzer Interaction Coefficients (Cation-Anion Interactions) for Ions Containing Iron Implemented in the WIPP Chemical Conditions Process Model for CRA-2019..... GEOCHEM-67

Table GEOCHEM-36. Pitzer Interaction Coefficients (Cation-Cation Interactions) for Ions Containing Iron Implemented in the WIPP Chemical Conditions Process Model GEOCHEM-68

Table GEOCHEM-37. Pitzer Interaction Coefficients (Cation-Cation-Anion Interactions) for Ions Containing Iron Implemented in the WIPP Chemical Conditions Process Model..... GEOCHEM-68

Table GEOCHEM-38. Near-Field Geochemical Conditions [Ionic Strength (m)], for Native[J] and Equilibrated WIPP Brines GEOCHEM-70

Table GEOCHEM-39. Descriptive Statistics for Ionic Strength (m) in WIPP Brines GEOCHEM-71

Table GEOCHEM-40. Descriptive Statistics for Carbon Dioxide Fugacity in WIPP Brines GEOCHEM-71

Table GEOCHEM-41. Descriptive Statistics for pcH in WIPP Brines GEOCHEM-72

Table GEOCHEM-42. Descriptive Statistics for Total Inorganic Carbon(m) in WIPP Brines GEOCHEM-72

Table GEOCHEM-43. Dissolution and Dissociation Reactions for Americium Solids and Species Implemented in the WIPP Dissolved Actinide Source Term Process Model for CRA-2019[A] GEOCHEM-79

Table GEOCHEM-44. Dissolution and Dissociation Reactions for Thorium Solids and Species Implemented in the WIPP Dissolved Actinide Source Term Process Model for CRA-2019[A] GEOCHEM-80

Table GEOCHEM-45. Dissolution and Dissociation Reactions for Neptunium Solids and Species Implemented in the WIPP Dissolved Actinide Source Term Process Model for CRA-2019[A] GEOCHEM-81

Table GEOCHEM-46. Equilibrium Constants for Dissolution and Dissociation Reactions for Americium Solids and Species Implemented in the WIPP Dissolved Actinide Source Term Process Model for CRA-2019[A] GEOCHEM-83

Table GEOCHEM-47. Pitzer Interaction Coefficients (Cation-Anion Interactions) for Ions Containing Americium Implemented in the WIPP Dissolved Actinide Source Term Process Model for CRA-2019 ..... GEOCHEM-85

Table GEOCHEM-48. Pitzer Interaction Coefficients (Cation-Cation; Anion-Anion Interactions) for Ions Containing Americium Implemented in the WIPP Dissolved Actinide Source Term Process Model for CRA-2019 ..... GEOCHEM-85

Table GEOCHEM-49. Pitzer Interaction Coefficients (Neutral-Cation; Neutral-Anion Interactions) for Ions Containing Americium Implemented in the WIPP Dissolved Actinide Source Term Process Model for CRA-2019 ..... GEOCHEM-86

Table GEOCHEM-50. Equilibrium Constants for Dissolution and Dissociation Reactions for Thorium Solids and Species Implemented in the WIPP Dissolved Actinide Source Term Process Model for CRA-2019[A] GEOCHEM-87

Table GEOCHEM-51. Pitzer Interaction Coefficients (Cation-Anion Interactions) for Ions Containing Thorium Implemented in the WIPP Dissolved Actinide Source Term Process Model for CRA-2019 ..... GEOCHEM-88

Table GEOCHEM-52. Pitzer Interaction Coefficients (Cation-Cation; Anion-Anion Interactions) for Ions Containing Thorium Implemented in the WIPP Dissolved Actinide Source Term Process Model for CRA-2019 ..... GEOCHEM-88

Table GEOCHEM-53. Pitzer Interaction Coefficients (Neutral-Cation; Neutral-Anion Interactions) for Ions Containing Thorium Implemented in the WIPP Dissolved Actinide Source Term Process Model for CRA-2019 ..... GEOCHEM-89

Table GEOCHEM-54. Pitzer Interaction Coefficients (Cation-Cation-Anion Interactions) for Ions Containing Thorium Implemented in the WIPP Dissolved Actinide Source Term Process Model for CRA-2019 ..... GEOCHEM-89

Table GEOCHEM-55. Equilibrium Constants for Dissolution and Dissociation Reactions for Neptunium Solids and Species Implemented in the WIPP Dissolved Actinide Source Term Process Model for CRA-2019[A] GEOCHEM-90

Table GEOCHEM-56. Pitzer Interaction Coefficients (Cation-Anion Interactions) for Ions Containing Neptunium Implemented in the WIPP Dissolved Actinide Source Term Process Model for CRA-2019 ..... GEOCHEM-91

Table GEOCHEM-57. Pitzer Interaction Coefficients (Cation-Cation; Anion-Anion Interactions) for Ions Containing Neptunium Implemented in the WIPP Dissolved Actinide Source Term Process Model for CRA-2019 ..... GEOCHEM-92

Table GEOCHEM-58. Pitzer Interaction Coefficients (Neutral-Cation; Neutral-Anion Interactions) for Ions Containing Neptunium Implemented in the WIPP Dissolved Actinide Source Term Process Model for CRA-2019 ..... GEOCHEM-92

Table GEOCHEM-59. Comparison of Actinide Solubilities (M) for Compliance-Related Calculations from the CCA to CRA-2014 ..... GEOCHEM-93

Table GEOCHEM-60. WIPP Colloid Model Parameter Summary and Description (U.S. DOE 2014, Appendix SOTERM, Table SOTERM-20) GEOCHEM-109

Table GEOCHEM-61. WIPP Colloid Parameter Values Used in CRA-2014 (U.S. DOE 2014, Appendix SOTERM, Table SOTERM-21) and CRA-2019 (Reed et al. 2019; Mariner 2019) GEOCHEM-110

Table GEOCHEM-62. Calculated Values of Humic-Bound Actinide Concentrations AnHs and Proportionality Constants (i.e., PHUMSIM and PHUMCIM) for U(VI), Np(V), and Am(III) for the CCA. Inputs from Papenguth (1996, Tables 1a, 1b, and 3) GEOCHEM-115

Table GEOCHEM-63. Concentrations of Intrinsic Colloids Measured in WIPP Brines in Long-Term Experiments at Anticipated pcH Values GEOCHEM-126

Table GEOCHEM-64. Average pH and 60-day Humic Acid Concentration in Presence and Absence of MgO in Wall and Mathews (2005) Study GEOCHEM-137

List of Figures

Figure GEOCHEM-1. Implementation Sequence Employed in WIPP PA. GEOCHEM-2

Figure GEOCHEM-2. Representation of How Uncertainty is Incorporated..... GEOCHEM-4

Figure GEOCHEM-3 General Stratigraphic Column of Geologic Units at the WIPP Site (U.S. DOE 2009, Appendix HYDRO)..... GEOCHEM-7

Figure GEOCHEM-4. CDFs for 0.58 ppm and 3.14 ppm (from Zeitler and Hansen 2015b), as Well as the Final Interpolated CDF for 5 ppm (from Zeitler 2018). The CDFs are Not Distinguishable From One Another. GEOCHEM-27

Figure GEOCHEM-5. Example of Uncertainty in pmH by Varying Log K of Hydromagnesite GEOCHEM-74

Figure GEOCHEM-6. Example Distribution Function for *D*..... GEOCHEM-98

Figure GEOCHEM-7. Solubility of Pu(IV)-Polymer in NaCl Media as a Function of pcH (U.S. DOE 1996, Figure SOTERM-8). GEOCHEM-112

Figure GEOCHEM-8. Colloid Concentrations From Natural Systems and Simple Salt Solutions as Function of Ionic Strength as Compiled by Serco (Alexander et al. 2011, Figure 5.1, Blue Hatch - Ruprechtov; Red Hatch - Grimsel CRR tunnel; Grey Hatch - Äspö tunnel). Approximate Relative Location of Range Assumed in the WIPP PA for Mineral Fragment Colloids is Indicated to the Right of the Figure (Green Hatch)..... GEOCHEM-120

Figure GEOCHEM-9. Humic acid Concentration Over Time for Different Liquid:Solid Ratios for both 95% GWB and 95% ERDA-6 (Graphic From Wall and Mathews [2003])..... GEOCHEM-138

Acronyms and Abbreviations

%	percent
A	surface area
α	alpha particle
α_i	constant in Pitzer model, i = 1 or 2
a_i	activity of a chemical species
am	amorphous
aq	aqueous
atm	atmosphere
β	(apparent) stability constant, or beta particle
$\beta^{(0)}$, $\beta^{(1)}$, $\beta^{(2)}$	parameters within Pitzer's 2nd virial coefficient term B_{MX}
b	constant in f^{γ}, f^{φ}
B_{fc}	parameter to account for the uncertainty in microbial gas generation
bgs	below ground surface
BRAGFLO	Brine and Gas Flow code
C	Celsius; centigrade; concentration
C^{φ}_{MX}, C_{MX}	Pitzer parameter for osmotic and activity coefficient functions representing interaction between cation M and anion X
CAPHUM	maximum (cap) actinide concentration associated with mobile humic colloids
CAPMIC	maximum actinide concentration that could be associated with microbes
CCA	Compliance Certification Application
CCDF	Complementary Cumulative Distribution Functions
CDF	cumulative distribution function
CFR	Code of Federal Regulations
c_i	Aqueous species concentrations at equilibrium
CONCINT	actinide concentration associated with mobile actinide intrinsic colloids
CONCMIN	actinide concentration associated with mobile mineral fragment colloids
CPR	cellulosic, plastic, and rubber materials
cr	crystalline phase
CRA	Compliance Recertification Application
DBR	direct brine release
D_c	mass concentration of cellulosics; (material mass)/(disposal volume)
D_{HM}	mass concentration of MgO; (hydromagnesite mass)/(disposal volume)
DLVO	Derjaguin and Landau 1941; Verwey and Overbeek 1948
D_m	mass concentration of MgO; (MgO mass)/(disposal volume)
DOE	U.S. Department of Energy
DRZ	Disturbed Rock Zone
D_s	surface area concentration of steel; (surface area steel)/(disposal volume)
EDTA	ethylenediaminetetraacetic acid
E_h	Oxidation-reduction (redox) potential under specific conditions
EPA	U.S. Environmental Protection Agency
EQ3/6	software program for geochemical modeling of aqueous systems
EQ3NR	An aqueous solution speciation-solubility modeling code
ERDA-6	Energy Research and Development Administration Well 6
eV	electron volt

F	Fahrenheit or function containing f^{γ} and ionic strength derivatives of Pitzer model 2nd virial coefficient terms
f^{γ}, f^{φ}	Debye-Hückel function for activity and osmotic coefficients, respectively
FA-Suw	Suwannee River fulvic acid
f_{CO_2}	fugacity of carbon dioxide
FEPs	features, events and processes
FMT	Fracture-Matrix Transport code
F_{NO3}, F_{SO4}	fraction of carbon consumed through microbial denitrification or sulfate reduction
ft	foot/feet
γ	gamma radiation or activity coefficient
G	molecular yield in molecules/100 eV of absorbed ionizing radiation or Gibbs free energy (G^{xs} is excess or non-ideal contribution to Gibbs free energy)
g	gaseous, or gram, or gravity of Earth
GWB	Generic Weep Brine
h	hours
HAal-Gor	Gorleben humic acid
HAal-LBr	Lake Bradford humic acid
I	ionic strength
ICP-MS	inductively coupled plasma-mass spectrometry
IUPAC	International Union of Pure and Applied Chemists
K	degree Kelvin or stability constant
K_d	distribution coefficient
kg	kilogram
K_s	solubility constant, K_{sp}
ksp	solubility product constant
L	liter
LANL	Los Alamos National Laboratory
LHS	Latin Hypercube Sampling
log	logarithm
µ, or µm	micrometer, micron
M	mole per liter or molecular mass of subscripted species
m	meter, molal
m^2	square meter
m^3	cubic meter
MB	marker beds
meq	milliequivalents
mg	milligram
min	minimum
mL	Milliters-
mM	millimole per liter
mol	mole
MPa	megapascal
N	degree of polymerization number
n	neutron, number, or number of moles
NEA	Nuclear Energy Agency
nm	Nanometer

φ	osmotic coefficient
P	Pressure
PA	performance assessment
PABC	Performance Assessment Baseline Calculation
PAIR	Performance Assessment Inventory Report
PAVT	Performance Assessment Verification Test
pC_{H+} or pcH	Negative logarithm of H^+ concentration in moles per liter
pH	negative logarithm of H^+ activity
PHUMCIM	Proportionality constant for the actinide concentration associated with mobile humic colloids, in Castile brine
PHUMSIM	Proportionality constant for the actinide concentration associated with mobile humic colloids, in Salado brine
pmH	negative logarithm of H^+ concentration in molal
ppm	parts per million
PROPMIC	proportionality constant describing the bioassociation of actinides with mobile microorganisms
q_r	gas (q_{rg}), brine (q_{rb}) generation rates by corrosion, sulfidation, microbes, MgO, or hydromagnesite – trailing subscripted c, s, m, h, & hc, respectively
ρ	Density
R	gas constant, 8.31446 J/(mol·K)
R_c	corrosion rate in either inundated (R_{ci}) or humid air (R_{ch})
redox	Oxidation-reduction
RH	relative humidity
R_h	MgO hydration rate in either inundated (R_{hi}) or humid air (R_{hh})
R_{hc}	rate of conversion of hydromagnesite to magnesite
R_m	biodegradation rate in either inundated (R_{mi}) or humid air (R_{mh})
s	solid or second
S_b	brine saturation
SIT	Specific Ion Interaction theory
SNL	Sandia National Laboratories
SOTERM	Actinide Chemistry Source Term (WIPP)
SPC	Salado Primary Constituents
σ	Standard deviation of a normal distribution
T	Temperature
TIC	Total Inorganic Carbon
TRU	Transuranic
TSD	Technical Support Document
V	volt, vanadium, or volume
WIPP	Waste Isolation Pilot Plant
X	stoichiometric coefficient for gas generation by corrosion, sulfidation, microbes, MgO hydration, or hydromagnesite conversion– trailing subscripted c, s, m, h, & hc, respectively
Xm	stoichiometric coefficient for gas generation by microbes
yr	Year
Z	sum of products for each species' molality multiplied by absolute value of its valence charge
z_s	valence charge of solute species s

Elements and Chemical Compounds

Am	Americium
Am^{3+}	Americium cation in the +3 oxidation state
$AmCl^{2+}$	Americium (III) chloride ion – (1:1) complex
$AmCl_2^{+}$	Americium (III) chloride ion – (1:2) complex
$AmCO_3^{+}$	Americium (III) carbonate ion – (1:1) complex
$Am(CO_3)^{2-}$	Americium (III) carbonate ion – (1:2) complex
$Am(CO_3)_3^{3-}$	Americium (III) carbonate ion – (1:3) complex
$Am(CO_3)_4^{5-}$	Americium (III) carbonate ion – (1:4) complex
$AmOH^{2+}$	Americium (III) hydroxide ion – (1:1) complex
$Am(OH)_2^{+}$	Americium (III) hydroxide ion – (1:2) complex
$Am(OH)_3$	Americium hydroxide
$AmOHCO_3$	Americium (III) carbonate hydroxide
$AmSO_4^{+}$	Americium (III) sulfate ion – (1:1) complex
$Am(SO_4)_2^{-}$	Americium (III) sulfate ion – (1:2) complex
An	Actinide
An(III)	General actinide in the +3 oxidation state
An(IV)	General actinide in the +4 oxidation state
An(V)	General actinide in the +5 oxidation state
An(VI)	General actinide in the +6 oxidation state
AnHS	Actinide (III) hydrogen sulfide
$B(OH)_3$	Hydroxyborate, boric acid
$B(OH)_4^{-}$	Orthoborate, tetrahydroxyborate anion
$B_3O_3(OH)_4^{-}$	Triborate anion
$B_4O_5(OH)_4^{2-}$	Tetraborate anion
Br^{-}	Bromide anion
C	Carbon or concentration
Ca	Calcium
Ca^{2+}	Calcium cation
$CaB(OH)_4^{+}$	Calcium boron hydroxide
$CaCl_2$	Calcium chloride
$CaCl_2 \cdot 4H_2O$	Calcium dichloride tetrahydrate

$Ca_2Cl_2(OH)_2 \bullet H_2O$	Calcium oxychloride hydrate
$Ca_4Cl_2(OH)_6 \bullet 13H_2O$	Calcium oxychloride triskaidecahydrate
$CaCO_3$	Calcium carbonate, aragonite, calcite
$Ca_2EDTA \bullet 7H_20$	Di-calcium ethylenediaminetetraacetic acid hydrate
$C_6H_{10}O_5$	Cellulose
$CaMg(CO_3)_2$	Calcium magnesium carbonate, dolomite
$CaNa_2(CO_3)_2 \bullet 5H_2O$	Calcium sodium carbonate pentahydrate, gaylussite
$Ca(OH)_2$	Calcium hydroxide, portlandite
$CaOxalate \bullet 2H_2O$	whewellite
$CaSO_4$	Calcium sulfate, anhydrite
$CaSO_4 \bullet 2H_2O$	Calcium sulfate dihydrate, gypsum
CH_4	Methane
CH_3COO^-	Acetate anion
$(CH_2COO)_2C(OH)(CO_2)^{3-}$	Citrate anion
$(CH_2COO)_2N(CH_2)_2N(CH_2COO)_2^4$	Ethylenediaminetetraacetate (EDTA) anion
Cl	Chlorine
Cl^-	Chloride anion
ClO_4^-	Perchlorate anion
Cm(III)	Curium in the +3 oxidation state
$C_2O_4^{2-}$	Oxalate anion
CO_2	Carbon dioxide
CO_3^{2-}	Carbonate anion
Eu(III)	Europium in the +3 oxidation state
F^-	Fluoride anion
Fe	Iron
Fe(0), Fe0	Zero-valent iron, metallic iron
Fe^{2+}	Iron cation in the +2 oxidation state, ferrous cation
Fe^{3+}	Iron cation in the +3 oxidation state, ferric cation
$Fe_2Cl(OH)_3$	Ferrous iron chloride trihydroxide, hibbingite
$FeCO_3$	Iron (II) carbonate, ferrous carbonate, siderite
$Fe(CO_3)_2^{2-}$	Ferrous iron carbonate dianion
$Fe_2CO_3(OH)_2$	Ferrous iron carbonate dihydroxide, chukanovite

Fe_3O_4	Magnetite, iron (II,III) oxide
$FeOH^+$	Ferrous iron hydroxide ion
$Fe(OH)_2$	Ferrous iron hydroxide
$Fe(OH)_3^-$	Ferric iron trihydroxide ion
$Fe(OH)_4^{2-}$	Ferrous iron tetrahydroxide ion
FeS	Iron (II) sulfide, mackinawite
$FeSO_4$	Ferrous iron sulfate
$FeSO_4 \bullet H_2O$	Ferrous iron sulfate monohydrate, szomolnokite
$FeSO_4 \bullet 4H_2O$	Ferrous iron sulfate tetrahydrate
$FeSO_4 \bullet 7H_2O$	Ferrous iron sulfate heptahydrate, melanterite
H^+	Hydrogen cation
H_2	Hydrogen
HCl	Hydrochloric acid
HCO_3^-	Bicarbonate anion, hydrogen carbonate anion
H_2O	Water
HPO_4^{2-}	Hydrogen phosphate anion
$H_2PO_4^-$	Dihydrogen phosphate anion
H_2S	Hydrogen sulfide
HS^-	Hydrogen sulfide anion
HSO_4^-	Hydrogen sulfate anion
K	Potassium
K+	Potassium cation
$KB_5O_8 \bullet 4H_2O$	Potassium pentaborate
$K_2B_4O_7 \bullet 4H_2O$	Potassium tetraborate
$K_2Ca(SO_4)2 \bullet H_2O$	Potassium calcium sulfate hydrate, syngenite
KCl	Potassium chloride, sylvite
$K_2CO_3 \bullet 3/2H_2O$	Potassium carbonate hydrate
$KHCO_3$	Potassium bicarbonate, kalicinite
$K_8H_4(CO_3)_6 \bullet 3H_2O$	Potassium bicarbonate trihydrate
$KHSO_4$	Potassium bisulfate, mercallite
$K_3H(SO_4)_2$	Potassium hydrogen sulfate
$K_8H_6(SO_4)_7$	Potassium hydrogen sulfate, misenite
$K_2MgCa_2(SO_4)_4 \bullet 2H_2O$	Potassium magnesium calcium sulfate dihydrate, polyhalite

$KMgCl_3 \cdot 6H_2O$	Potassium magnesium chloride hexahydrate, carnallite
$KMgClSO_4 \cdot 3H_2O$	Potassium magnesium chloride sulfate trihydrate, kainite
$K_2Mg(SO_4)2 \cdot 4H_2O$	Potassium magnesium sulfate tetrahydrate, leonite
$KNaCO_3 \cdot 6H_2O$	Potassium sodium carbonate hexahydrate
$K_2NaH(CO_3)_2 \cdot 2H_2O$	Potassium sodium bicarbonate dihydrate, trona
$KNpO_2CO_3$	Potassium neptunium (V) oxide carbonate – (1:1:1) complex
K_2SO_4	Potassium sulfate, arcanite
Mg^{2+}	Magnesium cation
$MgB(OH)_4^+$	Magnesium orthoborate ion
$Mg_2CaCl_6 \cdot 12H_2O$	Magnesium calcium chloride dodecahydrate, tachyhydrite
$MgCl_2 \cdot 6H_2O$	Magnesium chloride hexahydrate, bischofite
$Mg_2Cl(OH)_3 \cdot 4H_2O$	Magnesium chloride hydroxide tetrahydrate, phase 3, korshunovskite
$Mg_3Cl(OH)_5 \cdot 4H_2O$	Magnesium chloride hydroxide tetrahydrate, phase 5
$MgCO_3$	Magnesium carbonate, magnesite
$MgCO_3 \cdot 3H_2O$	Magnesium carbonate trihydrate, nesquehonite
$Mg_4(CO_3)_3(OH)_2 \cdot 3H_2O$	Magnesium carbonate hydroxide trihydrate, hydromagnesite-4323
$Mg_5(CO_3)_4(OH)_2 \cdot 4H_2O$	Magnesium carbonate hydroxide tetrahydrate, hydromagnesite-5424
MgO	Magnesium oxide, periclase
$Mg(OH)_2$	Magnesium hydroxide, brucite
$MgOH^+$	Magnesium hydroxide ion
$MgSO_4$	Magnesium sulfate
$MgSO_4 \cdot H_2O$	Magnesium sulfate hydrate, kierserite
$MgSO_4 \cdot 6H_2O$	Magnesium sulfate hexahydrate, hexahydrite
$MgSO_4 \cdot 7H_2O$	Magnesium sulfate heptahydrate, epsomite
N_2	Nitrogen
Na	Sodium
Na^+	Sodium cation
$NaAm(CO_3)_2$	Sodium americium (III) carbonate
$NaAm(CO_3)_2 \cdot 6H_2O$	Sodium americium (III) carbonate hexahydrate
$NaB(OH)_4$	Sodium tetrahydroxyborate

$Na_2B_4O_7 \bullet 10H_2O$	Sodium tetraborate decahydrate, borax
$NaB_5O_8 \bullet 5H_2O$	Sodium pentaborate hexahydrate
$NaBO_2 \bullet 4H_2O$	Sodium metaborate tetrahydrate
$NaBO_2 \bullet NaCl \bullet 2H_2O$	Sodium metaborate sodium chloride dihydrate, teepleite
$Na_2Ca(CO_3)_2 \bullet 2H_2O$	Sodium calcium carbonate dihydrate, pirssonite
$Na_2Ca(SO_4)_2$	Sodium calcium disulfate, glauberite
$Na_4Ca(SO_4)_3 \bullet 2H_2O$	Sodium calcium trisulphate dihydrate, labile salt
$NaClO_4$	Sodium perchlorate
$NaCl$	Sodium chloride, halite
$Na_2CO_3 \bullet H_2O$	Sodium carbonate hydrate, thermonatrite
$Na_2CO_3 \bullet 7H_2O$	Sodium carbonate heptahydrate
$Na_2CO_3 \bullet 10H_2O$	Sodium carbonate decahydrate, natron
$Na_6CO_3(SO_4)_2 \bullet 2H_2O$	Sodium carbonate sulfate tetrahydrate, burkeite
$NaHCO_3$	Sodium bicarbonate, nahcolite
$Na_3H(CO_3)_2 \bullet 2H_2O$	Sodium hydrogen carbonate, trona
$Na_3H(SO_4)_2$	Sodium hydrogen disulphate
$NaK_3(SO_4)_2$	Sodium potassium disulphate, Aphthitalite, Glaserite
$Na_2Mg(SO_4)_2 \bullet 4H_2O$	Sodium magnesium sulfate tetrahydrate, bloedite
$NaNpO_2CO_3 \bullet 3.5H_2O$	Sodium neptunium (V) oxide carbonate hydrate – (1:1:1) complex
$Na_3NpO_2(CO_3)_2$	Sodium neptunium (V) oxide carbonate – (3:1:2) complex
$NaOH$	Sodium hydroxide
$NaPb_2(CO_3)_2(OH)$	Abellaite
Na_2SO_4	Sodium sulfate, thenardite
$Na_2SO_4 \bullet 10H_2O$	Sodium sulfate decahydrate, mirabilite
Nd	Neodymium
Nd^{3+}	Neodymium cation in the +3 oxidation state
$NdCl_3$	Neodymium (III) chloride
NdF_3	Neodymium (III) fluoride
$Nd(OH)_3$	Neodymium (III) hydroxide
$Nd(OH)^{2+}$	Neodymium hydroxide cation
NH_3	Ammonia
NO_3^-	Nitrate anion

Np	Neptunium
Np^{4+}	Neptunium cation in the +4 oxidation state
Np^{5+}	Neptunium cation in the +5 oxidation state
NpO_2^+ or $Np(V)O_2^+$	Neptunyl cation – Aqueous form of neptunium in the +5 oxidation state
$NpO_2CO_3^-$	Neptunium (V) oxide carbonate ion – (1:1) complex
$NpO_2(CO_3)_2^{3-}$	Neptunium (V) oxide carbonate ion – (1:2) complex
$NpO_2(CO_3)_3^{5-}$	Neptunium (V) oxide carbonate ion – (1:3) complex
NpO_2OH	Neptunium (V) oxide hydroxide
$NpO_2(OH)_2^-$	Neptunium (V) oxide hydroxide ion – (1:2) complex
O	Oxygen
O_2	Molecular oxygen
OH^-	Hydroxide anion
Pb	Lead
Pb^{2+}	Lead cation – Aqueous form of the lead at the +2 oxidation state
$PbCl_2$	Lead (II) chloride
$PbCl^+$	Chloridoplumbate (II) ion
$PbCl_3^-$	Trichloridoplumbate (II) ion
$PbCO_3$	Lead (II) carbonate, cerussite
$Pb(CO_3)_2^{2-}$	-Lead (II) carbonate ion
$Pb(CO_3)Cl^-$	Lead (II) carbonate chloride ion
$Pb(CO_3)(OH)$	Lead hydroxy carbonate
PbO	Lead (II) oxide, litharge
$PbOH^+$	Lead (II) hydroxyl ion
$Pb(OH)_2$	Lead (II) hydroxide
$Pb(OH)_3^-$	Lead (II) hydroxyl complex ion
$Pb_2(OH)_2CO_3$	Lead (II) hydroxide carbonate
$Pb(SO_4)$	Lead sulfate
PO_4^{3-}	Phosphate anion
Pu	Plutonium
Pu^{3+}	Plutonium cation in the +3 oxidation state
Pu^{4+}	Plutonium cation in the +4 oxidation state

PuO_2	Plutonium (IV) oxide
$Pu(OH)_3$	Plutonium Hydroxide
SO_4^{2-}	Sulfate anion
Th^{4+}	Thorium cation in the +4 oxidation state
$Th(CO_3)_5^{6-}$	Thorium (IV) pentacarbonyl ion complex
ThO_2	Thorium dioxide
$Th(OH)_2^{2+}$	Thorium (IV) hydroxide ion – (1:2) complex
$Th(OH)^{3+}$	Thorium (IV) hydroxide ion – (1:3) complex
$Th(OH)_4$	Thorium hydroxide
$Th_4(OH)_{12}^{4+}$	Thorium (IV) hydroxide ion – (4:12) complex
$Th_6(OH)_{15}^{9+}$	Thorium (IV) hydroxide ion – (6:15) complex
$Th(OH)_3CO_3^-$	Thorium (IV) hydroxide carbonate ion – (1:3:1) complex
$ThOn(OH)_4^{-2n}\cdot xH_2O$	Thorium (IV) oxide hydroxide hydrate ion – (n:-2n) complex
$Th(SO_4)_3^{2-}$	Thorium (IV) sulfate ion – (1:3) complex
$Th(SO_4)_2$	Thorium (IV) sulfate
$Th(SO_4)_2\bullet 8H_2O$	Thorium (IV) sulfate octahydrate
$Th(SO_4)_2\bullet 9H_2O$	Thorium (IV) sulfate enneahydrate
$Th(SO_4)_2\bullet K_2SO_4\cdot 4H_2O$	Thorium (IV) sulfate potassium sulfate tetrahydrate
$Th(SO_4)_2\bullet 2K_2SO_4\cdot 2H_2O$	Thorium (IV) sulfate potassium sulfate dihydrate
$Th(SO_4)_2\bullet 3.5K_2SO_4$	T-horium (IV) sulfate potassium sulfate
$Th(SO_4)_2\bullet Na_2SO_4\bullet 6H_2O$	Thorium (IV) sulfate sodium sulfate hexahydrate
U^{4+}	Uranium cation in the +4 oxidation state
U^{6+}	Uranium cation in the +6 oxidation state
UO_2^{2+}	Uranium oxide cation in the +6 oxidation state

This page intentionally left blank.

GEOCHEM-1.0 INTRODUCTION

The Waste Isolation Pilot Plant (WIPP) is owned by the U.S. Department of Energy (DOE), operated by the management and operating contractor, and must be recertified every 5 years by the U.S. Environmental Protection Agency (EPA). The EPA's assessment of the WIPP's ability to comply with containment requirements specified in 40 Code of Federal Regulations (CFR) 191.13 is based, in part, on performance assessment (PA) calculations. WIPP PA calculations are carried out by the DOE using linked computer models that calculate the probabilities of cumulative radionuclide releases from the disposal system during the 10,000 years following closure. These computer models and many of the parameters included in the calculations are based on conceptual models that describe the expected performance of the disposal system.

The WIPP chemistry-related conceptual models include: Gas Generation, Chemical Conditions, Dissolved Actinide Source Term, and Colloidal Actinide Source Term. Since the Conceptual Models Peer Review, the DOE has continued studying processes related to WIPP repository chemistry. Consequently, additional information has become available regarding actinide solubilities, the magnesium oxide [MgO] engineered barrier, and the roles of borate, lead, iron, corrosion, and colloids in the repository. Some of this additional information has been incorporated into the Gas Generation, Chemical Conditions, Dissolved Actinide Source Term, and the Colloidal Actinide Source Term models as WIPP recertification has progressed through three recertification cycles. The purpose of Appendix GEOCHEM is to document the evolution of the conceptual models, the process models, the process-model parameterization, and quantification of uncertainty.

GEOCHEM-1.1 How Chemistry is Incorporated in Performance Assessment

Knowledge of the repository system chemistry is essential to quantify gas generation rates, brine production rates, and to determine how and if contaminants (in this case actinides) are mobilized in repository brine. Actinides [An] may be mobilized in brine in two principal ways: (1) as dissolved species and (2) as colloidal species.

Quantities of dissolved actinides, lanthanides, and transition metals depend on the available brine volume and composition. One of the most important variables in brine composition is pH. Actinide, lanthanide, and transition metal solubilities, in general, increase with decreasing pH. Although amphotericity is not routinely observed, there are some speciation scenarios where high solubilities can be observed at high pH (pH> 12) as well. To control the pH within an advantageous region, the DOE is emplacing MgO in the waste-disposal region of the WIPP. The reaction of MgO with moisture in the air or brine yields brucite, which buffers the system pH to mildly alkaline pH values (pH ~9). The reaction of MgO and aqueous solution also consumes dissolved carbon dioxide [CO_2] and buffers the fugacity of CO_2 (U.S. DOE 2014, Appendix MgO, Section MgO-1.0).

Concentrations of actinides, lanthanides, and transition metals also depend on the redox potential (E_h) within the repository. Near-field conditions will be strongly reducing due to enormous quantities of metallic iron [Fe^0] manifested as steel drums. Although plutonium [Pu] can exist in multiple oxidation states in the external environment, only the lower-solubility oxidation states

[Pu(III) and Pu(IV)] will persist in the repository (U.S. DOE 2019, Appendix SOTERM, Section SOTERM-3.4.3).

Temperature is also a major influence on actinide, lanthanide, and transition metal behavior. However, at the depth of disposal (2,150 ft below ground surface), the repository temperature is constant at ~27 degrees centigrade (°C) (300 Kelvin [K]). When experimental data is collected at temperatures that deviate from ~27°C (300 K), temperature effects must be evaluated and considered.

Within the constraints to pH, redox potential, temperature, and CO_2 fugacity described above, the chemistry can be analyzed in a systematic way utilizing both experiment and modeling. To assess which reactions and phases are important to WIPP performance, a protocol has been established, and is described below.

GEOCHEM-1.1.1 Features, Events, and Processes

PA begins with identifying, classifying, and screening of Features, Events, and Processes (FEPs), which is discussed in further detail in the Compliance Certification Application (CCA), Appendix SCR (U.S. DOE 1996). The screening process indicates which FEPs will be included in the conceptual models and PA simulations. *Features* are characteristics of the repository, such as waste drums, sacks of MgO, etc. *Events* are phenomena that occur to the repository and lead to changed repository conditions, such as borehole intrusion. *Processes* are physical, chemical, and biological phenomena that occur in the repository setting, such as corrosion of steel, microbial degradation of organic matter, formation of colloids, precipitation of solid phases, and speciation of elements and molecules. FEPs are screened in or out of PA according to probability, consequence or by regulation. A FEPs screening has been performed prior to each PA, the results of which determine the set of features, events, and processes to be included in the analysis.

The WIPP PA implements the FEPs that determine repository performance, as shown in Figure GEOCHEM-1, by first creating a conceptual model. Next, a process model is developed and parameterized, and finally, probabilistic methods are used to quantify uncertainty.

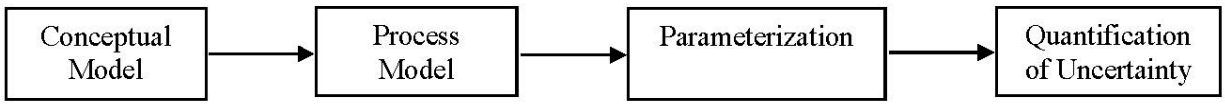

Figure GEOCHEM-1. Implementation Sequence Employed in WIPP PA.

The implementation sequence is defined and described below.

GEOCHEM-1.1.2 Conceptual and Process Models

A *conceptual model* is developed using a list of assumptions that are made so that FEPs can be modeled. Each section in this appendix begins with a discussion of the assumptions of the individual conceptual model.

A *process model* is the mathematical description of the chemical or physical phenomena. In the WIPP PA, the process model simulates how the process will proceed.

GEOCHEM-1.1.3 Parameterization

Parameters are numerical or other measurable factors forming one of a set that defines a system or sets the conditions of operation. These include fixed parameters in which the value is not varied in the calculation. There are also parameters that vary as described in the section on quantification of uncertainty.

GEOCHEM-1.1.4 Quantification of Uncertainty

Predictive modeling of natural processes, like those pertinent to deep geologic disposal of radioactive waste, is inherently uncertain (Helton et al. 1998). No predictive tool can accurately account for all natural processes or variations in material properties. Therefore, analysis of these uncertainties is needed to understand the limits of performance simulations. Analysis of uncertainty begins with identification of the sources of uncertainty. Uncertainties fall into categories like: uncertainty in the geologic future, model uncertainty, and parameter uncertainty. To use the paradigm that has been developed for PA, uncertainties could be categorized as: uncertainty in the conceptual model, uncertainty in the process model, and uncertainty in parameterization of the process model, as shown in Figure GEOCHEM-2.

Figure GEOCHEM-2 shows how uncertainty in the geological future, model uncertainty, and parameter uncertainty fit into the PA paradigm of conceptual models, process models, and parameters. The fourth element of the PA paradigm is quantification of uncertainty, which expands the domain of model simulations, and is also shown in Figure GEOCHEM-2. It creates variability in model simulations.

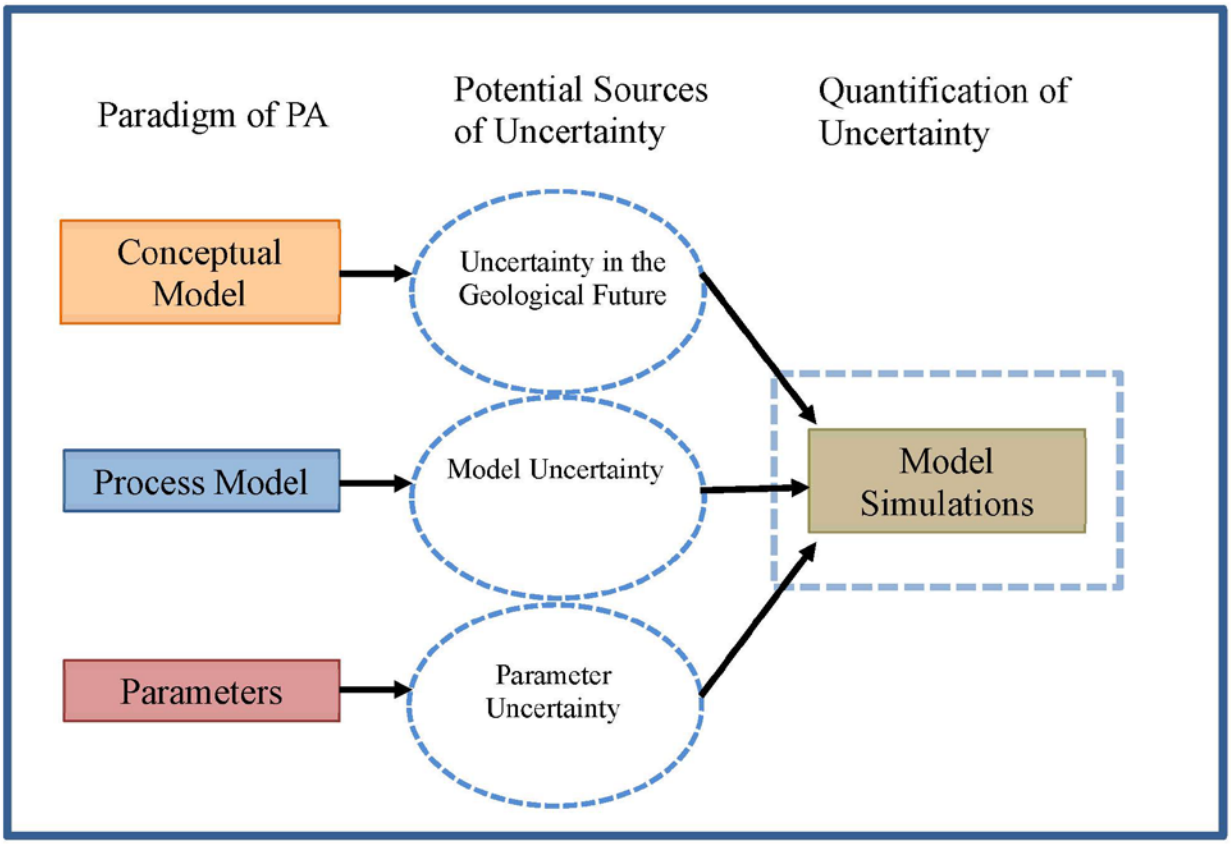

Figure GEOCHEM-2. Representation of How Uncertainty is Incorporated

Strategies for handling uncertainty once identified are:

1. Demonstrating that the uncertainty is irrelevant. For example, uncertainty in a certain process is not important because the safety case is controlled by other processes. This can be done via FEPs analysis that shows there is no adverse consequence associated with an uncertainty or sensitivity studies. Typically, a sensitivity study is used to rank the significance of individual sampled parameters on the overall calculated result. An example application of this approach can be seen in GEOCHEM-2.3.3 and GEOCHEM-2.3.4, where the MgO hydration rate that was once a sampled parameter has become a fixed parameter because the sensitivity analysis performed by Kirchner (2013) shows that radionuclide releases are not sensitive to the MgO hydration rate.
2. Bounding the uncertainty and showing that even the bounding case gives acceptable results. For example, in some cases the WIPP PA includes or excludes processes or assigns parameter values that will lead to an over-estimate of releases. An application of this approach can be found in GEOCHEM-3.2.8, where the process model introduced for dissolved iron only includes Fe^{2+} interactions with inorganic species in the brines. Interaction with organic species in the brines is omitted, an omission that will likely result in higher dissolved actinide concentrations.

3. Ruling out an uncertainty, usually on the grounds of very low probability of occurrence, or because other consequences, were the uncertainty to happen, would far outweigh concerns over WIPP performance (for example a direct meteorite strike). An application of this approach can be found in GEOCHEM-4.2.1, where the DOE has decided to omit a possible Am-tetraborate species discussed during the 2014 Compliance Recertification Application (CRA-2014) (U.S. DOE 2014) because it is not likely to exist, and the interactions with carbonate species are likely to have a much greater impact on Am^{3+} solubility than borate.
4. If one has observations of the system being studied, a comparison can be made between the model simulations and the observations. The discrepancies can be used to refine the model or simply to quantify the uncertainty. For a deep geologic repository like the WIPP, there are no post-closure system observations. However, there may be observations of subsystems that have been made in a laboratory or in a field setting which can be used for model refinement or quantification of uncertainty. An example application of this approach can be seen in GEOCHEM-4.4, where laboratory observations are used to quantify uncertainty in the dissolved actinide source term process model and parameters (Domski 2019b).
5. Using a probabilistic approach to address the uncertainty explicitly.

The WIPP PA uses all of the approaches listed above, but relies heavily on the explicit probabilistic approaches listed as numbers 4 and 5. PA determines how likely certain outcomes for the WIPP are if some aspects of the system are not exactly known. This includes both "epistemic" uncertainty (also known as systematic uncertainty or subjective uncertainty) and "aleatory" uncertainty (also known as stochastic uncertainty) (U.S. DOE 2019, Appendix PA, Section PA-5.3).

GEOCHEM-1.1.4.1 Epistemic Uncertainty

Epistemic uncertainty is the scientific uncertainty in the model and parameters. It arises from a lack of knowledge about processes and parameter values that are inputs to the computational implementation of PA. An example of epistemic uncertainty for the WIPP PA is variability in reported iron corrosion rates. In principle, epistemic uncertainties are reducible, for example, by making more experimental measurements or by refining a model.

Implementation involves sampling certain parameter values from probability distributions that cover the range of uncertainty. Latin Hypercube Sampling (LHS) is used to define 100 sets of uncertain parameters. One realization of the sampled parameters is a "vector." The group of 100 vectors is a "replicate." The replicate essentially covers the full range of all the uncertain parameter distributions. LHS minimizes the correlation between parameters unless directed otherwise. Three replicates are run to determine the 95 percent confidence limit on mean normalized release.

GEOCHEM-1.1.4.2 Aleatory Uncertainty

Aleatory uncertainties are, for all practical purposes, irreducible due to some inherent randomness. In the context of the WIPP, aleatory uncertainty arises from a lack of knowledge

about future events. A good example of this is timing and location of future drilling events. A "future" in PA is defined as a combination of possible events over 10,000 years. The WIPP PA treats aleatory uncertainty through Monte Carlo sampling methods on possible futures. Ten thousand futures are evaluated for each vector to assign a probability to releases. Order statistics are used to generate Complementary Cumulative Distribution Functions (CCDFs). The results from all 100 vectors are combined to determine mean releases for a single replicate (and percentiles). Three replicates are used to ensure the maximum CCDFs generated exceed the 99th percentile of the population of CCDFs with at least a 0.95 probability.

GEOCHEM-1.2 Initial and Boundary Conditions

This section provides an overview of the site conditions and waste characteristics.

GEOCHEM-1.2.1 Geologic Setting

The WIPP repository is located 2,150 ft below ground surface (bgs) in the Permian Salado Formation. In the area around the WIPP, the Salado Formation is a relatively thick bedded salt, composed mainly of layers of impure halite [NaCl] with interbedded marker beds (MB) of anhydrite [$CaSO_4$] and polyhalite [$K_2MgCa_2(SO_4)_4 \bullet 2H_2O$], clay, and mudstone (Lambert 1992). Figure GEOCHEM-3 depicts the general stratigraphic column of geologic units at the WIPP site (U.S. DOE 2009, Appendix HYDRO).

The low permeability of the Salado Formation (< 10^{-20} square meters [m^2]; Roberts et al. 1999) provides a significant hydrologic barrier between the repository and more transmissive water-bearing strata. A more permeable, transitory region forms around the repository in response to the disturbance in the stress field caused by repository excavation. This region is the Disturbed Rock Zone (DRZ) (U.S. DOE 2004, Chapter 6). The DRZ is small relative to the thickness of the Salado Formation surrounding the repository (U.S. DOE 2004, Chapter 6).

The Salado Formation is underlain by the Castile Formation. The Castile Formation is mainly composed of thick beds of high-purity halite alternating with thick beds of interlaminated carbonate and anhydrite. The Castile Formation has been significantly deformed in some areas around the WIPP and pressurized brines are associated with the deformed volumes (U.S. DOE 2004).

The Rustler Formation overlies the Salado Formation and is composed of evaporitic and dolomitic members named from bottom to top: Los Medanos, Culebra Dolomite, Tamarisk, Magenta Dolomite, and Forty-Niner. The Culebra Dolomite is mostly composed of dolomite [$CaMg(CO_3)_2$], with minor amounts of anhydrite [$CaSO_4$] or gypsum [$CaSO_4 \bullet 2\ H_2O$] (Lambert 1992). The Culebra Dolomite is the most transmissive continuously saturated unit above the WIPP repository. Apart from potential direct brine releases to the surface, it provides the most direct pathway from the repository to the accessible environment for human intrusion scenarios (U.S. DOE 2004, Chapter 2).

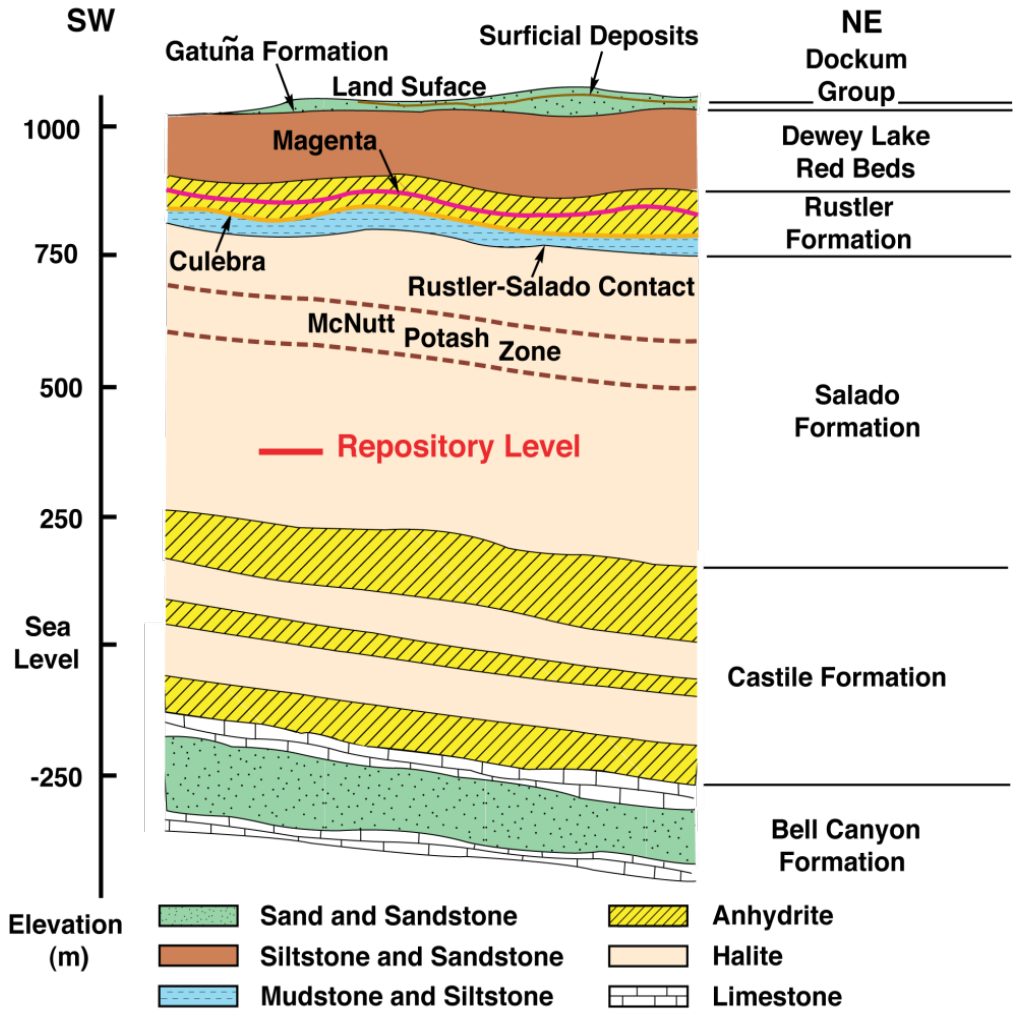

Figure GEOCHEM-3 General Stratigraphic Column of Geologic Units at the WIPP Site (U.S. DOE 2009, Appendix HYDRO)

GEOCHEM-1.2.2 Hydrologic Setting

The presence of brine in the WIPP repository is important to modeling of radionuclide releases. Several release mechanisms for the WIPP are related to the presence of brine in the repository at some time during the 10,000-year regulatory period. There are different ways in which antecedent brine could enter the repository.

Although the permeability of the undisturbed Salado Formation is low (10^{-24} to10^{-21} m^2), excavation of the repository affects both the hydraulic gradient and permeability of the DRZ, resulting in a low flow of interstitial brine from the halite to the anhydrite marker beds and into the repository. During operations, small brine seeps have been observed in the underground workings at the WIPP (U.S. DOE 2004, Chapter 6).

Once active institutional control at the WIPP ends (100 years after closure), intrusions into the repository might occur while drilling for natural resources such as oil or natural gas. Intrusions

could be a pathway for large volumes of water entering the repository if, for example, an intruding borehole passes through the repository into a pressurized brine region in the Castile Formation. Under such a scenario, Castile brine could flow up the borehole into the repository through the borehole (scenarios S2, S3, and S6 in the WIPP PA). If an intruding borehole does not encounter pressurized Castile brine (scenarios S4 and S5 in the WIPP PA), there is still an enhanced pathway for Salado brine, but no enhanced pathway for Castile brine to enter the repository.

GEOCHEM-1.2.3 Waste Characteristics

The WIPP is a repository for permanent disposal of defense-related transuranic (TRU) waste. The waste disposed in the WIPP typically contains residue from laboratory operations (glassware, paper goods, by-products from laboratory analysis) and materials from demolition and clean-up of facilities contaminated with TRU isotopes. This can include cellulosic, plastic, and rubber (CPR) materials. It can also contain contaminated soil, cement, and metal. Also, organic complexants including citrate [$(CH_2COO)_2C(OH)(CO_2)^{3-}$], acetate [$CH_3COO^-$], oxalate [$C_2O_4^{2-}$], and EDTA [$(CH_2COO)_2N(CH_2)_2N(CH_2COO)_2^{4-}$] have been identified in certain waste streams destined for the WIPP (Van Soest 2018). The impact of organic complexation on TRU solubility and mobility is a focus of DOE's geochemical investigations.

The waste emplaced in the repository has no limit on adsorbed liquid within the waste, but cannot have more than 1 percent free liquid by volume (U.S. DOE 2016), so free liquid in the waste is not expected to be a significant source of water in the repository.

GEOCHEM-1.2.4 Emplacement Material Characteristics

The WIPP repository will contain a large quantity of metallic iron and lead due to the use of iron and lead-based containers for much of the emplaced TRU waste. In addition, cardboard (cellulose) and plastic are added during operations in the form of slip sheets and bags of MgO placed on top of waste stacks.

GEOCHEM-1.2.5 Repository Conditions

Post-closure repository conditions that could potentially affect chemistry in the repository are briefly summarized in this section. These include repository pressure and environment, repository temperature, water content and relative humidity, and brine volumes.

GEOCHEM-1.2.5.1 Repository Pressure and Environment

The lithostatic pressure (Stein 2005; U.S. DOE 2019, Appendix SOTERM, Section SOTERM-2.1.1) at repository depth is about 15 megapascal (MPa) (148 atmosphere [atm]), which is equivalent to the lithostatic stress at the repository level; a hydrostatic pressure of about 8 MPa (79.0 atm) at the bottom of an intrusion borehole at repository depth. This pressure can be reestablished after repository closure due to salt creep and gas generation (Mendenhall and Gerstle 1995). However, PA simulations predict pressure may not be fully restored to lithostatic pressure even by the end of the 10,000-year period of WIPP performance (U.S. DOE 2019, Appendix PA, Section PA-8.3). Final pressures may range from 6 to 15 MPa (in the undisturbed scenario) and from 0.1 to 15 MPa (in the disturbed scenarios) considered in PA. The pressure in

the repository after closure cannot significantly exceed the far-field confining stress of about 15 MPa (U.S. DOE 2019, Appendix SOTERM, Section SOTERM-2.2.1).

The effect of pressure on actinide concentration is not considered in the WIPP PA (U.S. DOE 2019, Appendix SOTERM, Section SOTERM-2.2.1).

Soon after repository closure, the self-sealing salt will geologically isolate the repository. Very shortly thereafter, the excess iron and microbial activity is predicted to consume all of the oxygen, initially leading to an anoxic environment.

GEOCHEM-1.2.5.2 Repository Temperature

The ambient pre-emplacement temperature at the WIPP repository horizon is 300 K (27 ºC [80 degrees Fahrenheit {ºF}]) (Bennett et al. 1996). The materials introduced into the WIPP may undergo exothermic reactions: MgO hydration, MgO carbonation, microbial degradation, corrosion, and cement hydration. The potential impact of these reactions on repository temperature was re-evaluated for CRA-2014 (see U.S. DOE 2019, Appendix SCR, Section SCR-6.3.4.1.3). A conclusion of that study was that the temperature may rise to 39 ºC, a 12 ºC increase. However, elevated temperatures are expected to persist for only a few years or decades because of the high thermal conductivity of salt. A potential transitory increase in temperature is also discussed in Sanchez and Trellue (1996) and Wang and Brush (1996). For the purposes of PA and all chemistry-related calculations, the temperature of the WIPP underground repository is assumed to be constant with time at 300 K (27 ºC [80 ºF]) (U.S. DOE 2019, Appendix PA, Section PA-4.2.1).

The fact that repository temperature will vary slightly over time introduces a small uncertainty in calculated results. However, when compared to other uncertainties inherent in the measurements and calculations discussed in the appendix, the uncertainty due to temperature variation in the repository is expected to be very small. For this reason, uncertainty due to temperature variations in the repository is not considered in the WIPP PA calculations.

GEOCHEM-1.2.5.3 Water Content and Relative Humidity

The expected initial brine content in the repository is determined by the Salado Formation in which the WIPP is excavated. Small quantities of intergranular and intragranular Salado brines are associated with the salt at the repository horizon. The amount of brine present as inclusions in the salt is between 0.057 to 3 weight percent based on what was measured in pre-excavation salt (Skokan et al. 1987; Powers et al. 1978). The presence of brine in the WIPP creates an atmosphere of ~73 percent relative humidity (RH) (Domski and Sisk-Scott 2019). The RH of the repository will be determined by the vapor pressure of saturated brine at the repository temperature.

GEOCHEM-1.2.5.4 Brine Volumes

The minimum brine volume, defined as the lowest amount of brine required to be in the repository in order for a Direct Brine Release (DBR) to occur (and multiples thereof), are needed to derive the initial concentrations of organic ligands used in baseline solubility calculations. Actinide solubilities (the sums of the concentrations of all dissolved actinide species in chemical

equilibrium with actinide-bearing solid phases) are often referred to as the "baseline solubilities" because they comprise unique values predicted using thermodynamic models for each actinide analog element and WIPP brine under expected near-field chemical conditions. Baseline solubilities are inputs for PA simulations. The brine volume used to calculate concentrations is chosen prior to the PA simulation. The brine volume chosen for CRA-2009 for calculating baseline solubilities is the minimum brine volume (17,400 cubic meters [m^3]) for DBR. The intent was to maximize the concentration of organic ligands mobilized in the brine, which is "inventory-limited." Using the minimum brine volume is a conservative estimate in terms of actinide releases, since larger volumes would dilute the organic ligands and lower the actinide solubility. The *initial* concentrations of acetate, citrate, oxalate, and EDTA, in EQ3/6 calculations, are defined by their initial Performance Assessment Inventory Report (PAIR) inventory divided by the assumed brine volume.

In more recent PA simulations for CRA-2014 and CRA-2019, PA used five sets of concentrations based on five brine volumes: the minimum brine volume as well as 2, 3, 4, and 5 times the minimum. PA simulations (i.e., PANEL) are run using the five baseline solubilities to better correlate repository brine volumes with organic ligand concentrations. Later, CCDFGF code then interpolates between PANEL code outputs.

The minimum brine volume is given in Equation (GEOCHEM.1).

$$(V_{brine})_{Min} = S_{b,med}\ V_{void,consolidated}\ N_{rooms,equivalent} \qquad \text{(GEOCHEM.1)}$$

Where

$(V_{brine})_{Min}$ = minimum brine volume (in the entire repository)

$S_{b,med}$ = median sampled residual brine saturation

$V_{void,consolidated}$ = consolidated void volume of a single room

$N_{rooms,equivalent}$ = number of equivalent repository rooms

The minimum brine volume was most recently recalculated by Clayton (2008) to be 17,400 m^3. This value corresponds to a consolidated void volume of a single room of 523 m^3, 120 equivalent rooms in the repository, and a median value for the sampled residual brine saturation of 0.276. These parameters were calculated based on the method recommended by Stein (2005), except that the drilling fluid hydrostatic pressure (8 MPa) was used in evaluating the consolidated void volume rather than the lowest pressure realization at 10,000 years.

GEOCHEM-2.0 GAS GENERATION AND BRINE PRODUCTION

Some of the materials in this section may also be reproduced from Appendix PA where necessary for clarity (U.S. DOE 2019, Appendix PA, Section PA-4.2). Throughout the discussion, changes that have been agreed to with the EPA through CRA-2014 comment resolution and DOE/EPA technical exchanges are noted.

GEOCHEM-2.1 Gas Generation and Brine Production Conceptual Model

The Gas Generation Conceptual Model includes gas generation by anoxic corrosion of elemental iron (manifested as steel) and by microbial degradation of CPR materials; this conceptual model also includes removal of CO_2 by reaction with the MgO emplaced as an engineered barrier (Wilson et al. 1996). The Gas Generation Conceptual Model used in the WIPP PA is the average stoichiometry model in order to differentiate it from alternative gas generation conceptual models considered for the CCA (Wilson et al. 1996). Information used to develop this conceptual model included the quantities and compositions of WIPP waste, observation of brine seepage into excavated salt, Salado and Castile brine compositions, observation of halophilic microbes in brine seepage and salt lakes near the WIPP site, experimental investigation of steel corrosion rates, experimental investigation of microbial degradation of CPR materials, and measured rates of radiolytic gas generation from water and plastics (Wilson et al. 1996). Radiolytic gas generation from brine has been included in CRA-2019, but that from CPR is continued to be screened out (Day 2019). Gas generation from lead corrosion has been screened out of past PA calculations. Due to the expected increase in lead inventory and the capability of passivation in lead systems, the potential for lead gas corrosion has been re-evaluated and screened out of PA calculations for CRA-2019 (Kirkes 2019; U.S. DOE 2019, Appendix SCR Section SCR-6.5.1.4.3). Assumptions about gas generation and brine production discussed in this section were part of the original Gas Generation Conceptual Model (U.S. DOE 1996; Wilson et al. 1996) and have not changed since that time. This section provides a brief outline of the assumptions that make up the Gas Generation Conceptual Model.

GEOCHEM-2.1.1 Homogeneous Gas Generation

Gas generation will take place homogeneously throughout the repository because of the assumed homogeneous distribution of waste.

Corrosion reactions between brine and iron waste containers can produce H_2, and reactions between microbes, brine, and CPR materials can yield CO_2, N_2, H_2S, and CH_4. The consumable materials are assumed to be homogeneously distributed throughout the waste disposal regions. A separate analysis examined the potential effects on PA results of spatially varying iron and CPR material concentrations, and concluded that PA results are not affected by representing these materials with spatially invariant concentrations (Hansen et al. 2003).

GEOCHEM-2.1.2 Oxygen Depletion

While the repository is open, oxygen is present. Alpha radiolysis of the water in the waste and brine could consume water and brine, producing hydrogen and oxygen. A variety of gases can also be produced by the alpha radiolysis of cellulosics, rubbers, and plastics in the waste (Molecke 1979). In the model, oxygen is assumed to be quickly consumed by corrosion of metals.

GEOCHEM-2.1.3 Corrosion of Ferrous Metals

Because oxygen trapped in the repository upon closure is quickly consumed and an anoxic environment is established, anoxic conditions are assumed to occur in the repository soon after the shafts are sealed. For these reasons, all iron corrosion will occur under anoxic conditions.

GEOCHEM-2.1.4 Corrosion of Non-Ferrous Metals

The Gas Generation Conceptual Model does not presently account for corrosion of non-ferrous metals. In past PA calculations it was reasonable to assume that gas generation from lead was insignificant based on PAIR inventory. Due to the expected increase in lead PAIR inventory and the availability of some experimental lead corrosion data, the potential for gas generation has been re-evaluated and screened out of PA calculations for CRA-2019 (Kirkes 2019; U.S. DOE 2019, Appendix SCR, Section SCR-6.5.1.4.3).

GEOCHEM-2.1.5 Microbial Degradation of CPR Materials

The original assumptions of the conceptual model for microbial gas generation are (U.S. EPA 2008; U.S. DOE 2019, Appendix SOTERM):

1. Microbial degradation of CPR materials in the waste and waste emplacement materials may produce CO_2, N_2, H_2S, and CH_4.
2. A detailed discussion of the current understanding of WIPP microbial processes is given in Appendix SOTERM, Chapter 4. Based on energy yield, CPR material degradation is assumed by PA to occur in the following sequence:

   denitrification → sulfate reduction → methanogenesis.
3. CPR material degradation is represented by a zero-order reaction rate, so the microbial gas generation rate is independent of the CPR concentration. However, the total moles of organic carbon that can be consumed by microbes is tracked during the PA simulation, and when depleted gas generation from biodegradation ceases.
4. CO_2 will be removed from the repository brines and gas phase by reaction with the MgO emplaced as an engineered barrier, so CO_2 generated from CPR material degradation will not significantly affect repository gas pressures, nor will it passivate steel.
5. The amount of N_2 produced by microbial degradation of CPR materials will be negligible because of limited nitrate in the waste. The amount of N_2 is treated as H_2 in PA calculations.
6. The amount of H_2S produced by microbial degradation of CPR material will be negligible because of limited sulfate in the waste. The amount of H_2S is treated as H_2 in PA calculations.

In the CCA, there were assumptions about the importance of the three microbial degradation reactions. The original thesis for microbial degradation of CPR materials was that processes proceeded sequentially as shown in assumption 2 above, and that the first two processes, denitrification and sulfate reduction, were limited in their impact on gas generation because of limited quantities of nitrates and sulfates in the waste emplaced in the WIPP. Once the nitrates

and sulfates from the waste were consumed, the only mechanism for CPR degradation would be methanogenesis. As a result, the quantities of N_2 and H_2S produced by microbial degradation of CPR would be negligible.

However, EPA (2008) questioned the assumption regarding depletion of sulfate. The EPA argued that the amount of sulfate in the repository will not be limited by sulfate in the waste, but by the presence of anhydrite in the formation. Therefore, sulfate is expected to be present in WIPP brines in steady supply. Because of the potential availability of substantial amounts of sulfate for CPR material degradation reactions, the EPA pointed out that microbial populations never consume CPR materials through methanogenesis. Therefore, methanogenesis is not included as a degradation pathway in CRA-2019 due to uncertainty about the availability of sulfate (see U.S. DOE 2019, Appendix SOTERM, Section SOTERM-4.1.1) in the DRZ, and its exclusion is a conservative assumption relative to the amount of carbon dioxide that could be produced (Leigh et al. 2005). In addition, substantial quantities of H_2S could be produced, and passivation of steel by H_2S could occur.

GEOCHEM-2.1.6 Steel Passivation

Substantial quantities of hydrogen sulfide [H_2S] and carbon dioxide [CO_2] may be produced during the lifetime of the repository. However, it is assumed that CO_2 generated by microbial degradation of CPR will not passivate steel because CO_2 will be consumed by reaction with the MgO emplaced as an engineered barrier.

The DOE considered passivation of steel by H_2S in CRA-2014 by including the relevant reactions (see U.S. DOE 2014, Appendix PA, Section PA-2.1.1):

$$Fe(s) + H_2S(g) \rightarrow FeS(s) + H_2(g)$$ Reaction 3 in Table GEOCHEM-1

$$Fe(OH)_2(s) + H_2S(g) \rightarrow FeS(s) + 2H_2O(l)$$ Reaction 4 in Table GEOCHEM-1

Table GEOCHEM-1. Iron Corrosion Reactions in the WIPP Gas Generation Process Model

		Iron Corrosion Reactions
1	CCA [A]	$Fe(s) + 2H_2O(l) \rightarrow Fe(OH)_2(s) + H_2(g)$
2	CCA [A]	$3Fe(s) + 4H_2O(l) \rightarrow Fe_3O_4(s) + 4H_2(g)$
3	CRA-2014 [B]	$Fe(s) + H_2S(g) \rightarrow FeS(s) + H_2(g)$
4	CRA-2014 [B]	$Fe(OH)_2(s) + H_2S(g) \rightarrow FeS(s) + 2H_2O(l)$

[A]These reactions were considered for gas generation starting with the CCA and have been included in the CCA and subsequent recertifications. They will be included in CRA-2019 as well. [B]These reactions were included in the CRA-2014 PA, but will not be included in the CRA-2019 PA.

GEOCHEM-2.1.7 Radiolysis

Radiolysis was fully considered in the CCA based on projected waste PAIR inventory at the time. It was dismissed then as a relatively small contributor to overall gas generation. In CRA-

2004, CRA-2009, and CRA-2014, it was assumed that radiolysis of water in the waste and brine and radiolysis of plastic and rubber in the waste did not contribute to the volume of gas generated (U.S. DOE 2019, Appendix SOTERM, Section 3.4). However, in CRA-2019, radiolysis of water in the waste and brine will be included as a gas generation mechanism with the process model and parameterization for gas generation due to radiolysis documented in Appendix PA, Section PA-4.2.5. Radiolysis of cellulose, plastics, and rubber in CRA-2019 will continue to be excluded as a gas generation mechanism, as documented in U.S. DOE 2019, Appendix SCR, Section SCR-6.5.1.7.3.

GEOCHEM-2.2 Gas Generation and Brine Production Process Models

Changes made to the PA Process Model based on EPA and DOE agreement during CRA-2014 comment resolution and DOE/EPA technical exchanges are noted.

Gas production is assumed to result from corrosion of steel, the microbial degradation of CPR materials, and radiolysis. The gas generation due to radiolysis is discussed in Day (2019). The remaining section only discusses gas generation from corrosion of steel and microbial degradation of CPR. Thus, the gas generation rate q_{rg} is written as:

$$q_{rg} = q_{rgc} + q_{rgm} + q_{rgs} \qquad \text{(GEOCHEM.2)}$$

where q_{rgc} is the rate of gas production per unit volume of waste (kg/m^3/s) due to corrosion of iron-based metals, q_{rgs} is the rate of gas production per unit volume of waste (kg/m^3/s) due to sulfidation of iron-based metals, and q_{rgm} is the rate of gas production per unit volume of waste (kg/m^3/s) due to microbial degradation of CPR materials. Furthermore, the brine production rate q_{rb} is of the form:

$$q_{rb} = q_{rbc} + q_{rbs} + q_{rbm} + q_{rbh} + q_{rbhc} \qquad \text{(GEOCHEM.3)}$$

where q_{rbc} is the rate of brine production per unit volume of waste (kg/m^3/s) due to corrosion of iron-based metals, q_{rbs} is the rate of brine production per unit volume of waste (kg/m^3/s) due to sulfidation of iron-based metals, q_{rbm} is the rate of brine production per unit volume of waste (kg/m^3/s) due to microbial degradation of CPR materials, q_{rbh} is the rate of brine production per unit volume of waste (kg/m^3/s) due to hydration of MgO, and q_{rbhc} is the rate of brine production per unit volume of waste (kg/m^3/s) due to hydromagnesite [$Mg_5(CO_3)_4(OH)_2{\cdot}4H_2O$] conversion to magnesite [$MgCO_3$], as shown by Clayton (2013). Two additional reactions are included in the model to account for the consumption of the CO_2 produced by CPR degradation. q_{rHMp} is the hydromagnesite (HM) production rate due to brucite carbonation, q_{rmp} is the magnesite (mag) production rate due to MgO carbonation.

The rates q_{rgc}, q_{rgs}, q_{rgm}, q_{rbc}, q_{rbs}, q_{rbm}, q_{rbh}, q_{rbhc}, q_{rHMp}, q_{rmp} (kg/m^3/s) are defined by:

gas generation by corrosion:

$$q_{rgc} = \left(R_{ci}S_{b,eff} + R_{ch}S_g^*\right)D_s\rho_{Fe}X_c\left(\mathrm{H_2}\,|\,\mathrm{Fe}\right)M_{\mathrm{H_2}} \qquad \text{(GEOCHEM.4)}$$

gas generation by iron sulfidation:

$$q_{rgs} = \left(\frac{q_{rgm}}{X_m(H_2|C)M_{H_2}}\right) X_m(H_2S|C)X_{s,Fe}(H_2|H_2S)M_{H_2} \qquad \text{(GEOCHEM.5)}$$

gas generation by microbial degradation:

$$q_{rgm} = \left(R_{mi}S_{b,eff} + R_{mh}S_g^*\right)D_c X_m(H_2|C)M_{H_2}B_{fc} \qquad \text{(GEOCHEM.6)}$$

brine production by corrosion:

$$q_{rbc} = q_{rgc}X_c(H_2O|H_2)M_{H_2O}/M_{H_2} \qquad \text{(GEOCHEM.7)}$$

brine production by iron hydroxide sulfidation:

$$q_{rbs} = \left(\frac{q_{rgm}}{X_m(H_2|C)M_{H_2}}\right) X_m(H_2S|C)X_{s,Fe(OH)_2}(H_2O|H_2S)M_{H_2O} \qquad \text{(GEOCHEM.8)}$$

microbial brine production:

$$q_{rbm} = q_{rgm}X_m(H_2O|H_2)M_{H_2O}/M_{H_2} \qquad \text{(GEOCHEM.9)}$$

brine production by MgO hydration:

$$q_{rbh} = \left(R_{hi}S_{b,eff} + R_{hh}S_g^*\right)D_m X_h(H_2O|MgO)M_{H_2O} \qquad \text{(GEOCHEM.10)}$$

brine production by hydromagnesite conversion to magnesite:

$$q_{rbhc} = R_{hc}D_{HM}X_{hc}(H_2O|HM)M_{H_2O} \qquad \text{(GEOCHEM.11)}$$

Hydromagnesite production rate due to brucite carbonation:

$$q_{rHMp} = \left(\frac{q_{rgm}}{X_m(H_2|C)M_{H_2}}\right) X_m(CO_2|C)X_{HMprod}(HM|CO_2)M_{brucite} \qquad \text{(GEOCHEM.12)}$$

Magnesite production rate due to MgO carbonation:

$$q_{rmp} = \left(\frac{q_{rgm}}{X_m(H_2|C)M_{H_2}}\right) X_m(CO_2|C)X_{mag_prod}(Mag|CO_2)M_{mag} \qquad \text{(GEOCHEM.13)}$$

where

D_s = initial surface area concentration of steel in the repository (m^2 surface area steel/ m^3 disposal volume)

D_C = initial mass concentration of cellulosics in the repository (kg carbon equivalent cellulosics /m^3 disposal volume)

D_m = initial mass concentration of MgO in the repository (kg MgO/m^3 disposal volume)

D_{HM} = instantaneous mass concentration of hydromagnesite in the repository (kg hydromagnesite/m^3 disposal volume)

M_{H2} = molecular weight of H_2 (kg H_2/mol H_2) (Lide 1991)

M_{H2O} = molecular weight of water (H_2O) (kg H_2O/mol H_2O) (Lide 1991)

M_{HM} = molecular weight of hydromagnesite magnesite (mol hydromagnesite/kg hydromagnesite) (Lide 2006)

$M_{brucite}$ = molecular weight of brucite (mol brucite/kg brucite) (Lide 1997)

M_{mag} = molecular weight of magnesite (mol magnesite/kg magnesite) (Lide 1997)

R_{ci} = corrosion rate under inundated conditions (m steel/s)

R_{ch} = corrosion rate under humid conditions (m steel/s)

R_{mi} = rate of carbon-equivalent cellulosics biodegradation under inundated conditions (mol $C_6H_{10}O_5$/kg $C_6H_{10}O_5$/s)

R_{mh} = rate of carbon-equivalent cellulosics biodegradation under humid conditions (mol $C_6H_{10}O_5$/kg $C_6H_{10}O_5$/s)

R_{hi} = MgO hydration rate under inundated conditions (mol MgO/kg MgO/s)

R_{hh} = MgO hydration rate under humid conditions (mol MgO/kg MgO/s)

R_{hc} = rate of hydromagnesite conversion to magnesite (mol hydromagnesite/kg hydromagnesite/s)

S_b = brine saturation

S_{wick} = brine saturation due to wicking

S_{min} = minimum brine saturation

$S_{b,eff}$ = effective brine saturation due to capillary action in the waste materials where

$$S_{b,eff} = \mathrm{Max}\left[\mathrm{Min}\left(S_b - S_{min} + S_{wick}\left\{1 - \exp\left[200\alpha\left(\mathrm{Max}\left(S_b - S_{min}, 0\right)\right)^2\right]\right\}, 1\right), 0\right]$$

$$S_g^* = \begin{cases} 1 - S_{b,eff} & \text{if } S_{b,eff} > 0 \\ 0 & \text{if } S_{b,eff} = 0 \end{cases}$$

α = numerical smoothing parameter (-1000) (Stein et al. 2018)

$X_c(H_2|Fe)$ = stoichiometric coefficient for gas generation due to corrosion of steel, i.e., moles of H_2 produced by the consumption of 1 mole of Fe (mol H_2/mol Fe)

$X_{s,Fe}(H_2|H_2S)$= stoichiometric coefficient for gas generation due to sulfidation of iron, i.e., moles of H_2 generated per mole of H_2S consumed by the sulfidation of Fe (mol H_2/mol H_2S)

$X_m(H_2S|C)$ = stoichiometric coefficient for H_2S generation due to microbial degradation of cellulose, i.e., moles of H_2S generated per mole of carbon consumed by microbial degradation of cellulose (mol H_2S/mol C)

$X_m(H_2|C)$ = stoichiometric coefficient for H_2 generation due to microbial degradation of cellulose, i.e., moles of H_2 generated per mole of carbon consumed by microbial degradation of cellulose (mol H_2/mol C)

$X_m(H_2O|C)$ = stoichiometric coefficient for H_2O generation due to microbial degradation of cellulose, i.e., moles of H_2O generated per mole of carbon consumed by microbial degradation of cellulose (mol H_2O/mol C)

$X_m(CO_2|C)$ = stoichiometric coefficient for CO_2 generation due to microbial degradation of cellulose, i.e., moles of CO_2 generated per mole of carbon consumed by microbial degradation of cellulose (mol CO_2/mol C)

$X_c(H_2O|H_2)$ = stoichiometric coefficient for brine production due to corrosion of steel, i.e., moles of H_2O produced per mole of H_2 generated by corrosion (mol H_2O/mol H_2)

$X_{s,Fe(OH)_2}(H_2O|H_2S)$ = stoichiometric coefficient for brine production due to sulfidation of iron hydroxide, i.e., moles of H_2O generated per mole of H_2S consumed by the sulfidation of $Fe(OH)_2$ (mol H_2O/mol H_2S).

$X_m(H_2O|H_2)$ = stoichiometric coefficient for brine production due to microbial degradation of cellulose, i.e., moles of H_2O produced per mole of H_2 generated by microbial degradation of cellulose (mol H_2O/mol H_2)

$X_h(H_2O|MgO)$ = stoichiometric coefficient for brine production due to MgO hydration, i.e., moles of H_2O produced per mole of MgO generated by hydration (mol H_2O/mol MgO)

$X_{hc}(H_2O|HM)$ = stoichiometric coefficient for brine production due to hydromagnesite conversion to magnesite, i.e., moles of H_2O produced per mole of hydromagnesite converted to magnesite (mol H_2O/mol hydromagnesite)

$X_{HMprod}(HM|CO_2)$ =stoichiometric coefficient for hydromagnesite production due to brucite carbonation, i.e., moles of hydromagnesite produced per mole of CO_2 consumed

$X_{mag,prod}(Mag|CO_2)$ = stoichiometric coefficient for magnesite production due to MgO carbonation, i.e., moles of magnesite produced per mole of CO_2 consumed

ρ_{Fe} = molar density of steel (mol/m^3), 1.41×10^5 mol/m^3 (Telander and Westerman 1993)

B_{fc} = parameter uniformly sampled from 0 to 1, used to account for the uncertainty in whether microbial gas generation could be realized in the WIPP at experimentally measured rates.

The reactions are assumed to continue until the associated substrate (i.e., iron-based metal, CPR, MgO, etc.) is exhausted. The terms $S_{b,eff}$ and $\mathcal{S}_g^*$, which are functions of location and time, correct for the amount of substrate exposed to inundated and humid conditions, respectively. All the corrosion and microbial action is assumed to cease when no brine is present, which is the reason that 0 replaces $S_g = 1$ in the definition of $\mathcal{S}_g^*$.

The surface area concentration D_s is defined by Equation (GEOCHEM.14):

$$D_s = A_d n_d / V_R \qquad \text{(GEOCHEM.14)}$$

where

A_d = surface area of steel associated with a waste disposal drum (m^2/drum)
V_R = initial volume of a single room in the repository (m^3)
n_d = ideal number of waste drums that can be close-packed in a single room

In PA, A_d = 6 m^2/drum, V_R = 3,640 m^3, and n_d = 6800 drums.

The biodegradable materials in the WIPP consist of cellulosic materials, plastics, and rubber materials. Cellulosics have been demonstrated experimentally to be the most biodegradable of these materials (Francis et al. 1997). The occurrence of significant microbial gas generation in the repository will depend on whether (1) microbes capable of consuming the emplaced organic materials will be present and active, (2) sufficient electron acceptors will be present and available, and (3) enough nutrients will be present and available.

In vectors where biodegradation of rubber materials and plastics occur, they are converted into an equivalent quantity of cellulosics based on their carbon equivalence (Wang and Brush 1996). The density of this material can be computed as:

$$D_c = \begin{cases} m_{cel} / V_R & \text{for biodegradation of cellulosics only} \\ \left(m_{cel} + m_r + 1.7 m_p\right) / V_R & \text{for biodegradation of CPR materials} \end{cases} \quad \text{(GEOCHEM.15)}$$

where V_R is the excavated storage volume of the repository (this is different from the V_R in equation GEOCHEM.7). m_{cel} is the mass of cellulosics (kg), m_r is the mass of rubber materials (kg), and m_p is the mass of plastics (kg) in the waste PAIR inventory. The factor 1.7 is the (assumed) molar-mass ratio of cellulose to plastics (on an equivalent carbon-number basis).

GEOCHEM-2.2.1 Process Model for Corrosion of Ferrous Metals

WIPP-specific experiments (Telander and Westerman 1993; Telander and Westerman 1997) showed that steels and other iron-based alloys could possibly corrode by the first two reactions shown in Table GEOCHEM-1.

$Fe(s) + 2H_2O(l) \rightarrow Fe(OH)_2 + H_2(g)$ Reaction 1 in Table GEOCHEM-1

$3Fe(s) + 4H_2O(l) \rightarrow Fe_3O_4(s) + 4H_2(g)$ Reaction 2 in Table GEOCHEM-1

Their results are consistent with production of magnetite [Fe_3O_4] from ferrous iron hydroxide [$Fe(OH)_2$], via the Schikorr reaction. Although Fe_3O_4 has been observed to form on Fe as a corrosion product in low-Mg anoxic brines at elevated temperatures (Telander and Westerman 1997) and in oxic brine (Haberman and Frydrych 1988), ongoing research is being conducted to conclude whether or not it will form at WIPP repository temperatures. If Fe_3O_4 were to form, H_2 would be produced (on a molar basis) in excess of the amount of Fe consumed. However, anoxic corrosion experiments (Telander and Westerman 1993) did not indicate the production of H_2 in excess of the amount of Fe consumed. After the experiments of Telander and Westerman (1993; 1997), a new series of steel and lead corrosion experiments was conducted (Roselle 2009; Roselle 2010; Roselle 2011a; Roselle 2011b; Roselle 2013c) that showed it is possible for other corrosion products to form, such as green rust [$Fe(III)_2Fe(II)_4(OH)_{12}CO_3 \bullet 2H_2O$] and hibbingite [$Fe_2 Cl (OH)_3$] (Roselle 2009; Roselle 2010; Roselle 2011a; Roselle 2011b; Roselle 2013c; Nemer et al. 2011). Only the iron hydroxide formation reaction is currently implemented in PA.

In CRA-2014, reactions between steel or $Fe(OH)_2$ and $H_2S(g)$ were considered:

$Fe(s) + H_2S(g) \rightarrow FeS(s) + H_2(g)$ Reaction 3 in Table GEOCHEM-1

$Fe(OH)_2(s) + H_2S(g) \rightarrow FeS(s) + 2H_2O(l)$ Reaction 4 in Table GEOCHEM-1

An agreement between the DOE and the EPA (U.S. EPA 2018a) states:

> Based on the results of the SEN4 study (U.S. EPA 2017), DOE has agreed to turn off reactions related to steel corrosion by sulfide as a means to represent passivation for CRA-2019.

Therefore, Reactions 3 and 4 in Table GEOCHEM-1 will not be included in CRA-2019.

GEOCHEM-2.2.2 Process Model for Microbial Degradation of CPR Materials

Microbial activity, if it occurs to a significant extent in the WIPP, would consume CPR materials by the reactions of denitrification, sulfate reduction, and methanogenesis (Brush 1990; Francis and Gillow 1994; Brush 1995; Wang and Brush 1996; Francis 1998). These mechanisms are shown in Table GEOCHEM-2. Methanogenesis is currently understood to be thermodynamically unfavorable under the expected conditions in the WIPP (see discussion in Appendix SOTERM, Section 4.1.1). This degradation pathway was removed at the direction of the EPA in CRA-2005 (Cotsworth 2005) by requiring the project to assume infinite availability of sulfate from the anhydrite interbeds. The DOE has removed the methanogenesis reaction (Reaction 3 in Table GEOCHEM-2) from the PA (see Nemer et al. 2005 for a discussion of the CRA-2005 rationale). The omission of methanogenesis, as written in Table GEOCHEM-2, is also supported by the inverse relationship between ionic strength and methanogenesis (Oren 2011).

Table GEOCHEM-2. Microbial Gas Generation Reactions in the WIPP Gas Generation Process Model

		Microbial Degradation Reactions
1	CCA[A]	$C_6H_{10}O_5(s) + 4.8H^+(aq) + 4.8NO_3^-(aq) \rightarrow 7.4H_2O(l) + 6CO_2 + 2.4N_2(g)$[B]
2	CCA [A]	$C_6H_{10}O_5(s) + 6H^+(aq) + 3SO_4^{2-}(aq) \rightarrow 5H_2O(l) + 6CO_2(g) + 3H_2S(g)$[C]
3	CCA[E]	$C_6H_{10}O_5(s) + H_2O(l) \rightarrow 3CH_4(g) + 3CO_2(g)$[D]

[A]These reactions were considered for microbial degradation starting with the CCA and have been included in the CCA and subsequent recertifications. They will be included in CRA-2019 as well. [B]Denitrification. [C]Sulfate Reduction. [D]Methanogenesis. [E]This reaction was considered for microbial degradation starting with the CCA. It was eliminated as a microbial degradation mechanism after CRA-2004. It will not be included in CRA-2019.

The average stoichiometry of the three reactions shown in Table GEOCHEM-2 is:

$$C_6H_{10}O_5/6 + \text{microbes} = y\ (\text{mol})\ \text{gas} + z\ (\text{mol})\ H_2O + \text{unknowns} \qquad \text{(GEOCHEM.16)}$$

where the average stoichiometric factors y and z represent the number of moles of gas (assumed to be H_2) and brine produced from each mole of carbon consumed, respectively. In PA, CO_2 is not included in the "moles of gas," as it is assumed to be consumed by reactions with MgO materials in the repository. Accordingly, $X_m(H_2|C)$ is equal to y, z is equal to $X_m(H_2O|C)$, and $X_m(H_2O|H_2)$ is equal to the ratio of z to y.

In the absence of methanogenesis, y and z from Equation (GEOCHEM.16) becomes:

$$y = \frac{2.4}{6} F_{NO3} + \frac{3}{6} F_{SO4} \qquad \text{(GEOCHEM.17)}$$

$$z = \frac{7.4}{6} F_{NO3} + \frac{5}{6} F_{SO4} \qquad \text{(GEOCHEM.18)}$$

where F_{NO3} is the fraction of carbon consumed through the denitrification reaction and F_{SO4} is the fraction of carbon consumed by sulfate reduction. The term F_{NO3} is calculated by comparing the concentration of NO_3^- (mol) initially present in the repository and the moles of carbon that could be consumed by biodegradation (see GEOCHEM-2.4.2 for a description of how this parameter is calculated). F_{SO4} is then just one minus F_{NO3} (this gives priority to cellulose degradation by sulfate reduction). With biodegradation by sulfate reduction, H_2S is produced. Because $X_m(H_2S|C)$ only considers H_2S, the stoichiometric factor for H_2S generation is:

$$X_m(H_2S|C) = \frac{3}{6}F_{SO4} \qquad \text{(GEOCHEM.19)}$$

The stoichiometric factors for reactions of iron and its corrosion products with H_2S (assuming only Reactions 3 and 4 from Table GEOCHEM-1) are:

$$X_{s,Fe}(H_2|H_2S) = 1\ mol/mol \qquad \text{(GEOCHEM.20)}$$

$$X_{s,Fe(OH)_2}(H_2O|H_2S) = 2\ mol/mol \qquad \text{(GEOCHEM.21)}$$

However, for the CRA-2019 PA, the stoichiometric coefficients for the reactions of iron and its corrosion products with H_2S [Equations (GEOCHEM.20) and (GEOCHEM.21)] will be set to zero (U.S. EPA 2018b).

GEOCHEM-2.2.3 Process Model for MgO Hydration and Carbonation

To provide added assurance of WIPP performance, an adequate amount of periclase [MgO] is added to the repository to remove CO_2 (Bynum et al. 1996). MgO is emplaced such that there is an excess of MgO in the repository (see U.S. DOE 2009, Appendix MgO, Section MgO-6.2.4.6). MgO in polypropylene “supersacks” is currently being emplaced based on the amount of CPR in the disposal room to create conditions that reduce actinide solubilities in the repository (see U.S. DOE 2014, Appendix MgO, Section MgO-2.1.1, and U.S. DOE 2019, Appendix SOTERM, Section SOTERM-2.3). Table GEOCHEM-3 shows the MgO hydration and carbonation reactions.

Table GEOCHEM-3. MgO Hydration and Carbonation Reactions in the WIPP Gas Generation Process Model

		MgO Hydration and Carbonation Reactions
1	CCA	$MgO(s) + H_2O(aq,g) \rightarrow Mg(OH)_2(s)$
2	CCA	$5\ Mg(OH)_2(s) + 4\ CO_2(g) \rightarrow Mg_5(CO_3)_4(OH)_2{\cdot}4\ H_2O(s)$
3	CCA	$Mg_5(CO_3)_4(OH)_2 \cdot 4\ H_2O(s) \rightarrow 4\ MgCO_3(s) + Mg(OH)_2(s) + 4\ H_2O(l)$

The mass concentration of MgO in the repository is calculated by:

$$D_m = 1.2 D_c\, M_{MgO}/M_c \qquad \text{(GEOCHEM.22)}$$

where

D_c	=	mass concentration of cellulosics in the repository (kg biodegradable material/m^3 disposal volume)
M_{MgO}	=	molecular weight of MgO (kg MgO/mol MgO), 4.03×10^{-2} kg/mol (Lide 1997, pp. 4-68)
M_c	=	molecular weight of cellulosics (kg cellulosics/mol cellulosics), 2.70×10^{-2} kg/mol
1.2	=	MgO excess factor in units mol MgO to mole organic carbon

If brine flows into the repository, MgO will react with water in liquid and in gaseous phases to produce brucite [$Mg(OH)_2$] (Reaction 1 in Table GEOCHEM-3). In this reaction, "aq, g" indicates that H_2O in either liquid or gaseous form will react with MgO, and so

$$X_h(H_2O|MgO) = -1/1 = -1\ mol/mol \qquad \text{(GEOCHEM.23)}$$

Brucite will in turn react with the CO_2 produced by microbial consumption of the CPR materials to yield hydromagnesite [$Mg_5(CO_3)_4(OH)_2{\cdot}4\ H_2O$] (Reaction 2 in Table GEOCHEM-3).

Since hydromagnesite is not thermodynamically stable under repository conditions, it is expected to dehydrate to form magnesite [$MgCO_3(s)$], as shown in Reaction 3 in Table GEOCHEM-3, and so

$$X_{hc}(H_2O|HM) = 4/1 = 4\ mol/mol \qquad \text{(GEOCHEM.24)}$$

The mass concentration of hydromagnesite, mass of hydromagnesite divided by the repository volume, D_{HM}, is calculated dynamically and is a function of the biodegradation rate and hydromagnesite conversion to magnesite rate.

GEOCHEM-2.2.4 Process Model for Hydromagnesite to Magnesite Conversion

Hydromagnesite was not included in the CCA. It was added to the WIPP Chemical Conditions Process Model (see GEOCHEM-3.2) for the Performance Assessment Verification Test (PAVT).

However, for the PAVT, it was assumed that hydromagnesite was stable in the WIPP environment and would persist through the regulatory time period of 10,000 years. This assumption was maintained through CRA-2004 and CRA-2009. That is, conversion of hydromagnesite to magnesite (a reaction that produces water) was not added to the Gas Generation and Brine Production Process Model.

For CRA-2014, the DOE added the conversion of hydromagnesite to magnesite to the Gas Generation and Brine Production Process Model

The reaction was incorporated into the Gas Generation and Brine Production Process Model by adding the q_{rbhc} term to Equation (GEOCHEM.3).

GEOCHEM-2.3 Parameterization of Gas Generation and Brine Production Process Models

A few of the parameters for the Gas Generation and Brine Production Process Model will be revised for CRA-2019. They are discussed below.

GEOCHEM-2.3.1 Parameters for Ferrous Metal Corrosion

Both the inundated and humid corrosion rates are sampled parameters for PA. Discussion of the range and distribution of those parameters is deferred to GEOCHEM-2.4.1.

GEOCHEM-2.3.2 Parameters for Microbial Gas Generation

Both the inundated and humid microbial gas generation rates are sampled parameters for PA. Discussion of the range and distribution of those parameters is deferred to GEOCHEM-2.4.2.

GEOCHEM-2.3.3 Parameters for MgO Hydration and Carbonation

For CRA-2014, both the humid and inundated hydration rates were sampled parameters. However, the sensitivity analysis performed as part of that PA indicated that radionuclide release rates did not appear to be sensitive to the MgO hydration rates (Kirchner 2013). During review of CRA-2014, the EPA expressed concern that the DOE used MgO hydration rates obtained from experiments using Premier MgO. Martin Marietta is the current MgO supplier and the mass percent of MgO from Martin Marietta in the repository is now greater than 70 percent.

The DOE provided a copy of the sensitivity analysis (Kirchner 2013) to the EPA during the comment resolution cycle for CRA-2014. The EPA indicated that they accept that “MgO hydration rates do not significantly impact releases in the WIPP performance assessment.”

GEOCHEM-2.3.4 Parameters for Hydromagnesite to Magnesite Conversion

Conversion of hydromagnesite to magnesite produces four moles of water. Thus, the stoichiometric coefficient is four. The molecular weight and density of hydromagnesite were taken from Lide (2006) and are 467.64×10^{-3} kg/mol and 2300 kg/m^3, respectively. The hydromagnesite to magnesite conversion rate is discussed in GEOCHEM-2.4.4 because it is a sampled parameter. Note that the baseline actinide solubility model (GEOCHEM-3.2.2) assumes

that hydromagnesite forms and persists for the regulatory period, while the gas generation model assumes that hydromagnesite forms and transforms to magnesite, as a function of a sampled conversion rate (GEOCHEM-2.4.4), during the regulatory period. The assumption that hydromagnesite persists in the actinide solubility model is conservative because the brucite-hydromagnesite buffer maintains a higher f_{CO2} than the brucite-magnesite buffer, which can increase actinide solubility.

GEOCHEM-2.4 Quantification of Uncertainty in Gas Generation and Brine Production

As noted in GEOCHEM-1.1.4, uncertainties for the WIPP PA can be categorized as: uncertainty in the conceptual model, uncertainty in the process model, and uncertainty in parameterization of the process model.

With regard to the conceptual model for gas generation and brine production, there is uncertainty about all of the assumptions discussed in GEOCHEM-2.1. However, all of the assumptions are supported by reasoned argument. The reasoned arguments were presented for peer review prior to the CCA and the assumptions have been accepted for use in the WIPP PA.

There are five process models for gas generation and brine production/consumption: ferrous metal corrosion, microbial degradation of CPR materials, MgO hydration and carbonation, radiolysis, and conversion of hydromagnesite to magnesite. There are no identified uncertainties in the process models for MgO hydration and carbonation, or for conversion of hydromagnesite to magnesite. These processes are assumed to take place with known reactants and products and at known reaction rates.

There is uncertainty in the ferrous metal corrosion process model. The reactants are known, but all corrosion products are not known. Possible corrosion products include: $Fe(OH)_2$, Fe_3O_4(s), green rust, and FeS(s). This uncertainty falls into the category of epistemic uncertainty because it can be minimized with additional research. At the present time, this uncertainty is handled by assuming that $Fe(OH)_2$ is the main corrosion product in the ferrous metal corrosion process model, as explained in GEOCHEM-2.1.1. In addition, the extent of surface passivation due to formation of corrosion products is unknown. This uncertainty is also handled by making a conservative assumption. The conservative assumption is that ferrous metal surfaces are not passivated by the formation of corrosion products during a PA simulation for CRA-2019.

There is also uncertainty in the process model for microbial degradation of CPR materials. It is unclear if microbes might consume one or two of the CPR materials. This uncertainty is handled by making an assumption. The assumption is that 75 percent of the time microbes only consume cellulose. That implies that 25 percent of the time microbes consume cellulose, plastic, and rubber.

However, there remains uncertainty in the parameterization of the process models, namely in the reaction rates from Equation (GEOCHEM.1) and Equation (GEOCHEM.2). These are:

- the rate of gas production per unit volume of waste ($kg/m^3/s$) due to corrosion of iron-based metals (the inundated and humid corrosion rates are sample parameters in PA)

- the rate of gas production per unit volume of waste (kg/m^3/s) due to sulfidation of iron-based metals (set to zero by assumption for CRA-2019)
- the rate of gas production per unit volume of waste (kg/m^3/s) due to microbial degradation of CPR materials (the inundated and humid microbial gas generation rates are sampled parameters for PA)
- the rate of brine production per unit volume of waste (kg/m^3/s) due to corrosion of iron-based metals (the inundated and humid corrosion rates are sample parameters in PA)
- the rate of brine production per unit volume of waste (kg/m^3/s) due to sulfidation of iron-based metals (set to zero by assumption for CRA-2019)
- the rate of brine production per unit volume of waste (kg/m^3/s) due to microbial degradation of CPR materials (the inundated and humid microbial gas generation rates are sampled parameters for PA)
- the rate of brine production per unit volume of waste (kg/m^3/s) due to hydration of MgO (this was a sampled parameter prior to CRA-2019. For CRA-2019, this will be a fixed parameter as described in GEOCHEM-2.3.3)
- the rate of brine production per unit volume of waste (kg/m^3/s) due to hydromagnesite conversion to magnesite (the conversion rate is a sampled parameter for the CRA-2019 PA)

All of the reaction rates listed above, with the exception of the rate of brine production per unit volume of waste due to hydromagnesite conversion to magnesite, are measurable quantities. The DOE has conducted experiments to ascertain rates related to ferrous metal corrosion and microbial degradation of CPR materials. In particular, recent experiments conducted by Roselle (2013c) were used to calculate a gas generation rate due to ferrous metal corrosion as well as to quantify the uncertainty in that rate. For CRA-2019, Roselle (2013c) continues to be the primary source of information regarding uncertainty in gas production from ferrous metal corrosion.

Although the DOE is actively investigating if microbes can be active under WIPP conditions, and if they are active, at what rate they would consume CPR materials (U.S. DOE 2019, Appendix SOTERM, Section SOTERM-4.1), for CRA-2019, Swanson and Reed (2018), Swanson et al. (2019), and Francis et al. (1997) are the primary sources of information regarding uncertainty in gas production from microbial degradation of CPR materials.

GEOCHEM-2.4.1 Uncertainty in Corrosion of Steel

The parameters of interest are R_{ci}, which is the corrosion rate under inundated conditions (m/s), and R_{ch}, which is the corrosion rate under humid conditions (m/s). The DOE performed the CRA-2014 PA calculations using a singular value of 0 for humid rates recommended by Roselle (2013c). During their review, the EPA commented on this range and distribution noting that the DOE needed to re-evaluate their position and include results from Roselle for experiments with 350 parts per million (ppm) CO_2 (U.S. EPA 2015). Roselle's experiments were conducted at 1 atm and 350 ppm CO_2, which corresponds to a partial pressure of CO_2 of 3.5×10^{-4} atm. The steel corrosion rate is a function of the aqueous concentration of CO_2 (Roselle 2013c), which is directly related to the partial pressure of CO_2 by Henry's Law (Denbigh 1981).

The DOE did not include Roselle's 350 ppm CO_2 data in the CRA-2014 PA because the calculated fugacity of CO_2 in that PA was 3.14×10^{-6} atm, two orders of magnitude lower than the 350 ppm value for Roselle's experiments. Nevertheless, the DOE agreed that the Roselle anoxic corrosion experiments with 0 ppm and 350 ppm CO_2 concentrations bracket anticipated CO_2 gas phase concentration. Therefore, the DOE reanalyzed the data from iron corrosion experiments at 0 and 350 ppm CO_2 and developed a cumulative distribution function (CDF) to represent the inundated iron corrosion rate (STEEL:CORRMCO2) (Zeitler and Hansen 2015a).

The cumulative distribution in Figure GEOCHEM-4 reflects the observed variation in non-negative corrosion rates for all experiments with 0 ppm and 350 ppm CO_2, with the lower bound value of 0 m/s. The revised distribution considers all non-negative corrosion rates reported by Roselle (2013c) as equally likely (Zeitler and Hansen 2015a). Equally likely means they have the same probability of occurrence. A cumulative distribution for the STEEL:CORRMCO2 parameter will be incorporated in CRA-2019 (Zeitler 2018). This distribution includes a factor of two applied to the distribution derived by Zeitler and Hansen (2015a), which was included to account for repository pressure.

The DOE also reanalyzed the applicability of data from humid iron corrosion experiments at 0 and 350 ppm CO_2 (Roselle 2013c). The humid steel corrosion rate, R_{ch}, used in all past compliance PAs, was 0. The justification for this parameter value was given in Wang and Brush (1996):

> The corrosion rate observed on specimens exposed to humid conditions is negligible, based on essentially non-existent presence of corrosion product and lack of apparent H_2 generation (Telander & Westerman, 1997). Therefore, we set the humid steel corrosion rate to 0.

However, Roselle (2013c) indicated that some corrosion occurs under simulated WIPP conditions for humid environments. During the CRA-2014 recertification cycle, the EPA showed an interest in Roselle's 0 ppm data. As a result, Zeitler and Hansen (2015a and 2015b) derived CDFs for the corrosion rate under humid conditions for 0.58 ppm CO_2 and 3.14 ppm CO_2. Figure GEOCHEM-4 shows those CDFs. The CDFs basically overlap one another.

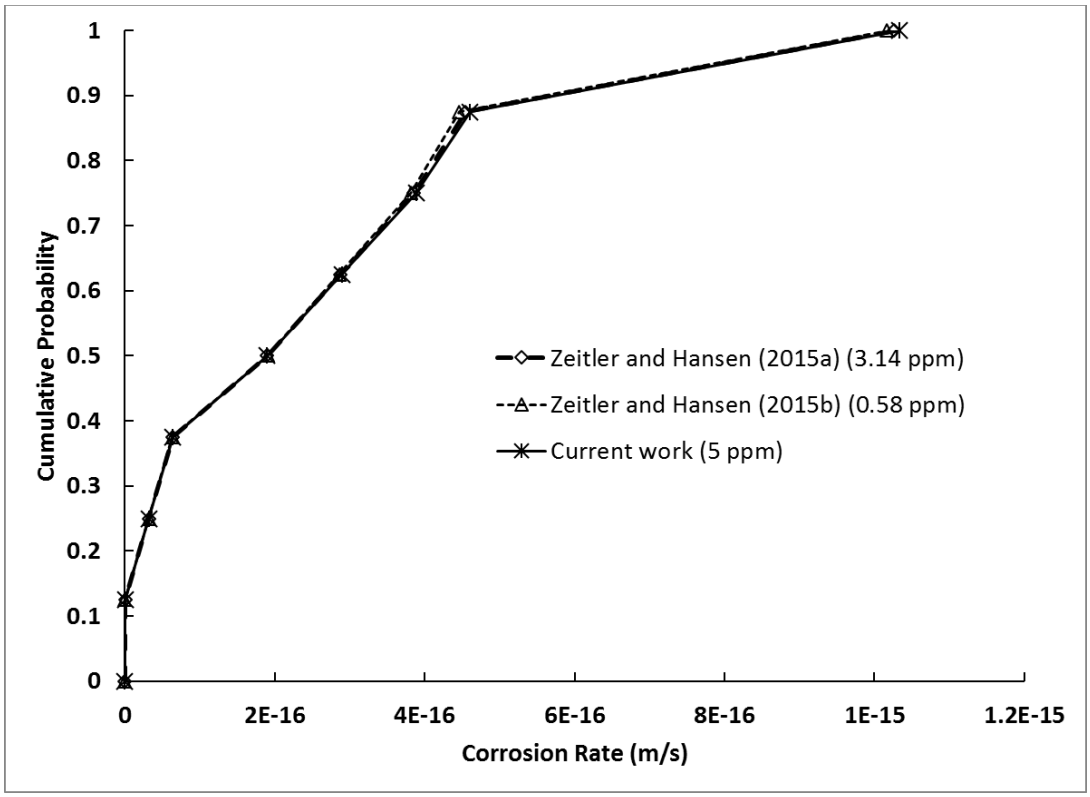

Figure GEOCHEM-4. CDFs for 0.58 ppm and 3.14 ppm (from Zeitler and Hansen 2015b), as Well as the Final Interpolated CDF for 5 ppm (from Zeitler 2018). The CDFs are Not Distinguishable From One Another.

For CRA-2019, the DOE has decided to use a CDF for humid corrosion rate derived for 5 ppm CO_2. The 5 ppm CO_2 value was chosen because it is at least an order of magnitude greater than the expected CO_2 fugacity in the repository, and is therefore considered bounding with regard to CO_2. The CDF for 5 ppm CO_2 is also shown in Figure GEOCHEM-4. The 5 ppm CO_2 CDF was derived by linearly interpolating between the 0 ppm and 350 ppm quantiles from the Roselle (2013c) humid corrosion rate data (Zeitler 2018). This CDF for humid corrosion rate will be incorporated in CRA-2019.

GEOCHEM-2.4.2 Uncertainty in Microbial Degradation of CPR Materials

The current approach to quantifying uncertainty in microbial gas generation rates was first implemented in the CRA-2004 Performance Assessment Baseline Calculation (PABC) (Leigh et al. 2005). The following is a summary of the current method.

There are four parameters sampled:

1. R_{mi}, which is the rate of cellulose biodegradation under inundated conditions (mol $C_6H_{10}O_5$/kg $C_6H_{10}O_5$/s); its values range uniformly between 3.08×10^{-11} and 5.57×10^{-10} moles organic carbon consumed per kg cellulose per second

2. R_{mh}, which is the rate of cellulose biodegradation under humid conditions (mol $C_6H_{10}O_5$/kg $C_6H_{10}O_5$/s); its values range uniformly between 0 and 1.03×10^{-9} moles organic carbon consumed per kg cellulose per second. Subsequent to sampling, a conditional relationship is applied between the humid and inundated rates, such that the inundated rate always exceeds the humid rate (Zeitler 2019).
3. B_{fc} is an uncertainty factor defining the probability that microbial activity will occur. B_{fc} will be set to 1 for CRA-2019
4. Parameter PROBDEG, probability of plastic and rubber degradation (in addition to cellulose degradation). PROBDEG will be set to 0.25 for CRA-2019.

The parameter ranges for inundated and humid gas generation rates are based on 10 years of data from Brookhaven National Laboratory (Francis et al. 1997, U.S. DOE 2002). They were derived by Nemer et al. (2005). Conditional sampling of the two rates is performed where:

$$R_{mh} = \text{minimum of } (R_{mi}, R_{mh}) \qquad \text{(GEOCHEM.25)}$$

R_{mh} is computed based on the sampled value of R_{mi} (Nemer, Stein, and Zelinski 2005).

Sampling of an uncertainty factor, B_{fc}, was added during the CRA-2004 PABC because Brush (2005) identified the concerns listed below about the direct relevance of the Brookhaven National Laboratory (Francis et al. 1997; U.S. DOE 2002) experiments to the WIPP. The concerns identified by Brush (2005) are:

1. Whether microbes will survive for a significant fraction of the 10,000-year regulatory period
2. Whether sufficient H_2O will be present
3. Whether sufficient quantities of biodegradable substrates will be present
4. Whether sufficient electron acceptors will be present and available

The Los Alamos National Laboratory (LANL) is investigating if microbes are active under WIPP conditions. That investigation is discussed in Appendix SOTERM.

The verdict of the CRA-2004 PABC was to set the probability of microbial gas generation to 1. However, there remains a distinction between consumption of cellulose and consumption of plastic and rubber materials. While cellulose is consumed in all PA vectors, plastic and rubber materials are consumed in only 25 percent of the vectors. This approach is summarized in Table GEOCHEM-4, and is discussed further in Nemer and Stein (2005), Section 5.4.

Table GEOCHEM-4. Probabilities for Biodegradation of Different Organic Materials in the CRA-2014 PA[A]

Parameter Value	Meaning	Probability in CRA 2014
0	No microbial degradation can occur	0.0
1	Biodegradation of only cellulose can occur	0.75
2	Biodegradation of all CPR materials can occur	0.25

[A]DOE proposes to use the same values for CRA-2019.

The values shown in Table GEOCHEM-4 for the probability of biodegradation of different organic materials is used in PA to determine the total moles of carbon that could be consumed by biodegradation. That is, 75 percent of the time, the total moles of carbon that could be consumed by biodegradation is derived from the mass of cellulose in the repository. Twenty-five percent of the time, the total moles of carbon that could be consumed by biodegradation is derived from the combined mass of cellulosic, plastic, and rubber materials in the repository.

GEOCHEM-2.4.3 Uncertainty in MgO Hydration Rate

Values for the two rates, inundated conditions (R_{hi}) and humid conditions (R_{hh}), were varied for CRA-2014. Because Kirchner (2013) and all previous sensitivity studies have indicated that computed radionuclide releases do not appear to be sensitive to the MgO hydration rates, values for the two rates, inundated conditions (R_{hi}) and humid conditions (R_{hh}), will be assumed constant in the CRA-2019 PA. Discussion of these two rates is given in CRA-2014, Appendix MgO.

GEOCHEM-2.4.4 Uncertainty in the Hydromagnesite Conversion Rate

There is uncertainty regarding the hydromagnesite to magnesite conversion rate. This uncertainty was characterized by the EPA (U.S. EPA 1998) as reacting on the order of “hundreds to thousands of years.” Therefore, for CRA-2014, an assumed range of reaction times of 100 to 10,000 years was used to capture uncertainty in the hydromagnesite to magnesite reaction rate.

The reaction time is converted to a reaction rate by dividing the molecular weight of hydromagnesite by the reaction time in seconds (because hydromagnesite conversion is modelled as a first order reaction, these reaction times correspond to 63% conversion, not 100% conversion).

A reaction time of 100 years results in the following rate:

$$1 / (100*3.1557 \text{ x } 10^{7})/467.64 \times 10^{-3} = 6.8 \times 10^{-10} \text{ mol/kg·s}$$

For a reaction time of 10,000 years, the calculation results in the following rate:

$$1 / (10{,}000*3.1557 \times 10^{7})/467.64 \times 10^{-3} = 6.8 \times 10^{-12} \text{ mol/kg·s}$$

With only a maximum and minimum value available for this parameter, a uniform distribution (recommended in Tierney [1996] in these cases) with a mean of 3.4×10^{-10} and a standard deviation of 1.9×10^{-10} was used in CRA-2014.

During the completeness review of CRA-2014, the EPA concluded (Shrader 2016):

> …that it was possible that no hydromagnesite would convert to magnesite over the 10,000 year period of performance…Consequently, the available data show that the lower limit of the reaction rate distribution should be 0 mol/kg·s.

The EPA (U.S. EPA 2017) also noted:

> The minimum 100-year reaction time is inconsistent with the available reaction rate data. For example, Zhang et al. (2000) extrapolated higher temperature experimental rate data obtained in GWB brine to 25°C and determined an induction period of 200 years and a reaction half-time of 73 years. This extrapolated rate is consistent with a higher minimum reaction time (on the order of 350 years), which would result in a lower maximum reaction rate than the 6.8×10^{-10} mol/kg·s maximum rate used by Clayton (2013).
>
> As a result, for CRA-2019 the range of reaction times is changed to a minimum of 200 years and a maximum of infinity. The new minimum reaction rate is 0 mol/kg·s. The new maximum reaction rate is 3.4×10^{-10} mol/kg·s. A uniform distribution with a mean of 1.7×10^{-10} mol/kg·s was used.

GEOCHEM-3.0 CHEMICAL CONDITIONS

Near-field chemical conditions are needed to perform actinide solubility calculations. This includes calculation of the solids, liquids, and gases that determine concentrations in brines after brine reacts with the waste, waste packages, and emplacement materials in the repository. The prevalent ions in WIPP brines are H^+, Na^+, K^+, Mg^{2+}, OH^-, Cl^-, CO_3^{2-}, SO_4^{2-}, and Ca^{2+} (U.S. EPA 2008).

In the last two recertification cycles, the presence of a tetraborate species in WIPP brines has become of interest because of its potential effect on actinide +III solubility. Discussions between the DOE and the EPA have focused on the possible formation of a tetraborate complex with +III actinides.

For CRA-2019, the DOE has reviewed the WIPP models for EDTA, citrate, and oxalate. Solubility-limiting phases added for EDTA, Citrate, and Oxalate, these being [$Ca_2EDTA{\bullet}7H_2O$(s)], earlandite (calcium citrate, and glushinskite [oxalate]), were included in the database. When available, parameters in the WIPP Chemical Conditions Process model were aligned with the Nuclear Energy Agency (NEA) database project. In the case of EDTA and citrate, thermodynamic values from Hummel et al. (2005) are employed for CRA-2019. Then, using project-specific solubility data for the three solids, CaEDTA (s), earlandite, and glushinskite, the DOE derives appropriate Pitzer interaction coefficients for the EDTA, citrate, and oxalate systems. These analyses are included Domski and Sisk-Scott (2019).

New to CRA-2019 is the addition of aqueous Pb^{2+} and Fe^{2+} to the WIPP Chemical Conditions Process Model. The DOE is limiting the models for both Pb^{2+} and Fe^{2+} to the inorganic systems. It should be noted that lead sorption to iron is not currently taken into consideration.

Solubility-limiting phases were added for iron hydroxide [$Fe(OH)_2$], hibbingite [$Fe_2Cl(OH)_3$], siderite [$FeCO_3$], and chukanovite [$Fe_2CO_3(OH)_2$]. Given the expected low solubility of lead, the lead model for CRA-2019 involves only the following reactions and their log K values. The reactions included are for lead with chloride, carbonate, hydroxide, and sulfate. Lead interactions with organic constituents, EDTA, citrate, and oxalate, will not be included in CRA-2019.

GEOCHEM-3.1 WIPP Chemical Conditions Conceptual Model

The WIPP Chemical Conditions Conceptual Model includes assumptions related to the mineralogy of the Salado Formation, the compositions of the Salado and Castile brines that may enter the repository and may be in contact with the waste, the waste components that are included in the process models, and the redox states of actinides and metals in solution. The expected chemical conditions in the repository determine the actinide solubilities in brine; these chemical conditions are addressed in the Dissolved Actinide Source Term conceptual model that is discussed in GEOCHEM-4.1 and CRA-2019 Appendix SOTERM.

Other information used to develop the WIPP Chemical Conditions Conceptual Model included experimental data, TRU waste PAIR inventory data, and information derived from literature reviews (Wilson et al. 1996). Although the process models and parameters that are used to calculate near-field chemical conditions have evolved since the CCA, the assumptions that constitute the conceptual model have remained the same.

GEOCHEM-3.1.1 Use of the Pitzer Model

Actinide solubilities and the chemistry of the near-field environment are calculated using the thermodynamic mass-action approach with the ion-specific aqueous model of Pitzer (Pitzer 1973) as implemented in EQ3/6 version 8.0a (Wolery and Jarek 2003).

GEOCHEM-3.1.2 The Presence of Carbon Dioxide Gas

As noted in GEOCHEM-2.1.5, it is assumed that only a few ppm of CO_2 gas is present in the post-closure repository due to microbial degradation of CPR materials both in the waste and in the emplacement materials. However, the fugacity of CO_2 is buffered by the presence of MgO, specifically the equilibrium between $Mg(OH)_2$ and $Mg_5(CO_3)_4(OH)_2{\cdot}4H_2O$.

GEOCHEM-3.1.3 A Well-Mixed Repository at Equilibrium

The chemistry analogy that is assumed for determining near-field chemical conditions is that of a batch reactor that has come to equilibrium. Thus, the MgO, waste, host rock, and brine are well-mixed and the possible presence of chemical microenvironments and supersaturated conditions are not assumed to persist in the repository for long time periods. The resulting brine compositions (as shown in Table GEOCHEM-5) are assumed to persist for the entire 10,000-year regulatory period.

GEOCHEM-3.1.4 Availability of Minerals

The Disturbed Rock Zone (DRZ), as a function of repository excavation, is a zone immediately surrounding the repository that has been altered by the redistribution of stress in the rocks closest to the repository. Combined with the drop in hydrostatic pressure in the repository, formation of this DRZ increases the permeability of the rock (halite and anhydrite layers) in the vicinity of the waste, rendering it more transmissive to gas and brine flow from the undisturbed surrounding host rock towards the waste-filled rooms.

The DRZ plays a role in the near-field chemical conditions because it increases the surface area of the halite and anhydrite layers close to the waste, which increases their availability. Of the two Salado Formation minerals considered in the model, halite and anhydrite, the latter is considered more significant with respect to near-field chemistry. In PA assumptions, anhydrite functions as a source for both calcium and sulfate for processes in the repository both before and after brine inundation. The high availability of sulfate is an assumption required by the EPA to suppress methanogenesis in the WIPP to maximize the potential for carbon dioxide formation (U.S. DOE 2019, Appendix SOTERM). Calcium forms a mineral phase with the complexant EDTA, $Ca_2EDTA(s)$, which has a limiting effect on actinide-EDTA complexation, thus decreasing actinide solubility.

GEOCHEM-3.1.5 Availability of Waste Materials

Because of the batch reactor assumption, all waste constituents and emplacement materials are available to react with the brine. Equilibrium between brine from the host rock and the waste materials is also assumed as mentioned in GEOCHEM-3.3.3. However, the brine composition at equilibrium is only calculated prior to initiation of PA. PA does not account for changes in brine composition as the PA simulation proceeds. The brine composition, in terms of radionuclide content, is assumed to change over the regulatory period in PA calculations.

GEOCHEM-3.1.6 The Use of End Member Brines

Brine that reacts with the waste under any intrusion scenario will have a composition like that of Salado brine, Castile brine, or a mixture of Salado and Castile brines. In the undisturbed scenario, Salado brine is assumed. Culebra groundwater that could enter the repository would quickly dissolve halite and develop a composition like Salado brine. Because the Salado and Castile brines bracket the possible brine compositions, experiments and modeling performed only with end member brine compositions are adequate for describing the repository geochemistry (see U.S. DOE 2014, Appendix SOTERM, Section SOTERM-3.2). The Generic Weep Brine (GWB) formulation is used to simulate Salado brine and Energy Research and Development Administration Well 6 (ERDA-6) brine is used to simulate Castile brine. Those compositions are shown in Table GEOCHEM-5. The brine compositions shown in Table GEOCHEM-5 are used in the PA simulations.

Table GEOCHEM-5. Composition of GWB and ERDA-6 Brine Before Reaction with Anhydrite, Brucite and Hydromagnesite

Ion or property[A]	GWB Brine Composition[B]	ERDA-6 Brine Composition[C]
$B(OH)_3$	158 mM	63 mM
Na^+	3.53 M	4.87 M
Mg^{2+}	1.02 M	19 mM
K^+	0.467 M	97 mM
Ca^{2+}	14 mM	12 mM
SO_4^{2-}	177 mM	170 mM
Cl^-	5.86 M	4.8 M
Br^-	26.6 mM	11 mM
Total Inorganic C (as HCO_3^-)	16 mM[D]	16 mM
pH	7.0[E]	6.17
Ionic Strength (M)	7.44	5.32

[A]Ions listed represent the total of all species with this ion. [B]From Snider 2003. [C]From Popielak et al. 1983. [D]The total inorganic carbon value for ERDA-6 is used for GWB because it was not reported. [E]GWB pH is set to 7 because it was not reported.

GEOCHEM-3.1.7 Reducing Conditions Due to Ferrous Metal Corrosion

The conceptual model assumes that steel corrosion will result in a reducing environment sometime after repository closure. However, oxidation-reduction equilibrium within the waste materials (including ferrous metal and CPR) is not considered. Ferrous metal corrosion and CPR degradation are represented by reaction rates instead of equilibrium (as discussed in GEOCHEM-2.2.1 and GEOCHEM-2.2.2). In most realizations, significant amounts of uncorroded ferrous metal will be present in the repository throughout the 10,000-year regulatory period. Radiolysis can lead to localized oxidizing conditions, but will not inherently change the reducing conditions established by the reduced iron phases present in the WIPP (see Appendix SOTERM, Section 3.4 for a more detailed discussion).

GEOCHEM-3.1.8 The Role of Magnesium Oxide

The magnesium oxide [MgO or periclase] emplaced as an engineered barrier acts as a pH buffer that offsets the effect of pH-lowering carbon dioxide produced by microbial activity in the post-closure repository. In the absence of MgO, high CO_2 fugacity could occur, creating low pH conditions in the repository brine. To mitigate this possibility, MgO will hydrate to form brucite [$Mg(OH)_2$], which will in turn react with CO_2 to form hydromagnesite and buffer the pH to values between 8.7 and 9.0, depending upon solution composition.

GEOCHEM-3.2 WIPP Chemical Conditions Process Models

The WIPP Chemical Conditions Process Model is composed of three elements: chemical reactions, mathematical expressions that represent the chemical reactions, and software that solves the mathematical expressions to obtain relevant chemical conditions. The following

sections provide information about the specific chemical reactions involved in the WIPP Chemical Conditions Process Model. The following is a summary of the software used to solve the mathematical expressions.

Prior to CRA-2014, the WIPP PA utilized the Fracture-Matrix Transport (FMT) code (Novak 1996a; see also Babb and Novak 1995; Babb and Novak 1997 and addenda; Wang 1998) as its principal tool for modeling geochemical interactions in the WIPP repository. The DOE used the FMT code for calculations for the CCA (U.S. DOE 1996), the CRA-2004 PA (U.S. DOE 2004), and the CRA-2009 PA (U.S. DOE 2009), and the associated calculations for CCA Performance Assessment Verification Test (CCA-PAVT), CRA-2004 Performance Assessment Baseline Calculations (CRA-2004 PABC), and CRA-2009 Performance Assessment Baseline Calculations (CRA-2009 PABC). During this period, in addition to the updates for the FMT database that were performed by Giambalvo (2003) and Nowak (2005), the updates also included Xiong (2004, 2005, 2009) and Xiong et al. (2009, 2010b).

The geochemistry part of that software uses Pitzer (1973, 1975, 1991), Pitzer and Kim (1974), and Pitzer and Silvester (1976) equations to represent the thermodynamic activity coefficients of aqueous species, including both solutes and the solvent, water, as described above. The standard form of the Pitzer equations is based on molalities and requires data for interaction parameters for pairs and triplets of the solute species included in the model (interaction parameters explicitly involving the solvent, water, are not employed). The FMT model is based on the classic Pitzer model of Harvie et al. (1984) for the "sea-salt" system at 25ºC, and has been extended by adding data for organic complexing agents (e.g., acetate, oxalate, citrate, ethylenediaminetetraacetic [EDTA]) and actinides that are present in the WIPP repository. The most recent FMT model consists of the code FMT v. 2.4 (Wang 1998) and the thermodynamic database fmt_050405.chemdat (Xiong 2005). The database extensions have drawn on several papers and reports that are too numerous to mention here (complete references are documented in the database itself). Database extensions are all in the FMT Software Records Package under ERMS210790 (Xiong 2005).

On September 27, 2011, the EPA approved the migration of the FMT code to EQ3/6 Version 8.0a (Wolery et al. 2010; Xiong 2011) for WIPP compliance recertification calculations (U.S. EPA 2011), and the FMT database was also migrated to the EQ3/6 Version 8.0a format (Xiong 2011) by porting the FMT thermodynamic database to an EQ3/6-compatible format.

The FMT data file, fmt_050405.chemdat (Xiong 2005), contains thermodynamic data in the form of standard Gibbs energies of formation at 25ºC. This data file does not contain chemical reactions. In EQ3/6, each species other than strict basis species is associated with a reaction in which that species is a reactant, and in which all other species are basis species of the strict or auxiliary type[1]. Instead of a Gibbs energy for the species, an equilibrium constant (log K) for the reaction is provided. As a result, all data from fmt_050405.chemdat (Xiong 2005) was used to create Log K values to use with EQ3/6, and the first EQ3/6 database, DATA0.FM0, was created

[1] In EQ3/6, basis species and auxiliary basis species are used to define the aqueous compositions used as EQ3 input, and they are used to define the dissolution of solid mineral phases and the dissociation of aqueous species.

via AP-140 (Wolery 2008). Note that in AP-140, Wolery (2008) erroneously calls this database DATA0.FMT.

Since the initial issue of DATA0.FM0 there have been four updates to the database, each with a higher number file extension (DATA0.FM1, FM2, FM3, and FM4). The first update, DATA0.FM1, involved changing the Debye-Huckel parameter AΦ from 0.39 to the correct value of 0.392. A second change involved correction of a typographical error in the Na^+ - Cl^- Pitzer parameter β(1), which was changed from 0.2644 to the correct value of 0.2664. A third change made to DATA0.FM1 involved addition of the mineral phase $Mg_3Cl(OH)_5 \bullet 4H_2O$, more commonly known as Phase 5 (Xiong 2011).

The next database was constructed from DATA0.FM1 and was called DATA0.FM2 (Domski 2015). DATA0.FM2 included the lead system, both thermodynamic and Pitzer data, an updated borate model, including Am-tetraborate species, various updates, and new data for EDTA, citrate, and oxalate. Nearly all of the new parameters were derived from experimental data collected at Sandia National Laboratories (SNL) in Carlsbad, New Mexico, with the remainder having been derived from literature data.

The next database, DATA0.FM3, was an exact replica of DATA0.FM2 with the addition of thermodynamic data for the lead sulfide phase galena. Galena was added for demonstrative purposes so that a simple modeling study (Xiong and Domski 2016) could be performed at the request of the EPA to determine if the Am(III) solubility was impacted by sulfide.

The latest version of the EQ3/6 Pitzer thermodynamic database, DATA0.FM4, was constructed from DATA0.FM1, not incorporating any of the data from DATA0.FM2, and it includes updates to the EDTA, citrate, and oxalate systems, and addition of two new systems for iron and lead. See GEOCHEM-3.2.5 and GEOCHEM-3.3.5 for discussions of the organic ligands parameter updates, and see GEOCHEM-3.3.7 and GEOCHEM-3.3.8 for discussions of the iron and lead parameter updates, respectively.

The EQ3/6 Version 8.0a software package for geochemical modeling consists of two primary codes. The first code, EQ3NR, is an aqueous solution speciation-solubility code that provides the state of the solution, and sets up the initial conditions for further reaction-path modeling with EQ6, the second primary code. EQ3NR computes the equilibrium state of an aqueous system by determination of the distribution of chemical species employing standard state thermodynamic data and various equations describing the thermodynamic activity coefficients of these species in a database. These species may include solids, simple ions, gases, and ion-complexes. The input files (*.3i) to EQ3NR include information about the aqueous solution, its density, total-dissolved solids, analytical data, and other parameters such as the pH, pcH, or pmH, and redox constraints. EQ3NR input may also include various constraints that set the initial conditions for forthcoming EQ6 simulations. Such constraints may include equilibrium with a specified pure mineral phase(s), or electrical charge balance for a specific ion. Additionally, a list of mineral phases is input in the EQ3NR input file that are to be “suppressed” in subsequent EQ6 simulations; in other words, these suppressed phases will not be allowed to form in the EQ6 run. The choice of which phases are included in this list is based on kinetic considerations, knowledge of the system being modeled, and the analyst’s expert opinion.

EQ3NR evaluates the degree of disequilibrium in terms of the saturation index (SI = log Q/K) for all mineral phases in the thermodynamic database that share a common element, as specified for the aqueous solution in the EQ3NR input file. EQ3NR also calculates the theoretical equilibrium gas fugacities for each gas in the thermodynamic database that shares a common element, as specified for the aqueous solution in the EQ3NR input file.

The chief numerical method employed in EQ3NR is a modified Newton-Raphson technique. EQ3NR produces an output file (*.3o) that contains all input solution properties, and an extensive list of calculated solution properties. EQ3NR creates a “pickup” file (*.3p), which is a shorthand version of the output file that is appended to any future EQ6 input file, and is used to initialize an EQ6 reaction path calculation.

After EQ3NR is executed and a pickup file is generated, an EQ6 input file can be built to simulate the desired conceptual model. EQ6 calculates reaction paths (chemical evolution) in reacting water-rock and water-rock-waste systems. For the WIPP, EQ6 is used in closed-system titration mode, which means that a specified mass of reactants, from the input file, are added to 1 kg of solution, as specified in the pickup file, and the state of the solution is calculated at every reaction step. As phases become supersaturated they “precipitate” from solution. The chemistry of the solution may change such that a phase that had previously precipitated may redissolve. The reaction path terminates either when the system reaches equilibrium or when the reactants are exhausted.

The following sections provide information about the specific chemical conditions included in the WIPP Chemical Conditions Process Model.

GEOCHEM-3.2.1 Ionic Strength, Brine pH, pcH, or pmH and E_h, and Fugacity of CO_2

The WIPP is considered to be an isothermal, isobaric system for thermodynamic modeling purposes. Consequently, the remaining variables to be considered within the Pitzer framework are compositional including molalities of each solute species, the solid phases in equilibrium with those solutes, and gas phase partial pressures or fugacities for cases involving substances such as CO_2 or H_2S. The quantity of proton (H^+ or H_3O^+) in the system can affect mineral and other solute stabilities disproportionately to its molality so the activity of proton, expressed indirectly as pH, is frequently an important quantity to be measured and modeled. In the radionuclide community, pH is frequently expressed as pcH or pmH, which is the transformed pH value accounting for high ionic strength and other pH interferences. Terms within the Pitzer model also utilize ionic strength (I) which is a charge weighted sum of ionic solute molalities. Ionic strength is central to the Debye-Huckel limiting law which is general to all aqueous electrolyte systems, and consequently, is the lead term in any rigorous aqueous activity coefficient model.

GEOCHEM-3.2.1.1 Ionic Strength

The ionic strength of a solution is a measure of the concentration of ions in that solution. The WIPP Chemical Conditions Process Model for ionic strength is based on molality (mol/kg of water) and can be written as shown in Equation (GEOCHEM.26).

$$I = \frac{1}{2}\sum m_s z_s^2 \qquad \text{(GEOCHEM.26)}$$

The symbols, m_s and z_s, refer to the molality and valence charge, respectively, of each solute species.

GEOCHEM-3.2.1.2 Brine pH, pcH, or pmH

The dissociation of water produces hydrogen ion (H^+, proton) and hydroxide ion (OH^-) via:

$$H_2O(l) \leftrightarrow OH^-(aq) + H^+(aq) \qquad \text{(GEOCHEM.27)}$$

The most common definition of pH, which is an indicator of the relative acidity of a solution, is:

$$pH = -\log a_{H+} \qquad \text{(GEOCHEM.28)}$$

where a_{H+} is the hydrogen ion activity. pH measurements can be adversely affected by temperature, ionic strength, dielectric constant, ion charge, the size of the ions and also the density of the medium being measured. When these interferences are present, pH may need to be corrected. In many cases these pH corrections are not well defined and need to be measured. Correction factors (A) for the hydrogen ion concentration (pmH or pC_{H+}) can be determined by completing Gran titrations of the specific solution in question. pC_{H+} can be determined using the following equation (Rai et al. 1995a):

$$pC_{H+} = pH_{obs} + A \qquad \text{(GEOCHEM.29)}$$

where pH_{obs} is the measured pH reading of the sample, and A is defined as:

$$A = \log \gamma_{H+} + (F/2.303RT)\Delta Ej \qquad \text{(GEOCHEM.30)}$$

Where, γ_{H+} is the molarity- or molality-scale activity coefficient of H+, and ΔEj is the difference in liquid-junction potential between the standard and solutions. Neither term on the right-hand side of equation GEOCHEM.25 can be independently measured and therefore must be measured in combination through a modified Gran titration (Roselle 2011c). Once Gran titration data are obtained, the pH correction factor (A) can be determined by plotting the H+ (M or m) observed versus the H+ (M or m) added, and then calculating the LOG 10-based logarithms of the slope of the line. Roselle 2011c developed formulas as follows for the specific systems.

For NaCl dominated brines (including $MgCl_2$ and complex brines):

$$A_{NaCl}\ (\pm 0.47) = 0.186\ I_M - 0.105 \qquad \text{(GEOCHEM.31)}$$

Where I_M is the molar ionic strength of the solution.

Xiong et al. (2010a) reported and used the formula for $MgCl_2$ and NaCl matrices for calculation of pcH on a molarity scale:

$$A_M = -0.37647 + 0.62209 \times mMgCl_2 + 0.22791 \times mNaCl \qquad \text{(GEOCHEM.32)}$$

In many cases, individual researchers develop their own value for the constant A. Examples include the values derived by Rai et al. (1995a) and those developed by Xiong et al. (2010a). DOE is currently conducting more research in this area in order to establish pH transformation factors/correction factors (A) for complex WIPP brines.

GEOCHEM-3.2.1.3 Brine E_h

Certain ions can act as either oxidizing or reducing agents. However, the WIPP Chemical Conditions Process Model does not include oxidation/reduction reactions. As noted in the section on the conceptual model (GEOCHEM-3.1.7), reducing conditions are assumed because the closed repository is isolated from the atmosphere and iron metal is assumed to coexist with ferrous iron species [Fe^{2+}] over the 10,000-year regulatory period. That corrosion reaction buffers E_h in the repository such that Fe^{2+} exists instead of Fe^{3+}.

GEOCHEM-3.2.1.4 Fugacity of CO_2

The carbonate system is a well-defined set of reactions that relates the fugacity of gaseous carbon dioxide ($f_{CO_2(g)}$) to all carbonate species contained in an aqueous system via the following chemical equations; both are included in the WIPP Chemical Conditions Process Model:

$$\mathrm{CO_2(g) + H_2O(l) \leftrightarrow HCO_3^-(aq) + H^+(aq)}\ \mathrm{LogK_{CO_2(g)}} = -7.8193 \qquad \text{(GEOCHEM.33)}$$

$$\mathrm{HCO_3^-(aq) + H^+(aq) \leftrightarrow CO_2(aq) + H_2O(l)}\ \mathrm{LogK_{CO_2(aq)}} = 6.3374 \qquad \text{(GEOCHEM.34)}$$

Combining Equation (GEOCHEM.33) and Equation (GEOCHEM.34) defines the thermodynamic relationship between $CO_2(g)$ and $CO_2(aq)$, the simplest carbonate species.

$$\mathrm{CO_2(g) \leftrightarrow CO_2(aq)}\quad \mathrm{Log\,K_{CO_2(aq)}}^* = -1.4819 \qquad \text{(GEOCHEM.35)}$$

$$\mathrm{K_{CO_2(aq)}}^* = \frac{\mathrm{a_{CO_2(aq)}}}{\mathrm{f_{CO_2(g)}}} \Leftrightarrow \mathrm{f_{CO_2(g)}} = \frac{\mathrm{a_{CO_2(aq)}}}{\mathrm{K_{CO_2(aq)}}^*} \qquad \text{(GEOCHEM.36)}$$

In Equation (GEOCHEM.36), $K_{CO_2(aq)}$ is the speciation constant for $CO_2(aq)$, $a_{CO_2(aq)}$ is the activity of $CO_2(aq)$, and f_{CO_2} is the fugacity of $CO_2(g)$.

In both real and theoretical systems, such as those being simulated for the WIPP, there may not exist an actual gas phase atmosphere in contact with the aqueous environment. However, the fugacity of carbon dioxide can still be calculated by EQ3/6 via Equation (GEOCHEM.35) with knowledge of the activity of $CO_2(aq)$. The log $f_{CO_2(g)}$ is the gas equivalent of the saturation index of a solid phase, it represents the degree of saturation of carbon dioxide in the system.

GEOCHEM-3.2.2 Salado and Castile Minerals

Minerals that might be present and in contact with WIPP repository waste were characterized prior to initial certification (Powers et al. 1978). No additional Salado and Castile minerals have

been identified since the Powers et al. 1978 research. These minerals have been included in all recertifications to date.

The fourteen sodium-bearing minerals in the WIPP Chemical Conditions Process Model include: halite, nahcolite, trona, natron, Na_2CO_3•$7H_2O$(s), thermonatrite, pirssonite, burkeite, mirabilite, thenardite, $Na_3H(SO_4)_2$(s), aphthitalite, glauberite, and labile salt.

The ten potassium-bearing solids include: mercallite, sylvite, misentite, arcanite, syngenite, kalicinite, K_2CO_3•$1.5H_2O$(s), $K_8H_4(CO_3)_6$•$3H_2O$(s), $KNaCO_3$•$6H_2O$(s), and K-trona.

The ten calcium-bearing solids include: $CaCl_2$•$4H_2O$(s), $Ca_4Cl_2(OH)_6$•$13H_2O$(s), $Ca_2Cl_2(OH)_2$•H_2O(s), aragonite, portlandite, calcite, gaylussite, anhydrite, dolomite, and gypsum.

These minerals were included in the CCA and have been included in all recertifications since then. They will be included in CRA-2019.

Brush et al. (2006) made the argument that some form of carbonate phase, either aragonite, a calcite polymorph of slightly lower solubility, or a magnesian calcite would likely form in the WIPP repository environment, rather than calcite. The argument was based on the effects of single- and multi-inhibitors, inorganic elements and compounds, and organic ligands expected to be present in the WIPP waste, and which are known to “decrease the rate of calcite precipitation” (Brush et al. 2006). However, Xiong and Lord (2008) observed, first-hand, calcite precipitation in XRD patterns of their study of carbonation products of MgO in GWB and ERDA-6. Regardless of this, it was recommended that calcite, aragonite, dolomite, magnesite, nesquehonite, and hydromagnesite4323 be “suppressed,” i.e., not allowed to precipitate, in the baseline solubility model. This assumption has been in place since the CRA-2014 PA, when the EQ3/6 code was first used for these calculations, and for PAs before 2014, when the FMT code was used for the baseline solubility calculations (Domski 2019c).

During the course of running the baseline solubility model for the CRA-2019 PA, it was observed that with the addition of the iron reactant, $Fe(OH)_2$-Hex, an interval near the end of the reaction path, for both brines, was dominated by high pH and high carbonate concentration. Further examination of the EQ6 output files for these runs revealed that calcite was 50 times supersaturated, as were other carbonate phases, aragonite, magnesite, and dolomite, during this interval of high pH and carbonate concentration. Domski (2019b) examined the effect of allowing the precipitation of a calcite-hydromagnesite solid-solution phase to form, and it had no impact on actinide solubility. Calcite is a very common phase in natural waters, and by preventing its formation in the baseline solubility runs it was forcing the solution chemistry into an unrealistic compositional space. Therefore, additional trial runs were executed with the full suite of reactants, i.e., lead and iron, and with calcite “unsuppressed.” The results of these trials were later agreed upon to form the final baseline solubility model for the CRA-2019 PA.

GEOCHEM-3.2.2.1 Mineral Dissolution Reactions

Table GEOCHEM-6 shows the dissolution reactions for Salado and Castile minerals. Boron-bearing solids and reactions are discussed in GEOCHEM-3.2.6.

Table GEOCHEM-6. Dissolution Reactions for Salado and Castile Minerals Implemented in the WIPP Chemical Conditions Process Model for CRA-2019[A]

First Use	Mineral Dissolution Reactions
CCA	$NaCl(halite) \leftrightarrow Na^+ + Cl^-$
CCA	$NaHCO_3(nahcolite) \leftrightarrow Na^+ + HCO_3^-$
CCA	$Na_3H(CO_3)_2 \cdot 2H_2O(trona) + H^+ \leftrightarrow 3Na^+ + 2HCO_3^- + 2H_2O$
CCA	$Na_2CO_3 \cdot 10H_2O(natron) + H^+ \leftrightarrow 2Na^+ + HCO_3^- + 10H_2O$
CCA	$Na_2CO_3 \cdot 7H_2O(s) + H^+ \leftrightarrow 2Na^+ + HCO_3^- + 7H_2O$
CCA	$Na_2CO_3 \cdot H_2O(thermonatrite) + H^+ \leftrightarrow 2Na^+ + HCO_3^- + H_2O$
CCA	$Na_2Ca(CO_3)_2 \cdot 2H_2O(pirssonite) + 2H^+ \leftrightarrow 2Na^+ + Ca^{2+} + 2HCO_3^- + 2H_2O$
CCA	$Na_6CO_3(SO_4)_2$ (burkeite) $+ H^+ \leftrightarrow 6Na^+ + HCO_3^- + 2SO_4^{2-}$
CCA	$Na_2SO_4 \cdot 10H_2O(mirabilite) \leftrightarrow 2Na^+ + SO_4^{2-} + 10H_2O$
CCA	$Na_2SO_4(thenardite) \leftrightarrow 2Na^+ + SO_4^{2-}$
CCA	$Na_3H(SO_4)_2$ (s) $\leftrightarrow Na^+ + H^+ + 2SO_4^{2-}$
CCA	$NaK_3(SO_4)_2$(aphthitalite, glaserite) $\leftrightarrow Na^+ + 3K^+ + 2SO_4^{2-}$
CCA	$Na_2Ca(SO_4)_2$(glauberite) $\leftrightarrow 2Na^+ + Ca^{2+} + 2SO_4^{2-}$
CCA	$Na_4Ca(SO_4)_3 \cdot 2H_2O$(labile salt) $\leftrightarrow 4Na^+ + Ca^{2+} + 3SO_4^{2-} + 2H_2O$
CCA	$KHSO_4$ (mercallite) $\leftrightarrow K^+ + SO_4^{2-} + H^+$
CCA	KCl (sylvite) $\leftrightarrow K^+ + Cl^-$
CCA	$K_8H_6(SO_4)_7$(misenite) $\leftrightarrow 8K^+ + 6H^+ + 7SO_4^{2-}$
CCA	$K_2SO_4(arcanite) \leftrightarrow 2K^+ + SO_4^{2-}$
CCA	$K_2Ca(SO_4)_2 \cdot H_2O$(syngenite) $\leftrightarrow K^+ + Ca^{2+} + 2SO_4^{2-} + H_2O$
CCA	$KHCO_3(kalicinite) \leftrightarrow K^+ + HCO_3^-$
CCA	$K_2CO_3 \cdot 1.5H_2O(s) + H^+ \leftrightarrow 2K^+ + HCO_3^- + 1.5H_2O$
CCA	$K_8H_4(CO_3)_6 \cdot 3H_2O(s) + 2H^+ \leftrightarrow 8K^+ + 6HCO_3^- + 3H_2O$
CCA	$KNaCO_3 \cdot 6H_2O(s) + H^+ \leftrightarrow K^+ + Na^+ + HCO_3^- + 6H_2O$
CCA	$K_2NaH(CO_3)_2 \cdot 2H_2O$(K-trona) $+ H^+ \leftrightarrow 2K^+ + Na^+ + 2HCO_3^- + 2H_2O$
CCA	$CaCl_2 \cdot 4H_2O(s) \leftrightarrow Ca^{2+} + 2Cl^- + 4H_2O$
CCA	$Ca_4Cl_2(OH)_6 \cdot 13H_2O(s) + 6H^+ \leftrightarrow 4Ca^{2+} + 2Cl^- + 19H_2O$
CCA	$Ca_2Cl_2(OH)_2 \cdot H_2O(s) + 2H^+ \leftrightarrow 2Ca^{2+} + 2Cl^- + 3H_2O$
CCA	$CaCO_3(aragonite) + H^+ \leftrightarrow Ca^{2+} + HCO_3^-$
CCA	$CaCO_3(calcite)^B + H^+ \leftrightarrow Ca^{2+} + HCO_3^-$
CCA	$CaMg(CO_3)_2$ (dolomite) $\leftrightarrow Ca^{2+} + Mg^{2+} + 2CO_3^{2-}$
CCA	$CaNa_2(CO_3)_2 \cdot 5H_2O$(gaylussite) $+ 2H^+ \leftrightarrow Ca^{2+} + 2Na^+ + 2HCO_3^- + 5H_2O$
CCA	$Ca(OH)_2$ (portlandite) $+ 2H^+ \leftrightarrow Ca^{2+} + 2H_2O$
CCA	$CaSO_4(anhydrite) \leftrightarrow Ca^{2+} + SO_4^{2-}$
CCA	$CaSO_4 \cdot 2H_2O(gypsum) \leftrightarrow Ca^{2+} + SO_4^{2-} + 2H_2O$

[A]The left-hand column indicates when the reaction was first introduced in the WIPP Chemical Conditions Process Model.

[B]Calcite precipitation was originally included in the CCA, CRA-2004, and CRA-2009, and has again been included in the deferred PA for CRA-2019 as necessitated by the inclusion of iron reactants in the model.

GEOCHEM-3.2.3 Salado and Castile Brines

The major elements in the Salado and Castile brines are sodium [Na^+], calcium [Ca^{2+}], magnesium [Mg^{2+}], potassium [K^+], chlorine [Cl^-], carbon [CO_3^{2-}], sulfur [HS^-], and boron [$B(OH)_3$] (brackets indicate basis species used for thermodynamic modelling). In the CCA, the WIPP Chemical Conditions Process Model included the following additional species of the major elements: HSO_4^-, SO_4^{2-}, HCO_3^-, $CaCO_3$(aq), $MgOH^+$, and $MgCO_3$(aq). These species were included in the Harvie et al. (1984) model. Harvie et al. (1984) did not include aqueous species of Na^+, K^+, or Cl^-.

Aqueous dissociation for boron-bearing species is discussed in GEOCHEM-3.2.6. Chemical reactions for HS^- have not been included heretofore, and will not be included in CRA-2019.

GEOCHEM-3.2.3.1 Aqueous Dissociation Reactions for Ions in Salado and Castile Brines

Table GEOCHEM-7 shows the aqueous dissociation reactions for Salado and Castile brines.

Table GEOCHEM-7. Dissociation Reactions for Ions in Salado and Castile Brines Implemented in the WIPP Chemical Conditions Process Model for CRA-2019[A]

First Use	Aqueous Dissociation Reactions
CCA	$H_2O \leftrightarrow OH^- + H^+$
CCA	$HSO_4^- + H^+ \leftrightarrow SO_4^{2-} + H^+$
CCA	$CO_3^{2-} + H^+ \leftrightarrow HCO_3^-$
CCA	$CaCO_3(aq) + H+ \leftrightarrow Ca^{2+} + CO_3^{2-}$
CCA	$MgOH^+ + H^+ \leftrightarrow Mg^{2+} + H_2O$
CCA	$MgCO_3(aq) + H^+ \leftrightarrow Mg^{2+} + HCO_3^-$

[A]The left-hand column indicates when the reaction was first introduced in the WIPP Chemical Conditions Process Model.

GEOCHEM-3.2.4 Magnesium Oxide

MgO solids were included in the CCA based on the Harvie et al. (1984) model. Magnesium-bearing solids in the WIPP Chemical Conditions Process Model include: brucite, bischofite, phase 3 [$Mg_2Cl(OH)_3 \cdot 4H_2O$], phase 5 [$Mg_3Cl(OH)_5 \cdot 4H_2O$], tachyhydrite, carnallite, dolomite, magnesite, nesquehonite, hydromagnesite4323 [$Mg_4(CO_3)_3(OH)_2 \cdot 3H_2O$], hydromagnesite-5424 [$Mg_5(CO_3)_4(OH)_2 \cdot 4H_2O$], leonite, bloedite, epsomite, hexahydrite, kieserite, and kainite. Solids included in the CCA are indicated in Table GEOCHEM-8. Phase 5, a magnesium bearing solid, was added to the WIPP Chemical Conditions Process Model for CRA-2009 because it was found to form from MgO in GWB (Xiong et al. 2010a).

GEOCHEM-3.2.4.1 Dissolution and Dissociation Reactions for MgO Solids and Species

Table GEOCHEM-8 shows dissolution reactions for magnesium-bearing solids.

Table GEOCHEM-8. Dissolution Reactions for MgO Solids Implemented in the WIPP Chemical Conditions Process Model for CRA-2019[A]

First Use	Solid Dissolution Reactions
CCA	$Mg(OH)_2$(brucite) + $2H^+ \leftrightarrow Mg^{2+} + 2H_2O$
CCA	$MgCl_2 \cdot 6H_2O$(bischofite) $\leftrightarrow Mg^{2+} + 2Cl^- + 6H_2O$
CCA	$Mg_2Cl(OH)_3 \cdot 4H_2O$(phase 3) + $3H^+ \leftrightarrow 2Mg^{2+} + Cl^- + 7H_2O$
CRA-2009	$Mg_3Cl(OH)_5 \cdot 4H_2O$(phase 5) + $5H^+ \leftrightarrow 3Mg^{2+} + Cl^- + 9H_2O$
CCA	$Mg_2CaCl_6 \cdot 12H_2O$(tachyhydrite) $\leftrightarrow 2Mg^{2+} + Ca^{2+} + 6Cl^- + 12H_2O$
CCA	$KMgCl_3 \cdot 6H_2O$(carnallite) $\leftrightarrow K^+ + Mg^{2+} + 3Cl^- + 6H_2O$
CCA	$CaMg(CO_3)_2$ (dolomite) $\leftrightarrow Ca^{2+} + Mg^{2+} + 2CO_3^{2-}$
CCA	$MgCO_3$(magnesite) + $H^+ \leftrightarrow Mg^{2+} + HCO_3^-$
CCA	$MgCO_3 \cdot 3H_2O$(nesquehonite) + $H^+ \leftrightarrow Mg^{2+} + HCO_3^- + 3H_2O$
CCA	$Mg_4(CO_3)_3(OH)_2 \cdot 3H_2O$(hydromagnesite4323) + $5H^+ \leftrightarrow 4Mg^{2+} + 3HCO_3^- + 5H_2O$
PAVT	$Mg_5(CO_3)_4(OH)_2 \cdot 4H_2O$(hydromagnesite5424) + $6H^+ \leftrightarrow 5Mg^{2+} + 4HCO_3^- + 6H_2O$
CCA	$K_2Mg(SO_4)_2 \cdot 4H_2O$(leonite) $\leftrightarrow 2K^+ + Mg^{2+} + 2SO_4^{2-} + 4H_2O$
CCA	$Na_2Mg(SO_4)_2 \cdot 4H_2O$(bloedite) $\leftrightarrow 2Na^+ + Mg^{2+} + 2SO_4^{2-} + 2H_2O$
CCA	$MgSO_4 \cdot 7H_2O$(epsomite) $\leftrightarrow Mg^{2+} + SO_4^{2-} + 7H_2O$
CCA	$MgSO_4 \cdot 6H_2O$(hexahydrite) $\leftrightarrow Mg^{2+} + SO_4^{2-} + 6H_2O$
CCA	$MgSO_4 \cdot H_2O$(kieserite) $\leftrightarrow Mg^{2+} + SO_4^{2-} + H_2O$
CCA	$KMgClSO_4 \cdot 3H_2O$(kainite) $\leftrightarrow K^+ + Mg^{2+} + Cl^- + SO_4^{2-} + 3H_2O$

[A]The left-hand column indicates when the reaction was first introduced in the WIPP Chemical Conditions Process Model.

GEOCHEM-3.2.5 Organic Ligands

Most of the reactions with organic ligands were added for the 2004 recertification (Giambalvo 2002a, 2002b, 2002c, 2002d, 2003). For CRA-2004, the WIPP Chemical Conditions Process Model included dissolution of four oxalate solids: NaHOxalate•H_2O(s), Na_2Oxalate(s), whewellite (CaOxalate•$2H_2O$), and H_2Oxalate•$2H_2O$(s). The addition of whewellite was based on Xiong (2004).

The species included in CRA-2004 were: $MgAcetate^+$, $CaAcetate^+$, H_3Citrate (aq), $H_2Citrate^-$, $HCitrate^{2-}$, $MgCitrate^-$, CaCitrate, H_4EDTA(aq), H_3EDTA^-, H_2EDTA^{2-}, $HEDTA^{3-}$, $MgEDTA^{2-}$, $CaEDTA^2$, H_2Oxalate(aq), $HOxalate^-$, MgOxalate(aq), CaOxalate(aq), HLactate(aq).

For CRA-2019, the DOE has reviewed the WIPP models for EDTA, citrate, and oxalate. Solubility-limiting phases are being added, one for each of the organic ligands, EDTA [$Ca_2EDTA \cdot 7H_2O$(s)], citrate (earlandite), and oxalate (glushinskite). The DOE has decided to align the WIPP Chemical Conditions Process Models and parameters with the NEA database

project results when appropriate. In the case of EDTA and citrate, thermodynamic values from Hummel et al. (2005) are employed for CRA-2019. These data were derived with the Specific Ion Theory (SIT) model and are paired with Pitzer aqueous model parameters in DATA0.FM4. While not ideal, inspection of Tables GEOCHEM-21 and GEOCHEM-22 reveal that the SIT values are close to the Pitzer derived log K's, see GEOCHEM-4.1.2 for further discussion.

GEOCHEM-3.2.5.1 Dissolution and Dissociation Reactions with Organic Ligands

Table GEOCHEM-9 shows the dissolution reactions for organic solids and the aqueous dissociation reactions for the organic ligands.

Table GEOCHEM-9. Reactions with Organic Ligands Implemented in the WIPP Chemical Conditions Process Model for CRA-2019[A]

First Use	Solid Dissolution Reactions
CRA-2019	$Ca_2EDTA{\bullet}7H_2O(s) \leftrightarrow 2Ca^{2+} + EDTA^{4-} + 7H_2O$
CRA-2019	$Ca_3(Citrate)_2{\bullet}4H_2O$ (earlandite) $\leftrightarrow 3Ca^{2+} + 2Citrate^{3-} + 4H_2O$
CRA-2004	$NaHOxalate{\bullet}H_2O(s) \leftrightarrow Na^+ + H^+ + Oxalate^{2-} + H_2O$
CRA-2004	$Na_2Oxalate(s) \leftrightarrow 2Na^+ + Oxalate^{2-}$
CRA-2004	$CaOxalate{\bullet}H_2O(s)$ (whewellite) $\leftrightarrow Ca^{2+} + Oxalate^{2-} + H_2O$
CRA-2004	$H_2Oxalate{\bullet}2H_2O(s) \leftrightarrow Oxalate^{2-} + 2H^+ + 2H_2O$
CRA-2019	$MgOxalate{\bullet}2H_2O(s)$ (glushinskite) $\leftrightarrow Mg^{2+} + Oxalate^{2-} + 2H_2O$
	Aqueous Dissociation Reactions
CRA-2004	$H_4EDTA(aq) \leftrightarrow EDTA^{4-} + 4H^+$
CRA-2004	$H_3EDTA^- \leftrightarrow EDTA^{4-} + 3H^+$
CRA-2004	$H_2EDTA^{2-} \leftrightarrow EDTA^{4-} + 2H^+$
CRA-2004	$HEDTA^{3-} \leftrightarrow EDTA^{4-} + H^+$
CRA-2019	$NaEDTA^{3-} \leftrightarrow Na^+ + EDTA^{4-}$
CRA-2004	$MgEDTA^{2-} \leftrightarrow Mg^{2+} + EDTA^{4-}$
CRA-2019	$MgHEDTA^- \leftrightarrow H^+ + MgEDTA^{2-}$
CRA-2004	$CaEDTA^{2-} \leftrightarrow Ca^{2+} + EDTA^{4-}$
CRA-2019	$CaHEDTA^{1-} \leftrightarrow Ca^{2+} + H^+ + EDTA^{4-}$
CRA-2004	$H_3Citrate\ (aq) \leftrightarrow Citrate^{3-} + 3H^+$
CRA-2004	$H_2Citrate^- \leftrightarrow Citrate^{3-} + 2H^+$
CRA-2004	$HCitrate^{2-} \leftrightarrow Citrate^{3-} + H^+$
CRA-2004	$MgCitrate^- \leftrightarrow Mg^{2+} + Citrate^{3-}$
CRA-2019	$MgHCitrate\ (aq) \leftrightarrow Mg^{2+} + H^+ + Citrate^{3-}$
CRA-2019	$Mg(H_2Citrate)^+ \leftrightarrow Mg^{2+} + 2H^+ + Citrate^{3-}$
CRA-2004	$CaCitrate^- \leftrightarrow Ca^{2+} + Citrate^{3-}$
CRA-2019	$CaHCitrate(aq) \leftrightarrow Ca^{2+} + HCitrate^{2-}$
CRA-2019	$Ca(H_2Citrate)^+ \leftrightarrow Ca^{2+} + H_2Citrate^-$

Table GEOCHEM-9 (continued). Reactions with Organic Ligands Implemented in the WIPP Chemical Conditions Process Model for CRA-2019[A]

First Use	Aqueous Dissociation Reactions
CRA-2004	$H_2Oxalate(aq) \leftrightarrow Oxalate^{2-} + 2H^+$
CRA-2004	$HOxalate^{-} \leftrightarrow Oxalate^{2-} + H^+$
CRA-2004	$MgOxalate(aq) \leftrightarrow Mg^{2+} + Oxalate^{2-}$
CRA-2004	$CaOxalate(aq) \leftrightarrow Ca^{2+} + Oxalate^{2-}$

[A]The left-hand column indicates when the reaction was first introduced in the WIPP Chemical Conditions Process Model.

GEOCHEM-3.2.6 Borate

For the CCA, the WIPP Chemical Conditions Process Model included dissolution of the following solids: $Na_2B_4O_7 \cdot 10H_2O$(borax), $B(OH)_3$(boric acid), $KB_5O_8 \cdot 4H_2O$(K-pentaborate), $K_2B_4O_7 \cdot 4H_2O$(K-tetraborate), $NaBO_2 \cdot 4H_2O$(Na-metaborate), $NaB_5O_8 \cdot 5H_2O$(Na-pentaborate), and $NaBO_2 \cdot NaCl \cdot 2H_2O$(teepleite). For the CCA, the solute species considered were: $B(OH)_4^-$, $B(OH)_3(aq)$, $CaB(OH)_4^+$, $MgB(OH)_4^+$, $B_3O_3(OH)_4^-$, and $B_4O_5(OH)_4^{2-}$. This model was derived by Felmy and Weare (1986).

In the last two recertification cycles, the presence of a tetraborate species in WIPP brines has become of interest because of its potential effect on actinide +III solubility. Discussions have focused on the possible formation of a tetraborate complex with +III actinides. A tetraborate complex has not been included in CRA-2019, and the borate model remains unchanged for CRA-2019.

GEOCHEM-3.2.6.1 Dissolution and Dissociation Reactions for Borate Solids and Species

Table GEOCHEM-10 shows the dissolution reactions for borate solids and the aqueous dissociation reactions for the borate species.

Table GEOCHEM-10. Reac with Borate Implemented in the WIPP Chemical Conditions Process Model for CRA-2019[A]

First Used	Solid Dissolution Reactions
CCA	$Na_2B_4O_7 \cdot 10H_2O(borax) \leftrightarrow 2Na^+ + 4B(OH)_4^- + 2H^+ + H_2O$
CCA	$B(OH)_3(s) + H_2O \leftrightarrow B(OH)_4^- + H^+$
CCA	$KB_5O_8 \cdot 4H_2O(K\text{-pentaborate})\ (s) + 8H_2O \leftrightarrow K^+ + 5B(OH)_4^- + 4H^+$
CCA	$K_2B_4O_7 \cdot 4H_2O(K\text{-tetraborate})\ (s) + 5H_2O \leftrightarrow 2K^+ + 4B(OH)_4^- + 2H^+$
CCA	$NaBO_2 \cdot 4H_2O(Na\text{-metaborate})\ (s) \leftrightarrow Na^+ + B(OH)_4^- + 2H_2O$
CCA	$NaB_5O_8 \cdot 5H_2O(Na\text{-pentaborate})\ (s) + 7H_2O \leftrightarrow Na^+ + 5B(OH)_4^- + 4H^+$
CCA	$NaBO_2 \cdot NaCl \cdot 2H_2O(teepleite)\ (s) \leftrightarrow 2Na^+ + B(OH)_4^- + Cl^-$
First Used	**Aqueous Dissociation Reactions**
CCA	$B(OH)_3(aq) + H_2O \leftrightarrow B(OH)_4^- + H^+$
CCA	$CaB(OH)_4^+ \leftrightarrow Ca^{2+} + B(OH)_4^-$
CCA	$MgB(OH)_4^+ \leftrightarrow Mg^{2+} + B(OH)_4^-$
CCA	$B_3O_3(OH)_4^- + 5H_2O \leftrightarrow 3B(OH)_4^- + 2H^+$
CCA	$B_4O_5(OH)_4^{2-} + 7H_2O \leftrightarrow 4B(OH)_4^- + 2H^+$

[A]The left-hand column indicates when the reaction was first introduced in the WIPP Chemical Conditions Process Model.

GEOCHEM-3.2.7 Lead

Because lead is present in the repository as waste, and significant quantities are anticipated to be added due to shielded containers, it is being added to the WIPP Chemical Conditions Process Model for CRA-2019. Reactions for lead include four lead-bearing solids: PbO(litharge), $PbCO_3$(cerussite), and $Pb(SO_4)(s)$. The aqueous species included are: Pb^{2+}, $PbCl^+$, $PbCl_2(aq)$, $PbCl_3^-$, $PbCO_3(aq)$, $Pb(CO_3)_2^{2-}$, $Pb(CO_3)Cl^-$, $PbOH^+$, $Pb(OH)_2(aq)$, $Pb(SO_4)(aq)$, and $Pb(CO_3)(OH)^-$. Lead sorption to iron is not included. A conservative choice, as inclusion could reduce both dissolved lead and colloidal actinide concentrations. A summary of the reactions being added for lead is provided in this section and a more detailed discussion of lead reactions is provided in GEOCHEM-3.3.7.

There is evidence (Xiong 2014a; Xiong 2014b) that Pb^{2+} may form species with EDTA, citrate, and oxalate and that formation of lead-bearing solids with EDTA, citrate, and oxalate may occur (Xiong 2014a; Xiong 2014b). However, development of parameters to support addition of those reactions is still underway and they will not be included in CRA-2019.

GEOCHEM-3.2.7.1 Dissolution and Dissociation Reactions with Lead Solids and Species

Table GEOCHEM-11 shows the dissolution reactions for lead solids and the aqueous dissociation reactions for the lead species.

Table GEOCHEM-11. Reactions with Lead Implemented in the WIPP Chemical Conditions Process Model For CRA-2019[A]

First Use	Solid Dissolution Reactions
CRA-2019	α-PbO(litharge) + $2H^+ \leftrightarrow Pb^{2+} + H_2O$
CRA-2019	$PbCO_3$(cerussite) + $H^+ \leftrightarrow Pb^{2+} + HCO_3^-$
CRA-2019	$Pb_2CO_3Cl_2 + H^+ \leftrightarrow 2Pb^{2+} + HCO_3^- + 2Cl^-$
CRA-2019	$PbSO_4(s) + H^+ \leftrightarrow Pb^{2+} + HSO_4^-$
First Use	Aqueous Dissociation Reactions
CRA-2019	$PbCl^+ \leftrightarrow Pb^{2+} + Cl^-$
CRA-2019	$PbCl_2(aq) \leftrightarrow Pb^{2+} + 2Cl^-$
CRA-2019	$PbCl_3^- \leftrightarrow Pb^{2+} + 3Cl^-$
CRA-2019	$PbOH^+ \leftrightarrow H^+ \leftrightarrow Pb^{2+} + H_2O$
CRA-2019	$Pb(OH)_2(aq) + 2H^+ \leftrightarrow Pb^{2+} + 2H_2O$
CRA-2019	$Pb(CO_3)(OH)^- + 2H^+ \leftrightarrow Pb^{2+} + HCO_3^- + H_2O(l)$
CRA-2019	$Pb(CO_3)Cl^- + H^+ \leftrightarrow Pb^{2+} + HCO_3^- + Cl^-$
CRA-2019	$PbCO_3(aq) + H^+ \leftrightarrow Pb^{2+} + HCO_3^-$
CRA-2019	$Pb(CO_3)_2^{2-} + 2H^+ \leftrightarrow Pb^{2+} + 2HCO_3^-$
CRA-2019	$PbSO_4(aq) + H^+ \leftrightarrow Pb^{2+} + HSO_4^-$

[A]The left-hand column indicates when the reaction was first introduced in the WIPP Chemical Conditions Process Model.

GEOCHEM-3.2.8 Iron

Because iron is present in the repository as waste, and insignificant quantities as TRU waste containers, it is being added to the WIPP Chemical Conditions Process Model for CRA-2019.

The DOE investigations into the effect of iron on brine chemistry for the WIPP began after CRA-2009. As mentioned in GEOCHEM-3.1.7, in the WIPP Chemical Conditions Conceptual Model for chemical conditions, it is assumed that iron corrosion will result in a reducing environment, within 100 years of repository closure. Aqueous iron in the repository has not been modeled explicitly until CRA-2019. For this recertification, iron in the aqueous form is being added to the WIPP Chemical Conditions Process Model. The species and reactions considered are discussed below.

The iron reactions include eight iron-bearing solids: $Fe(OH)_2(s)$ (Ferrous iron hydroxide), $Fe_2Cl(OH)_3(s)$ (hibbingite), $FeCO_3(s)$ (siderite), $Fe_2CO_3(OH)_2(s)$ (chukanovite). It is assumed that these solids are in their crystalline form.

The aqueous species included are: $FeOH^+$, $Fe(OH)_2(aq)$, $Fe(OH)^{3-}$, $Fe(OH)_4^{2-}$, $FeCO_3(aq)$, $Fe(CO_3)_2^{2-}$.

Jang (2017) lists Fe^{2+} organic ligand complexes such as FeOxalate(aq), $Fe(Oxalate)_2^{2-}$, $FeEDTA^2$, $FeHEDTA^-$, $FeOHEDTA^{3-}$, $Fe(OH)_2EDTA^{4-}$, $FeOHCitrate^{2-}$, $FeCitrate^-$, and

FeHCitrate(aq). However, development of parameters to support addition of those reactions is still underway and will not be included in CRA-2019.

GEOCHEM-3.2.8.1 Dissolution and Dissociation Reactions with Iron Solids and Species

Table GEOCHEM-12 shows the dissolution reactions for iron solids and the aqueous dissociation reactions for the iron species that will be included for CRA-2019.

Table GEOCHEM-12. Reactions with Iron Implemented in the WIPP Chemical Conditions Process Model for CRA-2019[A]

First Used	Solid Dissolution Reactions
CRA-2019	$Fe(OH)_2(s) + 2H^+$ (ferrous hydroxide) $\leftrightarrow Fe^{2+} + 2H_2O$
CRA-2019	$Fe_2Cl(OH)_3(s) + 3H^+$ (hibbingite) $\leftrightarrow 2Fe^{2+} + Cl^- + 3H_2O$
CRA-2019	$FeCO_3(s) + H^+$ (siderite) $\leftrightarrow Fe^{2+} + HCO_3^-$
CRA-2019	$Fe_2CO_3(OH)_2(s) + 3H^+$ (chukanovite) $\leftrightarrow 2Fe^{2+} + HCO_3^- + 2H_2O$
First Used	**Aqueous Dissociation Reactions**
CRA-2019	$FeOH^+ + H^+ \leftrightarrow Fe^{2+} + H_2O$
CRA-2019	$Fe(OH)_2(aq) + 2H^+ \leftrightarrow Fe^{2+} + 2H_2O$
CRA-2019	$Fe(OH)_3^- + 3H^+ \leftrightarrow Fe^{2+} + 3H_2O$
CRA-2019	$FeCO_3(aq) + H^+ \leftrightarrow Fe^{2+} + HCO_3^-$
CRA-2019	$Fe(CO_3)_2^{2-} + 2H^+ \leftrightarrow Fe^{2+} + 2HCO_3^-$

[A]The left-hand column indicates when the reaction was first introduced in the WIPP Chemical Conditions Process Model.

GEOCHEM-3.3 Parameterization of the WIPP Chemical Conditions Process Models

The current certified version of the thermodynamic database is DATA0.FM1 (Xiong 2011). The DOE will create a new thermodynamic database for CRA-2019, DATA0.FM4. DATA0.FM4 will contain most of the parameter values from DATA0.FM1. Exceptions are discussed below. However, DATA0.FM4 will contain some new parameters that have been derived specifically for CRA-2019.

Throughout this section the term “equilibrium constant” is used in a generic sense that encompasses “solubility constant,” “formation constant,” and “dissociation constant.” Also, log K is used generically to represent “equilibrium constant.”

GEOCHEM-3.3.1 Ionic Strength, Brine pcH and Eh, and Fugacity of CO_2

Ionic strength, brine pcH, and fugacity of CO_2 are calculated parameters.

Pitzer parameters are not appropriate for the interaction between H^+ and OH^- because those ions do not coexist in the concentration range where Pitzer parameters are applicable. For example, in pure water at pH = 7 the concentrations of H^+ and OH^- are 1.0×10^{-7} molal. This concentration of ions is addressed by the Debye-Hückel term of the Pitzer model. Higher or lower pH is

achieved by addition of base or acid that increases the concentration of OH^- or H^+ at the expense of the other, so at a pH = 12 the OH^-, concentration might be ~0.01 molal, but the H^+ concentration would be ~1×10^{-12} molal. In the acid case, the appropriate interaction would be between H^+ and the counter-anion of the acid (for example Cl^-). In the base case, the appropriate interaction would be between OH^- and the counter-cation (for example Na^+).

GEOCHEM-3.3.2 Salado and Castile Minerals

There are no parameter changes for the Salado and Castile mineral reactions that were implemented in CRA-2019. The parameters are summarized in Table GEOCHEM-13.

GEOCHEM-3.3.2.1 Equilibrium Constants for Dissolution Reactions for Salado and Castile Minerals

The equilibrium constants for the dissolution reactions for Salado and Castile minerals implemented in the WIPP Chemical Conditions Process Model for CRA-2019 are shown in Table GEOCHEM-13.

Table GEOCHEM-13. Equilibrium Constants for Dissolution Reactions for Salado and Castile Minerals Implemented in the WIPP Chemical Conditions Process Model for CRA-2019[A]

Reaction	log K
Solid Dissolution Reactions	
$NaCl(halite) \leftrightarrow Na^+ + Cl^-$	1.57
$NaHCO_3(nahcolite) \leftrightarrow Na^+ + HCO_3^-$	-0.403
$Na_3H(CO_3)_2 \cdot 2H_2O(trona) + H^+ \leftrightarrow 3Na^+ + 2HCO_3^- + 2H_2O$	9.30
$Na_2CO_3 \cdot 10H_2O(natron) + H^+ \leftrightarrow 2Na^+ + HCO_3^- + 10H_2O$	9.52
$Na_2CO_3 \cdot 7H_2O(s) + H^+ \leftrightarrow 2Na^+ + HCO_3^- + 7H_2O$	9.88
$Na_2CO_3 \cdot H_2O(thermonatrite) + H^+ \leftrightarrow 2Na^+ + HCO_3^- + H_2O$	10.8
$Na_2Ca(CO_3)_2 \cdot 2H_2O(pirssonite) + 2H^+ \leftrightarrow 2Na^+ + Ca^{2+} + 2HCO_3^- + 2H_2O$	11.4
$Na_2SO_4 \cdot 10H_2O(mirabilite) \leftrightarrow 2Na^+ + SO_4^{2-} + 10H_2O$	-1.23
$Na_2SO_4(thenardite) \leftrightarrow 2Na^+ + SO_4^{2-}$	-0.288
$Na_3H(SO_4)_2\ (s) \leftrightarrow Na^+ + H^+ + 2SO_4^{2-}$	-0.814
$NaK_3(SO_4)_2(aphthitalite, glaserite) \leftrightarrow Na^+ + 3K^+ + 2SO_4^{2-}$	-3.80
$Na_2Ca(SO_4)_2(glauberite) \leftrightarrow 2Na^+ + Ca^{2+} + 2SO_4^{2-}$	-5.25
$Na_4Ca(SO_4)_3 \cdot 2H_2O(labile\ salt) \leftrightarrow 4Na^+ + Ca^{2+} + 3SO_4^{2-} + 2H_2O$	-5.67
$KHSO_4\ (mercallite) \leftrightarrow K^+ + SO_4^{2-} + H^+$	-1.40
$KCl\ (sylvite) \leftrightarrow K^+ + Cl^-$	-10.80
$K_8H_6(SO_4)_7(misenite) \leftrightarrow 8K^+ + 6H^+ + 7SO_4^{2-}$	-1.78
$K_2SO_4(arcanite) \leftrightarrow 2K^+ + SO_4^{2-}$	-3.54
$K_2Ca(SO_4)_2 \cdot H_2O(syngenite) \leftrightarrow K^+ + Ca^{2+} + 2SO_4^{2-} + H_2O$	-7.45
$KHCO_3(kalicinite) \leftrightarrow K^+ + HCO_3^-$	0.281

Table GEOCHEM-13 (continued). Equilibrium Constants for Dissolution Reactions for Salado and Castile Minerals Implemented in the WIPP Chemical Conditions Process Model for CRA-2019[A]

Reaction	log K
Solid Dissolution Reactions	
$K_2CO_3 \cdot 1.5H_2O(s) + H^+ \leftrightarrow 2K^+ + HCO_3^- + 1.5H_2O$	13.4
$K_8H_4(CO_3)_6 \cdot 3H_2O(s) + 2H^+ \leftrightarrow 8K^+ + 6HCO_3^- + 3H_2O$	27.7
$KNaCO_3 \cdot 6H_2O(s) + H^+ \leftrightarrow K^+ + Na^+ + HCO_3^- + 6H_2O$	10.2
$K_2NaH(CO_3)_2 \cdot 2H_2O$(K-trona) $+ H^+ \leftrightarrow 2K^+ + Na^+ + 2HCO_3^- + 2H_2O$	11.6
$CaCl_2 \cdot 4H_2O(s) \leftrightarrow Ca^{2+} + 2Cl^- + 4H_2O$	5.72
$Ca_4Cl_2(OH)_6 \cdot 13H_2O(s) + 6H^+ \leftrightarrow 4Ca^{2+} + 2Cl^- + 19H_2O$	68.7
$Ca_2Cl_2(OH)_2 \cdot H_2O(s) + 2H^+ \leftrightarrow 2Ca^{2+} + 2Cl^- + 3H_2O$	26.5
$CaCO_3$(aragonite) $+ H^+ \leftrightarrow Ca^{2+} + HCO_3^-$	2.12
$CaCO_3$(calcite)[B] $+ H^+ \leftrightarrow Ca^{2+} + HCO_3^-$	1.93
$CaNa_2(CO_3)_2 \cdot 5H_2O$(gaylussite) $+ 2H^+ \leftrightarrow Ca^{2+} + 2Na^+ + 2HCO_3^- + 5H_2O$	11.3
$Ca(OH)_2$ (portlandite) $+ 2H^+ \leftrightarrow Ca^{2+} + 2H_2O$	22.80
$CaSO_4$(anhydrite) $\leftrightarrow Ca^{2+} + SO_4^{2-}$	-4.36
$CaSO_4 \cdot 2H_2O$(gypsum) $\leftrightarrow Ca^{2+} + SO_4^{2-} + 2H_2O$	-4.58

[A]The source for all data in this table is Harvie et al. (1984) who reported values for standard state chemical potential that was a direct input to FMT (Novak 1996a; see also Babb and Novak 1995; Babb and Novak 1997 and addenda; Wang 1998). These were later converted to log K values as documented in Ismail et al. (2009).

[B]Calcite precipitation was originally included in the CCA, CRA-2004, and CRA-2009, and has again been included in the deferred PA for CRA-2019 as necessitated by the inclusion of iron reactants in the model.

GEOCHEM-3.3.3 Salado and Castile Brines

There are no parameter changes for the Salado and Castile brine reactions that were implemented in CRA-2019. The parameters are summarized below.

GEOCHEM-3.3.3.1 Equilibrium Constants for Aqueous Dissociation Reactions for Ions in Salado and Castile Brines

The equilibrium constants for aqueous dissociation reactions for ions in Salado and Castile brines implemented in the WIPP Chemical Conditions Process Model for CRA-2019 are shown in Table GEOCHEM-14.

Table GEOCHEM-14. Equilibrium Constants for Aqueous Dissociation Reactions for Ions in Salado and Castile Brines Implemented in the WIPP Chemical Conditions Process Model for CRA-2019[A]

Reaction	log K	Source
Aqueous Dissociation Reactions		
$H_2O \leftrightarrow OH^- + H^+$	-14.0	Harvie et al. (1984)
$HSO_4^- + H^+ \leftrightarrow SO_4^{2-} + H^+$	-1.98	Harvie et al. (1984)
$CO_3^{2-} + H^+ \leftrightarrow HCO_3^-$	10.3	Harvie et al. (1984)
$CaCO_3(aq) + H^+ \leftrightarrow Ca^{2+} + CO_3^{2-}$	7.19	Harvie et al. (1984)
$MgOH^+ + H^+ \leftrightarrow Mg^{2+} + H_2O$	11.8	Harvie et al. (1984)
$MgCO_3(aq) + H^+ \leftrightarrow Mg^{2+} + HCO_3^-$	7.41	Harvie et al. (1984)

[A]Harvie et al. (1984) reported values for standard state chemical potential that was a direct input to FMT (Novak 1996a; see also Babb and Novak 1995; Babb and Novak 1997 and addenda; (Wang 1998). These were later converted to log K values as documented in Ismail et al. (2009).

GEOCHEM-3.3.3.2 Pitzer Interaction Coefficients for Ions in Salado and Castile Brines

The Pitzer interaction coefficients for ions in Salado and Castile brines are shown in Table GEOCHEM-15, Table GEOCHEM-16, Table GEOCHEM-17, Table GEOCHEM-18, and Table GEOCHEM-19.

Table GEOCHEM-15. Pitzer Interaction Coefficients (Cation-Anion Interactions) for Ions in Salado and Castile Brines Implemented in the WIPP Chemical Conditions Process Model for CRA-2019

I	*j*	α_1/α_2^A	$\beta^{(0)}$	$\beta^{(1)}$	$\beta^{(2)}$	C^{φ}	Source
Cation-Anion Interactions							
H+	Cl^-	2.0/12.0	0.178	0.295	0	0.0008	Harvie et al. (1984)
H+	SO_4^{2-}	2.0/12.0	0.0298	0	0	0.0438	Harvie et al. (1984)
H+	HSO_4^-	2.0/12.0	0.207	0.556	0	0	Harvie et al. (1984)
Na^+	OH^-	2.0/12.0	0.0864	0.253	0	0.0044	Harvie et al. (1984)
Na^+	Cl^-	2.0/12.0	0.0765	0.266	0	0.0013	Harvie et al. (1984)
Na^+	SO_4^{2-}	2.0/12.0	0.0196	1.11	0	0.0050	Harvie et al. (1984)
Na^+	HSO_4^-	2.0/12.0	0.0454	0.398	0	0	Harvie et al. (1984)
Na^+	CO_3^{2-}	2.0/12.0	0.0399	1.39	0	0.0044	Harvie et al. (1984)
Na^+	HCO_3^-	2.0/12.0	0.0277	0.0411	0	0	Harvie et al. (1984)
K^+	OH^-	2.0/12.0	0.130	0.32	0	0.0041	Harvie et al. (1984)
K^+	Cl^-	2.0/12.0	0.0484	0.212	0	-0.0008	Harvie et al. (1984)
K^+	SO_4^{2-}	2.0/12.0	0.0500	0.779	0	0	Harvie et al. (1984)
K^+	HSO_4^-	2.0/12.0	-0.0003	0.174	0	0	Harvie et al. (1984)
K^+	CO_3^{2-}	2.0/12.0	0.149	1.43	0	-0.0015	Harvie et al. (1984)
K^+	HCO_3^-	2.0/12.0	0.0296	-0.013	0	-0.008	Harvie et al. (1984)
Ca^{2+}	OH^-	2.0/12.0	-0.175	-0.230	-5.72	0	Harvie et al. (1984)
Ca^{2+}	Cl^-	2.0/12.0	0.316	1.61	0	-0.0003	Harvie et al. (1984)
Ca^{2+}	SO_4^{2-}	2.0/12.0	0.2	3.20	-54.2	0	Harvie et al. (1984)
Ca^{2+}	HSO_4^-	2.0/12.0	0.215	2.53	0	0	Harvie et al. (1984)
Ca^{2+}	HCO_3^-	2.0/12.0	0.4	2.98	0	0	Harvie et al. (1984)
Mg^{2+}	Cl^-	2.0/12.0	0.352	1.68	0	0.0052	Harvie et al. (1984)
Mg^{2+}	SO_4^{2-}	2.0/12.0	0.221	3.34	-37.2	0.025	Harvie et al. (1984)
Mg^{2+}	HSO_4^-	2.0/12.0	0.4746	1.73	0	0	Harvie et al. (1984)
Mg^{2+}	HCO_3^-	2.0/12.0	0.329	0.607	0	0	Harvie et al. (1984)
$MgOH^+$	Cl^-	2.0/12.0	-0.10	1.66	0	0	Harvie et al. (1984)

Table GEOCHEM-16. Pitzer Interaction Coefficients (Cation-Cation; Anion-Anion Interactions) for Ions in Salado and Castile Brines Implemented in the WIPP Chemical Conditions Process Model for CRA-2019

i	*j*	$\theta_{cc'}$ or $\theta_{aa'}$	Source
Cation-Cation Interactions			
Na^+	Ca^{2+}	0.07	Harvie et al. (1984)
Na^+	H^+	0.036	Harvie et al. (1984)
Na^+	K^+	-0.012	Harvie et al. (1984)
Na^+	Mg^{2+}	0.07	Harvie et al. (1984)
K^+	H^+	0.005	Harvie et al. (1984)
K^+	Ca^{2+}	0.032	Harvie et al. (1984)
Ca^{2+}	H^+	0.092	Harvie et al. (1984)
Ca^{2+}	Mg^{2+}	0.007	Harvie et al. (1984)
Mg^{2+}	H^+	0.1	Harvie et al. (1984)
Anion-Anion Interactions			
OH^-	ClO_4^-	-0.032	Pitzer (1991)
OH^-	CO_3^{2-}	0.1	Harvie et al. (1984)
Cl^-	CO_3^{2-}	-0.02	Harvie et al. (1984)
Cl^-	HCO_3^-	0.03	Harvie et al. (1984)
Cl^-	HSO_4^-	-0.006	Harvie et al. (1984)
Cl^-	OH^-	-0.05	Harvie et al. (1984)
Cl^-	SO_4^{2-}	0.02	Harvie et al. (1984)
SO_4^{2-}	CO_3^{2-}	0.02	Harvie et al. (1984)
SO_4^{2-}	HCO_3^-	0.01	Harvie et al. (1984)
SO_4^{2-}	OH^-	-0.013	Harvie et al. (1984)
HCO_3^-	ClO_4^-	0.095	Neck et al. (1995)
HCO_3^-	CO_3^{2-}	-0.04	Harvie et al. (1984)

Table GEOCHEM-17. Pitzer Interaction Coefficients (Neutral-Cation; Neutral-Anion Interactions) for Ions in Salado and Castile Brines Implemented in the WIPP Chemical Conditions Process Model for CRA-2019

i	*j*	$\lambda_{nc'}$ or $\lambda_{na'}$	Source
Neutral-Cation Interactions			
$CO_2(aq)$	Na^+	0.1	Harvie et al. (1984)
$CO_2(aq)$	K^+	0.051	Harvie et al. (1984)
$CO_2(aq)$	Ca^{2+}	0.183	Harvie et al. (1984)
$CO_2(aq)$	Mg^{2+}	0.183	Harvie et al. (1984)
Neutral-Anion Interactions			
$CO_2(aq)$	Cl^-	-0.005	Harvie et al. (1984)
$CO_2(aq)$	SO_4^{2-}	0.097	Harvie et al. (1984)
$CO_2(aq)$	HSO_4^-	-0.003	Harvie et al. (1984)

Table GEOCHEM-18. Pitzer Interaction Coefficients (Cation-Cation-Anion Interactions) for Ions in Salado and Castile Brines Implemented in the WIPP Chemical Conditions Process Model for CRA-2019

i	*j*	*k*	ψ_{ijk}	Source
Cation-Cation-Anion- Interactions				
Na^+	K^+	Cl^-	-0.0018	Harvie et al. (1984)
Na^+	K^+	SO_4^{2-}	-0.01	Harvie et al. (1984)
Na^+	K^+	HCO_3^-	-0.003	Harvie et al. (1984)
Na^+	K^+	CO_3^{2-}	0.003	Harvie et al. (1984)
Na^+	Ca^{2+}	Cl^-	-0.007	Harvie et al. (1984)
Na^+	Ca^{2+}	SO_4^{2-}	-0.055	Harvie et al. (1984)
Na^+	Mg^{2+}	Cl^-	-0.012	Harvie et al. (1984)
Na^+	Mg^{2+}	SO_4^{2-}	-0.015	Harvie et al. (1984)
Na^+	H^+	Cl^-	-0.004	Harvie et al. (1984)
Na^+	H^+	HSO_4^-	-0.0129	Harvie et al. (1984)
K^+	Ca^{2+}	Cl^-	-0.025	Harvie et al. (1984)
K^+	Mg^{2+}	Cl^-	-0.022	Harvie et al. (1984)
K^+	Mg^{2+}	SO_4^{2-}	-0.048	Harvie et al. (1984)
K^+	H^+	Cl^-	-0.011	Harvie et al. (1984)

Table GEOCHEM-18 (continued). Pitzer Interaction Coefficients (Cation-Cation-Anion Interactions) for Ions in Salado and Castile Brines Implemented in the WIPP Chemical Conditions Process Model for CRA-2019

i	*j*	*k*	ψ_{ijk}	Source
Cation-Cation-Anion- Interactions				
K^+	H^+	SO_4^{2-}	0.197	Harvie et al. (1984)
K^+	H^+	HSO_4^-	-0.0265	Harvie et al. (1984)
Ca^{2+}	Mg^{2+}	Cl^-	-0.012	Harvie et al. (1984)
Ca^{2+}	Mg^{2+}	SO_4^{2-}	0.024	Harvie et al. (1984)
Ca^{2+}	H^+	Cl^-	-0.015	Harvie et al. (1984)
Mg^{2+}	$MgOH^+$	Cl^-	0.028	Harvie et al. (1984)
Mg^{2+}	H^+	Cl^-	-0.011	Harvie et al. (1984)
Mg^{2+}	H^+	HSO_4^-	-0.0178	Harvie et al. (1984)

Table GEOCHEM-19. Pitzer Interaction Coefficients (Anion-Anion-Cation Interactions) for Ions in Salado and Castile Brines Implemented in the WIPP Chemical Conditions Process Model for CRA-2019

i	*j*	*k*	ψ_{ijk}	Source
Anion-Anion-Cation Interactions				
Cl^-	SO_4^{2-}	Na^+	0.0014	Harvie et al. (1984)
Cl^-	SO_4^{2-}	Ca^{2+}	-0.018	Harvie et al. (1984)
Cl^-	SO_4^{2-}	Mg^{2+}	-0.004	Harvie et al. (1984)
Cl^-	HSO_4^-	Na^+	-0.006	Harvie et al. (1984)
Cl^-	HSO_4^-	H^+	0.013	Harvie et al. (1984)
Cl^-	OH^-	Na^+	-0.006	Harvie et al. (1984)
Cl^-	OH^-	K^+	-0.006	Harvie et al. (1984)
Cl^-	OH^-	Ca^{2+}	-0.025	Harvie et al. (1984)
Cl^-	HCO_3^-	Na^+	-0.015	Harvie et al. (1984)
Cl^-	HCO_3^-	Mg^{2+}	-0.096	Harvie et al. (1984)
Cl^-	CO_3^{2-}	Na^+	0.0085	Harvie et al. (1984)
Cl^-	CO_3^{2-}	K^+	0.004	Harvie et al. (1984)
SO_4^{2-}	HSO_4^-	Na^+	-0.0094	Harvie et al. (1984)
SO_4^{2-}	HSO_4^-	K^+	-0.0677	Harvie et al. (1984)
SO_4^{2-}	HSO_4^-	Mg^{2+}	-0.0425	Harvie et al. (1984)
SO_4^{2-}	OH^-	Na^+	-0.009	Harvie et al. (1984)
SO_4^{2-}	OH^-	K^+	-0.05	Harvie et al. (1984)
SO_4^{2-}	HCO_3^-	Na^+	-0.005	Harvie et al. (1984)
SO_4^{2-}	HCO_3^-	Mg^{2+}	-0.161	Harvie et al. (1984)

Table GEOCHEM-19 (continued). Pitzer Interaction Coefficients (Anion-Anion-Cation Interactions) for Ions in Salado and Castile Brines Implemented in the WIPP Chemical Conditions Process Model for CRA-2019

i	*j*	*k*	ψ_{ijk}	Source
Anion-Anion-Cation Interactions				
SO_4^{2-}	CO_3^{2-}	Na^+	-0.005	Harvie et al. (1984)
SO_4^{2-}	CO_3^{2-}	K^+	-0.009	Harvie et al. (1984)
OH^-	CO_3^{2-}	Na^+	-0.017	Harvie et al. (1984)
OH^-	CO_3^{2-}	K^+	-0.01	Harvie et al. (1984)
HCO_3^-	CO_3^{2-}	Na^+	0.002	Harvie et al. (1984)
HCO_3^-	CO_3^{2-}	K^+	0.012	Harvie et al. (1984)

GEOCHEM-3.3.4 Magnesium Oxide

The only change for MgO solids is a change in the log K for hydromagnesite5424. Recently, an error in transcription was discovered when the data from Robie and Hemingway (1973) was compared to that presented in DATA0.FM1. The error is in the FMT thermodynamic database fmt_050405.chemdat (Xiong 2005), where the μ^0/RT value attributed to Robie and Hemingway (1973) does not match what was reported by Robie and Hemingway (1973). It is unclear where the erroneous dimensionless standard state chemical potential value in fmt_050405.chemdat (Xiong et al. 2005b) came from.

Using either the μ^0/RT value derived from Robie and Hemingway (1973; -2365.82) or the standard free energy of formation (-5,864.74 kJ/mol), the log K values are: 62.77 and 31.49, respectively.

The value that will be used for CRA-2019 is 31.49.

GEOCHEM-3.3.4.1 Equilibrium Constants for Dissolution Reactions for MgO Solids

The equilibrium constants for dissolution reactions for MgO solids implemented in the WIPP Chemical Conditions Process Model are shown in Table GEOCHEM-20.

Table GEOCHEM-20. Equilibrium Constants for Dissolution Reactions for MgO Solids Implemented in the WIPP Chemical Conditions Process Model for CRA-2019[A]

Reaction	log K	Source
Solid Dissolution Reactions		
$Mg(OH)_2$(brucite) + $2H^+ \leftrightarrow Mg^{2+} + 2H_2O$	17.1	Harvie et al. (1984)
$MgCl_2 \cdot 6H_2O$(bischofite) $\leftrightarrow Mg^{2+} + 2Cl^- + 6H_2O$	4.46	Harvie et al. (1984)
$Mg_2Cl(OH)_3 \cdot 4H_2O$(phase 3) + $3H^+ \leftrightarrow 2Mg^{2+} + Cl^- + 7H_2O$	26.0	Harvie et al. (1984)
$Mg_3Cl(OH)_5 \cdot 4H_2O$(phase 5) + $5H^+ \leftrightarrow 3Mg^{2+} + Cl^- + 9H_2O$	43.0	Xiong et al. (2010a)
$Mg_2CaCl_6 \cdot 12H_2O$(tachyhydrite) $\leftrightarrow 2Mg^{2+} + Ca^{2+} + 6Cl^- + 12H_2O$	17.4	Harvie et al. (1984)
$KMgCl_3 \cdot 6H_2O$(carnallite) $\leftrightarrow K^+ + Mg^{2+} + 3Cl^- + 6H_2O$	4.33	Harvie et al. (1984)
$MgCO_3$(magnesite) + $H^+ \leftrightarrow Mg^{2+} + HCO_3^-$	2.51	Harvie et al. (1984)
$MgCO_3 \cdot 3H_2O$(nesquehonite) + $H^+ \leftrightarrow Mg^{2+} + HCO_3^- + 3H_2O$	5.17	Harvie et al. (1984)
$Mg_4(CO_3)_3(OH)_2 \cdot 3H_2O$(hydromagnesite4323) + $5H^+ \leftrightarrow 4Mg^{2+} + 3HCO_3^- + 5H_2O$	28.8	Langmuir (1965)
$Mg_5(CO_3)_4(OH)_2 \cdot 4H_2O$(hydromagnesite5424) + $6H^+ \leftrightarrow 5Mg^{2+} + 4HCO_3^- + 6H_2O$	31.49	Robie and Hemingway (1973)[B]
$K_2Mg(SO_4)_2 \cdot 4H_2O$(leonite) $\leftrightarrow 2K^+ + Mg^{2+} + 2SO_4^{2-} + 4H_2O$	-3.97	Harvie et al. (1984)
$Na_2Mg(SO_4)_2 \cdot 4H_2O$(bloedite) $\leftrightarrow 2Na^+ + Mg^{2+} + 2SO_4^{2-} + 2H_2O$	-2.35	Harvie et al. (1984)
$MgSO_4 \cdot 7H_2O$(epsomite) $\leftrightarrow Mg^{2+} + SO_4^{2-} + 7H_2O$	-1.88	Harvie et al. (1984)
$MgSO_4 \cdot 6H_2O$(hexahydrite) $\leftrightarrow Mg^{2+} + SO_4^{2-} + 6H_2O$	-1.63	Harvie et al. (1984)
$MgSO_4 \cdot H_2O$(kieserite) $\leftrightarrow Mg^{2+} + SO_4^{2-} + H_2O$	-0.123	Harvie et al. (1984)
$KMgClSO_4 \cdot 3H_2O$(kainite) $\leftrightarrow K^+ + Mg^{2+} + Cl^- + SO_4^{2-} + 3H_2O$	-0.193	Harvie et al. (1984)

[A]All of the references cited in this table, with the exception of Xiong et al. (2010a), derived or reported values for standard state chemical potential that was a direct input to FMT (Novak 1996a; see also Babb and Novak 1995; Babb and Novak 1997 and addenda; Wang 1998). These were later converted to log K values as documented in Ismail et al. (2009). [B]The DOE will use a revised value of 31.49 based on Robie and Hemingway (1973).

GEOCHEM-3.3.5 Organic Ligands

A review of the literature was documented in Giambalvo (2002a, 2002b, 2002c, 2002d, and 2003). Giambalvo (2002) notes that most of the values chosen for parameterization of the organic ligand reactions in the WIPP Chemical Conditions Process Model were taken from Choppin et al. (2001) and other documents derived from the same experimental data and published concurrently (Pokrovsky et al. 1998; Mizera et al. 1999; Moore et al. 1999; Borkowski et al. 2001). The data analyses contained in the references listed above are based on the same data set used by Moore (1996). Using ionic strength data from Choppin et al. (2001), Giambalvo (2002) derived values for $MgAcetate^+$, MgOxalate(aq), $MgCitrate^-$, and $MgEDTA^{2-}$.

The DOE plans to deviate from the values reported in Giambalvo (2002a, 2002b, 2002c, 2002d, and 2003) for CRA-2019. To align the WIPP Chemical Conditions Process Model with publications from the thermodynamic database project at the NEA, the following values from Hummel et al. (2005) were used to the extent they are available in that document. In addition,

three solubility-limiting phases were added, one for each of three ligands, EDTA, citrate, and oxalate. Also, a new species, $NaEDTA^{3-}$, was added.

GEOCHEM-3.3.5.1 Equilibrium Constants for Reactions with Organic Ligands

The equilibrium constants for reactions with organic ligands implemented in the WIPP Chemical Conditions Process Model are shown in Table GEOCHEM-21, Table GEOCHEM-22, and Table GEOCHEM-23. In some cases, two values are listed, the value from DATA0.FM1 and the value in DATA0.FM4 for CRA-2019. In several cases there is only one reaction and log K value. This is due to the fact that there is only one relevant reportable reaction and value in the literature. Where a change is planned, the new values that will be used for CRA-2019 are marked in bold. Values for acetate and lactate reactions that are contained in DATA0.FM1 are not being changed and are not shown in the following tables in this section.

Table GEOCHEM-21. Equilibrium Constants for Reactions with EDTA Implemented in the WIPP Chemical Conditions Process Model[A]

Reaction	log K	Source
Solid Dissolution Reactions		
$Ca_2EDTA{\bullet}7H_2O(s) \leftrightarrow 2Ca^{2+} + EDTA^{4-} + 7H_2O$	-16.81	Domski (2018b)
Aqueous Dissociation Reactions		
$H_4EDTA(aq) \leftrightarrow EDTA^{4-} + 4H^+$	-23.04	Giambalvo (2002)
$H_4EDTA(aq) \leftrightarrow EDTA^{4-} + 4H^+$	-23.42	Hummel et al. (2005)
$H_3EDTA^- \leftrightarrow EDTA^{4-} + 3H^+$	-20.54	Giambalvo (2002)
$H_3EDTA^- \leftrightarrow EDTA^{4-} + 3H^+$	-21.19	Hummel et al. (2005)
$H_2EDTA^{2-} \leftrightarrow EDTA^{4-} + 2H^+$	-17.45	Giambalvo (2002)
$H_2EDTA^{2-} \leftrightarrow EDTA^{4-} + 2H^+$	-18.04	Hummel et al. (2005)
$HEDTA^{3-} \leftrightarrow EDTA^{4-} + H^+$	-10.57	Giambalvo (2002)
$HEDTA^{3-} \leftrightarrow EDTA^{4-} + H^+$	-11.24	Hummel et al. (2005)
$NaEDTA^{3-} \leftrightarrow Na^+ + EDTA^{4-}$		Not included in DATA0.FM1
$NaEDTA^{3-} \leftrightarrow Na^+ + EDTA^{4-}$	-2.80	Hummel et al. (2005)
$MgEDTA^{2-} \leftrightarrow Mg^{2+} + EDTA^{4-}$	-10.13	Giambalvo (2002)
$MgEDTA^{2-} \leftrightarrow Mg^{2+} + EDTA^{4-}$	-10.90	Hummel et al. (2005)
$MgHEDTA^{2-} \leftrightarrow H^+ + MgEDTA^{4-}$		Not in DATA0.FM1
$MgHEDTA^{2-} \leftrightarrow H^+ + Mg^{2+} + EDTA^{4-}$	-15.40	Hummel et al. (2005)
$CaEDTA^{2-} \leftrightarrow Ca^{2+} + EDTA^{4-}$	-10.13	Giambalvo (2002)
$CaEDTA^{2-} \leftrightarrow Ca^{2+} + EDTA^{4-}$	-12.69	Hummel et al. (2005)
$CaHEDTA^{2-} \leftrightarrow H^+ + CaEDTA^{2-}$		Not in DATA0.FM1
$CaHEDTA^{2-} \leftrightarrow H^+ + Ca^{2+} + EDTA^{4-}$	-16.23	Hummel et al. (2005)

[A]Values for CRA-2019 are shown in bold; Giambalvo (2002a), (2002b), (2002c), (2002d), (2003) recommended values for standard state chemical potential that was a direct input to FMT (Novak 1996a; see also Babb and Novak 1995; Babb and Novak 1997 and addenda; Wang 1998). These were later converted to log K values as documented in Ismail et al. (2009).

Table GEOCHEM-22. Equilibrium Constants for Reactions with Citrate Implemented in the WIPP Chemical Conditions Process Model for CRA-2019[A]

Reaction	log K	Source
Solid Dissolution Reactions		
$Ca_3(Citrate)_2 \bullet 4H_2O$ (earlandite) ↔ $3Ca^{2+} + 2Citrate^{3-} + 4H_2O$	-17.90	Hummel et al. (2005)
Aqueous Dissociation Reactions		
$H_3Citrate$ (aq) ↔ $Citrate^{3-} + 3H^+$	-14.5	Giambalvo (2002)
$H_3Citrate$ (aq) ↔ $3H^+ + Citrate^{3-}$	-14.27	Hummel et al. (2005)
$H_2Citrate^- ↔ Citrate^{3-} + 2H^+$	-11.14	Hummel et al. (2005)
$H_2Citrate^- ↔ Citrate^{3-} + 2H^+$	-11.3	Giambalvo (2002)
$HCitrate^{2-} ↔ Citrate^{3-} + H^+$	-6.42	Giambalvo (2002)
$HCitrate^{2-} ↔ Citrate^{3-} + H^+$	-6.36	Hummel et al. (2005)
MgHCitrate (aq) ↔ $Mg^{2+} + H^+ + Citrate^{3-}$		Not in DATA0.FM1
MgHCitrate (aq) ↔ $Mg^{2+} + H^+ + Citrate^{3-}$	-8.96	Hummel et al. (2005)
$Mg(H_2Citrate)^+ ↔ Mg^{2+} + 2H^+ + Citrate^{3-}$	-12.45	Hummel et al. (2005)
$MgCitrate^- ↔ Mg^{2+} + Citrate^{3-}$	-5.30	Giambalvo (2002)
$MgCitrate^- ↔ Mg^{2+} + Citrate^{3-}$	-4.81	Hummel et al. (2005)
$CaCitrate^- ↔ Ca^{2+} + Citrate^{3-}$	-5.30	Giambalvo (2002)
$CaCitrate^- ↔ Ca^{2+} + Citrate^{3-}$	-4.80	Hummel et al. (2005)
CaHCitrate(aq) ↔ $Ca^{2+} + H^+ + Citrate^{3-}$		Not in DATA0.FM1
CaHCitrate(aq) ↔ $Ca^{2+} + H^+ + Citrate^{3-}$	--9.28	Hummel et al. (2005)
$Ca(H_2Citrate)^+ ↔ Ca^{2+} + 2H^+ + Citrate^{3-}$		Not in DATA0.FM1
$Ca(H_2Citrate)^+ ↔ Ca^{2+} + 2H^+ + Citrate^{3-}$	-12.67	Hummel et al. (2005)

[A]Values for CRA-2019 are shown in bold; Giambalvo (2002a), (2002b), (2002c), (2002d), (2003) recommended values for standard state chemical potential that was a direct input to FMT (Novak 1996a; see also Babb and Novak 1995; Babb and Novak 1997 and addenda; Wang 1998). These were later converted to log K values as documented in Ismail et al. (2009).

Table GEOCHEM-23. Equilibrium Constants for Reactions with Oxalate Implemented in the WIPP Chemical Conditions Process Model[A]

Reaction	log K	Source
Solid Dissolution Reactions		
NaHOxalate•H_2O(s) ↔ Na^+ + H^+ + $Oxalate^{2-}$ +H_2O	-6.06	Giambalvo (2002d)
Na_2Oxalate(s) ↔ 2Na^+ + $Oxalate^{2-}$	-2.41	Giambalvo (2002d)
CaOxalate•H_2O(s) (whewellite)↔ Ca^{2+} + $Oxalate^{2-}$ + H_2O	-8.75	Xiong (2004)
CaOxalate•H_2O(s) (whewellite)↔ Ca^{2+} + $Oxalate^{2-}$ + H_2O	-8.60	Hummel et al. (2005)
MgOxalate•2H_2O(s) (glushinskite) ↔ Mg^{2+} + $Oxalate^{2-}$ + 2H_2O	-6.41	Jang (2019)
H_2Oxalate•2H_2O(s) ↔ $Oxalate^{2-}$ + 2H^+ + 2H_2O	-5.66	Giambalvo (2002d)
Aqueous Dissociation Reactions		
H_2Oxalate(aq) ↔ $Oxalate^{2-}$ + 2H^+	-5.65	Giambalvo (2002)
$HOxalate^-$ ↔ $Oxalate^{2-}$ + H^+	-4.26	Giambalvo (2002)
MgOxalate(aq) ↔ Mg^{2+} + $Oxalate^{2-}$	-3.79	Choppin et al. (2001)
$MgOxalate_2^{2-}$ ↔ Mg^{2+} + 2$Oxalate^{2-}$	-5.24	Jang (2019)
CaOxalate(aq) ↔ Ca^{2+} + $Oxalate^{2-}$	-3.79	Giambalvo (2002)

[A]Values for CRA-2019 are shown in bold; Giambalvo (2002a), (2002b), (2002c), (2002d), (2003) recommended values for standard state chemical potential that was a direct input to FMT (Novak 1996a; see also Babb and Novak 1995; Babb and Novak 1997 and addenda; Wang 1998). These were later converted to log K values as documented in Ismail et al. (2009).

GEOCHEM-3.3.5.2 Pitzer Interaction Coefficients for Ions Containing Organic Ligands

The Pitzer interaction coefficients for ions containing organic ligands implemented in the WIPP Chemical Conditions Process Model are shown in Table GEOCHEM-24, Table GEOCHEM-25, Table GEOCHEM-26, and Table GEOCHEM-27.

Table GEOCHEM-24. Pitzer Interaction Coefficients (Cation-Anion Interactions) for Ions Containing EDTA Implemented in the WIPP Chemical Conditions Process Model[A]

I	*j*	α_1/α_2[A]	$\beta^{(0)}$	$\beta^{(1)}$	C^{φ}	Source
Cation-Anion Interactions						
$EDTA^{4-}$	Na^+	2.0/12.0	1.02	11.6	0.001	Giambalvo (2002)
$EDTA^{4-}$	Na^+	2.0/12.0	1.10	15.6	0.001	Felmy and Mason (2003)
$EDTA^{4-}$	K^+	2.0/12.0	1.02	11.6	0.001	Giambalvo (2002)
$EDTA^{4-}$	K^+	2.0/12.0	1.10	15.6	0.001	Felmy and Mason (2003)
$EDTA^{4-}$	Ca^{2+}	Not included in DATA0.FM1				
$EDTA^{4-}$	Ca^{2+}	1.4/12.0	2.48	0	0	Domski (2018c)[B]
$HEDTA^{3-}$	Na^+	2.0/12.0	0.546	5.22	-0.048	Giambalvo (2002)
$HEDTA^{3-}$	K^+	2.0/12.0	0.546	5.22	-0.048	Giambalvo (2002)
H_2EDTA^{2-}	Na^+	2.0/12.0	-0.126	1.74	0.054	Giambalvo (2002)
H_2EDTA^{2-}	K^+	2.0/12.0	-0.126	1.74	0.054	Giambalvo (2002)
H_3EDTA^-	Na^+	2.0/12.0	-0.235	0.29	0.059	Giambalvo (2002)
H_3EDTA^-	K^+	2.0/12.0	-0.235	0.29	0.059	Giambalvo (2002)
$NaEDTA^{3-}$	Na^+	Not included in DATA0.FM1				
$NaEDTA^{3-}$	Na^+	2.0/12.0	0.59	5.39	0	Felmy and Mason (2003)
$CaEDTA^{2-}$	Na^+	2.0/12.0	0.213	1.74	0.0087	Giambalvo (2002)
$CaEDTA^{2-}$	Na^+	2.0/12.0	0.185	2.41	0	Domski (2018b)
$CaEDTA^{2-}$	K^+	2.0/12.0	0.213	1.74	0.0087	Giambalvo (2002)
$CaEDTA^{2-}$	K^+	2.0/12.0	0.185	2.41	0	Domski (2018b)
$CaEDTA^{2-}$	Mg^{2+}	Not included in DATA0.FM1				
$CaEDTA^{2-}$	Mg^{2+}	1.4/12.0	0	7.21	0	Domski (2018c)[B]
$MgEDTA^{2-}$	Na^+	2.0/12.0	0.213	1.74	0.0087	Giambalvo (2002)
$MgEDTA^{2-}$	Na^+	Not included in DATA0.FM4				
$MgEDTA^{2-}$	K^+	2.0/12.0	0.213	1.74	0.0087	Giambalvo (2002)
$MgEDTA^{2-}$	K^+	Not included in DATA0.FM4				
$MgEDTA^{2-}$	Mg^{2+}	Not included in DATA0.FM1				
$MgEDTA^{2-}$	Mg^{2+}	1.4/12.0	0	7.27	0	Domski (2018c)[B]

[A]Values for CRA-2019 are shown in bold. All values for $\beta^{(2)}$ are 0.
[B]Errors in the draft Appendix Geochem were found for the following α_1 values; Parameter problem reports were generated and documented in Domski 2019d, 2019e, 2019f, 2019g, 2019h, 2019i, 2019j, 2019k, 2019l, and 2019m.

Table GEOCHEM-25. Pitzer Interaction Coefficients (Cation-Anion Interactions) for Ions Containing Citrate Implemented in the WIPP Chemical Conditions Process Model[A]

I	*j*	α_1/α_2[A]	$\beta^{(0)}$	$\beta^{(1)}$	C^{φ}	Source
Cation-Anion Interactions						
$Citrate^{3-}$	Na^+	2.0/12.0	0.0887	5.22	0.047	Giambalvo (2002)
$Citrate^{3-}$	K^+	2.0/12.0	0.0887	5.22	0.047	Giambalvo (2002)
$H_2Citrate^-$	Na^+	2.0/12.0	-0.127	0.29	0.013	Giambalvo (2002)
$H_2Citrate^-$	K^+	2.0/12.0	-0.130	0.29	0.013	Giambalvo (2002)
$HCitrate^{2-}$	Na^+	2.0/12.0	-0.0989	1.74	0.027	Giambalvo (2002)
$HCitrate^{2-}$	K^+	2.0/12.0	-0.0989	1.74	0.027	Giambalvo (2002)
$CaCitrate^-$	Na^+	2.0/12.0	0.174	0.29	-0.069	Giambalvo (2002)
$CaCitrate^-$	K^+	2.0/12.0	0.174	0.29	-0.069	Giambalvo (2002)
$MgCitrate^-$	Na^+	2.0/12.0	0.174	0.29	-0.069	Giambalvo (2002)
$MgCitrate^-$	K^+	2.0/12.0	0.174	0.29	-0.069	Giambalvo (2002)

[A]Values for CRA-2019 are shown in bold. All values for $\beta^{(2)}$ are 0. No changes will be made to create DATA0.FM4.

Table GEOCHEM-26. Pitzer Interaction Coefficients (Cation-Anion Interactions) for Ions Containing Oxalate Implemented in the WIPP Chemical Conditions Process Model for CRA-2019[A]

I	*j*	α_1/α_2[A]	$\beta^{(0)}$	$\beta^{(1)}$	C^{φ}	Source
Cation-Anion Interactions						
$Oxalate^{2-}$	Na^+	2.0/12.0	-0.218	1.74	0.122	Giambalvo (2002)
$Oxalate^{2-}$	K^+	2.0/12.0	-0.218	1.74	0.122	Giambalvo (2002)
$Mg(Oxalate)^{2-}_2$	Na^+	20./12.0	0.07	0	0	Jang (2019)
$HOxalate^-$	Na^+	2.0/12.0	-0.245	0.29	0.068	Giambalvo (2002)
$HOxalate^-$	K^+	2.0/12.0	-0.245	0.29	0.068	Giambalvo (2002)

[A]All values for $\beta^{(2)}$ are 0.

Table GEOCHEM-27. Pitzer Interaction Coefficients (Neutral-Cation; Neutral-Anion Interactions) for Ions Containing Organic Ligands Implemented in the WIPP Chemical Conditions Process Model for CRA-2019[A]

i	*j*	λ_{nc}, or λ_{na},	Source
Neutral-Cation Interactions			
MgOxalate(aq)	Na^+	Not Included in DATA0.FM1	
MgOxalate(aq)	Na^+	0.08	Jang (2019)
MgOxalate(aq)	Mg^{2+}	0.20	Jang (2019)
Neutral-Anion Interactions			
CaOxalate(aq)	Cl^-	0.0189	Giambalvo (2002)
MgOxalate(aq)	Cl^-	0.0189	Giambalvo (2002)

[A]Values for CRA-2019 are shown in bold.

GEOCHEM-3.3.6 Borate

The DOE is not planning any changes to the borate model that was developed by Felmy and Weare (1986).

GEOCHEM-3.3.6.1 Equilibrium Constants for Reactions with Borate

The equilibrium constants for reactions with borate implemented in the WIPP Chemical Conditions Process Model are shown in Table GEOCHEM-28. These values will be used in CRA-2019.

Table GEOCHEM-28. Equilibrium Constants for Reactions with Borate Implemented in the WIPP Chemical Conditions Process Model for CRA-2019[A]

SO_4^{2-}	OH^-
Solid Dissolution Reactions	
$Na_2B_4O_7 \cdot 10H_2O$(borax)$\leftrightarrow 2Na^+ + 4B(OH)_4^- + 2H^+ + H_2O$	-24.5
$B(OH)_3(s) + H_2O \leftrightarrow B(OH)_4^- + H^+$	-9.27
$KB_5O_8 \cdot 4H_2O$(K-pentaborate) (s)$+ 8H_2O \leftrightarrow K^+ + 5B(OH)_4^- + 4H^+$	-41.5
$K_2B_4O_7 \cdot 4H_2O$(K-tetraborate) (s) $+ 5H_2O \leftrightarrow 2K^+ + 4B(OH)_4^- + 2H^+$	-23.1
$NaBO_2 \cdot 4H_2O$(Na-metaborate) (s)$\leftrightarrow Na^+ + B(OH)_4^- + 2H_2O$	0.329
$NaB_5O_8 \cdot 5H_2O$(Na-pentaborate) (s) $+ 7H_2O \leftrightarrow Na^+ + 5B(OH)_4^- + 4H^+$	-40.3
$NaBO_2 \cdot NaCl \cdot 2H_2O$(teepleite) (s)$\leftrightarrow 2Na^+ + B(OH)_4^- + Cl^-$	1.60
Aqueous Dissociation Reactions	
$B(OH)_3(aq) + H_2O \leftrightarrow B(OH)_4^- + H^+$	-9.24
$CaB(OH)_4^+ \leftrightarrow Ca^{2+} + B(OH)_4^-$	-1.65
$MgB(OH)_4^+ \leftrightarrow Mg^{2+} + B(OH)_4^-$	-1.40
$B_3O_3(OH)_4^- + 5H_2O \leftrightarrow 3B(OH)_4^- + 2H^+$	-20.2
$B_4O_5(OH)_4^{2-} + 7H_2O \leftrightarrow 4B(OH)_4^- + 2H^+$	-20.8

[A]The source for all data in this table is Felmy and Weare (1986) who reported values for standard state chemical potential that was a direct input to FMT (Novak 1996a; see also Babb and Novak 1995; Babb and Novak 1997 and addenda; Wang 1998). These were later converted to log K values as documented in Ismail et al. (2009).

GEOCHEM-3.3.6.2 Pitzer Interaction Coefficients for Ions Containing Borate

The Pitzer interaction coefficients for ions containing borate implemented in the WIPP Chemical Conditions Process Model are shown in Table GEOCHEM-29, Table GEOCHEM-30, Table GEOCHEM-31, and Table GEOCHEM-32.

Table GEOCHEM-29. Pitzer Interaction Coefficients (Cation-Anion Interactions) for Ions Containing Borate Implemented in the WIPP Chemical Conditions Process Model for CRA-2019

I	*j*	α_1/α_2	$\beta^{(0)}$	$\beta^{(1)}$	$\beta^{(2)}$	C^{φ}
Cation-Anion Interactions						
$B(OH)_4^-$	Na^+	2.0/12.0	-0.0427	0.089	0	0.0114
$B(OH)_4^-$	K^+	2.0/12.0	0.035	0.14	0	0
$B_3O_3(OH)_4^-$	Na^+	2.0/12.0	-0.056	-0.91	0	0
$B_3O_3(OH)_4^-$	K^+	2.0/12.0	-0.13	0	0	0
$B_4O_5(OH)_4^{2-}$	Na^+	2.0/12.0	-0.11	-0.4	0	0
$B_4O_5(OH)_4^{2-}$	K^+	2.0/12.0	-0.022	0	0	0
$MgB(OH)_4^+$	Cl^-	2.0/12.0	0.16	0	0	0
$CaB(OH)_4^+$	Cl^-	2.0/12.0	0.12	0	0	0

[A]The source for all data in this table is Felmy and Weare (1986) who reported values for standard state chemical potential that was a direct input to FMT (Novak 1996a; see also Babb and Novak 1995; Babb and Novak 1997 and addenda; Wang 1998). These were later converted to log K values as documented in Ismail et al. (2009).

Table GEOCHEM-30. Pitzer Interaction Coefficients (Anion-Anion Interactions) for Ions Containing Borate Implemented in the WIPP Chemical Conditions Process Model for CRA-2019

i	*j*	$\theta_{cc'}$ or $\theta_{aa'}$	Source
Anion-Anion Interactions			
$B(OH)_4^-$	Cl^-	-0.065	Felmy and Weare (1986)
$B(OH)_4^-$	SO_4^{2-}	-0.012	Felmy and Weare (1986)
$B_3O_3(OH)_4^-$	Cl^-	0.12	Felmy and Weare (1986)
$B_3O_3(OH)_4^-$	SO_4^{2-}	0.1	Felmy and Weare (1986)
$B_3O_3(OH)_4^-$	HCO_3^-	-0.1	Felmy and Weare (1986)
$B_4O_5(OH)_4^{2-}$	Cl^-	0.074	Felmy and Weare (1986)
$B_4O_5(OH)_4^{2-}$	SO_4^{2-}	0.12	Felmy and Weare (1986)
$B_4O_5(OH)_4^{2-}$	HCO_3^-	-0.087	Felmy and Weare (1986)

Table GEOCHEM-31. Pitzer Interaction Coefficients (Neutral-Cation; Neutral-Anion Interactions) for Ions Containing Borate Implemented in the WIPP Chemical Conditions Process Model for CRA-2019

i	*j*	$\lambda_{nc'}$ or $\lambda_{na'}$	Source
Neutral-Cation Interactions			
$B(OH)_3(aq)$	Na^+	-0.097	Felmy and Weare (1986)
$B(OH)_3(aq)$	K^+	-0.14	Felmy and Weare (1986)
Neutral-Anion Interactions			
$B(OH)_3(aq)$	Cl^-	0.091	Felmy and Weare (1986)
$B(OH)_3(aq)$	SO_4^{2-}	0.018	Felmy and Weare (1986)
$B(OH)_3(aq)$	$B_3O_3(OH)_4^-$	-0.2	Felmy and Weare (1986)

Table GEOCHEM-32. Pitzer Interaction Coefficients (Neutral-Cation-Anion Interactions) for Ions Containing Borate Implemented in the WIPP Chemical Conditions Process Model for CRA-2019

I	*j*	*k*	ζ_{ijk}	Source
Neutral-Cation-Anion Interactions				
$B(OH)_3(aq)$	Cl^-	H^+	-0.0102	Felmy and Weare (1986)
$B(OH)_3(aq)$	SO_4^{2-}	Na^+	0.046	Felmy and Weare (1986)

GEOCHEM-3.3.7 Lead

Lead is being added to the WIPP Chemical Conditions Process Model for CRA-2019. The parameters for lead will be included in DATA0.FM4. A summary of the parameters is provided in this section. The lead system was initially parameterized primarily with data gathered as part of a geochemistry research program for the WIPP (Xiong 2013, 2014a, 2014b, 2015a, 2015b). Literature sources (Millero and Byrne 1984; Felmy et al. 2000; Powell et al. 2009; Easley and Byrne 2011) provided some of the parameters needed for the model. However, because of some uncertainty in the solids characterization in the lead experiments, a different lead model was applied.

A critical review of the lead solids and lead speciation reactions with inorganic ligands published as an International Union of Pure and Applied Chemists (IUPAC) technical document (Powell et al. 2009) was implemented for CRA-2019, despite that these data were derived with the SIT model and not the Pitzer model. Thus, the lead model used for CRA-2019 includes only thermodynamic data for lead inorganic aqueous complexes and lead solid phases with no accompanying Pitzer interaction parameters for the charged species. In the absence of Pitzer parameters, all activity coefficient calculations for charged lead species in EQ3/6 default to the extended Debye-Huckel expression, which would likely underestimate gamma values resulting in artificially inflated lead concentrations. The effect of high lead concentrations should not pose an issue in terms of the actinide solubility(s) when considered with regard to the reactions

outlined in Table GEOCHEM-33. The lead speciation reactions in Table GEOCHEM-33 suggest that lead-chloride species will dominate the lead chemistry. Considering that chloride has an infinite source in the form of halite in the repository, combined with knowledge that there are no lead-organic reactions included in the database, the possibility of lead competing for organic ligands is eliminated, which is conservative because it will increase the actinide concentrations via organic complexation.

The lead model of Powell et al. (2009) should be replaced with a more appropriate Pitzer model that includes lead speciation reactions with both inorganic and organic ligands to properly characterize the lead system in the WIPP. However, for CRA-2019 the current lead model provides insight into the effect of lead on actinide solubility.

GEOCHEM-3.3.7.1 Equilibrium Constants for Reactions with Lead

The equilibrium constants for reactions with lead implemented in the WIPP Chemical Conditions Process Model are shown in Table GEOCHEM-33. Note that sodium – lead carbonate phase abellaite [$NaPb_2(CO_3)_2(OH)(s)$] – was not included in DATA0.FM4 due to issues with solid phase characterization of the experimental data.

Table GEOCHEM-33. Equilibrium Constants for Reactions with Lead Implemented in the WIPP Chemical Conditions Process Model for CRA-2019

Reaction	log K	Source
Solid Dissolution Reactions		
α-PbO(litharge) + $2H^+ \leftrightarrow Pb^{2+} + H_2O$	-12.62	Powell et al. (2009)
$PbCO_3$(cerussite) + $H^+ \leftrightarrow Pb^{2+} + HCO_3^-$	-2.84	Powell et al. (2009)
$Pb2CO_3Cl_2(s) + 2H^+ \leftrightarrow 2Pb^{2+} + HCO_3^- + 2Cl^-$	0.41	Powell et al. (2009)
$PbSO_4(s) \leftrightarrow Pb^{2+} + SO_4^{2-}$	-7.80	Powell et al. (2009)
Aqueous Dissociation Reactions		
$PbCl^+ \leftrightarrow Pb^{2+} + Cl^-$	-1.50	Powell et al. (2009)
$PbCl_2(aq) \leftrightarrow Pb^{2+} + 2Cl^-$	-2.10	Powell et al. (2009)
$PbCl_3^- \leftrightarrow Pb^{2+} + 3Cl^-$	-2.00	Powell et al. (2009)
$PbOH^+ + H^+ \leftrightarrow Pb^{2+} + H_2O$	7.46	Powell et al. (2009)
$Pb(OH)_2(aq) + 2H^+ \leftrightarrow Pb^{2+} + 2H_2O$	16.94	Powell et al. (2009)
$Pb(CO_3)(OH)^- + 2H^+ \leftrightarrow Pb^{2+} + HCO_3^{1-} + H_2O(l)$	13.44	Powell et al. (2009)
$Pb(CO_3)Cl^- + H^+ \leftrightarrow Pb^{2+} + HCO_3^- + Cl^-$	3.87	Powell et al. (2009)
$PbCO_3(aq) + H^+ \leftrightarrow Pb^{2+} + HCO_3^-$	3.89	Powell et al. (2009)
$Pb(CO_3)_2^{2-} + 2H^+ \leftrightarrow Pb^{2+} + 2HCO_3^-$	10.55	Powell et al. (2009)
$PbSO_4(aq) \leftrightarrow Pb^{2+} + SO_4^{2-}$	-2.72	Powell et al. (2009)

GEOCHEM-3.3.7.2 Pitzer Interaction Coefficients for Ions Containing Lead

In preparation for CRA-2019, the DOE decided to use a lead model based on Powell et al. (2009) for the thermodynamic values required.

GEOCHEM-3.3.8 Iron

Iron is being added to the WIPP Chemical Conditions Process Model for CRA-2019. The parameters for iron will be included in DATA0.FM4. A summary of the parameters is provided in this section.

GEOCHEM-3.3.8.1 Equilibrium Constants for Reactions with Iron

The equilibrium constants for reactions with iron implemented in the WIPP Chemical Conditions Process Model are shown in Table GEOCHEM-34.

Table GEOCHEM-34. Equilibrium Constants for Reactions with Iron Implemented in the WIPP Chemical Conditions Process Model for CRA-2019

Reaction	log K	Source
Solid Dissolution Reactions		
$Fe(OH)_2(s) + 2H^+$ (ferrous hydroxide) $\leftrightarrow Fe^{2+} + 2H_2O$	12.89	Kim et al. (2017)
$Fe_2Cl(OH)_3(s) + 3H^+$ (hibbingite) $\leftrightarrow 2Fe^{2+} + Cl^- + 3H_2O$	17.08	Kim et al. (2017)
$FeCO_3(s) + H^+$ (siderite) $\leftrightarrow Fe^{2+} + HCO_3^-$	-0.12	Stumm and Morgan (1996)
$Fe_2CO_3(OH)_2(s) + 3H^+$ (chukanovite) $\leftrightarrow 2Fe^{2+} + HCO_3^- + 2H_2O$	12.32	Kim et al. (2017)
Aqueous Dissociation Reactions		
$FeOH^+ + H^+ \leftrightarrow Fe^{2+} + H_2O$	9.31	Shock et al. (1997)
$Fe(OH)_2(aq) + 2H^+ \leftrightarrow Fe^{2+} + 2H_2O$	20.82	Stumm and Morgan (1996)
$Fe(OH)_3^- + 3H^+ \leftrightarrow Fe^{2+} + 3H_2O$	31.0	Baes and Mesmer (1976)
$FeCO_3(aq) + H^+ \leftrightarrow Fe^{+2} + HCO_3^-$	4.83	Bruno et al. (1992)
$Fe(CO_3)_2^{2-} + 2H^+ \leftrightarrow Fe^{2+} + 2HCO_3^{1-}$	13.89	Kim et al. (2017)

GEOCHEM-3.3.8.2 Pitzer Interaction Coefficients for Ions Containing Iron

The Pitzer coefficients for ions containing iron are shown in Table GEOCHEM-35, Table GEOCHEM-36, and Table GEOCHEM-37.

Table GEOCHEM-35. Pitzer Interaction Coefficients (Cation-Anion Interactions) for Ions Containing Iron Implemented in the WIPP Chemical Conditions Process Model for CRA-2019

I	*j*	α_1/α_2^A	$\beta^{(0)}$	$\beta^{(1)}$	$\beta^{(2)}$	C^φ	Source
Fe^{2+}	Cl^-	2.0/12.0	0.37	1.14	0	-0.02	Moog et al. (2004)
Na^+	$Fe(CO_3)_2^{-2}$	2.0/12.0	-0.23	6.26	0	0	Kim et al. (2017)

Table GEOCHEM-36. Pitzer Interaction Coefficients (Cation-Cation Interactions) for Ions Containing Iron Implemented in the WIPP Chemical Conditions Process Model

i	*j*	$\theta_{cc'}$ or $\theta_{aa'}$	Source
Na^+	Fe^{2+}	0.110	Moog et al. (2004)
Mg^{2+}	Fe^{2+}	0.145	Moog et al. (2004)
K^+	Fe^{2+}	0.0274	Moog et al. (2004)
Ca^{2+}	Fe^{2+}	0.0811	Moog et al. (2004)

Table GEOCHEM-37. Pitzer Interaction Coefficients (Cation-Cation-Anion Interactions) for Ions Containing Iron Implemented in the WIPP Chemical Conditions Process Model

I	*j*	*k*	ψ_{ijk}	Source
Fe^{+2}	Na^+	Cl^-	-0.0161	Moog et al. (2004)
Fe^{+2}	K^+	Cl^-	-0.0252	Moog et al. (2004)
Fe^{+2}	Mg^{+2}	Cl^-	-0.0299	Moog et al. (2004)
Fe^{+2}	Ca^{+2}	Cl^-	-0.0160	Moog et al. (2004)

GEOCHEM-3.4 Quantification of Uncertainty in WIPP Chemical Conditions

As noted in GEOCHEM-1.1.4, uncertainties in the WIPP PA can be categorized as: uncertainty in the conceptual model, uncertainty in the process model, and uncertainty in parameterization of the process model.

Prior to CRA-2019, uncertainties in chemical conditions simulations were not investigated. Specifically, WIPP PA predictions of pH, ionic strength, carbon dioxide fugacity, and species concentrations in the two brines, GWB and ERDA-6, were not questioned. These chemical conditions affect the dissolved actinide source term (GEOCHEM-4.0).

During CRA-2014, experts were questioned about the range of values predicted for three of the chemical conditions: pcH, ionic strength (I), and total inorganic carbon (C_{TIC}) in the brines (U.S. EPA 2016). The purpose of setting ranges on the ionic strength, pH (pcH), and total inorganic carbon was to ensure the use of WIPP relevant studies in the actinide uncertainty analysis (Brush and Domski 2013b). The question asked of the researchers was: "What range of values is expected for the three chemical conditions (pH, I, and C_{TIC}) given the current conceptual model, process model, and parameters." The answers were:

1. 3.0 m≤ Ionic Strength
2. $8.0 \leq pcH \leq 11.2$
3. $0.0 \leq C_{TIC} \leq 1.4 \times 10^{-2}$ M

These ranges were used in the CRA-2014 actinide uncertainty analysis (Brush and Domski 2013b) as a screening criterion (G11) to screen potential laboratory studies for inclusion in the analysis. Note that the C_{TIC} selection criterion was updated for CRA-2019 to 2.0 x 10^{-2} M. The criteria are discussed further in GEOCHEM-4.4.3. The EPA asked the DOE to provide an upper

limit for ionic strength for the purpose of the actinide uncertainty analysis screening criteria. While investigating the upper limit on ionic strength, ranges of pH, f_{CO_2}, and total inorganic carbon (C_{TIC}) were calculated for WIPP reacted brine from previous PA cycles, and from native WIPP brines collected from boreholes in the repository. The investigation identified relevant uncertainties in brine properties, and did not impact the screening criteria for the actinide uncertainty analysis for CRA-2019.

GEOCHEM-3.4.1 Conceptual Model Uncertainty

One uncertainty that was identified in the WIPP Chemical Conditions Conceptual Model was the assumption of a well-mixed repository at equilibrium. This has been a fundamental assumption since the CCA, but the question is: "What if the repository is not well mixed, or not at equilibrium, and waste is actually in contact with native brines that have not equilibrated with the MgO barrier?" An investigation of this question follows. Both unequilibrated and equilibrated brines from the Salado and Castile formations are considered.

Table GEOCHEM-38 shows equilibrated brine values beginning with the CCA up to and including the CRA-2014 equilibrated brine values. In addition, several other native Salado Formation brines (Brush 1990; Deal et.al. 1991; and Roberts et. al. 1999) are included in Table GEOCHEM-39. For the native brines, their compositions were input into EQ3NR and the code was executed using DATA0.FM1 (Domski 2018a), and the resulting f_{CO_2}, pcH, I, and C_{TIC} values were calculated. All the native brines were saturated with respect to halite and anhydrite. The resulting uncertainty ranges identified by analyzing the numbers in Table GEOCHEM-38 are:

$5.7\ \text{m} \leq I \leq 9.1\ \text{m}$ (GEOCHEM-3.4.1.1)

$0\ \text{atm} \leq f_{CO_2} \leq 2.74 \times 10^{-3}\ \text{atm}$ (GEOCHEM-3.4.1.2)

$4.6 \leq \text{pcH} \leq 11.8$ (GEOCHEM-3.4.1.3)

$0\ \text{m} \leq C_{TIC} \leq 8.69 \times 10^{-4}\ \text{m}$ (GEOCHEM-3.4.1.4).

Note that these uncertainty ranges are not the same as those in the G11 criterion used in the actinide uncertainty analysis (Domski 2019a).

Table GEOCHEM-38. Near-Field Geochemical Conditions [Ionic Strength (m)], for Native[J] and Equilibrated WIPP Brines

Brine Type	*I*, mol•kg^{-1}	f_{CO_2} (atm)	pcH	TIC (m)
ERDA-6 (unequilibrated)[A]	5.95	1.91×10^{-4}	7.01	1.80×10^{-5}
Union[A]	6.22	N/A	6.87	N/A
CCA (ERDA-6, Magnesite, without Organics, All Vectors)[B]	6.66	1.29×10^{-7}	9.94	3.15×10^{-5}
PAVT (ERDA-6, Hydromagnesite, without Organics, All Vectors)[C]	6.67	3.14×10^{-6}	9.94	7.77×10^{-4}
CRA-2004 PA (ERDA-6, Hydromagnesite, with Organics, Microbial Vectors)[D]	6.73	3.16×10^{-6}	9.72	5.32×10^{-4}
WIPP-12[A]	6.73	6.83×10^{-6}	8.06	6.39×10^{-6}
CRA-2009 PABC (ERDA-6, Hydromagnesite, with Organics, All Vectors)[F]	6.77	3.14×10^{-6}	9.68	5.09×10^{-4}
CRA-2004 PABC (ERDA-6, Hydromagnesite, with Organics, All Vectors)[E]	6.80	3.16×10^{-6}	9.64	4.86×10^{-4}
CRA-2014 PA (ERDA-6$_{\text{min. vol.}}$, Hydromagnesite, with Organics, All Vectors)[G]	6.88	3.14×10^{-6}	9.69	4.55×10^{-4}
CCA (SPC, Magnesite, w/o Organics, All Vectors)[B]	7.40	1.29×10^{-7}	9.41	4.08×10^{-5}
PAVT (SPC,Hydromagnesite without Organics, All Vectors)[C]	7.41	3.14×10^{-6}	9.41	4.13×10^{-4}
G090[H]	7.42	1.76×10^{-3}	7.22	2.36×10^{-4}
H090[H]	7.44	1.32×10^{-3}	7.22	1.80×10^{-4}
CRA-2009 PABC (GWB, Hydromagnesite, with Organics, All Vectors)[F]	7.52	3.14×10^{-6}	9.39	4.02×10^{-4}
CRA-2004 PA (GWB, Hydromagnesite, with Organics, Microbial Vectors)[D]	7.54	3.16×10^{-6}	9.40	4.02×10^{-4}
OH23[H]	7.55	4.98×10^{-6}	8.77	8.52×10^{-5}
0H45[H]	7.58	1.41×10^{-3}	7.09	1.32×10^{-4}
L4P51[I]	7.59	1.10×10^{-3}	7.15	1.25×10^{-4}
G Seep[A]	7.61	1.14×10^{-4}	7.15	1.31×10^{-5}
CRA-2014 PA (GWB$_{\text{min. vol.}}$, Hydromagnesite, with Organics, All Vectors)[G]	7.64	3.14×10^{-6}	9.54	3.79×10^{-4}
DH36[A]	7.65	1.63×10^{-4}	7.10	1.58×10^{-5}
OH26[H]	7.66	7.82×10^{-4}	7.10	7.61×10^{-5}
CRA-2004 PABC (GWB, Hydromagnesite, with Organics, All Vectors)[E]	7.66	3.16×10^{-6}	9.39	4.02×10^{-4}
DHP402a[H]	7.72	9.46×10^{-4}	7.10	9.45×10^{-5}
DH28[H]	7.74	1.14×10^{-3}	7.21	1.41×10^{-4}
DH30[H]	7.76	4.49×10^{-4}	7.21	5.58×10^{-5}
DH32[H]	7.79	9.45×10^{-4}	7.11	9.49×10^{-5}
0H20[H]	7.81	6.78×10^{-4}	7.13	6.71×10^{-5}
SB-1[A]	8.18	3.12×10^{-3}	7.28	4.28×10^{-4}
SB-3[A]	8.20	N/A	7.27	N/A
SB-2[A]	8.21	N/A	7.37	N/A

[A]Calculated for this document based on the data given in Tables 2.1, 2.2, 2.3, and 2.4 from Brush (1990); [B]Novak (1996a); [C]From Novak (1997); [D]From Brush and Xiong (2003a, 2003b, 2003c, 2003d) and U.S. DOE 2004, Appendix SOTERM; [E]Brush and Xiong (2005a, 2005b) and Brush (2005); [F]Brush et al. (2009); [G]Brush and Domski (2013a); [H]Deal et al. (1991); [I]Roberts et al. (1999). [J] The pcH for the native brines was not corrected for loss of volatiles because these samples were collected in the repository as closed samples.

GEOCHEM-3.4.1.1 Uncertainty in Ionic Strength

Table GEOCHEM-38 shows the ionic strength values used for this analysis. Analysis of the values was performed to determine the degree of fit to a normal distribution. Domski (2018a) determined that the ionic strength data did not follow a normal distribution; therefore, it was not appropriate to apply +/- 2σ to the mean of the ionic strength to obtain a 95 percent confidence interval.

The resulting descriptive statistics for a normal distribution of the ionic strength values are listed in Table GEOCHEM-39.

Table GEOCHEM-39. Descriptive Statistics for Ionic Strength (m) in WIPP Brines

Property	I (m)	Property	I (m)
Number of samples (n)	31	Mean	7.37
Maximum	8.2	Median	7.55
Minimum	5.9	Standard deviation (σ)	0.56

To determine a range of values for ionic strength, the mean value from Table GEOCHEM-39 was used and assumed a 3σ variance on the mean. The resulting range is 5.7 m≤ I ≤ 9.1 m.

GEOCHEM-3.4.1.2 Uncertainty in Fugacity of Carbon Dioxide

Table GEOCHEM-38 shows the fugacity values used for this analysis. Analysis of the values was performed to determine the degree of fit to a normal distribution. Domski (2018a) determined that the data did not follow a normal distribution; therefore, it was not appropriate to apply +/- 2σ to the mean of the CO_2 fugacity to obtain a 95 percent confidence interval.

The resulting descriptive statistics for a normal distribution of the fugacity of carbon dioxide are listed in Table GEOCHEM-40.

Table GEOCHEM-40. Descriptive Statistics for Carbon Dioxide Fugacity in WIPP Brines

Property	f_{CO2} (atm)	Property	f_{CO2} (atm)
Number of samples (n)	28	Mean	5.06×10^{-4}
Maximum	3.12×10^{-3}	Median	6.05×10^{-5}
Minimum	1.29×10^{-7}	Standard deviation	7.46×10^{-4}

To determine a range of values for fCO2, the mean value from Table GEOCHEM-40 was used and assumed a 3σ variance on the mean. The resulting range is 0 atm ≤ fCO2 ≤ 2.74 × 10-3 atm.

GEOCHEM-3.4.1.3 Uncertainty in pcH

Table GEOCHEM-38 shows the pcH values used for this analysis. Analysis of the values was performed to determine the degree of fit to a normal distribution. Domski (2018a) determined that the data did not follow a normal distribution; therefore, it was not appropriate to apply +/- 2σ to the mean of the pcH data to obtain a 95 percent confidence interval.

The resulting descriptive statistics for a normal distribution of the pcH are listed in Table GEOCHEM-41.

Table GEOCHEM-41. Descriptive Statistics for pcH in WIPP Brines

Property	pcH	Property	pcH
Number of samples (n)	31	Mean	8.18
Maximum	9.94	Median	7.28
Minimum	6.87	Standard deviation	1.20

To determine a range of values for pcH, the mean value from Table GEOCHEM-41 was used and assumed a 3σ variance on the mean. The resulting range is $4.6 \leq pcH \leq 11.8$.

GEOCHEM-3.4.1.4 Uncertainty Total Inorganic Carbon

Table GEOCHEM-38 shows the C_{TIC} values used for this analysis. Analysis of the values was performed to determine the degree of fit to a normal distribution. Domski (2018a) determined that the data did not follow a normal distribution; therefore, it was not appropriate to apply +/- 2σ to the mean of the C_{TIC} data to obtain a 95 percent confidence interval.

The resulting descriptive statistics for a normal distribution of the C_{TIC} values are listed in Table GEOCHEM-42.

Table GEOCHEM-42. Descriptive Statistics for Total Inorganic Carbon(m) in WIPP Brines

Property	c_{TIC} (m)	Property	c_{TIC}(m)
Number of samples (n)	28	Mean	2.36×10^{-4}
Maximum	7.77×10^{-4}	Median	1.37×10^{-4}
Minimum	6.39×10^{-6}	Standard deviation	2.11×10^{-4}

To determine a range of values for C_{TIC}, the mean value from Table GEOCHEM-40 was used and assumed a 3σ variance on the mean. The resulting range is $0 \text{ m} \leq c_{TIC} \leq 8.68 \times 10^{-4}$ m.

GEOCHEM-3.4.2 Process Model Uncertainty

There are eight process models for chemical conditions: fundamental chemical conditions (ionic strength, brine pH, pcH, or pmH and E_h, and fugacity of CO_2), Salado and Castile minerals, Salado and Castile brines, MgO, organic ligands, borate, lead, and iron. There were no uncertainties identified in the process models for the fundamental chemical conditions, Salado and Castile minerals, Salado and Castile brines, MgO, and borate. These processes are assumed to take place with known solids and species that have been reviewed and accepted by the EPA four times (CCA, CRA-2004, CRA-2009, and CRA-2014).

Interestingly, there was a process model uncertainty resolved at the time of the PAVT. The uncertainty identified by the EPA was whether the magnesium hydroxycarbonate phase formed in the WIPP is magnesite [MgCO3] or hydromagnesite-5424 [Mg5(CO3)4(OH)2•4H2O(5424)]. Magnesite is the more thermodynamically stable form, but there may be kinetic roadblocks to its

formation. Hydromagnesite5424 is kinetically more easily formed, but it may not persist because it is not as thermodynamically stable as magnesite. By changing the process model to include hydromagnesite-5424, and suppressing the formation of magnesite, the uncertainty was moved to uncertainty in the parameterization of the model (see GEOCHEM-2.4.4). The process model change from magnesite in the CCA to hydromagnesite in the PAVT caused an order of magnitude increase in fCO2. The value for pcH in the CCA for ERDA-6 assuming the formation of magnesite instead of hydromagnesite was 9.94. The pcH of ERDA-6 for the PAVT (with hydromagnesite) was also 9.94. The pcH of Salado Primary Constituents (SPC) in the CCA (with magnesite) was 9.41. The pcH in the PAVT (with hydromagnesite) for SPC was also 9.41. The impact of changing from hydromagnesite to magnesite was smaller for pcH.

Since CRA-2004, the oxalate model included the solubility-limiting phase, whewellite [CaOxalate•H_2O(s)]. None of the other organic ligand models, EDTA, citrate, or acetate, included solubility-limiting phases. For CRA-2019, phases were added for EDTA and citrate, with an additional phase added for the oxalate model, and the acetate model still does not contain a solubility-limiting phase. Thus, prior to CRA-2019 the concentrations of EDTA and citrate were inventory limited without a solubility control. However, it was demonstrated by Domski and Sisk-Scott (2019) that the EDTA and citrate concentrations were below the solubility limits of their respective solubility-limiting phases, while the oxalate concentration exceeded the solubility of whewellite and the concentration was limited by the solubility product of the phase. Thus, the uncertainty of the EDTA, citrate, and acetate concentrations is linked to the PAIR inventory values, while the uncertainty in the concentration of oxalate in brine stems from the thermodynamics of whewellite solubility.

Similarly, the two new process models added to the chemical conditions calculations are for lead and iron. Uncertainty exists regarding the formation of lead and iron species with the organics. For CRA-2019, these formation reactions are omitted.

GEOCHEM-3.4.3 Parameter Uncertainty

There were no parameter uncertainties identified for any of the parameters associated with the eight process models, except regarding the log K value for dissolution of hydromagnesite-5424. Along with the process models, the associated parameters have been reviewed and accepted by the EPA four times (CCA, CRA-2004, CRA-2009, and CRA-2014).

The exception is the log K for hydromagnesite-5424. The presence of hydromagnesite (at early times in the repository) and brucite (at later times in the repository) buffers the pH. As a result, uncertainty in the log K for hydromagnesite creates an uncertainty in repository pH.

Figure GEOCHEM-5 presents an analysis of a number of possible values for the log K for hydromagnesite in terms of the effect on pmH. At infinite dilution, the pmH ranges from 8.77 to 8.96 (spread of 0.19). At 4m NaCl, the pmH ranges from 9.10 to 9.26 (spread of 0.16). This spread in the values for pmH is much smaller than the spread identified in GEOCHEM-3.4.1.3 ($4.58 \leq pcH \leq 11.78$), and therefore, inconsequential.

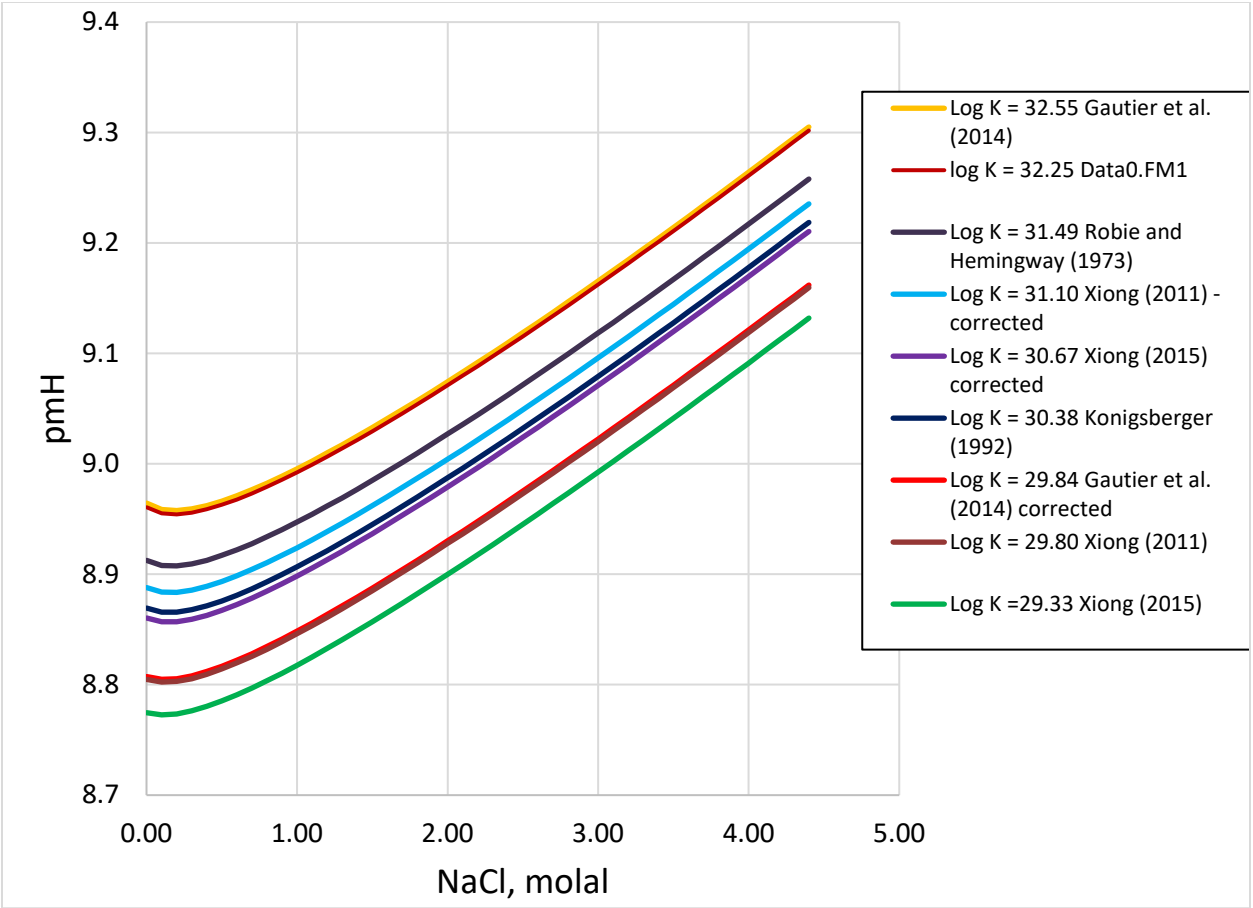

Figure GEOCHEM-5. Example of Uncertainty in pmH by Varying Log K of Hydromagnesite

GEOCHEM-3.5 WIPP Chemical Conditions Model Summary for CRA-2019

With the process models and parameters in place, simulations of two initial brine compositions (GWB and ERDA-6) for five brine volumes (1, 2, 3, 4, and 5 times the minimum brine volume) are performed at the beginning of a complete PA analysis with three independent replicates. Results from these calculations in terms of the near-field chemical conditions are estimates of the f_{CO2}, the pcH, the I, and the aqueous species concentrations at equilibrium (c_i).

All the results affect actinide solubility (discussed in GEOCHEM-4.0) and uncertainty in the results will contribute to uncertainty in actinide solubility. However, the WIPP PA does not attempt to directly calculate (as described in GEOCHEM-1.1.4.1) uncertainty in the results of near-field chemical conditions calculations; i.e., f_{CO2}, pcH, I, and c_i. Instead, the WIPP PA focuses on the uncertainty in the resulting actinide solubilities as discussed in GEOCHEM-4.4.

The key points for the WIPP Chemical Conditions Model for CRA 2019 are the following:

1. There have been no changes in the conceptual model.

2. The process model has been updated by adding reactions for solubility-limiting phases for EDTA, citrate, and oxalate. Reactions have been added for iron and lead interactions with chloride, hydroxide, and carbonate.
3. Parameterization of the process model has been revisited and changed:
    a. a new log K for dissolution of hydromagnesite-5424 of 31.49 will be used.
    b. all of the reactions with EDTA, citrate, and oxalate have been reparameterized.
4. Reactants for lead and iron were added to the model.

GEOCHEM-4.0 DISSOLVED ACTINIDE SOURCE TERM

This section in Appendix GEOCHEM is a companion to Appendix SOTERM, which discusses the dissolved actinide source term in detail. As a result, the material presented here is strictly summary-level information outlining the current implementation in PA of the Dissolved Actinide Source Term conceptual model, process model, parameters, and quantification of uncertainty. Its inclusion in Appendix GEOCHEM is only for continuity of the narrative thread established in the preceding sections. Discussion of data sources, both new and existing, is described in Appendix SOTERM. The DOE is not proposing any changes to the conceptual models and process models for calculating the Dissolved Actinide Source Term for CRA-2019. However, changes to the thermodynamic database, baseline solubilities, and uncertainty distribution applied to baseline solubilities are included in CRA-2019.

The purpose of calculating the Dissolved Actinide Source Term is for PA release mechanisms that involve discharge of brine from the repository to the Culebra, ground surface, or through the marker beds. The Chemical Conditions Conceptual Model, process model, and parameters set the backdrop for the Dissolved Actinide Source Term calculations. There are no new assumptions for the CRA-2019.

GEOCHEM-4.1 Dissolved Actinide Source Term Conceptual Model

In addition to the assumptions outlined in GEOCHEM-3.1, for the Chemical Conditions Conceptual Model, the following specific assumptions are made in the Dissolved Actinide Source Term Conceptual Model.

GEOCHEM-4.1.1 A Well-Mixed Repository at Equilibrium

The chemistry analogy assumed for determining near-field chemical conditions is that of a batch reactor that has come to equilibrium. Thus, brine and waste are well-mixed and the possible presence of chemical microenvironments and supersaturated conditions are not assumed to persist in the repository for long time periods. It follows that brine homogeneity will be maintained due to long-term mixing. Also, equilibrium is maintained between dissolved actinides and actinide solid phases. However, redox reactions among actinides are not assumed to be in equilibrium because redox conditions in the repository are set by the corrosion of ferrous metal. Dissolved actinide concentrations will be controlled by equilibrium with anhydrite, halite, MgO, PbO, actinide-bearing solid phases, and the appropriate brine.

GEOCHEM-4.1.2 Use of the Pitzer Model

Actinide solubilities and the chemistry of the near-field environment are calculated using the thermodynamic mass-action approach with the ion-specific aqueous model of Pitzer (Pitzer 1973) as implemented in EQ3/6 version 8.0a (Wolery and Jarek 2003). The Pitzer model is the most appropriate aqueous model for calculating activity coefficients in high concentration brines (6 – 11 molal) such as those observed at the WIPP. The Pitzer aqueous model has been used on the WIPP project since the CCA PA as it provides the most rigorous representation of activity coefficients at high ionic strength where the Debye-Huckel is invalid, and the SIT is beyond its upper limit of ~ 4 molal.

With knowledge of the applicability and limitations of the SIT model, with respect to WIPP conditions, a decision was made to use thermodynamic data, log K data for EDTA, citrate, and lead solids and aqueous species, derived using the SIT model in the EQ3/6 database, DATA0.FM4. The thermodynamic data for EDTA, citrate, and lead (see GEOCHEM-3.2.5 and GEOCHEM-3.3.5, respectively) that were included in the new EQ3/6 database used for CRA-2019, DATA0.FM4, included the data of Hummel et al. (2005) for EDTA and citrate, and for lead, the data of Powell et al. (2009).

These SIT derived values included in DATA0.FM4 were used in part to align the WIPP Chemical Conditions Process Model with data from the thermodynamic database project at the NEA as these data are considered the accepted standard by the international community. With regard to including SIT derived log K values in an otherwise Pitzer database, comparison of the log K values in Tables GEOCHEM-21 and GEOCHEM-22 reveals that the Hummel et al. (2005) data are within a small margin of the Giambalvo (2002) data, the data which is included in DATA0.FM1 and which had been used in previous PAs. It should be noted that the Hummel et al. (2005) log K data for EDTA species are systematically less than that of Giambalvo (2002). The effect of lower log K values for aqueous species is that it increases their stability relative to higher log K values. This may impact the solubility of Am(III) and Pu(III), which is strongly correlated to EDTA activity. No such systematic variation of log K values is observed in the citrate data, where some values are higher, and others lower compared to Giambalvo (2002).

See GEOCHEM-3.3.7 for a discussion of lead thermodynamic data.

GEOCHEM-4.1.3 The Use of End Member Brines

Because the Salado and Castile brines bracket the possible brine compositions likely to react in the WIPP, experiments and modeling performed with end-member brine compositions are adequate for describing actinide solubilities and calculating the chemistry within the repository.

GEOCHEM-4.1.4 Oxidation-state Analogy

All actinides in the same oxidation state will form the same aqueous species and isostructural compounds. The solubilities of americium, curium, and plutonium in the +III oxidation state are modeled using the solubility model for americium(III). This model is based on experimental data for americium(III), curium(III), and the lanthanide analogue neodymium(III). The solubilities of thorium, neptunium, plutonium, and uranium in the +IV oxidation state are modeled using the

solubility of thorium(IV). The solubility of neptunium(V) is based on experimental data for neptunium(V).

A thermodynamic model is not used for uranium(VI). Instead, an upper-limit solubility of 1×10^{-3} M is assumed (U.S. DOE 2014, Appendix SOTERM, Section SOTERM-5.5.1.3). Because this is an upper-limit solubility estimate, an uncertainty distribution is not sampled for this parameter.

GEOCHEM-4.1.5 Redox Status of the Actinides

The redox conditions of the repository at the time of human intrusion are assumed to be reducing. This assumption is based on a complex set of processes which may include, but is not limited to, iron corrosion, mirobial activity, and radiolysis. The expected oxidation states of the actinides are determined based on experimental data. Assumptions are stated here. For justification of the assumptions, consult Appendix SOTERM.

Currently, it is assumed that americium and curium will be present only in the +III oxidation state and thorium will be present only in the +IV oxidation state.

In the repository brines and equilibrium solid phases, three possible redox states are considered for plutonium, neptunium, and uranium: 1) plutonium may be present in the +III or +IV oxidation state, 2) neptunium may be present in the +IV or +V oxidation state, and 3) uranium may be present in the +IV or +VI oxidation state. There is a 50 percent probability that these actinides will be present in their more reduced states [neptunium(IV), plutonium(III), and uranium(IV)], and a 50 percent probability that they will be present in their more oxidized states [neptunium(V), plutonium(IV), and uranium(VI)]. For a more detailed discussion of the 50 percent reduced state / 50 percent oxidized state assumption, refer to Appendix SOTERM.

GEOCHEM-4.1.6 The Effect of Organic Ligands

The effects of organic ligands (acetate, citrate, EDTA, and oxalate) are included in actinide solubility calculations using experimentally derived complexation constants. The effects of competition by calcium and magnesium ions are included, using the complexation constants for calcium and magnesium. The effects of competition by transition metals such as iron have only been considered qualitatively in past CRAs, and this remains true for CRA-2019.

GEOCHEM-4.1.7 Immobile Substrates

Actinides will not be sorbed on immobile substrates in the repository. In particular, immobile substrates in the repository would be the host rock, waste emplacement materials, and waste packages. The impact of this assumption is that all dissolved radionuclides will remain in the aqueous phase (the mobile phase) and will not be immobilized due to sorption in the near-field environment.

GEOCHEM-4.1.8 Phase Stability

Metastable phases observed in laboratory experiments will become more stable with time. The project may use data collected on metastable phases, knowing that the data is most relevant at

early times in the repository lifetime before the metastable phase converts to the more stable phase. If the project chooses to use the data for a metastable phase and there is not a more stable phase included in a simulation, the results will tend to higher concentrations of contaminant because metastable phases are more soluble than their more stable counterparts. In general, it is believed that the solubilities observed in experiments with metastable phases provide an upper concentration limit.

GEOCHEM-4.1.9 Solubility-Controlling Phases

The inputs to the model include the solubility-controlling phases used to control the An(III), An(IV), and An(V) concentrations. For An(III), $Am(OH)_3(s)$ is used as the solubility-controlling phase, which represents a crystalline form of americium hydroxide (Morss and Williams 1994). The degree of crystallinity has a direct effect on the log K of this phase, with the solubility decreasing as the crystallinity of a mineral phase increases. The reasoning behind using the crystalline form of the $Am(OH)_3$ solid phase, and whether crystalline or amorphous phases would be dominant over the 10,000-year regulatory period, has been a topic of discussion. There is no way of knowing with any certainty which form would be dominant, and it is probable that some mixed phase intermediate might be the most appropriate choice. However, the approach is taken for which data exist, and use of a single log K, and one that is consistent with the americium model, is included in the database:

Giambalvo (2002a) states: “The Am-hydrolysis model is self-consistent, consistent with the Am-chloride model, and consistent with the choice of $Am(OH)_3(s)$ Ksp.” For this practical reason, the crystalline form of $Am(OH)_3(s)$ is used in the baseline solubility model.

The An(IV) model uses the amorphous form of thorium oxide [$ThO_2(am)$] as the solubility-controlling phase. This phase has been used as the An(IV) solubility-controlling phase since the CCA, and it is consistent with the thorium model included in the database. With regard to the apparent contradiction with the An(III) model which employs the crystalline form, a recent study of Simonnet et al. (2016) showed that crystalline forms of ThO_2 could not be formed at low temperatures, and that temperatures exceeding 850 °C are required for the crystalline form.

The solubility-controlling phase for An(V) since the CCA has been $KNpO_2CO_3$. Brush and Garner (2005) made the argument that dissolved An(V) releases do not affect the long-term performance of the WIPP, so this phase will continued to be used for the CRA-2019 PA.

GEOCHEM-4.2 Dissolved Actinide Source Term Process Models

The WIPP Dissolved Actinide Source Term is composed of three elements: chemical reactions, mathematical expressions that represent the chemical reactions, and software that solves the mathematical expressions to obtain relevant chemical conditions. The following sections provide information about the specific chemical reactions involved in the WIPP Dissolved Actinide Source Term. GEOCHEM-3.2 provided a summary of the software used to solve the mathematical expressions. The DOE is not proposing any process model changes for the Dissolved Actinide Source Term for CRA-2019.

GEOCHEM-4.2.1 +III Actinides

A comprehensive review of data related to An(III) solubility is provided in Appendix SOTERM-2019. The reactions for An(III) were included in the CCA and have been included in all recertifications since then. They will be included in CRA-2019.

GEOCHEM-4.2.1.1 Dissolution and Dissociation Reactions for Americium

Table GEOCHEM-43 shows the reactions with Am in the +III oxidation state implemented in the WIPP Dissolved Actinide Source Term process model. The solubilities of americium, curium, and plutonium in the +III oxidation state are modeled using the solubility model for americium(III).

Table GEOCHEM-43. Dissolution and Dissociation Reactions for Americium Solids and Species Implemented in the WIPP Dissolved Actinide Source Term Process Model for CRA-2019[A]

First Use	Solid Dissolution Reactions
CCA	$AmOHCO_3(s) + 2H^+ \leftrightarrow Am^{3+} + H_2O + HCO_3^-$
CCA	$Am(OH)_3(s) + 3H^+ \leftrightarrow Am^{3+} + 3H_2O$
CCA	$NaAm(CO_3)_2 \bullet 6H_2O(s) + 2H^+ \leftrightarrow Na^+ + Am^{3+} + 2HCO_3^- + 6H_2O$
First Use	**Aqueous Dissociation Reactions**
CCA	$AmCO_3^+ + H^+ \leftrightarrow Am^{3+} + HCO_3^-$
CCA	$Am(CO_3)_2^- + 2H^+ \leftrightarrow Am^{3+} + 2HCO_3^-$
CCA	$Am(CO_3)_3^{3-} + 3H^+ \leftrightarrow Am^{3+} + 3HCO_3^-$
CCA	$Am(CO_3)_4^{5-} + 4H^+ \leftrightarrow Am^{3+} + 4HCO_3^-$
CCA	$Am(OH)^{2+} + H^+ \leftrightarrow Am^{3+} + H_2O$
CCA	$Am(OH)_2^+ + 2H^+ \leftrightarrow Am^{3+} + 2H_2O$
CCA	$Am(OH)_3(aq) + 3H^+ \leftrightarrow Am^{3+} + 3H_2O$
CCA	$AmCl^{2+} \leftrightarrow Am^{3+} + Cl^-$
CCA	$AmCl_2^+ \leftrightarrow Am^{3+} + 2Cl^-$
CCA	$AmSO_4^+ \leftrightarrow Am^{3+} + SO_4^{2-}$
CCA	$Am(SO_4)_2^- \leftrightarrow Am^{3+} + 2SO_4^{2-}$
CCA	$AmAcetate^{2+} \leftrightarrow Am^{3+} + Acetate^-$
CCA	$AmCitrate(aq) \leftrightarrow Am^{3+} + Citrate^{3-}$
CCA	$AmEDTA^- \leftrightarrow Am^{3+} + EDTA^{4-}$
CCA	$AmLactate^{2+} \leftrightarrow Am^{3+} + Lactate^-$
CCA	$AmOxalate^+ \leftrightarrow Am^{3+} + Oxalate^{2-}$

[A]The left-hand column indicates when the reaction was first introduced in the WIPP Dissolved Actinide Source Term Model.

A reaction that has been discussed in recent years is the formation of an Am tetraborate species. This reaction is currently not in the An(III) process model and will not be included in CRA-2019.

GEOCHEM-4.2.2 +IV Actinides

The reader is referred to Appendix SOTERM for a comprehensive review of data related to An(IV) solubility. The reactions for An(IV) were included in the CCA and have been included in all recertifications since then. They will be included in CRA-2019.

GEOCHEM-4.2.2.1 Dissolution and Dissociation Reactions for Thorium

Table GEOCHEM-44 shows the reactions with Th in the +IV oxidation state implemented in the Dissolved Actinide Source Term process model. The solubilities of thorium, neptunium, plutonium, and uranium in the +IV oxidation state are modeled using the solubility of Th(IV).

Table GEOCHEM-44. Dissolution and Dissociation Reactions for Thorium Solids and Species Implemented in the WIPP Dissolved Actinide Source Term Process Model for CRA-2019[A]

First Use	Solid Dissolution Reactions
CCA	$ThO_2(am) + 4H^+ \leftrightarrow Th^{4+} + 2H_2O$
CCA	$Th(SO_4)_2{\bullet}9H_2O(s) \leftrightarrow Th^{4+} + 2SO_4^{2-} + 9H_2O$
CCA	$Th(SO_4)_2{\bullet}8H_2O(s) \leftrightarrow Th^{4+} + 2SO_4^{2-} + 8H_2O$
CCA	$Th(SO_4)_2{\bullet}Na_2SO_4{\bullet}6H_2O(s) \leftrightarrow Th^{4+} + 3SO_4^{2-} + 2Na^+ + 6H_2O$
CCA	$Th(SO_4)_2{\bullet}K_2SO_4{\bullet}4H_2O(s) \leftrightarrow Th^{4+} + 3SO_4^{2-} + 2K^+ + 4H_2O$
CCA	$Th(SO_4)_2{\bullet}2K_2SO_4{\bullet}2H_2O(s) \leftrightarrow Th^{4+} + 4SO_4^{2-} + 4K^+ + 2H_2O$
CCA	$2[Th(SO_4)_2{\bullet}7/2K_2SO_4(s)] \leftrightarrow 2Th^{4+} + 11SO_4^{2-} + 14K^+$
First Use	**Aqueous Dissociation Reactions**
CCA	$Th(CO_3)_5^{6-} + 5H^+ \leftrightarrow Th^{4+} + 5HCO_3^-$
CCA	$Th(OH)_3(CO_3)^- + 4H^+ \leftrightarrow Th^{4+} + 3H_2O + HCO_3^-$
CCA	$Th(OH)_4(aq) + 4H^+ \leftrightarrow Th^{4+} + 4H_2O$
CCA	$Th(SO_4)_2(aq) \leftrightarrow Th^{4+} + 2SO_4^{2-}$
CCA	$Th(SO_4)_3^{2-} \leftrightarrow Th^{4+} + 3SO_4^{2-}$
CCA	$ThAcetate^{3+} \leftrightarrow Th^{4+} + Acetate^-$
CCA	$Th(Acetate)_2^{2+} \leftrightarrow Th^{4+} + 2Acetate^-$
CCA	$ThCitrate^+ \leftrightarrow Th^{4+} + Citrate^{3-}$
CCA	$ThEDTA(aq) \leftrightarrow Th^{4+} + EDTA^{4-}$
CCA	$ThLactate^{3+} \leftrightarrow Th^{4+} + Lactate^-$
CCA	$Th(Lactate)_2^{2+} \leftrightarrow Th^{4+} + 2Lactate^-$
CCA	$ThOxalate^{2+} \leftrightarrow Th^{4+} + Oxalate^{2-}$

[A]The left-hand column indicates when the reaction was first introduced in the WIPP Dissolved Actinide Source Term Model.

GEOCHEM-4.2.3 +V Actinides

The reader is referred to Appendix SOTERM for a comprehensive review of data related to An(V) solubility. The reactions for An(V) were included in the CCA and have been included in all recertifications since then. They will be included in CRA-2019.

GEOCHEM-4.2.3.1 Dissolution and Dissociation Reactions for Neptunium

Table GEOCHEM-45 shows the reactions with Np in the +V oxidation state implemented in the Dissolved Actinide Source Term process model.

Table GEOCHEM-45. Dissolution and Dissociation Reactions for Neptunium Solids and Species Implemented in the WIPP Dissolved Actinide Source Term Process Model for CRA-2019[A]

First Use	Solid Dissolution Reactions
CCA	$NpO_2OH(aged) + H^+ \leftrightarrow NpO_2^+ + H_2O$
CCA	$NpO_2OH(am) + H^+ \leftrightarrow NpO_2^+ + H_2O$
CCA	$2[NaNpO_2CO_3 \bullet 7/2H_2O](s) + 2H^+ \leftrightarrow 2NpO_2^+ + 2HCO_3^- + 2Na^+ + 7H_2O$
CCA	$Na_3NpO_2(CO_3)_2(s) + 2H^+ \leftrightarrow NpO_2^+ + 2HCO_3^- + 3Na^+$
CCA	$KNpO_2CO_3(s) + H^+ \leftrightarrow NpO_2^+ + HCO_3^- + K^+$
CCA	$K_3NpO_2(CO_3)_2(s) + 2H^+ \leftrightarrow NpO_2^+ + 2HCO_3^- + 3K^+$
CCA	$NpO_2CO_3^- + H^+ \leftrightarrow NpO_2^+ + HCO_3^-$
CCA	$NpO_2(CO_3)_2^{3-} + 2H^+ \leftrightarrow NpO_2^+ + 2HCO_3^-$
CCA	$NpO_2(CO_3)_3^{5-} + 3H^+ \leftrightarrow NpO_2^+ + 3HCO_3^-$
CCA	$NpO_2(OH)(aq) + H^+ \leftrightarrow NpO_2^+ + H_2O$
CCA	$NpO_2(OH)_2^- + 2H^+ \leftrightarrow NpO_2^+ + 2H_2O$
CCA	$NpO_2Acetate(aq) \leftrightarrow NpO_2^+ + Acetate^-$
CCA	$NpO_2Citrate^{2-} \leftrightarrow NpO_2^+ + Citrate^{3-}$
CCA	$NpO_2H_2EDTA^- \leftrightarrow NpO_2^+ + EDTA^{4-} + 2H^+$
CCA	$NpO_2HEDTA^{2-} \leftrightarrow NpO_2^+ + EDTA^{4-} + H^+$
CCA	$NpO_2EDTA^{3-} \leftrightarrow NpO_2^+ + EDTA^{4-}$
CCA	$NpO_2Lactate(aq) \leftrightarrow NpO_2^+ + Lactate^-$
CCA	$NpO_2Oxalate^- \leftrightarrow NpO_2^+ + Oxalate^{2-}$

[A]The left-hand column indicates when the reaction was first introduced in the WIPP Dissolved Actinide Source Term Model.

GEOCHEM-4.3 Parameterization of Dissolved Actinide Source Term Process Models

In this section, parameter values used in PA are given in Tables GEOCHEM-46 through GEOCHEM-49.

GEOCHEM-4.3.1 +III Actinides

There are no parameter changes for the An(III) reactions that were implemented in CRA-2014. Parameterization of the model is described in Giambalvo (2002a). The parameters are summarized below.

GEOCHEM-4.3.1.1 Equilibrium Constants for Dissolution Reactions for Americium Solids and Species

About $Am(OH)_3(s)$, Giambalvo (2002a) states:

> The log K_{sp} for $Am(OH)_3(s)$ (-27.5) is equal to that recommended by Morss and Williams (1994) on the basis of a compilation of values from the literature. This is the value of Konnecke et al. (1997) successfully used to simulate Runde and Kim's (1994) $Am(OH)_3(s)$ solubility data.

About $AmOHCO_3(s)$, Giambalvo (2002a) states:

> The log K_{sp} for $AmHCO_3(c)$ (-22.7) is equal to that calculated by Fanghänel et al. (1999) on the basis of Felmy et al.'s (1990) $AmOHCO_3(s)$ solubility data.

About $Am(CO_3)_4^{5-}$, Giambalvo (2002a) states:

> An additional Am-carbonate species ($Am(CO_3)_4^{5-}$) is included on the basis of spectroscopic evidence for the existence of $Cm(CO_3)_4^{5-}$ (Fanghänel et al., 1999). Carbonate complexation constants and related Pitzer parameters are derived from Cm-carbonate speciation data collected over a range of NaCl concentrations from 0-6 mol/kg (Fanghänel et al., 1999). Fanghänel et al., (1999) neglected the formation of Am-chloride complexes in their model, a valid decision at chloride concentrations <6 mol/kg (Fanghänel et al., 1995). They verified their model by successfully simulating the solubility of $AmOHCO_3(c)$ (including the Felmy et al. (1990) data set) and $NaAm(CO_3)_2(s)$.

About $Am(OH)^{2+}$, Giambalvo (2002a) states:

> First and second hydrolysis constants remain equal to those calculated by Fanghänel et al. (1994) from Cm speciation data. Related Pitzer parameters are set equal to those calculated by Konnecke et al. (1997) from the Fanghänel et al. (1994) data set. The Konnecke et al. (1997) recalculation of these Pitzer parameters accounts for the presence of Cm-chloride complexes and includes a term describing the interaction of Cm^{3+} with Na^+ (Θ). Konnecke et al.'s (1997) successful use of their model to simulate Cm speciation in NaCl solution validates the absence of Pitzer parameters describing interaction between Am-chloride complexes and Na^+.

About $Am(OH)_3(aq)$, Giambalvo (2002a) states:

> The third hydrolysis constant is set equal to that recommended by the Nuclear Energy Agency (Silva et al., 1995). Konnecke et al. (1997) used this value and the Ksp for $Am(OH)_3(s)$ recommended by Morss and Williams (1994) to successfully simulate the $Am(OH)_3(s)$ solubility data of Runde and Kim (1994). Konnecke et al.'s (1997) model included Pitzer parameters describing the interaction of $Am(OH)_3(aq)$ with Na^+ and Cl^-.

About $AmCl_2^+$, Giambalvo (2002a) states:

> Am-chloride complexes ($AmCl_2^+$ and $AmCl^{2+}$) are included on the basis of spectroscopic evidence for the existence of $CmCl_2^+$ and $CmCl^{2+}$ in 2-6 mol/kg $CaCl_2$ (4-12 mol/kg Cl^-) solution (Fanghänel et al., 1995). Complexation constants for these chloride complexes, Pitzer parameters describing interaction of Am^{3+}, $AmCl_2^+$, Am Cl^{2+} with Cl^- and Ca^{2+} are set equal to those calculated by Konnecke et al. (1997) from the Cm speciation data of Fanghänel et al. (1995).

About $AmSO_4^+$, Giambalvo (2002a) states:

> Am-sulfate complexes are included on the basis of spectroscopic evidence for the existence of $Cm(SO_4)_2^-$ (Paviet et al., 1996). Related Pitzer parameters are derived from Cm-sulfate speciation data collected over a range of NaCl concentrations from 0-6 mol/kg (Fanghänel and Kim, 1998).

The equilibrium constants for reactions with Am in the +III oxidation state implemented in the Dissolved Actinide Source Term process model are shown in Table GEOCHEM-46.

Table GEOCHEM-46. Equilibrium Constants for Dissolution and Dissociation Reactions for Americium Solids and Species Implemented in the WIPP Dissolved Actinide Source Term Process Model for CRA-2019[A]

Reaction	log K	Source
Solid Dissolution Reactions		
$Am(OH)_3(s) + 3H^+ \leftrightarrow Am^{3+} + 3H_2O$	14.5	Giambalvo (2002a)
$AmOHCO_3(s) + 2H^+ \leftrightarrow Am^{3+} + H_2O + HCO_3^-$	1.64	Giambalvo (2002a)
$NaAm(CO_3)_2{\bullet}6H_2O(s) + 2H^+ \leftrightarrow Na^+ + Am^{3+} + 2HCO_3^- + 6H_2O$	-0.71	Rao et al. (1996b)
Aqueous Dissociation Reactions		
$AmCO_3^+ + H^+ \leftrightarrow Am^{3+} + HCO_3^-$	2.24	Fanghänel et al. (1999)
$Am(CO_3)_2^- + 2H^+ \leftrightarrow Am^{3+} + 2HCO_3^-$	7.68	Fanghänel et al. (1999)
$Am(CO_3)_3^{3-} + 3H^+ \leftrightarrow Am^{3+} + 3HCO_3^-$	15.8	Fanghänel et al. (1999)
$Am(CO_3)_4^{5-} + 4H^+ \leftrightarrow Am^{3+} + 4HCO_3^-$	28.4	Giambalvo (2002a)
$Am(OH)^{2+} + H^+ \leftrightarrow Am^{3+} + H_2O$	7.56	Giambalvo (2002a)
$Am(OH)_2^+ + 2H^+ \leftrightarrow Am^{3+} + 2H_2O$	15.7	Giambalvo (2002a)
$Am(OH)_3(aq) + 3H^+ \leftrightarrow Am^{3+} + 3H_2O$	25.7	Giambalvo (2002a)

Table GEOCHEM-46. (Continued) Equilibrium Constants for Dissolution and Dissociation Reactions for Americium Solids and Species Implemented in the WIPP Dissolved Actinide Source Term Process Model for CRA-2019[A]

Reaction	log K	Source
Aqueous Dissociation Reactions		
$AmCl^{2+} \leftrightarrow Am^{3+} + Cl^{-}$	-0.24	Giambalvo (2002a)
$AmCl_2^{+} \leftrightarrow Am^{3+} + 2Cl^{-}$	0.74	Giambalvo (2002a)
$AmSO_4^{+} \leftrightarrow Am^{3+} + SO_4^{2-}$	-3.25	Giambalvo (2002a)
$Am(SO_4)_2^{-} \leftrightarrow Am^{3+} + 2SO_4^{2-}$	-3.70	Giambalvo (2002a)
$AmAcetate^{2+} \leftrightarrow Am^{3+} + Acetate^{-}$	-2.74	Giambalvo (2002)
$AmCitrate(aq) \leftrightarrow Am^{3+} + Citrate^{3-}$	-8.80	Choppin et al. (2001)
$AmEDTA^{-} \leftrightarrow Am^{3+} + EDTA^{4-}$	-18.97	Choppin et al. (2001)
$AmLactate^{2+} \leftrightarrow Am^{3+} + Lactate^{-}$	-3.71	Choppin et al. (2001)
$AmOxalate^{+} \leftrightarrow Am^{3+} + Oxalate^{2-}$	-6.16	Choppin et al. (2001)

[A]All of the references cited in this table derived or reported values for standard state chemical potential that was an input to FMT instead of log K (Novak 1996a; see also Babb and Novak 1995; Babb and Novak 1997 and addenda; Wang 1998). These were later converted to log K values as documented in Ismail et al. (2009).

GEOCHEM-4.3.1.2 Pitzer Interaction Coefficients for Ions Containing Americium

Fanghänel et al. (1999) values for $Am(CO_3)_2^-$ and Na^+ are used for $Am(CO_3)_2^-$ and K^+. Fanghänel and Kim (1998) values for $Am(CO_3)_4^{5-}$ and Na^+ are used for $Am(CO_3)_4^{5-}$ and K^+. Fanghänel and Kim (1998) values for $Am(SO_4)_2^-$ and Na^+ are used for $Am(SO_4)_2^-$ and K^+.

The Pitzer coefficients for ions containing actinides in the +III oxidation state are shown in Table GEOCHEM-47, Table GEOCHEM-48**,** and Table GEOCHEM-49.

Table GEOCHEM-47. Pitzer Interaction Coefficients (Cation-Anion Interactions) for Ions Containing Americium Implemented in the WIPP Dissolved Actinide Source Term Process Model for CRA-2019

I	*J*	$\beta^{(0)}$	$\beta^{(1)}$	$\beta^{(2)}$	C^{φ}	Source
Cation-Anion Interactions						
Am^{3+}	Cl^-	0.586	5.6	0	-0.0166	Fanghänel and Kim (1998)
Am^{3+}	SO_4^{2-}	1.79	15.0	0	0.6	Fanghänel and Kim (1998)
Am^{3+}	ClO_4^-	0.8	5.35	0	-0.0048	Felmy et al. (1990)
$Am(CO_3)_2^-$	K^+	-0.24	0.224	0	0.0284	Fanghänel et al. (1999)
$Am(CO_3)_2^-$	Na^+	-0.24	0.224	0	0.0284	Fanghänel et al. (1999)
$Am(CO_3)_3^{3-}$	K^+	0.125	4.73	0	0.0007	Fanghänel et al. (1999)
$Am(CO_3)_3^{3-}$	Na^+	0.125	4.73	0	0.0007	Fanghänel et al. (1999)
$Am(CO_3)_4^{5-}$	K^+	2.02	19.2	0	-0.305	Fanghänel and Kim (1998)
$Am(CO_3)_4^{5-}$	Na^+	2.02	19.2	0	-0.305	Fanghänel and Kim (1998)
$AmCO_3^+$	Cl^-	-0.072	0.403	0	0.0388	Fanghänel and Kim (1998)
$Am(OH)_2^+$	Cl-	-0.616	-0.45	0	0.05	Fanghänel and Kim (1998)
$Am(SO_4)_2^-$	K^+	-0.354	0.4	0	0.051	Fanghänel and Kim (1998)
$Am(SO_4)_2^-$	Na^+	-0.354	0.4	0	0.051	Fanghänel and Kim (1998)
$AmSO_4^+$	Cl^-	-0.091	-0.39	0	0.048	Fanghänel and Kim (1998)
$AmCl^{2+}$	Cl^-	0.593	3.15	0	-0.006	Fanghänel and Kim (1998)
$AmCl_2^+$	Cl^-	0.516	1.75	0	0.01	Fanghänel and Kim (1998)
$AmOH^{2+}$	Cl^-	-0.055	1.6	0	0.05	Fanghänel and Kim (1998)
$AmEDTA^-$	K^+	-0.224	0.29	0	0.002	Choppin et al. (2001)
$AmLactate^{2+}$	Cl^-	0.840	1.74	0	-0.332	Moore et al. 1999
$AmAcetate^{2+}$	Cl^-	0.309	1.74	0	-0.132	Giambalvo (2002)
$AmOxalate^+$	Cl^-	-0.937	0.29	0	0.248	Choppin et al. (2001)
$AmEDTA^-$	Na^+	-0.224	0.29	0	0.002	Choppin et al. (2001)

Table GEOCHEM-48. Pitzer Interaction Coefficients (Cation-Cation; Anion-Anion Interactions) for Ions Containing Americium Implemented in the WIPP Dissolved Actinide Source Term Process Model for CRA-2019

i	*j*	$\theta_{cc'}$ or $\theta_{aa'}$	Source
Cation-Cation Interactions			
Am^{3+}	Na^+	0.1	Fanghänel and Kim (1998)
Am^{3+}	K^+	0.1	Fanghänel and Kim (1998)
Am^{3+}	Ca^{2+}	0.2	Fanghänel and Kim (1998)
Am^{3+}	Mg^{2+}	0.2	Fanghänel and Kim (1998)
$AmCl^{2+}$	Ca^{2+}	-0.014	Fanghänel and Kim (1998)
$AmCl_2^+$	Ca^{2+}	-0.196	Fanghänel and Kim (1998)
$AmCl^{2+}$	Mg^{2+}	-0.014	Fanghänel and Kim (1998)
$AmCl_2^+$	Mg^{2+}	-0.196	Fanghänel and Kim (1998)

Table GEOCHEM-49. Pitzer Interaction Coefficients (Neutral-Cation; Neutral-Anion Interactions) for Ions Containing Americium Implemented in the WIPP Dissolved Actinide Source Term Process Model for CRA-2019

i	*j*	$\lambda_{nc'}$ or $\lambda_{na'}$	Source
Neutral-Cation Interactions			
$Am(OH)_3(aq)$	H^+	0	Felmy and Weare (1986)
$Am(OH)_3(aq)$	Na^+	-0.2	Felmy and Weare (1986)
$Am(OH)_3(aq)$	K^+	-0.2	Fanghänel and Kim (1998)
Neutral-Anion Interactions			
$Am(OH)_3(aq)$	Cl^-	-0.2	Felmy and Weare (1986)
AmCitrate(aq)	Cl^-	-0.406	Choppin et al. (2001)

GEOCHEM-4.3.2 +IV Actinides

There are no parameter changes for the An(IV) reactions that were implemented in CRA-2014. Parameterization of the model is described in Giambalvo (2002) and Giambalvo (2002b). The parameters are summarized below.

GEOCHEM-4.3.2.1 Equilibrium Constants for Dissolution Reactions for Thorium Solids and Species

The solubility product constant (Ksp) for $ThO_2(am)$ was calculated by Felmy et al. (1991) from Th solubility data collected in dilute solution at pH <7 (Ryan and Rai 1987). Felmy et al. (1991) neglected all hydrolysis species in their calculation of Ksp. They successfully simulated Th solubility in NaCl solutions up to 3 mol/L using their calculated Ksp and Pitzer parameters describing the interaction of Th^{4+} and Cl^- from Pitzer and Mayorga (1973).

Values of μ^0/RT for Th-sulfate complexes, related Pitzer parameters, and Ksp values for Th sulfate solid phases were derived from various data sets by Felmy and Rai (1992). Like Felmy et al. (1991), Felmy and Rai (1992) used the Pitzer and Mayorga (1973) Th^{4+} - Cl^- interaction parameters in their calculations.

Th-carbonate complexes include $Th(CO_3)_5^{6-}$ and $Th(OH)_3CO_3^-$. Novak (1996b) determined μ^0/RT values for these species by comparing $ThO_2(am)$ solubility in the presence of carbonate (Felmy et al. 1997) to $ThO_2(am)$ solubility in the absence of carbonate (Felmy et al. 1991). Felmy et al. (1997) determined the solubility of $ThO_2(am)$ in the presence of carbonate from solubility experiments run in dilute to moderately concentrated (<2 mol/L) $NaHCO_3$, Na_2CO_3, and $NaClO_4/CO_2(g)$ solutions. Pitzer parameters describing interaction of $Th(CO_3)_5^{6-}$ with Na^+ ($\beta^{(0)}$, $\beta^{(1)}$, and C^{φ}) and with ClO_{4-} (Θ) are from Felmy et al. (1997). Pitzer parameters describing the ternary interaction of $Th(CO_3)_5^{6-}$, Cl^-, and Na+ (Θ, Ψ) result from Felmy's preliminary analysis of $ThO_2(am)$ solubility in mixed $NaCl/Na_2CO_3$ solutions (Novak 1997).

The equilibrium constants for reactions with Th in the +IV oxidation state implemented in the Dissolved Actinide Source Term process model are shown in Table GEOCHEM-50.

Table GEOCHEM-50. Equilibrium Constants for Dissolution and Dissociation Reactions for Thorium Solids and Species Implemented in the WIPP Dissolved Actinide Source Term Process Model for CRA-2019[A]

Reaction	log K	Source
Solid Dissolution Reactions		
$ThO_2(am) + 4H^+ \leftrightarrow Th^{4+} + 2H_2O$	10.5	Felmy et al. (1991)
$Th(SO_4)_2{\bullet}9H_2O(s) \leftrightarrow Th^{4+} + 2SO_4^{2-} + 9H_2O$	-13.0	Felmy and Rai (1992)
$Th^{4+} + 2SO_4^{2-} + 8H_2O \leftrightarrow Th(SO_4)_2{\bullet}8H_2O(s)$	-12.9	Felmy and Rai (1992)
$Th(SO_4)_2{\bullet}Na_2SO_4{\bullet}6H_2O(s) \leftrightarrow Th^{4+} + 3SO_4^{2-} + 2Na^+ + 6H_2O$	-17.6	Felmy and Rai (1992)
$Th(SO_4)_2{\bullet}K_2SO_4{\bullet}4H_2O(s) \leftrightarrow Th^{4+} + 3SO_4^{2-} + 2K^+ + 4H_2O$	-18.1	Felmy and Rai (1992)
$Th(SO_4)_2{\bullet}2K_2SO_4{\bullet}2H_2O(s) \leftrightarrow Th^{4+} + 4SO_4^{2-} + 4K^+ + 2H_2O$	-21.2	Felmy and Rai (1992)
$2[Th(SO_4)_2{\bullet}7/2K_2SO_4(s)] \leftrightarrow 2Th^{4+} + 11SO_4^{2-} + 14K^+$	-49.3	Felmy and Rai (1992)
Aqueous Dissociation Reactions		
$Th(CO_3)_5^{6-} + 5H^+ \leftrightarrow Th^{4+} + 5HCO_3^-$	24.6	Novak (1996b)
$Th(OH)_3(CO_3)^- + 4H^+ \leftrightarrow Th^{4+} + 3H_2O + HCO_3^-$	14.0	Novak (1996b)
$Th(OH)_4(aq) + 4H^+ \leftrightarrow Th^{4+} + 4H_2O$	17.5	Novak (1996b)
$Th(SO_4)_2(aq) \leftrightarrow Th^{4+} + 2SO_4^{2-}$	-11.6	Felmy and Rai (1992)
$Th(SO_4)_3^{2-} \leftrightarrow Th^{4+} + 3SO_4^{2-}$	-12.4	Felmy and Rai (1992)
$ThAcetate^{3+} \leftrightarrow Th^{4+} + Acetate^-$	-7.36	Giambalvo (2002)
$Th(Acetate)_2^{2+} \leftrightarrow Th^{4+} + 2Acetate^-$	-11.2	Moore et al. (1999)
$ThCitrate^+ \leftrightarrow Th^{4+} + Citrate^{3-}$	-15.2	Choppin et al. (2001)
$ThEDTA(aq) \leftrightarrow Th^{4+} + EDTA^{4-}$	-23.6	Giambalvo (2002)
$ThLactate^{3+} \leftrightarrow Th^{4+} + Lactate^-$	-6.83	Choppin et al. (2001)
$Th(Lactate)_2^{2+} \leftrightarrow Th^{4+} + 2Lactate^-$	-11.2	Choppin et al. (2001)
$ThOxalate^{2+} \leftrightarrow Th^{4+} + Oxalate^{2-}$	-11.4	Choppin et al. (2001)

[A]All of the references cited in this table derived or reported values for standard state chemical potential that was a direct input to FMT (Novak 1996a; see also Babb and Novak 1995; Babb and Novak 1997 and addenda; Wang 1998). These were later converted to log K values as documented in Ismail et al. (2009).

GEOCHEM-4.3.2.2 Pitzer Interaction Coefficients for Ions Containing Thorium

The Pitzer coefficients for ions containing actinides in the +IV oxidation state are shown in Table GEOCHEM-51, Table GEOCHEM-52, and Table GEOCHEM-53.

Table GEOCHEM-51. Pitzer Interaction Coefficients (Cation-Anion Interactions) for Ions Containing Thorium Implemented in the WIPP Dissolved Actinide Source Term Process Model for CRA-2019

I	*j*	α_1/α_2	$\beta^{(0)}$	$\beta^{(1)}$	$\beta^{(2)}$	C^{φ}	Source
Cation-Anion Interactions							
Th^{4+}	Cl^-	2.0/12.0	1.09	13.7	-160	-0.112	Roy et al. (1992)
Th^{4+}	SO_4^{2-}	1.4/50.0	1.56	0	0	0	Felmy and Rai (1992)
Th^{4+}	HSO_4^-	2.0/12.0	1.44	0	0	0	Felmy and Rai (1992)
Th^{4+}	ClO_4^-	2.0/12.0	1.19	27.3	0	-0.057	Novak (1996b)
$Th(SO_4)_3^{2+}$	K^+	2.0/12.0	0.9	0	0	0	Felmy and Rai (1992)
$Th(SO_4)_3^{2+}$	H^+	2.0/12.0	0.84	0	0	0	Felmy and Rai (1992)
$Th(SO_4)_3^{2+}$	Na^+	2.0/12.0	0.12	0	0	0	Felmy and Rai (1992)
$Th(CO_3)_5^{6-}$	K^+	2.0/12.0	1.31	30	0	0	Felmy et al. (1997)
$Th(CO_3)_5^{6-}$	Na^+	2.0/12.0	1.31	30	0	0	Felmy and Rai (1992)
$Th(Acetate)_2^{2+}$	Cl^-	2.0/12.0	0.467	1.74	0	0.143	Moore et al. (1999)
$ThAcetate^{3+}$	Cl^-	2.0/12.0	1.06	5.22	0	0.109	Choppin et al. (2001)
$ThCitrate^+$	Cl^-	2.0/12.0	-0.747	0.29	0	0.319	Choppin et al. (2001)
$ThLactate^{3+}$	Cl^-	2.0/12.0	0.668	5.22	0	0.341	Choppin et al. (2001)
$Th(Lactate)_2^{2+}$	Cl^-	2.0/12.0	0.506	1.74	0	0.225	Moore et al. (1999)
$ThOxalate^{2+}$	Cl^-	2.0/12.0	-0.343	1.74	0	0.5	Choppin et al. (2001)

Table GEOCHEM-52. Pitzer Interaction Coefficients (Cation-Cation; Anion-Anion Interactions) for Ions Containing Thorium Implemented in the WIPP Dissolved Actinide Source Term Process Model for CRA-2019

i	*j*	$\theta_{cc'}$ or $\theta_{aa'}$	Source
Cation-Cation Interactions			
Th^{4+}	Na^+	0.42	Rai et al. (1997)
Th^{4+}	H^+	0.6	Roy et al. (1992)
Th^{4+}	Ca^{2+}	0.6	Rai et al. (1997)
Th^{4+}	K^+	0.42	Rai et al. (1997)
Mg^{2+}	Th^{4+}	0.6	Rai et al. (1997)
Anion-Anion Interactions			
$Th(CO_3)_5^{6-}$	Cl^-	1.8	Moore et al. (1999)
$Th(CO_3)_5^{6-}$	ClO_4^-	5.5	Felmy et al. (1997)

Table GEOCHEM-53. Pitzer Interaction Coefficients (Neutral-Cation; Neutral-Anion Interactions) for Ions Containing Thorium Implemented in the WIPP Dissolved Actinide Source Term Process Model for CRA-2019

i	*j*	$\lambda_{nc'}$ or $\lambda_{na'}$	Source
Neutral-Anion Interactions			
$Th(SO_4)_2(aq)$	Cl^-	0.29	Roy et al. (1992)
$Th(SO_4)_2(aq)$	HSO_4^-	0.68	Roy et al. (1992)
ThEDTA(aq)	Cl^-	0.111	Giambalvo (2002)

Table GEOCHEM-54. Pitzer Interaction Coefficients (Cation-Cation-Anion Interactions) for Ions Containing Thorium Implemented in the WIPP Dissolved Actinide Source Term Process Model for CRA-2019

I	*j*	*k*	ψ_{ijk}	Source
Cation-Cation-Anion Interactions				
Th^{4+}	Mg^{2+}	Cl^-	0.21	Rai et al. (1997)
Th^{4+}	Ca^{2+}	Cl^-	0.21	Rai et al. (1997)
Th^{4+}	H^+	Cl^-	0.37	Roy et al. (1992)
Th^{4+}	Na^+	Cl^-	0.21	Rai et al. (1997)
Th^{4+}	K^+	Cl^-	0.21	Rai et al. (1997)
$Th(CO_3)_5^{6-}$	Na^+	Cl^-	0.3	Felmy and Rai (1999)
$Th(CO_3)_5^{6-}$	K^+	Cl^-	0.3	Felmy and Rai (1999)[A]

[A] Felmy and Rai (1999) values for $Th(CO_3)_5^{6-}$ and Na^+ are used for $Th(CO_3)_5^{6-}$ and K^+.

GEOCHEM-4.3.3 +V Actinides

There are no parameter changes for the An(V) reactions that were implemented in CRA-2014. Parameterization of the model is described in Giambalvo (2002) and Giambalvo (2002b). The parameters are summarized below.

GEOCHEM-4.3.3.1 Equilibrium Constants for Dissolution Reactions for Neptunium Solids and Species

The equilibrium constants for reactions with Np in the +V oxidation state implemented in the Dissolved Actinide Source Term process model are shown in Table GEOCHEM-55.

Table GEOCHEM-55. Equilibrium Constants for Dissolution and Dissociation Reactions for Neptunium Solids and Species Implemented in the WIPP Dissolved Actinide Source Term Process Model for CRA-2019[A]

Reaction	log K	Source
Solid Dissolution Reactions		
$NpO_2OH(aged) + H^+ \leftrightarrow NpO_2^+ + H_2O$	4.52	Fuger and Oetting (1976)
$NpO_2OH(am) + H^+ \leftrightarrow NpO_2^+ + H_2O$	5.22	Neck et al. (1995)
$2[NaNpO_2CO_3 \bullet 7/2H_2O](s) + 2H^+ \leftrightarrow 2NpO_2^+ + 2HCO_3^- + 2Na^+ + 7H_2O$	-1.50	Neck et al. (1995)
$Na_3NpO_2(CO_3)_2(s) + 2H^+ \leftrightarrow NpO_2^+ + 2HCO_3^- + 3Na^+$	6.50	Neck et al. (1995)
$KNpO_2CO_3(s) + H^+ \leftrightarrow NpO_2^+ + HCO_3^- + K^+$	-3.26	Novak et al. (1997)
$K_3NpO_2(CO_3)_2(s) + 2H^+ \leftrightarrow NpO_2^+ + 2HCO_3^- + 3K^+$	4.75	Novak et al. (1997)
Aqueous Dissociation Reactions		
$NpO_2CO_3^- + H^+ \leftrightarrow NpO_2^+ + HCO_3^-$	5.32	Fanghänel et al. (1995)
$NpO_2(CO_3)_2^{3-} + 2H^+ \leftrightarrow NpO_2^+ + 2HCO_3^-$	14.2	Fanghänel et al. (1995)
$NpO_2(CO_3)_3^{5-} + 3H^+ \leftrightarrow NpO_2^+ + 3HCO_3^-$	25.7	Fanghänel et al. (1995)
$NpO_2(OH)(aq) + H^+ \leftrightarrow NpO_2^+ + H_2O$	11.3	Fanghänel et al. (1995)
$NpO_2(OH)_2^- + 2H^+ \leftrightarrow NpO_2^+ + 2H_2O$	23.5	Fanghänel et al. (1995)
$NpO_2Acetate(aq) \leftrightarrow NpO_2^+ + Acetate^-$	-1.37	Giambalvo (2002)
$NpO_2Citrate^{2-} \leftrightarrow NpO_2^+ + Citrate^{3-}$	-3.50	Choppin et al. (2001)
$NpO_2H_2EDTA^- \leftrightarrow NpO_2^+ + EDTA^{4-} + 2H^+$	-20.9	Choppin et al. (2001)
$NpO_2HEDTA^{2-} \leftrightarrow NpO_2^+ + EDTA^{4-} + H^+$	-15.5	Choppin et al. (2001)
$NpO_2EDTA^{3-} \leftrightarrow NpO_2^+ + EDTA^{4-}$	-8.54	Choppin et al. (2001)
$NpO_2Lactate(aq) \leftrightarrow NpO_2^+ + Lactate^-$	-1.97	Choppin et al. (2001
$NpO_2Oxalate^- \leftrightarrow NpO_2^+ + Oxalate^{2-}$	-4.24	Choppin et al. (2001)

[A]All of the references cited in this table derived or reported values for standard state chemical potential that was a direct input to FMT (Novak 1996a; see also Babb and Novak 1995; Babb and Novak 1997 and addenda; Wang 1998). These were later converted to log K values as documented in Ismail et al. (2009).

GEOCHEM-4.3.3.2 Pitzer Interaction Coefficients for Ions Containing Neptunium

The Pitzer coefficients for ions containing actinides in the +IISI oxidation state are shown in Table GEOCHEM-56, Table GEOCHEM-57, and Table GEOCHEM-58.

Table GEOCHEM-56. Pitzer Interaction Coefficients (Cation-Anion Interactions) for Ions Containing Neptunium Implemented in the WIPP Dissolved Actinide Source Term Process Model for CRA-2019

I	*j*	α_1/α_2	$\beta^{(0)}$	$\beta^{(1)}$	$\beta^{(2)}$	C^{φ}	Source
Cation-Anion Interactions							
NpO_2^+	Cl^-	2.0/12.0	0.142	0.281	0	0	Neck et al. (1995)
NpO_2^+	ClO_4^-	2.0/12.0	0.257	0.18	0	0.0081	Neck et al. (1995)
$NpO_2(CO_3)_2^{3-}$	Na^+	2.0/12.0	0.48	4.4	0	0	Fanghänel et al. (1995)
$NpO_2(CO_3)_2^{3-}$	K^+	2.0/12.0	0.48	4.4	0	0	Novak et al. (1997)
$NpO_2(CO_3)_2^{3-}$	Ca^{2+}	2.0/12.0	0.48	4.4	0	0	Al Mahamid et al. (1998)
$NpO_2(CO_3)_2^{3-}$	Mg^{2+}	2.0/12.0	0.48	4.4	0	0	Al Mahamid et al. (1998)
$NpO_2(CO_3)_3^{5-}$	Na^+	2.0/12.0	1.8	22.7	0	0	Fanghänel et al (1995)
$NpO_2(CO_3)_3^{5-}$	K^+	2.0/12.0	2.34	22.7	-96	-0.22	Novak et al. (1997)
$NpO_2(CO_3)_3^{5-}$	Ca^{2+}	2.0/12.0	2.07	22.7	-48	-0.11	Al Mahamid et al. (1998)
$NpO_2(CO_3)_3^{5-}$	Mg^{2+}	2.0/12.0	2.07	22.7	-48	-0.11	Al Mahamid et al. (1998)
$NpO_2CO_3^-$	Na^+	2.0/12.0	0.1	0.34	0	0	Fanghänel et al. (1995)
$NpO_2CO_3^-$	K^+	2.0/12.0	0.1	0.34	0	0	Novak et al. (1997)
$NpO_2CO_3^-$	Ca^{2+}	2.0/12.0	0.1	0.34	0	0	Al Mahamid et al. (1998)
$NpO_2CO_3^-$	Mg^{2+}	2.0/12.0	0.1	0.34	0	0	Al Mahamid et al. (1998)
$NpO_2Citrate^{2-}$	K^+	2.0/12.0	-0.423	1.75	0	0.142	Choppin et al. (2001)
$NpO_2Citrate^{2-}$	Na^+	2.0/12.0	-0.423	1.75	0	0.142	Choppin et al. (2001)
$NpO_2Oxalate^-$	K^+	2.0/12.0	-0.542	0.29	0	0.095	Choppin et al. (2001)
$NpO_2Oxalate^-$	Na^+	2.0/12.0	-0.542	0.29	0	0.095	Choppin et al. (2001)
NpO_2EDTA^{3-}	Na^+	2.0/12.0	0.683	5.91	0	0	Choppin et al. (2001)
$NpO_2H_2EDTA^-$	Na^+	2.0/12.0	-0.829	0.258	0	0.256	Pokrovsky et al. (1998)
NpO_2HEDTA^{2-}	Na^+	2.0/12.0	0.473	-1.50	0	0	Pokrovsky et al. (1998)
NpO_2EDTA^{3-}	K^+	2.0/12.0	0.683	5.91	0	0	Pokrovsky et al. (1998)
$NpO_2H_2EDTA^-$	K^+	2.0/12.0	-0.829	0.258	0	0.256	Pokrovsky et al. (1998)
NpO_2HEDTA^{2-}	K^+	2.0/12.0	0.473	-1.50	0	0	Pokrovsky et al. (1998)

Table GEOCHEM-57. Pitzer Interaction Coefficients (Cation-Cation; Anion-Anion Interactions) for Ions Containing Neptunium Implemented in the WIPP Dissolved Actinide Source Term Process Model for CRA-2019

i	*j*	θ_{cc}, or θ_{aa},	Source
Anion-Anion Interactions			
$NpO_2(CO_3)_2^{3-}$	Cl^-	-0.26	Fanghänel et al. (1995)
$NpO_2(CO_3)_3^{5-}$	Cl^-	-0.26	Fanghänel et al. (1995)
$NpO_2(OH)_2^-$	Cl^-	-0.24	Fanghänel et al. (1995)
$NpO_2CO_3^-$	Cl^-	-0.21	Fanghänel et al. (1995)
$NpO_2(CO_3)_3^{5-}$	CO_3^{2-}	-1.9	Neck et al (1995)

Table GEOCHEM-58. Pitzer Interaction Coefficients (Neutral-Cation; Neutral-Anion Interactions) for Ions Containing Neptunium Implemented in the WIPP Dissolved Actinide Source Term Process Model for CRA-2019

i	*j*	λ_{nc}, or λ_{na},	Source
Neutral-Anion Interactions			
$NpO_2OH(aq)$	Cl^-	-0.19	Fanghänel et al. (1995)
$NpO_2Lactate(aq)$	Cl^-	0.015	Choppin et al. (2001)
$NpO_2Acetate(aq)$	Cl^-	-0.104	Giambalvo (2003)

GEOCHEM-4.4Quantification of Uncertainty in the Dissolved Actinide Source Term

As noted in GEOCHEM-1.1.4, uncertainties in the WIPP PA can be categorized as: uncertainty in the conceptual model, uncertainty in the process model, and uncertainty in parameterization of the process model. Overall, after six compliance calculations in two brines, the variability in dissolved actinide baseline concentrations for An(III), An(IV), An(V) is shown in Table GEOCHEM-59.

Table GEOCHEM-59. Comparison of Actinide Solubilities (M) for Compliance-Related Calculations from the CCA to CRA-2014

PA Calculation	Th(IV) (M)	Np(V) (M)	Am(III) (M)
CCA (SPC, Magnesite, without Organics, All Vectors) [A]	4.4×10^{-6}	2.3×10^{-6}	5.82×10^{-7}
PAVT (SPC, Hydromagnesite without Organics, All Vectors)[B]	1.3×10^{-8}	2.4×10^{-7}	1.2×10^{-7}
CRA-2004 PA (GWB, Hydromagnesite, with Organics, Microbial Vectors)[C]	1.19×10^{-8}	1.02×10^{-6}	3.07×10^{-7}
CRA-2004 PABC (GWB, Hydromagnesite, with Organics, All Vectors)[D]	5.64×10^{-8}	3.55×10^{-7}	3.87×10^{-7}
CRA-2009 PABC (GWB, Hydromagnesite, with Organics, All Vectors)[E]	5.63×10^{-8}	3.90×10^{-7}	1.66×10^{-6}
CRA-2014 PA ($GWB_{min.\ vol.}$, Hydromagnesite, with Organics, All Vectors)[F]	6.05×10^{-8}	2.77×10^{-7}	2.59×10^{-6}
CCA (ERDA-6, Magnesite, without Organics, All Vectors)[A]	6.0×10^{-9}	2.2×10^{-6}	6.52×10^{-8}
PAVT (ERDA-6, Hydromagnesite, without Organics, All Vectors)[B]	4.1×10^{-8}	4.8×10^{-7}	1.3×10^{-8}
CRA-2004 PA (ERDA-6, Hydromagnesite, with Organics, Microbial Vectors)[C]	2.47×10^{-8}	5.08×10^{-6}	1.69×10^{-7}
CRA-2004 PABC (ERDA-6, Hydromagnesite, with Organics, All Vectors)[D]	6.79×10^{-8}	8.24×10^{-7}	2.88×10^{-7}
CRA-2009 PABC (ERDA-6, Hydromagnesite, with Organics, All Vectors)[E]	6.98×10^{-8}	8.75×10^{-7}	1.51×10^{-6}
CRA-2014 PA ($ERDA\text{-}6_{min.\ vol.}$, Hydromagnesite, with Organics, All Vectors)[F]	7.02×10^{-8}	8.76×10^{-7}	1.48×10^{-6}

A. From Novak et al. (1996b) and U.S. DOE 1996, Appendix SOTERM, except that Novak et al. (1996b) used molal instead of molar units. U.S. EPA (1998) cited Novak and Moore (1996) as the source of the CCA PA solubilities, but the Am(III) solubilities from Novak and Moore (1996) differ from those in Novak et al. (1996b) and U.S. DOE 1996.
B. From Trovato (1997). Novak (1997) also calculated actinide solubilities for the PAVT, but the EPA used the results of its own calculations.
C. From Brush and Xiong (2003a, 2003b, 2003c, 2003d) and U.S. DOE 2004, Appendix SOTERM. D Brush and Xiong (2005a, 2005b) and Brush (2005). These solubilities were also used for the CRA-2009 PA calculations.
E. Brush et al. (2009)
F. Brush and Domski (2013a)

GEOCHEM-4.4.1 Conceptual Model Uncertainty for the Dissolved Actinide Source Term

Conceptual model uncertainty originates in the assumptions that are made in characterizing the modeled system. These assumptions include variables and processes. For example, the mineralogy of the reactants would be considered variables, while the assumption of a well-mixed batch reactor would be classified as a process. Since neither of these assumptions can be tested first hand, they constitute uncertainty in the conceptual model. Given that it is not possible to test

every permutation of possible conceptual models, the result is variability in chemical conditions due to conceptual uncertainty.

GEOCHEM-4.4.1.1 Conceptual Model Uncertainty for Dissolved An(IV)

CRA-2019 Appendix SOTERM, Section SOTERM-6.4 identifies sources of uncertainty in the WIPP conceptual model for dissolved An(IV). Primarily, the use of Th(IV) as an analog for An(IV) is an uncertainty in the conceptual model. This uncertainty cannot be resolved until data specific to each of the An(IV) actinides (namely Pu(IV)) are available.

The solubility-controlling phase for Th(IV) is amorphous thorium oxide [ThO_2(am)]. The conceptual model for An(IV) is predicated on the observation that amorphous, rather than crystalline, solids initially precipitate, even though the latter is more thermodynamically stable than the former. This is an expression of Ostwald's Step Rule, in which less soluble crystalline compounds are thermodynamically more stable, but their amorphous counterparts are kinetically favored and tend to precipitate first. A recent investigation by Simonnet et al. (2016) reported that a fully crystalline state for ThO_2 could only be achieved through a high-temperature (between 850 and 1500 °C) synthesis route. Attempts to synthesize ThO_2(cr) at room temperature were not successful. These observations support the contention that the WIPP conceptual model should assume that an amorphous or partially crystalline An(IV) phase controls the concentration of aqueous An(IV) in solution.

The DOE has not quantified the effect of ThO_2 crystallinity because the conceptual model assumptions are well supported by experimental data.

GEOCHEM-4.4.1.2 Conceptual Model Uncertainty for Dissolved An(V)

The DOE has not examined conceptual model uncertainty for dissolved An(V) because releases of this element do not affect the long-term performance of the WIPP (Brush and Garner 2005).

GEOCHEM-4.4.1.3 Conceptual Model Uncertainty for Dissolved An(VI)

There is no conceptual model for dissolved An(VI) (U.S. DOE 2019, Appendix SOTERM, Section SOTERM-6.1.2).

GEOCHEM-4.4.2 Process Model Uncertainty for the Dissolved Actinide Source Term

There are four process models for the dissolved actinide source term: dissolved +III actinides, dissolved +IV actinides, dissolved +V actinides, and dissolved +IV actinides. Process model uncertainty would include uncertainty about which solids and species to include in the process models.

GEOCHEM-4.4.2.1 Process Model Uncertainty for Dissolved An(III)

Variability in the An(III) dissolved concentration derived from process model uncertainty can be discerned readily from Table GEOCHEM-59. The first process model for An(III) dissolved concentration did not include hydromagnesite. The CCA solubilities were 5.82×10^{-7} M (SPC brine) and 6.52×10^{-8} M (ERDA-6 brine). Hydromagnesite was added for the PAVT. The

solubilities were 1.2×10^{-7} M (Salado PA brine) and 1.3×10^{-8} M (ERDA-6 brine). Organics were not included in the CCA or PAVT, but were added for CRA-2004. The solubilities were 3.87×10^{-7} M (GWB brine), and 2.88×10^{-8} M (ERDA-6 brine).

The process model change for CRA-2009 was the addition of MgO Phase 5 to the model. The solubilities were 1.66×10^{-6} M (GWB brine) and 1.51×10^{-6} M (ERDA-6 brine). The order of magnitude change in solubility in this case was not because of the process model change; the root cause for the elevated concentrations was an increase in the EDTA inventory. In CRA-2004, CRA-2009, and CRA-2014, organic ligand concentrations were PAIR inventory limited, not solubility limited, so any increase in inventory increased the organic ligand concentrations. The organic ligand concentrations for CRA-2019 may be solubility limited, depending on the final PAIR inventory. Finally, there were no process model changes for CRA-2014, but the solubilities were 2.59×10^{-6} M (GWB brine) and 1.48×10^{-6} M (ERDA-6 brine).

The process model changes discussed above involve changes to the process model for chemical conditions. There have been no changes in the Dissolved Actinide Source Term Process Model. However, one process model change that has been discussed at length is the inclusion of a tetraborate species in WIPP brines that could complex with Am^{+3}. The DOE has chosen not to make this change for CRA-2019.

While it is possible to quantify the potential impact of these uncertainties on dissolved An(IV) concentrations, the DOE has not quantified this impact because experimental data have supported the current process model for the chemical conditions expected in the WIPP.

GEOCHEM-4.4.2.2 Process Model Uncertainty for Dissolved An(IV)

CRA-2019 Appendix SOTERM, Section SOTERM-5.4 identifies sources of uncertainty in the WIPP process model for dissolved An(IV) using a set of screening criteria. Of note, the following researchers have investigated the hydrolysis of Th^{4+}: Ekberg et al. (2000), Rai et al. (2000), Moulin et al. (2001), and Okamoto, Mochizuki, and Tsushim (2003). In addition, the hydrolysis of Th^{4+} was critically reviewed by Neck and Kim (2001) and Moriyama et al. (2005). Those authors proposed an alternative process model that includes amorphous $Th(OH)_4$(am) (Neck et al. 2002; Altmaier et al. 2005 and 2006), crystalline ThO_2(cr) (Neck et al. 2003), $Th(OH)_3^+$, $Th(OH)_2^{2+}$, $Th(OH)_4$ (aq), $Th_6(OH)_{15}^{9+}$, and $Th_4(OH)_{12}^{4+}$ (Neck, Altmaier, and Fanghänel 2006). The only species from this list included in the WIPP Dissolved Actinide Source Term Process Model is $Th(OH)_4$(aq). The solubility-controlling phase for the Th^{4+}/water system in the WIPP Dissolved Actinide Source Term Process Model is ThO_2(am).

For the Th^{4+} system with carbonate, CRA-2019 Appendix SOTERM, Section SOTERM-5.4 identifies $Th(OH)_2(CO_3)_2^{2-}$ as a species likely to be present under WIPP conditions. However, this species is not currently included in the WIPP Dissolved Actinide Source Term Process Model. Instead, the WIPP Dissolved Actinide Source Term Process Model includes $Th(CO_3)_5^{6-}$ and $Th(OH)_3(CO_3)^-$. Data from Altmaier et al. (2005) indicates the use of the pentacarbonyl complex for the IV actinides is a conservative assumption that overpredicts the solubility of the Th^{4+} at pH > 10.

CRA-2019 Appendix SOTERM, Section SOTERM-5.4 also notes that calcium enhancement of solubility of An(IV) is being confirmed and is also found in Pu(IV) and U(IV) systems. Currently, the WIPP Dissolved Source Term Process Model only includes one interaction with Ca^{2+}, the interaction of Th^{4+} with Ca^{2+}. The DOE contends that this single interaction is sufficient to represent the role that Ca^{2+} may play in dissolving the An(IV) solid, given the calcium levels predicted in the WIPP.

GEOCHEM-4.4.2.3 Process Model Uncertainty for Dissolved An(V)

The DOE has not examined process model uncertainty for dissolved An(V) because releases of this element do not affect the long-term performance of the WIPP (Brush and Garner 2005).

GEOCHEM-4.4.2.4 Process Model Uncertainty for Dissolved An(VI)

There is no process model for dissolved An(VI). The EPA specified a fixed value for its estimate of the solubility of U(VI) in GWB and ERDA-6 (U.S. EPA 2006).

GEOCHEM-4.4.3 Parameter Uncertainty for the Dissolved Actinide Source Term Process Model

The only area of uncertainty that has been addressed by the DOE explicitly for the Dissolved Actinide Source Term is parameterization of the process models which was performed nearly 30 years ago. Since then, with each recertification of the repository, the DOE has examined laboratory data for actinide solubility produced since the first certification to see if new data can be used to either re-parameterize the model or quantify uncertainty in parameterization of the Dissolved Actinide Source Term Process Model.

Data can be utilized a couple of ways. First, new data could be used to re-parameterize part of the EQ3/6 thermodynamic database. This only applies to data that qualifies for parameterization, data for a simple system (at most, only one or two salts involved), and experiments performed at conditions that allow the analyst to derive the parameter of interest. An example would be for experiments on a simple system where the dissolved ion concentrations are sufficient ($>10^{-3}$ m), but the presence of colloids is expected. Unless the dissolved fraction of ion can be separated from the colloidal fraction of ions, the data should not be used to parameterize the dissolved ion process model.

In the EPA Completeness Comment 3-C-3, the EPA noted (U.S. EPA 2015):

> … DOE must: 1) carry out and document a thorough review of all available +III and +IV actinide aqueous speciation and solubility data and hydromagnesite solubility data; 2) use the results of this review to defensibly update the EQ3/6 database.

A thorough review of all available +III and +IV aqueous speciation and solubility data was completed prior to each major recertification activity. This review is documented in the uncertainty analyses of actinide solubility distributions for CRA-2004 PA, CRA-2004 PABC, CRA-2009 PA, CRA-2009 PABC, CRA-2014 PA (Xiong et al. 2005b; 2011; Brush and Domski

2013b), and in U.S. DOE 2014, Appendix SOTERM, Section SOTERM-3.7, Americium and Curium Chemistry).

A summary of the evaluations of the available data for parameterization of the Th(IV) and The reviewed literature data is not suitable for parameterization due to the following factors:

- Experiments were conducted at one single ionic strength;
- Important experimental parameters such as pH and solubility-controlling phase(s) were not characterized;
- Experiments were conducted under conditions that are not relevant to the WIPP. For instance, the experiments of Migdisov and Williams-Jones (2007) were conducted far above 25°C (i.e., 150°C, 200°C, and 250°C) with NdF_3 as a solubility-controlling phase. Under WIPP conditions, the temperature is around 27°C and the WIPP brines do not contain fluoride at a detectable level.

Therefore, the DOE has not re-parameterized the Dissolved Actinide Source Term Process Model since the initial certification. For CRA-2019, the process model and parameters described in GEOCHEM-4.2 and GEOCHEM-4.3 will not be updated. Instead, data that is identified as useful for quantification of parameter uncertainty will be used as described below for an explicit analysis of uncertainty in parameterization of the process model.

The method used by the DOE for quantification of uncertainty in the parameters for the Dissolved Actinide Source Term Model is an explicit method involving sampling from a distribution of difference values. Single baseline estimates for the +III and +IV actinide solubilities will be made using the process model and parameters described in GEOCHEM-4.2 and GEOCHEM-4.3. Then an uncertainty factor, *D*, is chosen using Latin Hypercube Sampling and the baseline estimate is multiplied by the ten to the power of the uncertainty factor to obtain a solubility estimate (only the dissolved portion) for an individual PA vector.

$$\mathbf{S_{(PA\ Vector,\ oxidation\ state)} = S_{(oxidation\ state)}} \times 10^{\boldsymbol{D}\mathbf{(PA\ Vector,\ oxidation\ state)}} \qquad \text{(GEOCHEM.37)}$$

$S_{(\text{PA Vector, oxidation state})}$ is the actinide solubility value in moles/kg that is used in the PA calculation for a specific vector. $S_{(\text{oxidation state})}$ is the actinide solubility for a given oxidation state (also called the baseline solubility). $D_{(\text{PA Vector, oxidation state})}$ is the uncertainty factor.

The question of how to obtain a range and distribution for the parameter, *D*, arises. If *D* is thought of as model prediction error, that is, how well does the process model and its parameters predict relevant experimental results, comparisons between model results and experimental results can be used to develop a range and distribution for *D*. The procedure for obtaining a range and distribution for *D* is as follows:

1. Perform a search of the literature
2. Screen the literature for WIPP relevant experimental data on actinide solubility
3. Use the process model and parameters for WIPP actinide solubility to simulate the reported experimental results

4. Compare the simulation to the experimental results
5. Calculate the difference, *D*, between the model results and the experimental results
6. Derive a distribution for that difference

A separate range for *D* is developed for each actinide oxidation state, +III and +IV.

An example distribution function for *D* is shown in Figure GEOCHEM-6. *D* is the difference between the logarithm of the measured value and the logarithm of the value produced by a model simulation of the experiment.

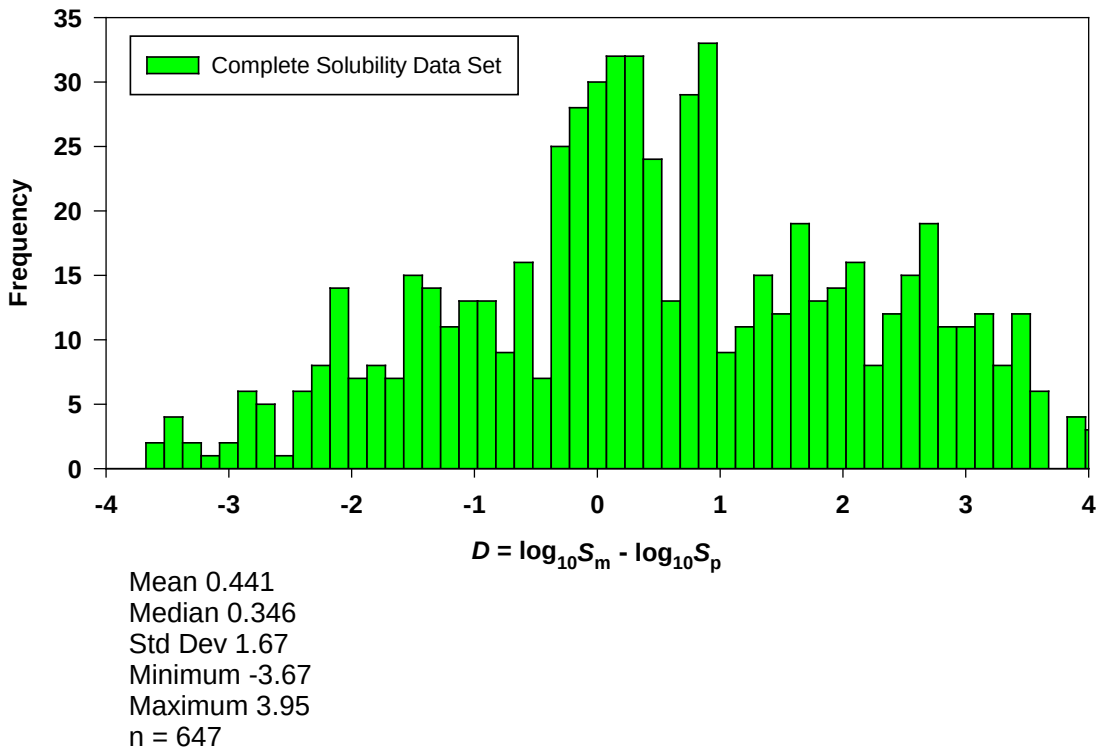

Figure GEOCHEM-6. Example Distribution Function for *D*

Identification of data that is useful for quantification of uncertainty is made by applying screening criteria to experimental data found through the literature search. The screening criteria have evolved each time this procedure has been applied (from the CCA through CRA-2014). The screening criteria that will be used in CRA-2019 are discussed below. The implications of each screening criterion for CRA-2019 are also discussed.

> The measured Am(III) solubilities from published papers and unpublished reports evaluated previously (Xiong 2005; and/or Xiong 2011) include: Borkowski et al. (2009), Borkowski (2010), Bunyakina and Storozhenko (2004), Khalili et al. (1994), Lucchini et al. (2007), Makino et al. (1993), Meinrath and Kim (1991), Meinrath and Takeishi (1993), Peretrukhin et al. (1996), Rao et al. (1996a, 1996b,

1999), Runde et al. (1992), Runde and Kim (1994), Silva (1982), and Wood et al. (2002).

The measured Am(III) solubilities from published papers and unpublished reports that Brush and Domski (2013a) evaluated for their analysis include: Borkowski et al. (2010), Borkowski (2012), Migdisov and Williams-Jones (2007), Neck et al. (2009), Rabung et al. (2008), and Vitorge and Tran (1991).

The measured Th(IV) solubilities from published papers and unpublished reports evaluated previously by Xiong (2005) and/or Xiong (2011) include: Altmaier et al. (2004, 2005, 2006, 2008), Baston et al. (1996), Felmy et al. (1991, 1997, 2006), Neck et al. (2002, 2003), Östhols et al. (1994), and Rai et al. (1995b, 1997, 2000).

The measured Th(IV) solubilities that Brush and Domski (2013a) evaluated for their analysis include: Borkowski (2012), Borkowski et al. (2012), Brendebach et al. (2007), Colàs et al. (2011), Fellhauer et al. (2010), Kim et al. (2010), Rai et al. (2005, 2008, 2009, 2011), Vandenborre et al. (2008, 2010), Wood (2005), and Xia et al. (2003).

GEOCHEM-4.4.3.1 Criterion G1

"Include only results from January 1990 to December 2018."[2]

This criterion is set to allow time to process all data that is discovered. All of the data sets listed above meet this criterion.

GEOCHEM-4.4.3.2 Criterion G2

"Include only results from peer reviewed journals, or government sponsored laboratory data."

All of the data sources listed above have met this criterion.

GEOCHEM-4.4.3.3 Criterion G3

"Include only results from solubility studies, exclude other studies such as corrosion, sorption etc."

All of the data sources listed above have met this criterion. The uncertainty being examined is uncertainty in parameterization of a process model and parameters for solubility.

[2] The uncertainty analysis will be performed as part of the deferred PA.

GEOCHEM-4.4.3.4 Criterion G4

> "Include only results where water was the solvent."

A process model and parameters for solubility in a medium other than water will differ greatly from the process model described in GEOCHEM-4.2. All of the data sources listed above have met this criterion.

GEOCHEM-4.4.3.5 Criterion G5

> "Include only results obtained from studies at pressures at or close to atmospheric, at temperatures at or close to those expected in the WIPP (i.e., 20 to 30 ºC), and with post-test phase-separation methods similar to the experiments used to parameterize the model for WIPP."

Temperature and pressure do have an effect on solubility, but the process model for the dissolved actinide source term does not include temperature and pressure effects. Therefore, only data for temperatures and pressures close to WIPP conditions should be used.

However, the clause regarding post-test phase separation has been questioned by the EPA. Only one data set has been excluded from the uncertainty analysis because of the post-test phase separation criterion, Altmaier et al. (2004).

Altmaier et al. (2004) measured the solubilities of ThO_2(cr) and $ThO_n(OH)_{4-2n}\cdot xH_2O$(am) in NaCl and $MgCl_2$ solutions with various ionic strengths. Xiong (2005) did not consider the results of Altmaier et al. (2004) in their uncertainty analyses of Th(IV) solubilities for the CRA-2004 PABC because this paper came to their attention after they completed their analysis. For the CRA-2009 PABC, Xiong (2011) included all six of the uncentrifuged results from solutions with $I \geq 3$ M from Altmaier et al. (2004, Figure 2), two from their 5 M NaCl solutions, two from their 2.5 M $MgCl_2$ solutions, and two from their 4.5 M $MgCl_2$ solutions. However, Xiong (2011) excluded the ultracentrifuged results of Altmaier et al. (2004) because this post-test phase-separation method was significantly different from those employed in the studies used to parameterize the WIPP Th(IV) solubility model (e.g., centrifugation or filtration) and appeared to support a significantly different solubility model than that established for the WIPP (i.e., ultracentrifugation showed that 99 percent or more of what had been interpreted as dissolved Th(IV) present as the $Th(OH)_4$(aq) species appeared to be present as the eigencolloid $Th(OH)_4$(col)). Borkowski et al. (2012) performed thorium analog studies in WIPP simulated brine noting that possibly a 40 percent colloidal fraction (but 15 typically 20 percent or less) could exist, but most likely there was much less intrinsic colloid formation than reported in Altmaier et al. (2004).

> The WIPP Th(IV) model was parameterized in the mid-1990s, before it was realized that the phase-separation methods used then might not have removed all of the $Th(OH)_4$(col). Thus, the calculated dissolved component using the WIPP process model and parameters is larger than expected. Including the ultracentrifuged results of Altmaier et al. (2004) in the uncertainty distribution for Th(IV) would generally decrease the estimate used in PA. As a result, Altmaier et

al. (2004) results in the uncertainty analysis for CRA-2009, CRA-2014, and CRA-2019 were excluded.

GEOCHEM-4.4.3.6 Criterion G6

> "Include only results from studies of Th(IV); and Nd(III), Am(III), and Cm(III)."

These elements are used as analogs for An(III) and An(IV). All of the data sources listed above have met this criterion.

GEOCHEM-4.4.3.7 Criterion G7

> "Include only results from studies with a characterized solubility-controlling solid for which solubility data is in the WIPP Th(IV) or Am(III) model (i.e., in the EPA-certified thermodynamic database), and in which the quantity of solid initially present was sufficient to prevent complete dissolution of this solid during the experiments."

This criterion was added because if all of the solid material dissolves in an experiment, the dissolved component is actually PAIR inventory limited. This is not a valid solubility experiment, and violates Criterion G7.

Furthermore, even if the solid remains throughout the experiment but is not characterized at the end of the experiment, the composition of the solid may have changed as the experiment progressed. For example, DOE experiments for siderite solubility started with siderite and ended with both siderite and chukanovite in the experiments. Solids characterization proved this outcome. Modeling of this system is possible as long as the presence of both solids is acknowledged.

For CRA-2019, the most significant consequence of applying this criterion is that results in Borkowski et al. (2009), and Borkowski (2010), which superseded Borkowski et al. (2009), were excluded because they violate Criterion G7, as noted by the EPA in Comment 3-C-5 during completeness review of CRA-2014. One hundred six data points were removed from the uncertainty analysis for Am(III) because of this.

GEOCHEM-4.4.3.8 Criterion G8

> "Include only studies for which the composition of the aqueous solution is known."

Much like Criterion G7 for the solid phase, G8 asserts that the aqueous phase characteristics must be known.

GEOCHEM-4.4.3.9 Criterion G9

> "Include only results from studies with dissolved elements or species that are present in WIPP brines. Exclude studies with dissolved elements or species that

> are absent in WIPP repository brines and for which the model does not include association/dissociation constants or Pitzer parameters."

Because the uncertainty that is sought is uncertainty in parameterization of the process model, all data used for quantification of uncertainty should be for systems whose reactions fall within the scope of the process model. Reactions and species that are not included in the process model should be examined under process model uncertainty, not parameter uncertainty.

GEOCHEM-4.4.3.10 Criterion G10

> "Include only studies where a complete description of the experimental procedure and method are provided."

Without a full description of the experimental procedure, simulation of the experiment with a process model is not possible. During their review of CRA-2014, the EPA found data published by Khalili et al. (1994) that, upon examination by the DOE, fell into this category.

The DOE was able to pull 26 data points from Figure 1 of Khalili et al. (1994) at a pcH value of 8.4. However, the experimental system of Khalili et al. (1994) contained inadequately defined variables to simulate accurately in EQ3/6. The brine composition is given in terms of a salt recipe; i.e., the brine composition was not determined through chemical analysis. The system was not closed to the atmosphere, therefore CO_2(g) could dissolve in the samples. The reaction vessels were merely flushed with N_2 gas before sealing, and after subsequent sample removals.

The very high initial carbonate concentration (10^{-2} M) of the brine renders it impossible for $Nd(OH)_3$ to be the solubility-controlling phase. Thus, creative model construction was required to maximize $Nd(OH)_3$(am) production, which was the stated solubility-controlling phase, a phase not included in the WIPP process model.

With the combined uncertainty of all of the experimental parameters, one could imagine large absolute *D* values would result; however, the range was $-0.27 < D < 0.42$. This relatively small range leads (erroneously) to high confidence in this data set.

The (Khalili et al. 1994) data set violates multiple screening criteria, G7, G8, and G10. If compounding violations exist, in this case the experimental setup/procedure, missing analyses (both liquid and solid), the absence of the presumed solubility-controlling phase in the process model, then the data set cannot be used to quantify uncertainty.

GEOCHEM-4.4.3.11 Criterion G11

> "Include only results from experimental studies carried out under conditions at, or close to those predicted for WIPP disposal rooms. Specifically, experimental studies with (1) $I \geq 3$ m or M, (2) pcH = 8.0–11.2, and (3) total inorganic C (TIC) = 0 - 2 x 10^{-2} M (Domski 2019a)."

This criterion was established for CRA-2014. The intent in adding Criterion G11 was to capture parameter uncertainty under WIPP relevant conditions.

GEOCHEM-4.4.4 Quantification of Uncertainty Summary for CRA-2019

The data set used to develop the An(III) uncertainty distribution for the SEN4 calculation[3] included 108 data points:

1. Twenty-six samples from Khalili et al. (1994)
2. Eleven samples in carbonate-free 5 M NaCl from Runde and Kim (1994)
3. Fifteen samples in ERDA-6 brine from Rao et al. (1999)
4. Zero samples in 5 M NaCl and 0 samples in ERDA-6 from Borkowski et al. (2009) and Borkowski (2010)
5. Fifty-six samples from Neck et al. (2009) were included in this analysis as follows: 8 samples in 5 M NaCl; 5 samples in 1 M $MgCl_2$; 3 samples in 2.5 M $MgCl_2$; 8 samples in 5 M $MgCl_2$; 9 samples in 1 M $CaCl_2$; and 23 samples in 3 M $CaCl_2$.
6. Zero samples in 3 – 5 M NaCl with $Na_2B_4O_7$ from Borkowski et al. (2010) and Borkowski et al. (2012)

The DOE and the EPA have had a number of technical discussions about the data set to be used to develop the An(III) uncertainty distribution for CRA-2019. The DOE has asserted, and the EPA has agreed, that the Khalili et al. (1994) data should not be included because of uncertainties in experimental conditions and solid phases. Thus, the SEN4 data set without the Khalili et al (1994) data will be used for CRA-2019.

Therefore, for CRA-2019, the DOE will include 82 data points to develop the An(III) uncertainty distribution. The data set includes:

1. Zero samples from Khalili et al. (1994)
2. Eleven samples in carbonate-free 5 M NaCl from Runde and Kim (1994)
3. Fifteen samples in ERDA-6 brine from Rao et al. (1999)
4. Zero samples in 5 M NaCl and 0 samples in ERDA-6 from Borkowski et al. (2009) and Borkowski (2010)
5. Fifty-six samples from Neck et al. (2009) were included in this analysis, per EPA's instructions, as follows: 8 samples in 5 M NaCl; 5 samples in 1 M $MgCl_2$; 3 samples in 2.5 M $MgCl_2$; 8 samples in 5 M $MgCl_2$; 9 samples in 1 M $CaCl_2$; and 23 samples in 3 M $CaCl_2$
6. Zero samples in 3 – 5 M NaCl with $Na_2B_4O_7$ from Borkowski et al. (2010) and Borkowski et al. (2012)

[3] The current PA baseline calculation is the PA performed for CRA-2014. A subsequent PA calculation, called CRA14_SEN4, was performed during the completeness review for CRA-2014.

The data set used to develop the An(IV) uncertainty distribution for the SEN4 calculation included 44 data points:

1. Eighteen samples in 3 M NaCl, $8.0 \leq pcH \leq 11.2$ from Felmy et al. (1991)
2. Ten ultracentrifuged samples, 5 in 5 M NaCl, and 5 in 2.5 M $MgCl_2$ from Altmaier et al. (2004)
3. Twelve samples in 4 M NaCl with 0.02 M c_{TIC} from Altmaier et al. (2006)
4. Four samples in 5.26 M $CaCl_2$ with pcH < 10 from Altmaier et al. (2008)
5. Zero samples from Borkowski et al. (2010) and) Borkowski et al. (2012)

The DOE and the EPA have had a number of technical discussions regarding which data sets would be used to develop the An(IV) uncertainty distribution for CRA-2019. It was agreed upon to continue using the 44 data points that were used in the SEN4 calculation in the CRA-2019 PA.

GEOCHEM-4.5 WIPP Dissolved Actinide Source Term Model Summary for CRA-2019

Discussions between the DOE and the EPA during the comment resolution phase for CRA-2014 examined the possibility of updating the Dissolved Actinide Source Term Process Model (by adding species and reactions) and parameterization (by using more recent data for parameter development). However, the DOE has decided to forego implementation of changes for CRA-2019. The DOE is not proposing any changes to the conceptual models and process models for calculating the Dissolved Actinide Source Term for CRA-2019. However, changes to the thermodynamic database, baseline solubilities, and uncertainty distribution applied to baseline solubilities are included in CRA-2019.

One of the changes for CRA-2019 is in quantification of parameter uncertainty. The uncertainty distributions for CRA-2014 were altered with the addition of Criterion G11. Criterion G11 is being updated for CRA-2019 to align with the DOE's derivation of possible ranges in the repository for ionic strength, pcH, and total inorganic carbon.

GEOCHEM-5.0 COLLOIDS

Colloids are important to PA because they can be responsible for significant fractions of mobile actinides. In the CRA-2014 PA calculations, the colloidal fractions of total mobile actinide concentrations at median solubility limits were approximately 86 percent for Th(IV), U(IV), and Pu(IV) in both the Salado and Castile brines (U.S. DOE 2014, Appendix SOTERM-2014, Section SOTERM-5.4). For Pu(III) they were 67 and 77 percent for the Salado and Castile brines, respectively. For Am(III), they were 22 and 60 percent for the Salado and Castile brines, respectively.

The WIPP colloid model was developed for the CCA (U.S. DOE 1996, Appendix SOTERM, Section SOTERM.6.3) and repeated in the CRA-2004 (U.S. DOE 2004, Appendix PA, Section PA-4.3, Appendix SOTERM, Section SOTERM-6.0) and CRA-2009 (U.S. DOE 2009, Appendix SOTERM-2009, Sections SOTERM-4.7 and SOTERM-5.0). For CRA-2014, the

WIPP PA intrinsic colloid and microbial colloid enhancement parameter values were updated based on new information (U.S. DOE 2014, Appendix SOTERM-2014, Sections SOTERM-3.9.2 and SOTERM-4.6). For CRA-2019, there are changes to the values of the An(III) and An(IV) proportionality constants for humic substance colloids (GEOCHEM-5.5.3.6 and GEOCHEM-5.5.3.7) and to the implementation of the microbial colloids model (GEOCHEM-5.5.4.1).

Appendix SOTERM is the source of data for the colloid model in the CRA-2019 PA, with the exception of the humic colloids. GEOCHEM-5.1 and GEOCHEM-5.2 provide an overview of potentially important colloid types and of the primary factors that influence colloid stability. GEOCHEM-5.3 discusses the overall WIPP PA colloid model and the associated primary assumptions. GEOCHEM-5.4 presents an overview of the WIPP PA colloid model mathematical equations and parameters associated with each type of colloid as implemented for the CRA-2014. GEOCHEM-5.5 reviews the WIPP PA colloid model, and addresses CRA-2019 changes to proportionality constants for the humic colloid models and changes to the implementation of the microbial colloids model. A summary of major findings is presented in GEOCHEM-5.6.

GEOCHEM-5.1 Types of Colloids

Colloids are composed of minute particles of phases, ranging in size from approximately one nanometer (nm) to one micron, that are less stable than macroscopic particles of the same phase because of a combination of high surface free energy and small particle diameter. Though the particles are metastable, they may persist in systems because of kinetic inhibitions to achieve equilibrium, proximity to an unstable generating source of metastable colloids, or both. Solution pH and ionic strength (in particular, cation concentration) are the major influences that cause colloids to transition from “stable” (i.e., persisting in solution without changing in concentration or size) to “unstable” (i.e., aggregating and flocculating) such that the concentration in the aqueous phase decreases by orders of magnitude.

Groundwater colloids that can harbor actinides are found in a variety of forms. One form is intrinsic (or true) colloids. Intrinsic colloids are macromolecules of actinides in which the actinides are a structural part of the colloid atomic makeup. These colloids form in the nm range and may grow into larger particles. When immature they are hydrophilic, but as they grow they become hydrophobic, meaning that the stability of their suspension becomes dependent on the electrostatic interactions within the solution. When mature they can act as mineral fragment colloids, allowing for other dissolved constituents to attach to their surfaces.

Mineral fragment colloids, also known as pseudo-colloids, are hydrophobic hard-sphere particles whose suspensions are stabilized or destabilized by electrostatic forces between their surfaces and the solution. A variety of minerals/substances, either crystalline or amorphous, may form mineral fragment colloids; they are thermodynamically metastable versions of their larger or more crystalline counterpart minerals. Mineral fragment colloids provide sorptive substrates for transporting actinides and can incorporate actinides via coprecipitation mechanisms.

Colloids may also be organic. Humic substances colloids are hydrophilic molecules (up to 100,000 atomic mass units) stabilized in solution by solvation forces. These colloids provide complexation sites for actinides. Microbial colloids are comparatively large particles and are stabilized by hydrophilic coatings on their surfaces. Microbes provide sorptive substrates for

actinides and can also bioaccumulate actinides. Each of these types of colloids is included in the WIPP PA colloid model (GEOCHEM-5.4).

GEOCHEM-5.2 Colloid Stability

The solution composition (particularly the cation concentrations and the solution pH) is a key factor in the rate of colloid aggregation and the stability of colloids. At higher ionic strength and/or pH near the pH of net neutral charge for colloid particles (i.e., the isoelectric point, specific to the colloid, where the concentrations of positive and negative charges on the colloid surface are balanced), the rates of aggregation and flocculation tend to increase, reducing the stability of colloids. Considerations of whether colloids may be relevant to a system include identifying the colloid sources, determining whether these sources are local or distal, and evaluating the stability of the colloids given the aqueous chemical conditions and colloid surface properties.

Colloids have a high degree of stability when aggregation rates are low. This condition occurs when repulsive forces of electrostatic double layers are strong enough to prevent colloid particles from coming close enough to each other to bind together by attractive van der Waals forces. Because the chemistry of the water affects the charge and thickness of the double layer, it directly affects the magnitude of the energy barrier that inhibits close particle-particle encounters and hence aggregation. The energy barrier can be approximated by DLVO (Derjaguin and Landau 1941; Verwey and Overbeek 1948) theory by summing van der Waals forces and electric double layer forces as a function of inter-particle distance (Derjaguin and Landau 1941; Verwey and Overbeek 1948). Such calculations show that mineral fragment colloids have energy barriers to aggregation that are a function of pH and can decrease to zero at ionic strengths rising only into the tens of mM (millimole per liter) range (e.g., Hu et al. 2010; Abdel-Fattah et al. 2013). In the case of Pu(IV), its intrinsic colloids can readily aggregate with natural groundwater colloids to form highly mobile pseudocolloids (Abdel-Fattah et al. 2013). Data also indicate that the presence of humic acids can increase the stability of mineral fragment colloids by (1) increasing the electrostatic repulsion between particles and (2) presenting steric barriers to close encounters between mineral fragment colloid surfaces (Borgnino 2013).

Depending on the rates of generation and flocculation, colloids that are highly unstable may persist for extended periods of time. Proximal sources of colloids may have rates of production that maintain a state far from equilibrium. This can be the case for waste forms and engineered materials that are undergoing chemical transformations in a localized environment. Because colloid formation is a path-dependent process, evaluations of suspended colloid concentrations must consider the paths involved.

Traexler et al. (2004) and Zhao and Steward (1997) extensively reviewed colloid formation from nuclear waste forms and concluded that all waste forms may yield colloids as they degrade. The models developed for high level waste disposal at Yucca Mountain (Buck and Sassani 2007) focused on both the colloid-formation processes and colloid stability within the waste package and engineered barrier system environments. That work provides a detailed discussion of the chemical environment controls on colloid stability, and a rigorous quantitative model of colloid stability. That model is supported by observations for natural mineral colloids from a variety of systems, as discussed in GEOCHEM-5.5.1.3. Although certain colloids (i.e., waste form

colloids) considered for the Yucca Mountain PA are not relevant to the WIPP source term, the general discussion of colloid sources and the specific considerations of colloid stability are directly relevant.

GEOCHEM-5.3 Conceptual WIPP PA Colloid Model

Colloids are included in the WIPP PA because colloids can increase the mobility of actinides (e.g., Abdel-Fattah et al. 2013) and therefore can increase the potential quantity of actinides released to the accessible environment. The colloid model is implemented in the WIPP PA to guard against the possibility of underestimating the release of actinides to the biosphere.

There are four types of colloids in the WIPP colloid model: intrinsic, mineral fragments, humic substances, and microbes. Each of these colloid types is defined and described in GEOCHEM-5.1. In the conceptual model, inorganic colloids (intrinsic and mineral fragments) may form by nucleation when the aqueous phase becomes supersaturated with respect to the mineral phase or when mixed metal ions undergo hydrolysis reactions (Kim 1992). Intrinsic colloids form readily under a variety of groundwater conditions (e.g., Johnson and Toth 1978; Nitsche et al. 1992; Nitsche et al. 1994; Reed et al. 2013a). In addition to nucleation, natural mineral fragment particles may be released from the host rock due to changes in chemistry or physical disruption. Mineral fragment colloids may also be introduced by the corrosion of the waste materials and solid materials within the waste, by the degradation of cement, and by drilling mud. Potential sources of organic colloids (humic substances and microbes) include organic and soil-bearing wastes disposed in the repository as well as naturally-occurring organic colloids in the groundwaters of the Salado, Castile, and Culebra formations. Humic substances may additionally be generated by the degradation of insoluble organic wastes. It is assumed that natural microbial populations will increase due to the introduction of a variety of new materials. The WIPP PA model was developed to account for the presence, introduction, and generation of each of these potential colloid sources (U.S. DOE 1996, Appendix SOTERM, Section SOTERM-6.3).

Each colloid type in the conceptual colloid model has a different primary mechanism for incorporating actinides. Intrinsic colloids are largely composed of a single actinide and are not considered to appreciably sorb other actinides. Mineral fragment colloids incorporate actinides by sorption or surface co-precipitation. Humic substance colloids incorporate actinides by complexation with their carboxylic and hydroxyl functional groups. Microbes can incorporate actinides both externally and internally. Each of these mechanisms is conceptually considered in the quantitative constraints developed for the colloid model (GEOCHEM-5.4).

The conceptual WIPP colloid model is designed to be conservative and includes the following assumptions (U.S. DOE 1996, Appendix SOTERM, Section SOTERM-6.3):

- The mobile colloid concentrations are assumed fixed (U.S. DOE 1996, Appendix SOTERM, pg. 70).
- Colloids remain in the mobile phase.
- Colloidal actinides that are not suspended in the aqueous phase (that is, not mobile) are not included in the colloidal actinide source term (U.S. DOE 1996, Appendix SOTERM, pg. 41).

- Each actinide fills the entire site capacity of mineral fragment colloids (i.e., the concentration of each actinide associated with mineral fragment colloids is equivalent to the site capacity of the colloid), provided sufficient actinide inventory.
- There is no competition among different actinides for sorption or complexation sites on colloids.

GEOCHEM-5.4 WIPP PA Colloid Model

In the WIPP PA, the actinide source term contains both dissolved actinides constrained by solubility limits of actinide phases (i.e., non-colloidal aqueous actinide) and actinides that are associated with colloids. The concentration limit of each actinide associated with each colloid type is determined individually and added to the dissolved (non-colloidal) actinide concentration limit to compute the total mobilized concentration limit of each actinide. For inorganic colloids, an absolute concentration limit of the colloidally-bound actinide is added to the dissolved source term. For organic colloids, proportionality constants and upper limits on capacity are used.

Table GEOCHEM-60 lists and summarizes the WIPP colloid model parameters. These parameters are described mathematically in GEOCHEM-5.4.1 through GEOCHEM-5.4.4, where the model equations for each colloid type are summarized.

Based on these parameters, the mobile actinide concentration limits in Castile and Salado brines are calculated as in Equation (GEOCHEM.38) and Equation (GEOCHEM.39) below, provided (1) sufficient actinide inventory and (2) maximum concentration limit caps for microbial and humic colloids, as defined using CAPHUM and CAPMIC, are not invoked (U.S. DOE 1996, Appendix SOTERM, Section SOTERM-6.2):

$$MobileAnCastile = DissolvedAnCastile * (1 + \text{PROPMIC} + \text{PHUMCIM}) + \text{CONCINT} + \text{CONCMIN} \quad \text{(GEOCHEM.38)}$$

$$MobileAnSalado = DissolvedAnSalado * (1 + \text{PROPMIC} + \text{PHUMSIM}) + \text{CONCINT} + \text{CONCMIN} \quad \text{(GEOCHEM.39)}$$

The parameters $DissolvedAnSalado$ and $DissolvedAnCastile$ are typically represented in this appendix as [An]. When the calculated humic-colloid-associated actinide concentrations exceed CAPHUM, the humic contributions are limited to CAPHUM. In previous PA calculations, when total mobile concentrations exceed CAPMIC, the microbial colloid contributions were limited by a toxicity relationship (U.S. DOE 2014, Appendix SOTERM, Equations SOTERM.78 and SOTERM.79). In CRA-2019, the toxicity relationship is removed (U.S. DOE 2019, Appendix SOTERM, Section SOTERM-4.3.4). Details of the CRA-2019 colloid models are discussed in the subsections below.

The WIPP PA colloid model and parameter values are re-examined in GEOCHEM-5.5. The CRA-2014 values of these parameters are shown in Table GEOCHEM-61.

Table GEOCHEM-60. WIPP Colloid Model Parameter Summary and Description (U.S. DOE 2014, Appendix SOTERM, Table SOTERM-20)

Material	Property	Brief Description of Parameter
Th, U, Np, Pu, Am	CONCMIN	Concentration of actinide associated with mobile mineral fragment colloids
Th, U, Np, Pu, Am	CONCINT	Concentration of actinide associated with mobile intrinsic actinide colloids
Th, U, Np, Pu, Am	PROPMIC	Proportionality constant for concentration of actinides associated with mobile microbes
PHUMOX3 [a] PHUMOX4 PHUMOX5 PHUMOX6	PHUMCIM	Proportionality constant for concentration of actinides associated with mobile humic colloids; in Castile brine; actinide solubilities include organics (complexes with man-made organic ligands); solubilities were calculated assuming equilibrium with Mg-bearing minerals (brucite and hydromagnesite)
PHUMOX3 [a] PHUMOX4 PHUMOX5 PHUMOX6	PHUMSIM	Proportionality constant for concentration of actinides associated with mobile humic colloids; in Salado brine; actinide solubilities include organics (complexes with man-made organic ligands); solubilities were calculated assuming equilibrium with Mg-bearing minerals (brucite and hydromagnesite)
Th, U, Np, Pu, Am	CAPMIC	Maximum (cap) concentration of actinide associated with mobile microbes
Th, U, Np, Pu, Am	CAPHUM	Maximum (cap) concentration of actinide associated with mobile humic colloids

a Proportionality constant for actinide concentrations associated with mobile humic substances for PHUMOX3, for actinide elements with oxidation state *III* (that is, Pu(III) and Am(III)); PHUMOX4, oxidation state IV (Th(IV), U(IV), Np(IV), and Pu(IV)); PHUMOX5, oxidation state V (Np(V)); and PHUMOX6, oxidation state VI (U(VI)).

Table GEOCHEM-61. WIPP Colloid Parameter Values Used in CRA-2014 (U.S. DOE 2014, Appendix SOTERM, Table SOTERM-21) and CRA-2019 (Reed et al. 2019; Mariner 2019)

Recommended Oxidation State Specific Colloid Parameters for CRA-2014							
Actinide	**CONCMIN[a]**	**CONCINT[a]**	**PROPMIC[b]**	**CAPMIC**	**PHUMSIM[b]**	**PHUMCIM[b]**	**CAPHUM[a]**
Th(IV)	2.6×10^{-8}	2×10^{-8}	1.76	2.3×10^{-6}	6.3	6.3	1.1×10^{-5}
U(IV)	2.6×10^{-8}	2×10^{-8}	1.76	2.3×10^{-6}	6.3	6.3	1.1×10^{-5}
U(VI)	2.6×10^{-8}	3×10^{-8}	1.76	2.3×10^{-6}	0.12	0.51	1.1×10^{-5}
Np(IV)	2.6×10^{-8}	2×10^{-8}	1.76	2.3×10^{-6}	6.3	6.3	1.1×10^{-5}
Np(V)	2.6×10^{-8}	ND	1.76	2.3×10^{-6}	9.1×10^{-4}	7.4×10^{-3}	1.1×10^{-5}
Pu(III)	2.6×10^{-8}	2×10^{-8}	1.76	2.3×10^{-6}	0.19	1.37[c]	1.1×10^{-5}
Pu(IV)	2.6×10^{-8}	2×10^{-8}	1.76	2.3×10^{-6}	6.3	6.3	1.1×10^{-5}
Am(III)	2.6×10^{-8}	4×10^{-9}	0.32	3.1×10^{-8}	0.19	1.37[c]	1.1×10^{-5}
Recommended Oxidation State Specific Colloid Parameters for CRA-2019							
Actinide	**CONCMIN[a]**	**CONCINT[a]**	**PROPMIC[b]**	**CAPMIC**	**PHUMSIM[b]**	**PHUMCIM[b]**	**CAPHUM[a]**
Th(IV)	2.6×10^{-8}	4.3×10^{-8}	0.21	3.8×10^{-8}	0.01	0.01	1.1×10^{-5}
U(IV)	2.6×10^{-8}	4.3×10^{-8}	0.21	3.8×10^{-8}	0.01	0.01	1.1×10^{-5}
U(VI)	2.6×10^{-8}	1.4×10^{-6}	ND[d]	3.8×10^{-8}	0.12	0.51	1.1×10^{-5}
Np(IV)	2.6×10^{-8}	4.3×10^{-8}	0.21	3.8×10^{-8}	0.01	0.01	1.1×10^{-5}
Np(V)	2.6×10^{-8}	ND[d]	ND[d]	3.8×10^{-8}	9.1×10^{-4}	7.4×10^{-3}	1.1×10^{-5}
Pu(III)	2.6×10^{-8}	9.5×10^{-9}	0.03	3.8×10^{-8}	0.2	0.2	1.1×10^{-5}
Pu(IV)	2.6×10^{-8}	4.3×10^{-8}	0.21	3.8×10^{-8}	0.01	0.01	1.1×10^{-5}
Am(III)	2.6×10^{-8}	9.5×10^{-9}	0.03	2.3×10^{-9}	0.2	0.2	1.1×10^{-5}

[a] In units of moles colloidal actinide per liter
[b] In units of moles colloidal actinide per mole dissolved actinide
[c] Median value
[d] In PA calculations, for values listed as ND, the value of the lower oxidation-state of the same element were used.

GEOCHEM-5.4.1 Mineral Fragment Colloids Model

The mineral fragment colloid model considers the maximum concentration of actinides that may be mobilized by this type of colloid. The concentration of mineral fragment colloids is limited by the high ionic strength expected in the waters that may contact the waste (GEOCHEM-5.2). The concentration of actinides adsorbed to these colloids is further limited by the specific surface area and sorption site density of the colloids.

For the CCA, experiments were performed to measure the stability of mineral fragment colloids in WIPP brines. The colloids tested included bentonite, kaolinite, montmorillonite, vermiculite, illite, anhydrite, calcium carbonate, magnesite, hematite, limonite, goethite, magnetite, quartz, siderite, brucite, strontianite, diatomaceous earth, pyrite, and cellulosic materials (U.S. DOE 1996, Appendix SOTERM, Section SOTERM-6.3.1). The brines included simulants of Salado groundwater, “Culebra brine,” and a NaCl-$CaCl_2$ solution. These brines were diluted sequentially to produce a set of solutions covering a broad range of salinity (Papenguth and Behl 1996).

Stable mineral fragment colloid concentrations observed in solutions were converted to actinide concentrations by considering the surface area and sorption site density of the colloids. Assuming spherical particles, the associated (adsorbed) actinide concentrations, CONCMIN, were conservatively determined using the following relationship:

$$\text{CONCMIN} = \frac{\pi D^2 N_s N_P}{N_A} f_a f_c \qquad \text{(GEOCHEM.40)}$$

where D is the particle diameter (nm), N_s is the adsorption site density (sites nm^{-2}), N_P is the number of particles per liter of solution determined in the laboratory experiments, N_A is the Avogadro constant, and f_a and f_c are factors used to conservatively account for additional mineral fragment colloids from the Culebra that might sorb actinides and for uncertainty, respectively. The final values determined for CONCMIN shown in Equation GEOCHEM.40 assume 1 site nm^{-2} for N_s for each actinide, a particle concentration N_P equivalent to the observed geometric mean value for hematite, goethite, and bentonite measured after 12.8 to 12.9 days in factor-of-10 diluted brine, a value of 2 for f_a to account for natural colloids potentially existing in the Culebra, and a value of 10 for f_c to account for uncertainty, mainly due to uncertainty in N_s (U.S. DOE 1996, Appendix SOTERM, Section SOTERM-6.3.1). This calculation, its assumptions, and recent data regarding the stability of mineral fragment colloids under WIPP conditions are examined in GEOCHEM-5.5.1.

GEOCHEM-5.4.2 Intrinsic Colloids Model

The intrinsic colloid model is based on intrinsic colloid solubility. Because the solubility of intrinsic colloids is generally low and depends on the oxidation state of the actinide, intrinsic colloids are assumed in the WIPP PA to be present at concentrations equal to their solubility. Accordingly, a single parameter is used in the model to represent the intrinsic colloid contribution to total mobile actinide concentrations: CONCINT, the molar concentration of the actinide associated with intrinsic colloids at its solubility limit at the specified oxidation state. This parameter is simply added to the other forms of mobile actinides to calculate total mobile actinide concentrations as shown in Equation GEOCHEM.38 and Equation GEOCHEM.39.

During the development of the WIPP colloid model, a review of the literature and experimental studies conducted at Lawrence Livermore National Laboratory indicated that Pu(IV) was the only actinide and oxidation state in the WIPP waste PAIR inventory that could potentially form a significant concentration of intrinsic colloids under the alkaline conditions expected in the repository (U.S. DOE 1996, Appendix SOTERM, Section SOTERM-6.3.2). The experimental data produced a highly correlated linear inverse relationship between the log of the intrinsic colloid concentration and pcH (negative log of the concentration of hydrogen ion) over a range of pcH from 3 to 8.5 (U.S. DOE 1996, Appendix SOTERM, Figure SOTERM-8). These data are shown in Figure GEOCHEM-7. Extrapolation of this relationship indicates that Pu(IV) intrinsic colloid solubility is less than 3×10^{-10} M at the expected repository pcH of 9.3 (and much lower for the measurements in 5 M NaCl). Because the minimum analytical detection limit was 1×10^{-9} M, and this value is conservative relative to the extrapolated value, this limit was chosen as the Pu(IV) CONCINT value for the CCA.

The value of CONCINT was set to zero in the CCA for all other actinides and oxidation states because of the absence of conclusive evidence of intrinsic colloids. In the CRA-2009, the CONCINT for Pu(III) was set to 1×10^{-9} M, removing the effects of oxidation state for Pu. Since then, experimental studies at LANL provided new data on intrinsic colloid solubility under WIPP conditions (Reed et al. 2013a). These data, discussed in GEOCHEM-5.5.2, led to the specification of CONCINT values for nearly all actinide species for the CRA-2014 PA, as shown in Table GEOCHEM-61.

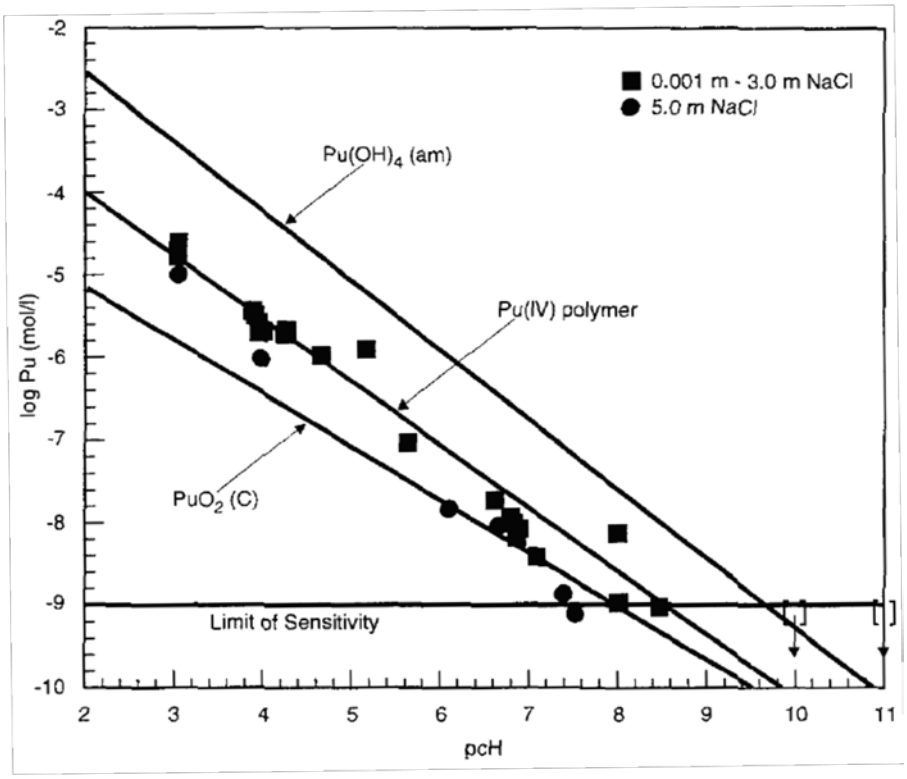

Figure GEOCHEM-7. Solubility of Pu(IV)-Polymer in NaCl Media as a Function of pcH (U.S. DOE 1996, Figure SOTERM-8).

GEOCHEM-5.4.3 Humic Substance Colloids Model

Two approaches were used in the CCA to develop the model and parameters for the humic substance colloids. For actinides at the IV oxidation state (i.e., Th(IV), U(IV), Np(IV), and Pu(IV)), a single value of 6.3 was calculated for the PHUMSIM and PHUMCIM proportionality constants (Table GEOCHEM-61). This calculation was based on the colloidal partitioning of Th(IV) in seawater reported in Baskaran et al. (1992), and assumes that the humic substance concentration in seawater is 2.0 mg L^{-1} (U.S. DOE 1996, Appendix SOTERM, Section SOTERM-6.3.3.1). For all other actinide oxidation states, a process model was developed based on binary complexation data involving isolated humic substances. This latter approach produced an analytical model that includes actinide-humic complexation reactions and the competition for complexation sites by dissolved calcium (Ca^{2+}) and magnesium (Mg^{2+}).

The complexation of a dissolved actinide species (An^{m+}) with an available humic substance complexation site (Hs^{-}) is described by the chemical reaction

$$An^{m+} + Hs^{-} \Leftrightarrow AnHs \qquad \text{(GEOCHEM.41)}$$

where $AnHs_m$ is the actinide-humic substance complex. This treatment of the reaction does not conserve charge and assumes homogeneous complexation sites with no acido-basic properties; however, this approach is acceptable when stability constants for humic complexation reactions are conditional (Reiller et al. 2008). The stability constant ($\beta_{m:An}$) for this reaction is represented by

$$\beta_{m:An} = \frac{[AnHs]}{[An^{m+}][Hs^{-}]} \qquad \text{(GEOCHEM.42)}$$

where brackets denote equilibrium concentration of the species. For the CCA, humic complexation stability constants were determined for each actinide having oxidation states of III, V, and VI. Constants for the III and VI oxidation states were derived from laboratory experiments conducted at Florida State University as described below. For the V oxidation state, a stability constant of $10^{3.67}$ reported for Np(V) and Gorleben humic acid in a pH 9 solution was used (Kim and Sekine 1991).

Ca^{2+} and Mg^{2+} are abundant in the WIPP brines. The high concentrations of these cations and their affinity for humic complexation sites act to reduce the humic-bound concentrations of actinides. The WIPP colloid model for actinides at the III, V, and VI oxidation states accounts for this effect by including terms for humic-bound calcium and magnesium in the calculation of $[Hs^{-}]$. The model also assumes that (1) the concentration of An^{m+} is equal to the total dissolved non-colloidal concentration of An, (2) the combined concentration of Ca^{2+} and Mg^{2+} is equal to the combined total dissolved concentration of Ca and Mg, and (3) only 1:1 binding of An^{m+} and Hs^{-} occurs. These assumptions result in the following equation used in the CCA for the concentration of Hs^{-} (U.S. DOE 1996, Equation 6-20):

$$[Hs^{-}] = \frac{[Hs_{tot}]}{\beta_{1:An}[An] + \beta_{1:CaMg}[Ca + Mg] + 1} \qquad \text{(GEOCHEM.43)}$$

$\beta_{1:CaMg}$ is the combined stability constant for the humic complexation of Ca^{2+} and Mg^{2+}, $[Ca + Mg]$ is the sum of the dissolved Ca and Mg concentrations, $[Hs_{tot}]$ is the total concentration of humic complexation sites, and [An] is the total dissolved non-colloidal concentration of actinide. In the CCA, the log value for $\beta_{1:CaMg}$ was set to 2.0 based on literature values from experiments investigating complexation of Ca^{2+} and $Mg^{2+}$with humic and fulvic acids under acidic conditions in low-ionic-strength solutions (U.S. DOE 1996, Appendix SOTERM, Section SOTERM.6.3.3.1). The values for $[Ca + Mg]$ were taken from representative Salado and Castile brine compositions, 0.542 M and 0.0576 M, respectively (Papenguth 1996, Tables 1a and 1b); it is this term that explains the model dependence on the brine type.

The values used for $\beta_{1:An}$ and $[Hs_{tot}]$ in Equation GEOCHEM.43 were determined from experiments using Lake Bradford humic acid (HAal-LBr), Gorleben humic acid (HAal-Gor), and Suwannee River fulvic acid (FA-Suw). These experiments involved Am(III) and U(VI) in NaCl solutions of 3 and 6 molal. The pH values of these experiments were fixed in the acidic range at either 4.8 or 6 (these experiments were completed prior to the DOE establishing that MgO buffer would be emplaced and would fix the pcH at about 9.3 [U.S. DOE 1996, Appendix SOTERM, Section SOTERM-6.3.3.1]). Data from the 6 molal NaCl solutions at pH 6 were used in the derivation of the PHUMSIM and PHUMCIM proportionality constants. The site binding capacities of these humic substances were determined to be 4.65, 5.38, and 5.56 milliequivalent (meq) g^{-1}, respectively. The concentration of humic substances in the Salado and Castile brines was set at the upper value (2.0 mg L^{-1}) of the solubility range observed in systems containing Ca^{2+} and Mg^{2+} at concentrations of at least 10 mM (U.S. DOE 1996, Appendix SOTERM, Section SOTERM-6.3.3.1). Multiplying this value by the site binding capacities gives the following values for $[Hs_{tot}]$: 9.3×10^{-6} M (HAal-LBr), 1.1×10^{-5} M (HAal-Gor), and 1.1×10^{-5} M (FA-Suw).

Table GEOCHEM-62 shows the values of $\beta_{1:An}$ and [An] used in the derivation of the PHUMSIM and PHUMCIM values (Mariner and Sassani 2014, Table 4-3). The concentration of [AnHs] in Table GEOCHEM-62 is calculated by solving Equation (GEOCHEM.43) for $[Hs^{-}]$, substituting the result into Equation (GEOCHEM.44), and solving for [AnHs]. This gives the following expression for [AnHs]:

$$[\mathrm{AnHs}] = \frac{\beta_{1:\mathrm{An}}[\mathrm{An}][\mathrm{Hs_{tot}}]}{\beta_{1:\mathrm{An}}[\mathrm{An}] + \beta_{1:\mathrm{CaMg}}[\mathrm{Ca} + \mathrm{Mg}] + 1} \qquad \text{(GEOCHEM. 44)}$$

This expression, which conservatively assumes a 1:1 binding between An^{m+} and Hs^{-} and assumes that there is no competition between different actinides for binding sites, is used to calculate the [AnHs] values shown in Table GEOCHEM-63. The values in this table for [An] are those assumed in the CCA for the brines in the Salado and Castile in the presence of MgO (Papenguth 1996, Tables 1a and 1b).

The PHUMSIM and PHUMCIM values in Table GEOCHEM-61 for actinides at the III, V, and VI oxidation states were obtained by selecting the highest (most conservative) values of [AnHs]/[An] in Table GEOCHEM-62. Only the III oxidation state in the Castile brine was defined as a distribution. Based on the three values in Table GEOCHEM-62 (0.065, 1.6, and 1.6), this distribution was defined with a minimum of 0.065, a mean of 1.1, a median of 1.37, and a maximum of 1.6 (Tierney 1996). It is a piecewise uniform distribution such that a random value between 0.065 and 1.37 is as equally likely as a random value between 1.37 and 1.6.

To ensure that calculations of humic-bound actinide concentrations in Equation GEOCHEM.44 were not excessive, a maximum concentration parameter called CAPHUM was defined in the CCA to set the upper limit. The value of this parameter was set at 1.1×10^{-5} M, which is the maximum $[Hs_{tot}]$ value used in the calculations in Table GEOCHEM-62. This is a conservative value because it assumes a 1:1 binding between An^{m+} and Hs^{-} and assumes that there is no competition between different actinides for binding sites. It also assumes a stable humic substance concentration of 2.0 mg L^{-1}. When a calculation using PHUMSIM or PHUMCIM and

the dissolved actinide concentration exceeds CAPHUM, the WIPP PA sets the humic-bound actinide concentration at CAPHUM.

The values of the PHUMSIM, PHUMCIM, and CAPHUM used in the WIPP PA were reexamined, as discussed in GEOCHEM-5.5.3. As a result of this reexamination, the values of PHUMSIM and PHUMCIM for An(III) and An(IV) are updated for CRA-2019 and shown in Table GEOCHEM-61.

Table GEOCHEM-62. Calculated Values of Humic-Bound Actinide Concentrations [AnHs] and Proportionality Constants (i.e., PHUMSIM and PHUMCIM) for U(VI), Np(V), and Am(III) for the CCA. Inputs from Papenguth (1996, Tables 1a, 1b, and 3)

Formation	Actinide	[An] (M)	Humic Substance	$[Hs_{tot}]$ (M)	log $\beta_{1:An}$	[AnHs] (M)	[AnHs] /[An]
Salado (PHUMSIM)	U(VI)	1.00×10^{-5}	HAal-LBr	9.3×10^{-6}	5.91	1.2×10^{-6}	0.12
			HAal-Gor	1.1×10^{-5}	5.35	4.2×10^{-7}	0.042
			FA-Suw	1.1×10^{-5}	4.60	8.0×10^{-8}	0.0080
	Np(V)	2.64×10^{-6}	HAal-Gor	1.1×10^{-5}	3.67	2.4×10^{-9}	9.1×10^{-4}
	Am(III)	4.39×10^{-6}	HAal-LBr	9.3×10^{-6}	6.09	8.3×10^{-7}	0.19
			HAal-Gor	1.1×10^{-5}	6.02	8.3×10^{-7}	0.19
			FA-Suw	1.1×10^{-5}	4.60	3.5×10^{-8}	0.0080
Castile (PHUMCIM)	U(VI)	1.00×10^{-5}	HAal-LBr	9.3×10^{-6}	5.91	5.1×10^{-6}	0.51
			HAal-Gor	1.1×10^{-5}	5.35	2.7×10^{-6}	0.27
			FA-Suw	1.1×10^{-5}	4.60	6.2×10^{-7}	0.062
	Np(V)	2.53×10^{-6}	HAal-Gor	1.1×10^{-5}	3.67	1.9×10^{-8}	7.4×10^{-3}
	Am(III)	4.12×10^{-7}	HAal-LBr	9.3×10^{-6}	6.09	6.5×10^{-7}	1.6
			HAal-Gor	1.1×10^{-5}	6.02	6.5×10^{-7}	1.6
			FA-Suw	1.1×10^{-5}	4.60	2.7×10^{-8}	0.065

GEOCHEM-5.4.4 Microbial Colloids Model

Like the humic substance colloid model, the microbe colloid model for the WIPP PA uses a proportionality constant (PROPMIC) when the microbe colloid concentration is not limited to a maximum concentration. PROPMIC differs from the humic proportionality constant in that it depends on the element and not the oxidation state (Reed et al. 2019; Appendix SOTERM, Section SOTERM-3.5.2).

In previous PA calculations (e.g., CRA-2009 and earlier), the microbial colloid actinide concentrations were limited by toxicity when the total mobile concentrations exceeded CAPMIC (U.S. DOE 2014, Appendix SOTERM, Equations SOTERM.78 and SOTERM.79). In CRA-2014, the CAPMIC values were determined based on biomass rather than toxicity (Reed et al. 2013a), but this was not fully implemented in PA until CRA-2019. For CRA-2019, the microbial colloid model behaves like the humic colloid model. When the microbial colloid actinide concentration calculated using PROPMIC exceeds CAPMIC, the concentration is set to CAPMIC. The PROPMIC and CAPMIC parameters are discussed further in CRA-2019 Appendix SOTERM, Reed et al. (2019) and Sarathi (2019).

For the CCA, filtration experiments were conducted at Brookhaven National Laboratory and LANL to measure mobile indigenous microbial concentrations (U.S. DOE 1996, Appendix SOTERM, Section SOTERM-6.3.4.1). These experiments combined ^{232}Th, ^{238}U, ^{237}Np, ^{239}Pu, or ^{243}Am at various concentrations (with and without organic complexants such as EDTA) with two different microbe cultures that tolerate high salinity. A culture called WIPP-1A is fast-growing and was used for most of the experiments. This culture was isolated from saline surficial sediments at the WIPP site and prepared in a medium containing 200 g L^{-1} NaCl (Gillow et al. 1998). The other culture, called BAB, required at least three weeks to reach stationary phase growth.

The concentrations of colloids were determined by measuring the mobile cells that remained suspended after 11 to 15 days in the WIPP-1A mixed culture, and after as many as 21 days in the BAB mixed culture. A filtration sequence of 10 µm, 0.4 µm, and 0.03 µm was used to determine the dissolved actinide and microbial actinide concentrations. PROPMIC was set by the ratio of microbial actinide to dissolved actinide.

For the CRA-2014 PA and CRA-2019, a biomass approach was used to determine the values of PROPMIC and CAPMIC, and these values are shown in Table GEOCHEM-61. Section GEOCHEM-5.5.4 examines the effects of removing the toxicity functionality from the microbial colloid model.

GEOCHEM-5.5 New WIPP Colloid Model Parameter Analyses

The WIPP colloid models and their assumptions have been reexamined over the past several years, and recent experiments have provided new relevant information. This section presents important findings for each colloid type: mineral fragment colloids (GEOCHEM-5.5.1), intrinsic colloids (GEOCHEM-5.5.2), humic substance colloids (GEOCHEM-5.5.3), and microbial colloids (GEOCHEM-5.5.4). For CRA-2019, changes are summarized for parameter values of the humic substance colloids, intrinsic colloids, and to the implementation of the microbial colloid model.

GEOCHEM-5.5.1 Mineral Fragment Colloids

Since the CCA, new laboratory studies relevant to mineral fragment colloids have spurred reanalysis of possible concentrations of mineral fragment colloids in brines. Section GEOCHEM-5.5.1 and its subsections revisit the relevance of this and other studies to the WIPP PA representation of mineral fragment colloids. But first, interactions with the EPA regarding mineral fragment colloids are briefly reviewed.

In a letter to the DOE dated February 22, 2010, the EPA made the following comment with respect to intrinsic and mineral fragment colloids (Kelly 2010, Comment 4-C-36):

> DOE should address whether significant thorium intrinsic colloids and pseudocolloids could form in the WIPP repository. Unless the formation of such colloids can be ruled out by the available data, DOE should address the possible effects of such colloid formation on repository performance.

In the presence of ERDA-6 brine, no Mg-Cl-OH mineral phase is predicted to be thermodynamically stable, and no Mg-Cl-OH mineral phase is observed to precipitate in laboratory experiments (Xiong and Lord 2008). Thus, no Mg-Cl-OH colloids are expected to be thermodynamically stable in scenarios involving ERDA-6 brine, which is consistent with the absence of mineral colloids in the ERDA-6 experiments with MgO (Xiong et al. 2017). There remains a possibility that the Mg-Cl-OH colloids mentioned above may be metastable at low concentrations.

The subsections on mineral-fragment colloids below address the following topics:

- CRA-2014 PA representation of mineral fragment colloids (GEOCHEM-5.5.1.1)
- Literature review of relevant studies (GEOCHEM-5.5.1.2)
- Mineral fragment concentrations observed in nature (GEOCHEM-5.5.1.3)
- Effects of corrosion on mineral fragment concentrations (GEOCHEM-5.5.1.4)
- Conservative assumptions in the WIPP PA model (GEOCHEM-5.5.1.5), and
- Summary and recommendations for CRA-2019 (GEOCHEM-5.5.1.6).

GEOCHEM-5.5.1.1 CRA-2014 PA Representation of Mineral Fragment Colloids

The WIPP PA mineral fragment colloids model considers various mineral phases, including clays, sulfates, carbonates, and iron oxides. Experiments were conducted for the CCA to characterize concentrations of actinides associated with these mineral phases in simulated 10-fold-diluted WIPP brines (GEOCHEM-5.4.1). Averages of the concentrations of hematite, goethite, and bentonite colloids measured in those experiments led to the ultimate CONCMIN parameter value constraining the concentrations of each actinide bound to mineral fragment colloids to 2.6×10^{-8} M. As explained in GEOCHEM-5.4.1, a number of assumptions, many of them conservative, were used to establish this value for CONCMIN. These assumptions are evaluated in GEOCHEM-5.5.1.5.

GEOCHEM-5.5.1.2 Literature Review for Mineral Fragment Colloids

At LANL, solubility experiments were conducted for Nd(III), Th(IV), and U(VI) using GWB and ERDA-6 brines at pcH values between 7 and 12 and varying concentrations of carbonate and organic complexants (Borkowski et al. 2012; Reed et al. 2013a). Based on negligible differences in concentrations of actinides observed in unfiltered samples and samples that filtered out colloids of size 10 nm and greater, Reed et al. (2013a), concluded that mineral fragment colloids appear to be an insignificant component of mobile actinide concentrations in WIPP brines.

In iron corrosion experiments in WIPP brines, significant concentrations of Pu were associated with mineral fragment colloids (Reed et al. 2010, Section 4.3; Reed et al. 2013a, Section 4.2.3). In these experiments, which lasted nearly 6 years, iron coupons were placed in WIPP brine containing ~5×10^{-5} M Pu(VI). As the iron oxidized, the aqueous Pu(VI) reduced to Pu(IV) mineral phases Reed et al. 2010, Figure 4-13) and predominantly to Pu(III) aqueous species (Reed et al. 2013a, Table 4-3). Samples of the solution were filtered sequentially using 0.45 µm, 0.22 µm, 20 nm, 10 nm, 5 nm, and 2.5 nm filters. Intrinsic colloids were defined to be those in

the range of 2.5 to 10 nm, and mineral fragment colloids were defined to be those in the range of 10 nm to 0.45 µm. Based on this distinction, Pu concentrations associated with mineral fragment colloids in the samples identified to be most repository-relevant (i.e., the three ERDA-6 samples with pcH values in the range of 9.1 to 9.6) ranged from 8.6×10^{-9} to 2.3×10^{-8} M (Reed et al. 2013a, Table 4-4).

Prediction of mineral fragment colloid stability has been advanced by Abdel-Fattah et al. (2013). The Hamaker constant is needed to calculate van der Waals interactions between colloids, including natural groundwater colloids, and between colloids and surfaces of the porous medium. Abdel-Fattah et al. (2013) used this constant to develop response surfaces as a function of pH and ionic strength to show where energy barriers to aggregation are high between colloids of the same type, between colloids of different type, and between colloids and stationary surfaces. The results indicate that, at high ionic strength and high pH, the energy barrier for the aggregation of smectite colloids, Pu intrinsic colloids, and smectite colloids with Pu intrinsic colloids is very low. Bentonite, an impure clay consisting mostly of montmorillonite (a smectite), was found to provide stable colloids after 12.8 to 12.9 days in factor-of-10 diluted WIPP brines (GEOCHEM-5.4.1). Energy barriers involving other types of colloids were not analyzed in the Abdel-Fattah et al. (2013) study.

GEOCHEM-5.5.1.3 Analysis of Concentrations of Mineral Fragment Colloids Observed in Nature

Although Mg-Cl-OH mineral fragment colloids are not expected to occur in significant concentrations in WIPP PA release scenarios, other types of mineral fragment colloids have shown potential for significant stability in WIPP brines. Laboratory studies conducted for the CCA indicate that hematite, goethite, and bentonite showed some stability in 10-fold diluted WIPP brines (GEOCHEM-5.4.1). In addition to potential natural groundwater colloids, colloids in the WIPP repository may be generated by microbial activity and corrosion of waste forms and waste materials. Microbial degradation of organic materials can generate humic substance colloids, and corrosion of solids such as steel can generate iron oxide colloids.

Concentrations of mineral fragment colloids in natural groundwaters and simple salt solutions are observed to vary by orders of magnitude. Figure GEOCHEM-8 presents a plot prepared by Serco that shows a compilation of colloid concentrations measured in natural systems and simple salt solutions as a function of ionic strength (Alexander et al. 2011, Figure 5.1). Hatched red, blue, and gray regions indicate ranges observed at Grimsel, Ruprechtov, and Äspö, yellow triangles represent measurements largely from granitic groundwaters, and circles and diamonds represent colloids in simple salt solutions.

Consistent with Derjaguin, Landau, Verwey, and Overbeek (DLVO) theory (GEOCHEM-5.2), measurements of high colloid concentrations in the Serco plot are noticeably absent at high ionic strength (>0.2 M). Much of the scatter in the plot at lower ionic strength is attributed to different solution compositions, pH values, and sampling procedures. Some of the scatter at lower ionic strength may also be the result of the association of mineral fragment colloids with other types of colloids that can act to stabilize mineral fragment colloids in solution (Abdel-Fattah et al. 2013; Borgnino 2013).

The range of concentrations of mineral fragment colloids simulated in the WIPP PA is approximately 40 to 400 μg L^{-1}, as explained below. Because the ionic strength of WIPP brine is near of 6,000 mmol L^{-1}, this range of colloid concentrations would plot to the right of the Serco data, as indicated in Figure GEOCHEM-8. This range was calculated assuming the following:

- Each of the five actinide elements (Th, U, Np, Pu, and Am) sorb at a site density (N_s) of 10 nm^{-2}.
- The colloids are spherical and have a representative diameter (D) of between 10 and 100 nm.
- The colloid solid density is 3 g mL^{-1}.

The first assumption is consistent with assumptions used in the original calculation of CONCMIN; specifically, the site density for each actinide is equivalent to the originally assumed 1 nm^{-2} site density multiplied by the uncertainty factor of 10 included in the CONCMIN calculation. Because the mineral fragment colloid model assumes that all surface sites are occupied by the five actinide elements (except when the system is limited by the actinide PAIR inventory), the total concentration of actinides associated with mineral fragment colloids in the WIPP PA model is five times CONCMIN. The second and third assumptions are used to estimate a colloid concentration (C_c) in units of mass colloids per volume of water (e.g., μg L^{-1}). The calculation is made using the following equation:

$$C_c = \frac{5\ \text{CONCMIN}\ N_A\ \rho_c D}{6\ N_s} \qquad \text{(GEOCHEM.45)}$$

where 5 CONCMIN is the total concentration of the five actinides associated with mineral fragment colloids (1.3×10^{-7} M), ρ_c is the colloid solid density (3 g mL^{-1}), and $D/6$ is the ratio of the colloid particle volume to its surface area. Varying the colloid diameter between 10 and 100 nm gives the calculated 40 to 400 μg L^{-1} concentrations effectively used in the WIPP PA.

This effective concentration range for mineral fragment colloids appears to be highly conservative for high-ionic-strength brines. The lower end of the range (40 μg L^{-1}) is ~2,000 times higher than any of the data in the Serco plot for ionic strength greater than 0.2 M, and ~4,000 times higher than the 0.01 μg L^{-1} colloid concentration used for the Yucca Mountain PA (Buck and Sassani 2007). The only mineral fragment colloid measurements that approach this range for undiluted WIPP brines are those observed to be generated in iron corrosion experiments where soluble Pu(VI) is reduced to insoluble Pu(IV) (GEOCHEM-5.5.1.4).

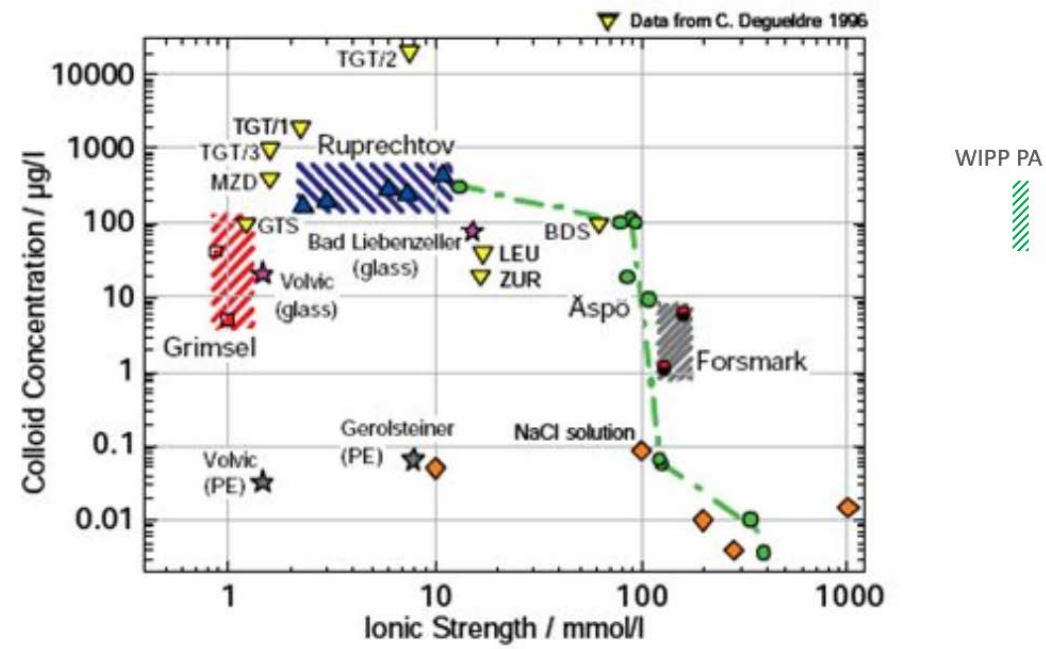

Figure GEOCHEM-8. Colloid Concentrations From Natural Systems and Simple Salt Solutions as Function of Ionic Strength as Compiled by Serco (Alexander et al. 2011, Figure 5.1, Blue Hatch - Ruprechtov; Red Hatch - Grimsel CRR tunnel; Grey Hatch - Äspö tunnel). Approximate Relative Location of Range Assumed in the WIPP PA for Mineral Fragment Colloids is Indicated to the Right of the Figure (Green Hatch).

GEOCHEM-5.5.1.4 Analysis of Effect of Corrosion on Mineral Fragment Colloid Concentrations

The Pu concentrations observed in the 10 nm to 0.45 µm fraction of the long-term Pu-iron interaction experiments (8.6×10^{-9} to 2.3×10^{-8} M) are nearly as high as the 2.6×10^{-8} M value set for CONCMIN (Reed et al. 2013a, Section 4.2.3; Reed et al. 2013b). As shown in GEOCHEM-5.5.1.3, the CONCMIN value is consistent with assuming a colloid concentration in the range of 40 to 400 µg L^{-1}, which is much higher than colloid concentrations typically observed in highly saline waters.

An explanation for the high concentrations of Pu in the 10 nm to 0.45 µm fraction may be continuous corrosion of iron in these experiments. Continuous corrosion could generate a continuous supply of colloids, which could support a relatively high, steady-state concentration of mineral fragment colloids and therefore a high concentration of Pu associated with these colloids. Continuous corrosion would require a continuous supply of oxidants (e.g., via radiolysis). A steady high concentration of colloids could therefore be maintained by a balance between colloid generation rates and rates of colloid aggregation and flocculation.

Another possible explanation for the high concentration of Pu in the 10 nm to 0.45 µm size fraction is that much of it may have been in mineral form. Addition of the iron coupons in these experiments caused the aqueous Pu(VI) to reduce and to precipitate as Pu(IV) mineral phases

(Reed et al. 2010, Figures 4-12 and 4-13). This Pu(IV) mineral phase was closely associated with the formation of green rust on the iron coupons. Steel corrosion in WIPP brines has been found to produce a green Fe(±Mg)-chlori-hydroxide phase at low CO_2 concentrations (<1500 ppm) and a Fe-Mg-Ca hydroxicarbonate phase at higher CO_2 concentrations (Roselle 2013a). The identities of these phases could not be confirmed, but their chemical compositions are consistent with phases like green rust. Thus, the mineral fragment colloids that were isolated in the Pu-iron interaction experiments may have included Pu(IV) mineral phases and/or Pu(IV) otherwise incorporated into colloid structures. In addition, intrinsic Pu(IV) colloids may attach to mineral fragment colloids and thereby be retained in the 10 nm to 0.45 µm size fraction. If it is true that the bulk of the Pu in the 10 nm to 0.45 µm size fraction is not sorbed, but rather is in mineral form, then the observed Pu concentrations in this size fraction could have been associated with a very low concentration of mineral fragment colloids, as might be expected in a highly saline system at equilibrium or under conditions of very low corrosion rates.

The generation of Pu(IV) mineral phases in the Pu-iron interaction experiments are a result of oversaturation caused by the introduction of zero-valent iron and subsequent reduction of Pu(VI). This sequence of events could potentially occur in isolated microenvironments with high Pu loadings where considerable radiolytic oxidation could occur.

GEOCHEM-5.5.1.5 Analysis of Conservatism in WIPP Mineral Fragment Colloid Model

The mineral fragment colloid model for the WIPP PA is based on two conservative model assumptions and three conservative assumptions used to calculate CONCMIN. The conservative model assumptions are:

- Mineral fragment colloids will be fully loaded. The actinide concentration associated with these colloids will be a constant value (CONCMIN) and equals the concentration of surface sites on these colloids (GEOCHEM-5.4.1).
- Mineral fragment colloids will be fully loaded with each actinide. Because there are five primary actinides in the WIPP colloid model (Th, U, Np, Pu, and Am), this assumption means that the total concentration of all actinides sorbed to mineral fragment colloids is five times greater than the mineral fragment colloid surface site concentration, i.e., five times CONCMIN.

The value determined for CONCMIN (2.6×10^{-8} M) for each actinide is set equal to a mineral fragment colloid surface site concentration, which was determined based on measurements of mineral fragment colloid particles in dilute WIPP brine and conservative assumptions regarding the surface site concentration associated with these particles. The conservative assumptions used to calculate CONCMIN include the following:

- The particle concentration in WIPP brines is equivalent to the observed geometric mean value for hematite, goethite, and bentonite measured after 12.8 to 12.9 days in factor-of-10 diluted brine. This assumption is conservative because undiluted WIPP brines and longer equilibration times would have resulted in lower observed particle concentrations. In the experimental work, there was a notation that the colloidal components were flocculating rapidly in the brines (Papenguth and Behl 1996). This is expected as discussed above regarding the expected instability of colloids in such brines; however,

without a long-term benchmark, the short-term experiments were used as the basis for the parameter value.

- A factor of two was added to the site concentration to account for natural colloids potentially existing in the Culebra. This adjustment is conservative because not all releases occur in the Culebra, and for those that do, there is little evidence that they would enhance the mineral fragment component of total mobile actinide concentrations.
- An additional factor of ten was added to the site concentration to account for uncertainty (GEOCHEM-5.4.1). This factor is a direct conservative assumption.

The five conservative assumptions listed above are independent and multiplicative and likely result in predicted actinide concentrations associated with mineral fragment colloids that are at least two orders of magnitude above expected values. Based on the trends in Figure GEOCHEM-8, these predicted concentrations may be at least three orders of magnitude too high for sustainable conditions.

GEOCHEM-5.5.1.6 Conclusions for Mineral Fragment Colloids

The value of CONCMIN should not be increased to account for potential Mg-Cl-OH colloids.

Mg-Cl-OH colloids have not been observed in hydration and solubility experiments involving WIPP brines and have not been observed in concentrations approaching CONCMIN. Thus, there is no reason to increase the value of CONCMIN to account for potential Mg-Cl-OH colloids.

The CONCMIN value of 2.6×10^{-8} M was determined based on conservative assumptions that were applied to concentration measurements of hematite, goethite, and bentonite colloids in 10-fold diluted WIPP brine. The analyses in GEOCHEM-5.5.1.3 and GEOCHEM-5.5.1.5 indicate that a more realistic estimate of the mineral fragment contribution to mobile actinide concentrations is likely at least two orders of magnitude lower than the current value of CONCMIN.

Although the association of Pu with mineral fragment colloids in iron corrosion experiments in WIPP brines appear to support the current value of CONCMIN, the form of Pu associated with these colloids has not been fully investigated. In the experiments, dissolved Pu(VI) is reduced by the introduction of the iron coupon, and rapid precipitation of Pu(IV) ensues. It is conceivable, therefore, that much of the Pu observed in the 10 nm to 0.45 μm size fraction may exist as Pu(IV) mineral phases and intrinsic colloids attached to mineral fragment colloids. If this is true, then these colloids would be specific to Pu and more appropriately modeled as Pu intrinsic colloids.

GEOCHEM-5.5.2 Intrinsic Colloids

For the CRA-2014, values of the intrinsic colloid model parameter CONCINT were changed to increase the intrinsic colloid concentrations of several actinides (GEOCHEM-5.5.2.1). Section GEOCHEM-5.5.2 and its subsections revisit the relevant studies and examine PA implications and the importance of distinguishing intrinsic colloids in solubility and corrosion experiments. But first, interactions with the EPA regarding intrinsic colloids are briefly reviewed.

As stated in GEOCHEM-5.5.1, the EPA asked the DOE to address thorium intrinsic colloids and whether a significant amount of these colloids could form in the WIPP repository (Kelly 2010, Comment 4-C-36). In the response by the DOE, Xiong et al. (2010b). noted that intrinsic colloid data for Th(IV) in WIPP brines were not available, and that the data provided by Altmaier et al. (2004) were for pure NaCl or $MgCl_2$ solutions. Xiong et al. (2010b). also noted that the higher non-ultracentrifuged Th(IV) concentrations from Altmaier et al. (2004), which included intrinsic colloids, were conservatively included in the WIPP Th(IV) solubility uncertainty analysis instead of the much lower concentrations measured after ultracentrifugation. Additional analysis is presented in the subsections that follow.

In the 2010 Technical Support Document (TSD) for Section 194.24, the EPA evaluated the potential effects of intrinsic colloids on PA results by including Th(IV) data reported in Altmaier et al. (2004) . The EPA used Table SOTERM-25 (U.S. DOE 2009, Appendix SOTERM) that provided values of dissolved and colloidal actinide concentrations based on the median parameter values for the CCA PA (U.S. DOE 1996) and the CRA-2004 PA baseline calculations (U.S. DOE 2004), summarizing those values in Table 8.1 (U.S. EPA 2010). The results of the EPA sensitivity study, which also included changes for dissolved actinide concentrations, were summarized in Table 8.2 (U.S. EPA 2010).

For the concentrations of dissolved Th(IV) and Th(IV) associated with intrinsic colloids, the EPA used the measurements of Altmaier et al. (2004), i.e., 8.49×10^{-10} M and 5.01×10^{-7} M, respectively. The results showed increased mobilized concentrations of Th(IV) in the Salado and Castile by factors of 1.85 and 1.52, respectively. Much of the increase from the intrinsic colloid component was offset by decreases in the dissolved, humic, and microbial components. The humic colloid Th(IV) concentration decreased from 1.60×10^{-7} M (Salado) and 1.98×10^{-7} M (Castile) to 5.35×10^{-9} M (both), while the microbial colloid Th(IV) concentration decreased from 7.87×10^{-8} M (Salado) and 9.75×10^{-8} M (Castile) to 2.63×10^{-9} M (both). The humic and microbial Th(IV) concentrations decreased because they are calculated as being proportional to the dissolved Th(IV) concentrations, as discussed in GEOCHEM-5.4. The EPA concluded that the effects on PA results were relatively small because of the minor inventory of Th(IV) in the WIPP waste forms (as compared to Am and Pu). In its evaluation, the EPA indicated that further evaluation was needed to rule out intrinsic thorium colloids as relevant to the WIPP repository.

As stated in the 2017 TSD for Section 194.24, the EPA recommended revising the CONCINT parameter to be consistent with upper bounding values for samples collected with a pcH range of 8.5 to 10.5 (U.S. EPA 2017, p. 143). This EPA Completeness comment is identified as EPA Comment 3-C-9 (2015). The DOE responded to this EPA Completeness comment in Bryson (2015) by stating that the CONCINT parameter values recommended by Reed et al. (2013a) and used in CRA-2014 were purposefully selected from long-term experiments based on pH values being near expected reference pH values. Long-term experiments result in lower intrinsic colloid concentrations and indicate that the short-term experiments are far from equilibrium (see GEOCHEM-5.5.2.3 and GEOCHEM-5.5.2.4). This comment was resolved with the CONCINT parameter being re-evaluated and including new data (Reed et al. 2019). These new values are provided in Table GEOCHEM-61 with the broader pH range accounting for differences in values.

GEOCHEM-5.5.2.1 CRA-2014 PA Representation of Intrinsic Colloids

Until the CRA-2014 PA, Pu intrinsic colloids were the only intrinsic colloids explicitly included in the WIPP PA. For the CRA-2014 PA, the following CONCINT values are used (Table GEOCHEM-61): 2×10^{-8} M for Th, Np, and Pu; 3×10^{-8} M for U; and 4×10^{-9} M for Am (Roselle 2013b). These values originate from recommendations in Reed et al. (2013a) and are based on recent long-term measurements of intrinsic colloids in WIPP-relevant brines. New data have been generated for the CRA-2019 Deferred PA, with the following CONCINT values used (Table GEOCHEM-61): 4.3×10^{-8} M for Th(IV), Np(IV), U(IV), and Pu(IV); 1.4×10^{-6} M for U(VI); and 9.5×10^{-9} M for Pu(III) and Am(III) (Reed et al. 2019).

GEOCHEM-5.5.2.2 Literature Review for Intrinsic Colloids

This literature review section focuses on intrinsic colloids and information in Altmaier et al. (2004), Altmaier et al. (2008), Borkowski et al. (2012), and other studies related to intrinsic colloids.

The Altmaier et al, (2004) publication indicated high concentrations of Th(IV) intrinsic colloid in carbonate-free NaCl or $MgCl_2$ solutions equilibrated with brucite ($Mg(OH)_2$(cr)) or magnesium hydroxychloride ($Mg_2(OH)_3Cl{\cdot}4H_2O$(cr)) (i.e., “phase 3”). In one set of experiments, Th(IV) was introduced into solutions undersaturated with Th(IV) via addition of excess ThO_2(cr) or $ThO_n(OH)_4^{-2n}{\cdot}xH_2O$(am). Samples in the $Th(OH)_4$(am) solubility experiments were equilibrated for 20 to 100 days before they were ultracentrifuged to separate intrinsic Th(IV) colloids from the remaining dissolved Th(IV). In a separate set of experiments, solubility measurements were conducted from the direction of oversaturation via NaOH titration. Samples from this latter set of experiments were equilibrated for one day prior to ultracentrifugation.

Intrinsic colloids formed in each of the Altmaier et al. (2004) experiments and could be separated by ultracentrifugation due to density differences between the colloids and the solutions. The noncolloidal fractions in the experiments that did not have magnesium hydroxychloride mineral fragment colloids (i.e., 0.5M NaCl, 5.0 M NaCl, and 0.25 M $MgCl_2$ solutions) were found to have concentrations in the range of approximately $10^{-9.1}$ M to $10^{-8.3}$ M (Altmaier et al. 2004, Table 2). This range is comparable to the solubility of $Th(OH)_4$(am) ($10^{-8.5}$ M) (Neck and Kim 2001) and also to the range of Th(IV) solubilities found in other studies (Altmaier et al. 2004, Figure 2). In these same solutions, intrinsic colloids were measured to have concentrations in the range of $10^{-7.3}$ M to $10^{-6.3}$ M (Altmaier et al. 2004, Table 2). In the corresponding 1-day oversaturation experiments, a higher range of concentrations of intrinsic colloids was measured ($10^{-6.6}$ M to $10^{-5.6}$ M) (Altmaier et al. 2004, Figure 3).

In a related set of experiments conducted from undersaturation, but involving $CaCl_2$ solutions, calcium-associated Th(IV) intrinsic colloids are the dominant mobile Th(IV) species above a pH (molal) of 10.5 (Altmaier et al. 2008). Concentrations of these colloids increase rapidly with increasing alkalinity. The same trend is observed in the same study for Zr(IV), but begins at a pH (molal) of 9 to 9.5. The equilibration times for these tests were 7 to 198 days.

Intrinsic colloid data most relevant to the WIPP PA are data obtained from WIPP actinide solubility experiments (Borkowski et al. 2012; Reed et al. 2013a). Actinide solubilities have been

measured in GWB and ERDA-6 brines that have been equilibrated for 2 to 6 years. The results of these experiments are summarized in Table GEOCHEM-63.

The solubility of Th(IV) in carbonate-free and carbonate-containing GWB and ERDA-6 brine was measured as a function of pcH and time in a set of LANL experiments (Borkowski et al. 2012). After 2 years of equilibration, the concentrations of dissolved Th(IV) (6 to 7 × 10^{-7} M) were in the range of those reported in Altmaier et al. (2004), but the intrinsic colloid fraction was much lower, approximately 40 percent. To test whether the dissolved concentrations were at equilibrium, samples from the GWB solutions were re-examined after two more years. During this time, the total aqueous Th(IV) concentration decreased by more than an order of magnitude to 2 × 10^{-8} M at pcH 9.1, and to lower concentrations at pcH 9.6.

Long-term experiments relevant to actinides at other oxidation states have also shown measureable but low concentrations of intrinsic colloids in WIPP brines. Intrinsic colloids have been measured for Nd(III), Pu(III), and U(VI) at pcH values between 9.1 and 9.8 (Table GEOCHEM-63).

Since the CCA, other studies on intrinsic colloid formation for Pu(IV) and other actinides and actinide analogues have been reported in the literature. However, the solutions used in those experiments are either dilute compared to WIPP brines or the pcH is significantly different from the pcH expected for WIPP brines in contact with MgO. These studies include Neck and Kim (2001), Neck et al. (2002), Neck et al. (2003) , Bitea et al. (2003) , Vandenborre et al. (2008) , and Powell et al. (2011) .

Prediction of intrinsic Pu(IV) colloid stability has been advanced by Abdel-Fattah et al. (2013). These researchers calculated the Hamaker constant (~10^{-19} J) from optical parameters of PuO_2 calculated by Shi et al. (2010). The Hamaker constant is needed to calculate van der Waals interactions between colloids, including natural groundwater colloids, and between colloids and surfaces of the porous medium. Abdel-Fattah et al. (2013) used this constant to develop response surfaces as a function of pH and ionic strength to identify where energy barriers to aggregation are high between colloids of the same type, between colloids of different types, and between colloids and stationary surfaces. The results indicate that under WIPP conditions the energy barrier for intrinsic Pu(IV) colloid aggregation is very low.

Table GEOCHEM-63. Concentrations of Intrinsic Colloids Measured in WIPP Brines in Long-Term Experiments at Anticipated pcH Values

Actinide or Actinide Analogue	Intrinsic Colloid Concentration[a] (M)	Brine	Equilibration Time	Source
Nd(III)	4×10^{-9}	ERDA-6, pcH 9.14	2 to 6 years	Reed et al. (2013a)
Pu(III) [b]	4.8×10^{-9}	ERDA-6, pcH 9.1	6 years	Reed et al. (2013a)
Th(IV)	$\leq 2 \times 10^{-8}$	GWB, pcH 9.1	4 years	Borkowski et al. (2012)
U(VI)	1×10^{-8}	ERDA-6, pcH 9.3 to 9.8	5 years	Reed et al. (2013a)

[a] Concentration of element in 2.5 to 10 nm size fraction
[b] In the presence of metallic iron

GEOCHEM-5.5.2.3 Analysis of Long-Term Th(IV) Solubility Experiments

Recent Th(IV) solubility data from 4-year experiments on WIPP brines indicate that Th(IV) colloid concentrations continue to decrease significantly over time. The dissolved Th(IV) concentration measured by Borkowski et al. 2012 after 2 years of equilibration was in the range of 6 to 7×10^{-7} M, with intrinsic colloids accounting for approximately 40 percent of this concentration. After 4 years, the total dissolved Th(IV) concentration dropped more than an order of magnitude to 2×10^{-8} M (Borkowski et al. 2012). Because the 2×10^{-8} M measurement was performed without ultracentrifugation or ultrafiltration to separate the colloidal and truly dissolved Th(IV), the colloidal component is less than 2×10^{-8} M. This slow reduction in colloidal concentration is consistent with slow aggregation of Th(IV) colloids. It is also consistent with the formation of more crystalline forms of ThO_2.

Slow aggregation of Th(IV) intrinsic colloids in WIPP brines is consistent with energy barrier calculations for Pu(IV) intrinsic colloid aggregation (Abdel-Fattah et al. 2013). The energy barrier for intrinsic Pu(IV) colloid aggregation is very low for the ionic strength and pcH of WIPP brines. A low energy barrier implies that intrinsic colloids will sparingly resist aggregation. The slow aggregation observed in the case of Pu(IV) and Th(IV) is attributed to very low concentrations. At low concentrations, aggregation is diffusion limited, i.e., rapid aggregation is prevented by low collision frequency (Abdel-Fattah et al. 2013).

GEOCHEM-5.5.2.4 Analysis of Intrinsic Th(IV) Colloid Measurements of Altmaier et al. (2004)

The highest Th(IV) intrinsic colloid concentrations measured in the Altmaier et al. (2004) study were observed in carbonate-free NaCl or $MgCl_2$ solutions in 1-day oversaturation experiments ($10^{-6.6}$ M to $10^{-5.6}$ M). These concentrations were considerably higher than those measured in their undersaturation experiments ($10^{-7.3}$ M to $10^{-6.3}$ M) that lasted 20 to 100 days (Altmaier et al. 2004). Data from Borkowski et al. 2012 from experiments using WIPP brines also show a significantly decreasing trend in concentration as a function of equilibration time. This trend and the findings of the Abdel-Fattah et al. (2013) study suggest that the intrinsic colloid

concentrations measured in the Altmaier et al. (2004) study may have been unstable and slowly aggregating.

GEOCHEM-5.5.2.5 Analysis of Th(IV) Solubility for WIPP PA

For the CRA-2009 PABC and the CRA-2014 PA, Th(IV) concentration measurements from the non-centrifuged samples from Altmaier et al. (2004) are included in calculated solubility distributions, but the lower measurements from ultracentrifuged samples are not (Xiong 2011; Brush and Domski 2013b). The primary reason for this screening approach was to be consistent with the data set used for the original WIPP Th(IV) PABC model. Data for the original model was obtained using simple centrifugation and filtration methods.

For the CRA-2014 PA, CONCINT for Th(IV) was increased from 0 to 2×10^{-8} M based on the recommendations in Reed et al. (2013a); Roselle (2013b). The contribution of Th(IV) intrinsic colloids, therefore, is at least partially double-counted in the CRA-2014 PA because it is also at least partially included in the solubility calculations. This approach, however, reduces the chances that predicted Th(IV) solubilities and Th(IV) releases are underestimated in the WIPP PA.

GEOCHEM-5.5.2.6 Analysis of Effect of Intrinsic Colloids on Calculated Humic-Bound and Microbially-Bound Th(IV)

Intrinsic colloids should not be lumped with dissolved concentrations in the WIPP PA because intrinsic colloids react and migrate differently than dissolved species and may also behave differently than other types of colloids (e.g., Abdel-Fattah et al. 2013). In addition, if actinides associated with intrinsic colloids are lumped into the dissolved fraction, calculations of the concentrations of other actinide components that are proportional to the dissolved concentration will be inflated. In the WIPP PA, concentrations of humic-bound and microbially-bound actinides are defined to be directly proportional to the dissolved concentration (GEOCHEM-5.4); thus, overestimates of dissolved concentrations due to the inclusion of intrinsic colloids in the dissolved concentrations will result in overestimates of humic- and microbially-bound actinide concentrations.

GEOCHEM-5.5.2.7 Analysis of Intrinsic Colloids for An(III) and An(VI)

Results summarized in Reed et al. (2013a) show that intrinsic colloids of Nd(III), Pu(III), and U(VI) may also occur in brines. Though specific contributions of An(III) and An(VI) intrinsic colloids to total releases may be insignificant, their effects on truly dissolved concentrations, as in the case of Th(IV) and Pu(IV), may have significant effects on calculated humic-bound and microbially-bound actinides if intrinsic colloid contributions are not excluded from the dissolved concentration distributions (GEOCHEM-5.5.2.6).

GEOCHEM-5.5.2.8 Analysis of Potential Effects of Parsing Dissolved and Intrinsic Colloid Concentrations

The effects of excluding samples that have not undergone ultracentrifugation or ultrafiltration from the determination of WIPP PA dissolved concentrations are addressed here in a simple hypothetical example. It is supposed in this example that the truly dissolved concentration of

Pu(IV) is one-third of the value currently being used in the WIPP PA. Because humic-bound and microbially-bound Pu(IV) are proportional to the dissolved concentration, each of these organic colloid component concentrations would therefore be reduced by one-third (provided initial concentrations were not limited by the maximum values of CAPHUM and CAPMIC). Reductions in humic-bound and microbially-bound Th(IV) would be much greater for much lower solubilities. For example, in its 2009 TSD for Section 194.24, the EPA found that using a value of 8.49×10^{-10} M for dissolved Th(IV), based on ultracentrifuged solubility measurements from Altmaier et al. (2004), dropped the humic-bound and microbially-bound Th(IV) concentrations by more than an order of magnitude (GEOCHEM-5.5.2).

The extent of defensible reduction in dissolved concentrations for Pu(IV) and other actinide species due to the exclusion of samples that have not been ultracentrifuged or ultrafiltered is not investigated here. Currently available data have originated under different chemical conditions, different degrees of filtration and centrifugation, and different durations of equilibration, each of which have been shown to affect solubility measurements. However, the effects of the different conditions need to be better understood. For example, the Borkowski et al. (2012) study indicates that after 2 years of equilibration in WIPP brine, no more than 40 percent of the measured solubility of Th(IV) was due to intrinsic colloids. These results are in contrast to the Altmaier et al. (2004) results, which indicate that more than 99 percent of the measured Th(IV) solubility after 20 to 100 days in their salt solutions was due to intrinsic colloids. Whether these differences are due to equilibration time, different chemical conditions, different sampling procedures, other factors, or a combination of factors, is not clear.

The difference of two orders of magnitude observed in the Altmaier et al. (2004) study of colloidal Th(IV) to dissolved Th(IV) is consistent with the difference in the two sets of compiled Th(IV) solubility log K values in Rand et al. (2008, Table VII-20). The first set of solubility log K values includes measurements obtained without sufficient centrifugation or filtration to remove intrinsic colloids, and the second set includes measurements obtained after ultracentrifugation or ultrafiltration. Log K values for the first set range from -6.8 to -5.7 while those for the second set range from -9.5 to -7.4. These data strongly support the idea that true Th(IV) solubility cannot be measured without ultracentrifugation, ultrafiltration, or some other means to remove the contribution of intrinsic colloids.

Any reduction of dissolved concentrations by removal of intrinsic colloids would need to be accompanied by a corresponding representation of intrinsic colloids. In the context of the WIPP PA, the CONCINT values for actinide species showing significant intrinsic colloid concentrations would need to be adjusted accordingly.

GEOCHEM-5.5.2.9 Conclusions for Intrinsic Colloids

Data from the literature and from direct measurements on WIPP brines show that Th(IV) forms intrinsic colloids and that the concentrations of these colloids in alkaline brines are not an insignificant fraction of dissolved (<0.45 μm) thorium (Altmaier et al. 2004; Rand et al. 2008; Borkowski et al. 2012). In fact, numerous studies have found that the intrinsic colloid component may dominate dissolved Th(IV) concentrations (Altmaier et al. 2004; Rand et al. 2008). These intrinsic colloids may be unstable and may aggregate over time due to a low energy barrier to aggregation resulting from alkaline pH values and high ionic strength (Abdel-Fattah et al. 2013).

The concentration of Th(IV) associated with intrinsic colloids in WIPP brine experiments was measured to be approximately 40 percent of the 6 to 7 × 10^{-7} M total dissolved concentration after 2 years of equilibration (Borkowski et al. 2012). After 4 years of equilibration, the total dissolved Th(IV) concentration dropped to 2 × 10^{-8} M (Borkowski et al. 2012). This total concentration is less than 10 percent of both the colloidal Th(IV) and truly dissolved Th(IV) concentrations from 2 years prior. Thus, both the colloid and dissolved fractions of Th(IV) dropped markedly.

The CONCINT value of 2 × 10^{-8} M used in the CRA-2014 PA for Th(IV) is based on the lower 4-year measurement. The value for the CRA-2019 Deferred PA is increased to 4.3 × 10^{-8} M based on Reed et al. (2019).

GEOCHEM-5.5.3 Humic Substance Colloids

In its CRA-2009 TSD, the EPA noted that, based on the actinide solubilities used for the CCA PA, humic substances colloids and microbial colloids were the largest contributors to mobile actinides in the source term (U.S. EPA 2010, Table 8-1 and discussion). This continued to be the case in the CRA-2014. Since then, the EPA cited findings by Wall and Mathews (2005) that indicate humic substances may not be stable at all in WIPP brines in the presence of MgO (U.S. EPA 2017, p. 145). This possibility is examined further in GEOCHEM-5.5.3.8.

For CRA-2019, changes are made to the PHUMSIM and PHUMCIM parameters for An(III) and An(IV) (Mariner 2019). A revised process-level model was developed to update the An(III) and An(IV) PHUMSIM and PHUMCIM values to be consistent with the pH range expected for WIPP brines (Mariner 2016; Mariner 2018). Compared to previous values, the new PHUMSIM and PHUMCIM values are lower except for the An(III) PHUMSIM value, which is slightly higher than the previous value (Table GEOCHEM-61). The expected overall effects of the new values are a major decrease in humic colloid concentrations for An(IV) in Salado and Castile brines, and a major decrease in humic colloid concentrations for An(III) in Castile brines when previously-calculated An(III)-humic colloid concentrations were below CAPHUM.

The changes in the PHUMSIM and PHUMCIM values for An(III) and An(IV) are based on analyses reported in Mariner (2018) and Mariner (2016), respectively, and updated calculations for these analyses are based on the new DATA0.FM4 database and new baseline solubility calculations (Mariner 2019). The Mariner (2018) and Mariner (2016) analyses drew from additional data reported in the literature since the CCA and developed an improved humic complexation process model for calculating PHUMSIM and PHUMCIM values for An(III) and An(IV). The values calculated by the improved humic complexation process model account for the alkaline conditions expected in WIPP brines and incorporate the effects of free ion concentrations on humic complexation.

The subsections on humic substance colloids address the following topics:

- CRA-2014 representation of humic colloids (GEOCHEM-5.5.3.1)
- Literature review of humic colloid complexation (GEOCHEM-5.5.3.2)
- Humic colloid stability in WIPP brines (GEOCHEM-5.5.3.8)

- Factors affecting PHUMSIM and PHUMCIM (GEOCHEM-5.5.3.3)
- CAPHUM conservatism (GEOCHEM-5.5.3.4)
- Effects of multiple sources of conservatism (GEOCHEM-5.5.3.5)
- PHUMSIM and PHUMCIM values for An(III) (GEOCHEM-5.5.3.6)
- PHUMSIM and PHUMCIM values for An(IV) (GEOCHEM-5.5.3.7)
- PHUMSIM and PHUMCIM values for U(VI) (GEOCHEM-5.5.3.9)
- Conclusions and recommendations (GEOCHEM-5.5.3.9)

GEOCHEM-5.5.3.1 CRA-2019 PA Representation of Humic Substance Colloids

The current PA representation of the humic substance colloid model is explained in detail in GEOCHEM-5.4.3. The humic colloid model is more involved than the models for intrinsic and mineral fragment colloids because the concentration of actinides associated with humic substances is a function of the modeled dissolved concentration. At low values of dissolved actinide concentrations, the actinide concentration associated with humic substances is proportional to the dissolved concentration, and is calculated by multiplying the dissolved concentration by a proportionality constant, PHUMSIM or PHUMCIM, depending on whether the brine is from the Salado or the Castile, respectively (GEOCHEM-5.4). However, if this product exceeds the maximum actinide concentrations allowed to be bound to humic colloids, defined by the model parameter CAPHUM, then the CAPHUM value is used in place of the product. The established value for CAPHUM, 1.1×10^{-5} M, is based on a site-binding capacity of 5.56 meq g^{-1} and a maximum humic colloid concentration of 2.0 mg L^{-1}.

GEOCHEM-5.5.3.2 Literature Review for Humic Substance Colloids

Since the CCA, a number of studies have been published that address the stability of humic substances in brines and the effects of ionic strength and pH on the complexation of dissolved ions by aqueous humic substances. The more pertinent of these publications are mentioned here.

Wall and Choppin (2003) studied the solubility of humic acid in solution as a function of solution composition. The results indicate that coagulation, to a first approximation, is consistent with DLVO theory. Coagulation increased with increasing ionic strength, increasing cationic charge, and decreasing size of hydrated ions in the double layer.

Building on this work, Wall and Mathews (2005) studied the stability of humic acids in 95 percent GWB brine and 95 percent ERDA-6 brine in the presence and absence of MgO. This study showed that humic acids are not highly stable in the presence of MgO, and that their concentrations decrease below detection within 60 days of MgO addition. This study is examined in GEOCHEM-5.5.3.8.

The aqueous stability of humic substances and mineral fragments may be enhanced by the attachment of these colloids to one another. Hu et al. (2010) studied the stability of magnetite nanoparticles (58.0 ± 0.3 nm) in the presence and absence of humic acids over broad ranges of pH (3 to 10) and ionic strength (0.001 to 0.1 M NaCl). The results show that humic acid,

depending on pH and ionic strength, can act to stabilize or destabilize the magnetite particles. In the solutions with the highest ionic strength, humic acid at a concentration of 2 mg L^{-1} significantly stabilized the magnetite particles. These observations agree well with the DLVO calculations also presented in the paper. Similar trends are observed for fulvic acid in the presence of iron oxide nanoparticles (Palomino and Stoll 2013).

Studies since the CCA also include those pertaining to the complexation of metals and actinides to aqueous humic substances. Of particular note, complexation of Th(IV) and other (IV) metals with humic acid was measured over a broad range of pH, but at low (0.01 to 0.1 M) ionic strength (Reiller et al. 2008; Stern et al. 2014). In addition, laboratory studies have continued on humic acid complexation of actinides and lanthanides, particularly Am(III), Eu(III), and U(VI), but at low (0.001 to 0.1 M) ionic strength (Sakuragi et al. 2005; Sonke and Salters 2006; Moser et al. 2012). Only a few studies published since the CCA involve humic and fulvic acid complexation of actinides and other metals in solutions with high ionic strength and containing multivalent cations. They include the complexation of 10^{-6} M Ca with Aldrich humic acid in NaCl solutions up to 5 molal over a pcH range of 4.7 to 9.0 (Laszak and Choppin 2001), and complexation of 10^{-9} M Am(III) with humic acid from Lake Bradford in Florida and fulvic acid from Suwannee River in NaCl solutions up to 5 molal at a pcH of 5.0 to 5.1 (Wall et al. 2002). No studies of humic complexation with metals or actinides were found that involve high concentrations of Ca or Mg comparable to the Ca and Mg concentrations in WIPP brines.

GEOCHEM-5.5.3.3 Sensitivity Analysis of Factors Affecting PHUMSIM and PHUMCIM for An(III), An(V), and An(VI)

The PHUMSIM and PHUMCIM proportionality constants for An(III), An(V), and An(VI) species were derived as explained in GEOCHEM-5.4.3. PHUMSIM and PHUMCIM are distribution coefficients, i.e., calculated values of [AnHS]/[An] under conditions of low loading (i.e., $[AnHs] \ll [HS_{tot}]$). For the CCA, the following parameters were used to calculate PHUMSIM and PHUMCIM for An(III), An(V), and An(VI) (GEOCHEM-5.4.3):

- Humic complexation constants, $\beta_{1:An}$, for Am(III), Np(V), and U(VI)
- Humic-Ca/humic-Mg complexation constant, $\beta_{1:CaMg}$
- Humic binding site concentration, $[HS_{tot}]$
- Combined Ca and Mg concentrations in GWB and ERDA-6, $[Ca + Mg]$
- Total aqueous non-colloidal concentrations of Am(III), Np(V), and U(VI), [An]

The $\beta_{1:An}$ values for Am(III) and U(VI) came from experiments involving humic and fulvic acids performed in 6 molal NaCl solutions at pH 6 (U.S. DOE 1996, Appendix SOTERM, Section SOTERM-6.3.3.1). (Note: There is a possible error in the $\beta_{1:An}$ values used for U(VI). This is addressed in GEOCHEM-5.5.3.8.) The $\beta_{1:An}$ value for Np(V) was obtained from a study using Gorleben humic acid in a pH 9 solution in 0.1 M $NaClO_4$ (Kim and Sekine 1991). The $\beta_{1:CaMg}$ value came from experiments that involved humic and fulvic acids performed under acidic conditions in 0.1 M $NaClO_4$ (GEOCHEM-5.4.3). The value of $[HS_{tot}]$ assumes a 2.0 mg L^{-1} humic colloid concentration for the WIPP brines, and the total aqueous non-colloidal

concentrations of the actinides are those assumed for WIPP brines in the presence of MgO, as defined in Papenguth (1996, Tables 1a and 1b) and shown in Table GEOCHEM-64.

For the CCA, values for $\beta_{1:An}$, $\beta_{1:CaMg}$, $[HS_{tot}]$, and [An] were selected or assumed based on understood relationships, available data, and/or conservative assumptions. Low values of [An] were used in the calculation of PHUMSIM and PHUMCIM to conservatively assume low loadings. At low loadings, the values of [AnHS]/[An] are unaffected by [An]. At high loadings, increased [An] reduces [AnHS]/[An] because the limited availability of complexation sites limit the increase in [AnHS], as defined in Equation GEOCHEM.41.

PHUMSIM and PHUMCIM are directly proportional to the total humic colloid concentration $[HS_{tot}]$, i.e., CAPHUM, as indicated in Equation GEOCHEM.41. The concentration of $[HS_{tot}]$ is chosen to be 1.1×10^{-5} M, based on a concentration of 2.0 mg L^{-1} value (GEOCHEM-5.4.3). This concentration is likely conservatively high as discussed in GEOCHEM-5.5.3.8 and GEOCHEM-5.5.3.4. A lower value of $[HS_{tot}]$ results in proportionally lower PHUMSIM and PHUMCIM values.

The value of $\beta_{1:CaMg}$ has nearly the same magnitude of effect on PHUMSIM and PHUMCIM as $[HS_{tot}]$, but in the inverse direction (Mariner and Sassani 2014, Section 5.3.4.2). Its effect is large because the value of the product $\beta_{1:CaMg}$ [Ca + Mg] is generally much larger than the sum of $\beta_{1:An}$[An] + 1 in the denominator of Equation GEOCHEM.41 for the modeled actinides, implying the former will dominate the latter in the denominator. Its effect in the case of U(VI) in the Castile brine is diminished somewhat due to the order of magnitude lower [Ca + Mg] concentration in the Castile and the relatively high $\beta_{1:An}$[An] product for U(VI). However, as discussed in GEOCHEM-5.5.3.9, humic-bound U(VI) is generally limited to CAPHUM.

A reduction in the value of $\beta_{1:An}$ causes nearly the same proportional change to [AnHS]/[An] (Mariner and Sassani 2014, Section 5.3.4.2). This parameter is in both the numerator and denominator of Equation GEOCHEM.41. It has little effect in the denominator when $\beta_{1:An}$[An] is small relative to $\beta_{1:CaMg}$ [Ca + Mg] + 1. For U(VI) in Castile brine, this is not the case, and consequently the effect on PHUMCIM is diminished for U(VI). However, as discussed in GEOCHEM-5.5.3.9, humic-bound U(VI) is generally limited to CAPHUM.

GEOCHEM-5.5.3.4 Analysis of CAPHUM Conservatism

The CAPHUM value of 1.1×10^{-5} M, determined by multiplying the concentration of humic colloids (2 mg L^{-1}) by the maximum measured site binding capacity (5.56 meq g^{-1}), ensures that the humic-bound concentration of an actinide species does not exceed the capacity of available humic colloids. This value is conservative because:

- The concentration of humic substances in WIPP brines in the presence of MgO is likely to be much lower than 2 mg L^{-1} (GEOCHEM-5.5.3.8),
- The selected site binding capacity of 5.56 meq g^{-1} is the highest value measured among the three humic substances studied for the CCA (HAal-LBr, HAal-Gor, and FA-Suw),

- The site binding capacity assumes 1:1 binding of actinide to binding site,
- Full loading of all binding sites by actinides will not occur due to competition of non-actinides for binding sites, and
- The competition between each actinide for binding sites is ignored in the humic colloid model, allowing the total effective loading for five actinides to increase above a total of 1.1×10^{-5} M.

Because the stability of humic colloids in WIPP brines in contact with MgO is likely much lower than 2 mg L^{-1} (GEOCHEM-5.5.3.8), the bulk of the conservatism in CAPHUM is likely due to the humic colloid concentration assumption. The remaining four assumptions by themselves could also cause considerable overestimation in CAPHUM, depending on the number of actinides that have humic-bound concentrations that approach, or are limited by, CAPHUM.

GEOCHEM-5.5.3.5 Analysis of the Effect of Multiple Sources of Conservatism

The conservatisms in the values chosen for $\beta_{1:An}$, $\beta_{1:CaMg}$, $[HS_{tot}]$, and [An] propagate multiplicatively into the calculation of PHUMSIM and PHUMCIM. For example, if the values for $\beta_{1:An}$, $\beta_{1:CaMg}$, and $[HS_{tot}]$ are each conservative by a factor of 2, then based on the sensitivity analysis above, the PHUMSIM and PHUMCIM values would be conservative by nearly a factor of 8 (i.e., 2×2×2) for all but PHUMCIM for U(VI). Actual quantitative propagation of such a scenario shows that indeed PHUMSIM for An(III), An(V), and An(VI) and PHUMCIM for An(III) and An(V) would decrease by factors between 7 and 8 in this example (Mariner and Sassani 2014, Section 5.3.4.2). Calculated [AnHS]/[An] values for An(VI) in Castile brine for the same scenario would decrease by factors of 4.5 and 6.1, respectively. Greater decreases in calculated [AnHS]/[An] values are possible due to the potential for greater factors of conservatism in the $\beta_{1:An}$, $\beta_{1:CaMg}$, and $[HS_{tot}]$.

GEOCHEM-5.5.3.6 Analysis of PHUMSIM and PHUMCIM Values for An(III)

In 2018, an analysis of the An(III) humic colloid model and related recent literature was completed (Mariner 2018). That analysis developed a process for calculating An(III) PHUMSIM and PHUMCIM values similar to the process developed in Mariner (2016) for An(IV)-humic complexation. The developed process was later used to calculate updated values of PHUMSIM and PHUMCIM consistent with the new DATA0.FM4 thermodynamic database and CRA-2019 baseline solubility calculations (Mariner 2019).

- The 2019 update concludes that a value of 0.2 is appropriate for PHUMSIM and PHUMCIM for An(III) (Mariner 2019). The main reasons for the changes to PHUMSIM and PHUMCIM are (1) to bring the model in line with the expected alkaline pH range of WIPP brines, (2) to account for the thermodynamic database modifications to the Na-Ca-Mg-Am-EDTA-H_2O system, and (3) to make the PHUMSIM and PHUMCIM values consistent with the new baseline solubility calculations of Domski and Sisk-Scott (2019). This section summarizes the improvements to the process model and the calculation of PHUMSIM and PHUMCIM for the CRA-2019. When the An(III)-humic colloid process model was developed for the CCA, there were few published humic complexation data

for trivalent actinides in saline, alkaline waters. An(III) PHUMSIM and PHUMCIM determinations relied on stability constants measured in An(III)-humic complexation experiments conducted at pH 6 in NaCl solutions of 3 and 6 molal (U.S. DOE 1996, Appendix SOTERM, Section SOTERM-6.3.3.1). Since then, many studies have published humic complexation data for alkaline pH and high ionic strength for trivalent metals. Studies show that the actinide-humic stability constants increase by more than a log unit for each unit increase in pH (Maes et al. 1988; Maes et al. 1991; Sonke and Salters 2006; Pourret et al. 2007; Stern et al. 2007; Janot et al. 2013). Studies involving Ca^{2+} and Mg^{2+} since the CCA indicate that stability constants for Ca/Mg-humic complexation under WIPP conditions are also higher than assumed for the CCA (Lead et al. 1994; Laszak and Choppin 2001; Lu and Allen 2002).

As for the high-level WIPP PA model for An(III)-humic colloids, as abstracted using the parameters PHUMSIM, PHUMCIM, and CAPHUM, the Mariner (2018) report concludes that no modification is required at this time. These simple parameters and their use in the WIPP PA adequately contain the general understanding of the potential effects that humic colloids have on total An(III) mobile concentrations in projected WIPP brines.

Mariner (2018), however, also concludes that improvements and updates are needed at the process-model-level. A major improvement to the process model, as implemented in Mariner (2018, Section 4.1), is to use the free An(III), Ca, and Mg concentrations instead of the total concentrations in the model equations (analogous to the equations in GEOCHEM-5.4.3). An additional improvement is to require very low loading when the process model is used to calculate PHUMSIM and PHUMCIM. Also, the stability constants are updated to better represent trends in the literature for the expected pH and ionic strength conditions of WIPP brines (Mariner 2018, Sections 4.2 and 5.1).

For CRA-2019, new values for PHUMSIM and PHUMCIM were calculated because of the newly adopted DATA0.FM4 thermodynamic database (Domski 2019a) and new baseline solubility calculations (Domski and Sisk-Scott 2019). The earlier Mariner (2018) calculations derived a humic complexation stability constant for An(III) using the earlier DATA0.FM2 database in which the $AmEDTA^{-}$ formation constant was much higher and there was no $NaEDTA^{3-}$ species. These differences in EDTA reactivity are especially important in the calculations because the AnHs stability constant is calibrated based on the results of laboratory experiments in which EDTA and humic and fulvic acids compete for Am^{3+}. The updated calculations using DATA0.FM4 are documented and discussed in Mariner (2019).

Based on the results of the improved process model and updated inputs, the values for PHUMSIM and PHUMCIM determined in Mariner (2019) for the CRA-2019 calculations are 0.2 and 0.2.

The new values for PHUMSIM and PHUMCIM are expected based on the following assumptions used in their derivation:

- The model conservatively assumes that the entire concentration of humic colloids is composed of humic acid. Humic acid has a significantly greater affinity for complexing actinides than fulvic acid (e.g., Sonke and Salters 2006; Stern et al. 2007; Mariner and

Sassani 2014, Sections 4.2.3 and 5.3.4.2). Humic colloids in natural groundwater are a combination of humic and fulvic acids.

- The stability constants for An(III)-humic complexation are calculated assuming an ionic strength of 1 M instead of 6 M (Mariner 2018, Section 5.1). High ionic strength tends to reduce humic complexation (Laszak and Choppin 2001, Fig. 4; Sonke and Salters 2006, Eq. 9).
- The stability constant of 1000 for Ca/Mg-humic complexation is conservative (Mariner 2018, Section 4.2.1).
- The actual [AnHs]/[An] values calculated by the process model based on the above conservative assumptions are 0.11 and 0.12, which are lower than the 0.2 values adopted for PHUMSIM and PHUMCIM.

As for the value of the total concentration of humic complexation sites (equivalent to CAPHUM), it too is conservative because it assumes that humic colloids are stable at a concentration of 2 mg L^{-1} (U.S. DOE 1996, Appendix SOTERM, Section SOTERM-6.3.3). Humic acid is unstable in these brines in the presence of MgO (GEOCHEM-5.5.3.8).

Because these new values for PHUMSIM and PHUMCIM are conservative, distributions for these parameters are not determined. These values depend not only on the available humic complexation data and inherent assumptions, they also depend on the WIPP thermodynamic database and the equilibrated WIPP brine compositions.

GEOCHEM-5.5.3.7 Analysis of PHUMSIM and PHUMCIM Values for An(IV)

In 2016, an analysis of the An(IV) humic colloid model and related recent literature was completed (Mariner 2016). That analysis developed a new process for calculating PHUMSIM and PHUMCIM values for An(IV). The developed process was later used to calculate updated values of PHUMSIM and PHUMCIM consistent with the new DATA0.FM4 thermodynamic database and CRA-2019 baseline solubility calculations (Mariner 2019). The new value of 0.01 for PHUMSIM and PHUMCIM for An(IV) is much lower than the value of 6.3 established in the CCA.

The 6.3 value established in the CCA was based on measurements of Th(IV) in colloidal and non-colloidal size fractions in seawater, as reported in Baskaran et al. (1992) . This value is found to be highly conservative for WIPP brines in contact with MgO (Mariner 2016). The pH of brines in the repository is predicted to be around 8.8, not 8, the approximate pH of seawater. Increases in pH in the alkaline range significantly reduce An(IV)-humic complexation (e.g., Reiller et al. 2003, Fig. 8). In addition, Mg^{2+} from MgO will compete strongly with released actinides for humic complexation sites and limit the concentrations of humic-bound An(IV). Aqueous Mg^{2+} concentrations in WIPP brines equilibrated with MgO are expected to be significantly higher than in seawater (Mariner and Sassani 2014, Section 5.3.4.4).

Since the mid-1990s, a number of studies of An(IV)-humic complexation have been published (Reiller et al. 2003; Warwick et al. 2005; Gaona et al. 2008; Reiller et al. 2008; Evans et al. 2011; Stern et al. 2014; Zimmerman et al. 2014). These studies examine complexation over a broad pH range and include laboratory measurements of humic complexation with Th(IV),

Pu(IV), and U(IV). In addition, studies of the humic complexation of Ca^{2+} and Mg^{2+} over broad ranges of pH and salinity have been published (Lead et al. 1994; Laszak and Choppin 2001; Lu and Allen 2002). These studies were used in Mariner (2019) to build a An(IV)-humic complexation model to calculate new An(IV) PHUMSIM and PHUMCIM values for WIPP conditions.

The changes in the PHUMSIM and PHUMCIM values for An(III) and An(IV) are based on analyses reported in Mariner (2018) and Mariner 2016, respectively, and on updated calculations for these analyses based on the new DATA0.FM4 database (Domski 2019a) and new baseline solubility calculations (Domski and Sisk-Scott 2019).

Compared to the calculations in Mariner (2016), the [AnHS]/[An] values calculated for Castile brine, represented by equilibrated ERDA-6, decreased by about an order of magnitude while those for Salado brine, represented by equilibrated GWB, changed relatively little (Mariner 2019). Unlike the equilibrated GWB brine, equilibrated ERDA-6 brine changed markedly from the CRA-2014 (Domski and Sisk-Scott 2019). The total Ca^{2+} and Mg^{2+} concentration in equilibrated ERDA-6 brine increased by a factor of 6 while the pH decreased from 9.2 to 8.8. Although lower pH tends to enhance An(IV)-humic complexation, this effect is low in this pH range and is small compared to the increased competition for humic complexation sites by the much higher total concentrations of Ca^{2+} and Mg^{2+} in the new equilibrated ERDA-6 brine composition.

The new An(IV) PHUMSIM and PHUMCIM values of 0.01 and 0.01 are expected to be conservative based on the following conservative assumptions used in their derivation:

- The model conservatively assumes that the entire concentration of humic colloids is composed of humic acid.
- The stability constants for An(III)-humic complexation are calculated assuming an ionic strength of 0.1 M instead of 6 M (Mariner 2016, Section 5.2).
- The Ca/Mg-humic stability constants used are likely conservative (Mariner 2016, Section 4.2.1).
- The [AnHS]/[An] values calculated by the process model based on the above conservative assumptions are less than 0.002, which are lower than the adopted 0.01 value for PHUMSIM and PHUMCIM.

These assumptions are the same or analogous to the conservative assumptions used for the An(III) PHUMSIM and PHUMCIM calculations (GEOCHEM-5.5.3.6). In addition, as mentioned previously, the total concentration of humic complexation sites (equivalent to CAPHUM) is also likely conservative because it assumes that humic colloids are stable at a concentration of 2 mg L^{-1} (U.S. DOE 1996, Appendix SOTERM, Section SOTERM-6.3.3). Humic acid is likely unstable in these brines in the presence of MgO (GEOCHEM-5.5.3.8).

Because these new values for PHUMSIM and PHUMCIM are expected to be conservative, distributions for these parameters are not determined. These values depend not only on the available humic complexation data and inherent assumptions, they also depend on the WIPP thermodynamic database and the equilibrated WIPP brine compositions.

GEOCHEM-5.5.3.8 Analysis of Humic Colloid Stability in WIPP Brines

Wall and Mathews (2005) studied the stability of humic acid in 95 percent GWB brine and 95 percent ERDA-6 brine in the presence and absence of MgO. Results are shown in Table GEOCHEM-64 and Figure GEOCHEM-9. In the absence of MgO, humic acid was found to be stable at a concentration of approximately 30 mg L^{-1}. Addition of MgO, however, destabilized the humic acids and their concentrations fell below detection within 60 days. The detection limit in these experiments was not reported. Based on the error bars in the figures, it was likely greater than 1 mg L^{-1}.

Without the MgO addition, the average pH values in the solutions were in the range of 7 to 8. In the presence of MgO, the pH was generally higher, in the range of 8.1 to 12.8. Because WIPP waste forms are surrounded by MgO, these results suggest that humic substance colloids may be unstable in WIPP source-term brines. However, further study is needed to confirm this because fulvic acids were not included in this study, and detection limits were not low enough to rule out potentially significant concentrations of humic acids.

Table GEOCHEM-64. Average pH and 60-day Humic Acid Concentration in Presence and Absence of MgO in Wall and Mathews (2005) Study

Mineral Phase	Solution	Humic Acid (mg L^{-1})	pH
None	Deionized water	290 ± 10	NR[e]
	95% ERDA-6 brine	31 ± 4	7.92 ± 0.03
	95% GWB brine	30 ± 4	7.08 ± 0.08
Fisher MgO[a]	Deionized water	ND[d]	11.2 ± 0.5
	95% ERDA-6 brine	ND	10.7 ± 0.1
	95% GWB brine	ND	8.1 ± 0.2
Premier MgO[b]	Deionized water	ND	12.8 ± 0.1
	95% ERDA-6 brine	ND	12.1 ± 0.1
	95% GWB brine	ND	8.4 ± 0.1

[a] 97.0% MgO
[b] 87 – 89% MgO (impurities: monticellite, forsterite, lime, and spinel)
[c] For solutions containing MgO, pH was only reported for 2.4 g g^{-1} liquid:solid ratio
[d] Below detection for both liquid:solid ratios studied (2.4 and 10.0 g g^{-1})
[e] Not reported

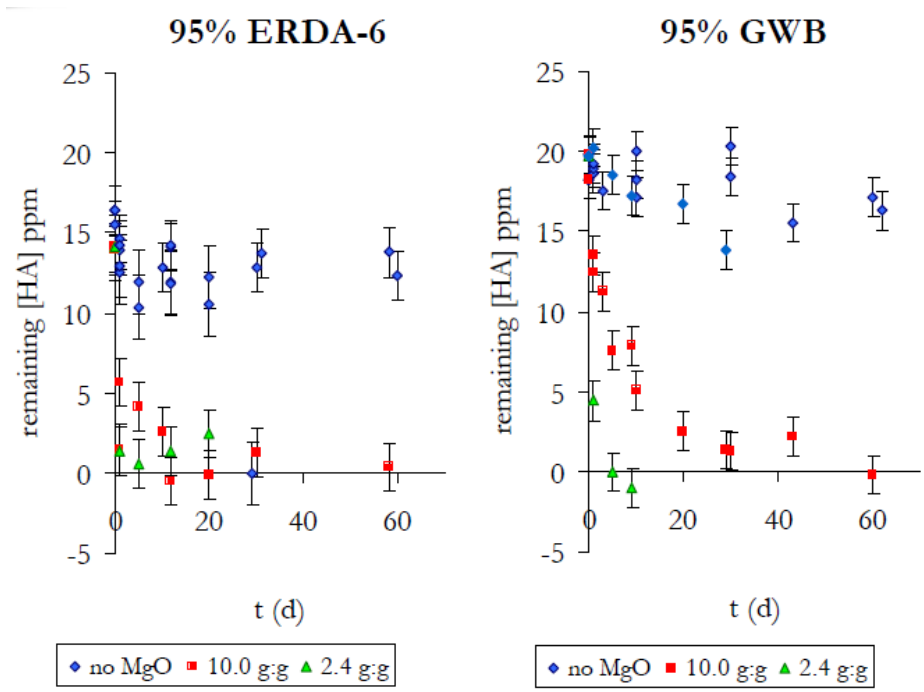

Figure GEOCHEM-9. Humic acid Concentration Over Time for Different Liquid:Solid Ratios for both 95% GWB and 95% ERDA-6 (Graphic From Wall and Mathews [2003]).

GEOCHEM-5.5.3.9 Analysis of PHUMSIM and PHUMCIM Values for U(VI)

There is a discrepancy in the U(VI) log $\beta_{1:An}$ values used to calculate PHUMSIM and PHUMCIM for U(VI) (shown Table GEOCHEM-64) and those reported in Labonne-Wall et al. (1999). The values reported in Labonne-Wall et al. (1999, Table 5) at pH 6.5, 6.6, and 6.5 in 6 m NaCl are 8.2 ± 0.5, 8.5 ± 0.1, and 7.8 ± 0.1 for HAal-LBr, HAal-Gor, and FA-Suw, respectively. Those presented in Papenguth (1996) and used to calculate PHUMSIM and PHUMCIM for U(VI) are much lower (5.91, 5.35, and 4.60). The lower values of Papenguth (1996) may be to compensate for using the total U(VI) dissolved concentration instead of the free concentration of UO_2^{2+} in the model equations (GEOCHEM-5.4.3). Regardless, the stability constants used in the Papenguth (1996) calculations are not adjusted to be consistent with the expected pH of WIPP brines, and low loadings are not applied in the calculations.

Despite these differences, the U(VI) colloid concentrations calculated in the WIPP PA using the legacy U(VI) PHUMSIM and PHUMCIM values are conservative because they are calculated to equal CAPHUM, the maximum U(VI)-humic colloid concentration achievable. With the U(VI) dissolved concentration set at a high value (10^{-3} M) and CAPHUM set at 1.1×10^{-5} M, the humic-bound U(VI) in the WIPP PA amounts to only 1.1 percent of the total mobile U(VI) concentration. Therefore, unless the U(VI) solubility is lowered or CAPHUM is increased, any adjustments to U(VI) PHUMSIM and PHUMCIM values in the WIPP PA will have little, if any, effect on U(VI) mobility.

GEOCHEM-5.5.3.10 Conclusions for Humic Substance Colloids

The laboratory experiments of Wall and Mathews (2005) indicate that humic acids are likely unstable in WIPP brines in the presence of MgO and imply that the value of the CAPHUM parameter is set too high. To rule out the stability of humic colloids under WIPP conditions, however, more definitive data are needed. Fulvic acids were not included in the analyses. In addition, the detection limit for humic acid was not reported in the publication and was likely greater than 1 mg L^{-1}, based on the error bars in the data presented.

A new value of 0.2 for An(III) PHUMSIM and PHUMCIM are adopted for the CRA-2019 based on new data from the literature and a new analysis for alkaline brines in the WIPP PA (Mariner 2019). This value is not much different than the legacy value of 0.19 for PHUMSIM, but is markedly lower than the nominal legacy value of 1.37 for PHUMCIM (Table GEOCHEM-61). The new value is based on experimental observations of humic complexation of trivalent metals in alkaline solutions containing EDTA as a competitive reactant.

For An(IV) PHUMSIM and PHUMCIM values, a value of 0.01 is used for the CRA-2019 based on new data from the literature and a new analysis for alkaline brines in the WIPP PA (Mariner 2019). Previously, these constants were set at a value of 6.3 based on Th(IV) measurements in particle size fractions of seawater. The new value is based on An(IV)-humic complexation observed in laboratory experiments in alkaline solutions. This value is expected to reduce the humic-bound An(IV) concentrations by more than 99 percent, causing a reduction in total mobile An(IV) concentrations of 85 percent to 86 percent, assuming no other type of An(IV) colloid (i.e., intrinsic, microbial, and mineral fragment colloids) is present.

The U(VI) PHUMSIM and PHUMCIM values calculated for the CCA, and still used in the WIPP PA calculations, are likely underestimated. Regardless, new values for these parameters are not expected to affect WIPP PA calculations for U(VI) humic colloids because the model already predicts [AnHS] values equal to CAPHUM. The U(VI) solubility is set so high (10^{-3} M) that U(VI) exhausts the humic complexation site capacity in the WIPP PA.

GEOCHEM-5.5.4 Microbial Colloids

As mentioned in GEOCHEM-5.5.3, the EPA in its CRA-2009 TSD noted, based on the actinide solubilities used for the CCA PA, that the humic substances colloids and microbial colloids were the largest contributors to mobile actinides in the source term (U.S. EPA 2010, Table 8-1 and discussion). They continued to be important contributors in the CRA-2014, though several of the microbially-bound actinide nominal concentrations changed noticeably due to changes in values of the microbial colloid parameters PROPMIC and CAPMIC. The median fractions of Am(III) and Th(IV) that were colloidal in the CRA-2014 were significantly lower than in previous years due to lower PROPMIC and/or CAPMIC values for these actinides (U.S. DOE 2014, Appendix SOTERM, Tables SOTERM-21 and SOTERM-23). For CRA 2014, new values were proposed that were based on the association of actinides with a fixed concentration of resting cells of halophilic organisms (Reed et al. 2013a). For the CRA 2019, more values have been generated, based on the same fixed biomass concept, but with longer term data (Swanson et al. 2019 and Reed et al. 2019). This section addresses some of the recent developments in the microbial

colloid model of the WIPP PA. The parameters CAPMIC and PROPMIC are discussed further in CRA-2019 Appendix SOTERM.

GEOCHEM-5.5.4.1 CRA-2014 PA Representation of Microbial Colloids

In the CRA-2014 PA, the values for PROPMIC and CAPMIC were updated as shown in GEOCHEM-5.4. In the CRA-2014 and earlier PA calculations, microbial colloid actinide concentrations were limited by a toxicity relationship when total mobile concentrations exceeded CAPMIC (e.g., U.S. DOE 2014, Appendix SOTERM, Equations SOTERM.78 and SOTERM.79). This relationship caused microbial actinide concentrations to fall to zero once the toxicity limit was reached. For CRA-2019, the toxicity limitation was removed (Sarathi 2019). This change is addressed in GEOCHEM-5.5.4.4.

GEOCHEM-5.5.4.2 Literature Review for Microbial Colloids

A review of the literature relevant to the WIPP microbial colloid model is documented in Reed et al. (2013a). In that report, studies involving high-ionic-strength water are cited, including McGenity et al. (2000), Gruber et al. (2004), Ams et al. (2013), Swanson et al. (2012), Swanson et al. (2013), and Swanson and Simmons (2013). The studies pertain to the types of microbes expected in the WIPP environment, the potential attachment of actinides to those microbes, and the abundance of those microbes. Several studies conducted under low-ionic-strength conditions are also identified in the report.

In addition to the literature review, the Reed et al. (2013a) report examines the WIPP microbial colloid model in light of recent data, and recommends specific changes to improve the model. The Reed et al. (2013a) recommendations include the following (paraphrased):

1. PROPMIC values calculated using biosorption data from solutions having a pcH of approximately 8.5 to avoid potential precipitation suspected at higher pcH,
2. PROPMIC and CAPMIC values assigned by oxidation state, and
3. CAPMIC values based on microbial biomass and sorption capacity.

Based on these recommendations, Reed et al. (2013a) proposed a new set of PROPMIC and CAPMIC values for the element-based approach and a separate set for an oxidation-state-based approach.

GEOCHEM-5.5.4.3 Analysis of Conservatism in Reed et al. (2013a) Recommended CAPMIC Values

The CAPMIC values recommended in Reed et al. (2013a) are calculated by multiplying microbial actinide concentrations (in units of moles microbial An per cell) by a high value for the number of cells per liter of solution. As explained by Reed et al. (2013a), most halite samples contain no cells, and brine samples from the WIPP underground contain between 10^7 and 10^{10} cell L^{-1} based on direct counts from matrices (Francis and Gillow 1994). Under growth conditions 10^{11} cells/mL were observed (Gillow and Francis 2006). The concentration used by Reed et al. (2013a) in the calculation of their recommended CAPMIC values is 10^{12} cell L^{-1}

based on growing cultures, which is one order of magnitude higher than the maximum value observed by Francis and Gillow (1994) under all conditions that they investigated.

GEOCHEM-5.5.4.4 Analysis of Microbial Actinide Concentration Calculation for CRA-2019

Using the PROPMIC and CAPMIC values in Table GEOCHEM-61, which are changed for CRA-2019, microbial actinide concentrations for CRA-2019 can be calculated as functions of the total dissolved actinide concentrations [An]. Additionally, the PROPMIC parameters are based on archaeal, rather than bacterial, data.

More discussion on the rationale for removing the toxicity limitation is in CRA-2019 Appendix SOTERM, Section SOTERM-4.3.1.

GEOCHEM-5.5.4.5 Conclusions for Microbial Colloids

For CRA-2019, toxicity limitations are removed from the WIPP microbial colloid model (GEOCHEM-5.5.4.1). PROPMIC and CAPMIC values are changed as seen in Table GEOCHEM-61.

The recommendations in Reed et al. (2019) pertaining to the WIPP microbial colloid model are based on data and arguments presented and cited in that report. The microbial colloid model is addressed in detail in Appendix SOTERM, Section SOTERM-4.3.

GEOCHEM-5.6 Summary

In accordance with the Analysis Plan for Evaluating Constraints on Colloid Parameters in the WIPP Repository, AP 152, Rev. 0 (Sassani 2011), and the Analysis Plan for the Evaluation of Humic-Actinide Complexation for WIPP Conditions, AP 167, Rev. 0 (Mariner 2014), analyses of WIPP colloid model constraints and parameter values have been performed. Work primarily focused on intrinsic colloids, mineral fragment colloids, and humic substance colloids, with a lesser focus on microbial colloids. Comments by the EPA concerning intrinsic Th(IV) colloids and Mg-Cl-OH mineral fragment colloids were addressed, assumptions and data used to constrain colloid model calculations were evaluated, and inconsistencies found between data and model parameter values were identified. This work resulted in the conclusions listed below. These conclusions are developed and discussed in this appendix and in four supporting documents (Mariner and Sassani 2014; Mariner 2016; Mariner 2018; Mariner 2019). The values of colloid parameters for CRA-2019 are summarized in Table GEOCHEM-61.

Mineral fragment colloids

- The value of CONCMIN should not be increased to account for potential Mg-Cl-OH colloids.
- The value of CONCMIN for each actinide element could justifiably be reduced, but doing so would have negligible effect on WIPP releases.

Intrinsic colloids

- A non-zero CONCINT value for Th(IV) intrinsic colloids should be used in the WIPP PA.
- The set of solubility data used to determine dissolved concentration distributions for the WIPP PA model should exclude solubility measurements known or likely to contain significant contributions from intrinsic colloids.
- CONCINT values should be used for each actinide species that forms significant concentrations of intrinsic colloids in WIPP brines.

Humic colloids

- Humic colloids are likely unstable in WIPP brines in the presence of MgO, as indicated in the Wall and Mathews (2005) study.
- A new value of 0.2 for PHUMSIM and PHUMCIM for An(III) is adopted for CRA-2019 based on new data from the literature and new calculations using an updated process model.
- A new value of 0.01 for PHUMSIM and PHUMCIM for An(IV) is adopted for CRA-2019 based on new data from the literature and new calculations using an updated process model.
- U(VI) PHUMSIM and PHUMCIM values are likely underestimated; however, increasing these values would not affect U(VI) mobility because the WIPP PA model already maximizes the humic-bound U(VI) concentration at the humic complexation site capacity (CAPHUM).

Microbial colloids

- A change in the microbial colloid model that eliminates toxicity limitations is adopted for CRA-2019.
- PROPMIC and CAPMIC values for CRA-2019 are changed.

GEOCHEM-6.0 References

Abdel-Fattah, A. I., D. Zhou, H. Boukhalfa, S. Tarimala, D. Ware, and A. A. Keller. 2013. Dispersion stability and electrokinetic properties of intrinsic plutonium colloids: Implications for subsurface transport. Environmental Science & Technology, Vol. 47:5626-5634.

Alexander, W. R., J. A. Berry, M. J. Kelly, and S. W. Swanton. 2011. Review of colloids in the geosphere and their treatment in performance assessments. Report to NDA-RWMD. Serco Ltd., Oxfordshire, UK. NPO003512.

Al Mahamid, I., C. F. Novak, K. A. Becraft, S. A. Carpenter, and N. Hakem. 1998. Solubility of Np(V) in K-Cl-CO_3 and Na-K-Cl-CO_3 solutions to high concentrations: Measurements and Thermodynamic Model Predictions. SAND 97-1230J.

Altmaier, M., V. Neck, and T. Fanghänel. 2004. Solubility and colloid formation of Th(IV) in concentrated NaCl and $MgCl_2$ solution. Radiochimica Acta, Vol. 92:537-543.

Altmaier, M., V. Neck, R. Müller, and T. Fanghänel. 2005. Solubility of $ThO_2 \cdot xH_2O$*(am)* in Carbonate Solution and the Formation of Ternary Th(IV) Hydroxide-Carbonate Complexes. Radiochimica Acta. Vol. 93, 83-92.

Altmaier, M., V. Neck, M. A. Denecke, R. Yin, and T. Fanghänel. 2006. Solubility of $ThO_2 \cdot xH_2O$(am) and the Formation of Ternary Th(IV) Hydroxide-Carbonate Complexes in $NaHCO_3$-Na_2CO_3 Solutions Containing 0–4 M NaCl. Radiochimica Acta. Vol. 94, 495-500.

Altmaier, M., V. Neck, and T. Fanghänel. 2008. Solubility of Zr(IV), Th(IV) and Pu(IV) hydrous oxides in CaCl(2) solutions and the formation of ternary Ca-M(IV)-OH complexes. Radiochimica Acta, Vol. 96(9-11):541-550.

Ams, D. A., J. S. Te, J. E. S. Szymanowski, J. B. Fein, M. Richmann, and D. T. Reed. 2013. The effect of high ionic strength on neptunium (V) adsorption to a halophilic bacterium. Geochimica Et Cosmochimica Acta, Vol. 110:45-57.

Babb, S. C., and C. F. Novak. 1995. WIPP PA User's Manual for FMT, Version 2.0. Albuquerque, NM: Sandia National Laboratories. ERMS 228119.

Babb, S. C., and C. F. Novak. 1997 and addenda. User's Manual for FMT Version 2.3: A Computer Code Employing the Pitzer Activity Coefficient Formalism for Calculating Thermodynamic Equilibrium in Geochemical Systems to High Electrolyte Concentrations. Albuquerque, NM: Sandia National Laboratories. ERMS 243037.

Baes, C. F., and R. E. Mesmer. The Hydrolysis of Cations. Wiley-Interscience: New York, 1976.

Baskaran, M., P. H. Santschi, G. Benoit, and B. D. Honeyman. 1992. Scavenging of thorium isotopes by colloids in seawater of the Gulf of Mexico. Geochimica et Cosmochimica Acta. Vol. 56(9):3375-3388.

Baston, G. M. N., M. Brownsword, A. J. Smith, and J. L. Smith-Briggs. 1996. Further Near-Field Solubility Studies. Harwell, UK: AEA Technology plc. NSS/R357.

Bennett, D., Y. Wang, T. Hicks. 1996. Memorandum to Distribution. Subject: An Evaluation of Heat Generation Processes for the WIPP. August 20, 1996. Albuquerque, NM: Sandia National Laboratories. ERMS 240635.

Bitea, C., C. Walther, J. I. Kim, H. Geckeis, T. Rabung, F. J. Scherbaum, D. G. Cacuci. 2003. Time-resolved observation of ZrO2-colloid agglomeration. Colloids and Surfaces A: Physicochemical Engineering Aspects, 215:55-66.

Borgnino, L. 2013. Experimental determination of the colloidal stability of Fe(III)-montmorillonite: Effects of organic matter, ionic strength and pH conditions. Colloids and Surfaces a-Physicochemical and Engineering Aspects, 423:178-187.

Borkowski, M., R. C. Moore, M. G. Bronikowski, J. Chen, O. S. Pokrovsky, Y. Xia, G. R. Choppin. 2001. Thermodynamic modeling of actinide complexation with oxalate at high ionic strength. Journal of Radioanalytical and Nuclear Chemistry, 248, 467-471.

Borkowski, M., J.-F. Lucchini, M. K. Richmann, and D. T. Reed. 2009. Actinide (III) Solubility in WIPP Brine: Data Summary and Recommendations. (Revision. 0). Carlsbad, NM: Los Alamos National Laboratory – Carlsbad Operations. LA-14360.

Borkowski, M. 2010. Numerical Values for Graphs Presented in the Report LCO-ACP-08, (Revision. 0), Entitled: Actinide (III) Solubility in WIPP Brine: Data Summary and Recommendations. Carlsbad, NM: Los Alamos National Laboratory, Carlsbad Operations. LANL CO ACRSP ACP 1002 05 17 01. LA UR 10 00898;

Borkowski, M., M. Richmann, D. T. Reed, and Y. Xiong. 2010. Complexation of Nd(III) with Tetraborate Ion and Its Effect on Actinide(III) Solubility in WIPP Brine. Radiochimica Acta. Vol. 98, nos. 9-11 (Migration 2009), 577–582.

Borkowski, M. 2012. Numerical Values for Graphs Presented in Report LCO-ACP-17 Entitled Solubility of An(IV) in WIPP Brine: Thorium Analog Studies in WIPP Simulated Brine, and for Graphs Published in Borkowski, M., et al., Carlsbad, NM: Los Alamos National Laboratory — Carlsbad Operations. Radiochimica Acta, Revision 0. 98 (9-11), 577–582 (2010). LA-UR 12–26640; LANL-CO ACRSP ACP-01/2012,

Borkowski, M., M. Richmann, and J. F. Lucchini. 2012. Solubility of An(IV) in WIPP Brine: Thorium Analog Studies in WIPP Simulated Brine. Carlsbad, NM: Los Alamos National Laboratory – Carlsbad Operations. LA UR 12 24417.

Brendebach, B., M. Altmaier, J. Rothe, V. Neck, and M. A. Denecke. 2007. EXAFS Study of Aqueous Zr^{IV} and Th^{IV} Complexes in Alkaline $CaCl_2$ Solutions: $Ca_3[Zr(OH)_6]^{4+}$ and $Ca_4[Th(OH)_8]^{4+}$. Inorganic Chemistry. Vol. 46, no. 16, 6804–6810.

Brush, L. H. 1990. Test Plan for Laboratory and Modeling Studies of Repository and Radionuclide Chemistry for the Waste Isolation Pilot Plant. Albuquerque, NM: Sandia National Laboratories. SAND90 0266. ERMS 226015.

Brush, L. H. 1995. Systems Prioritization Method-Iteration 2 Baseline Position Paper: Gas Generation in the Waste Isolation Pilot Plant (Unpublished Report, March), Sandia National Laboratories, Albuquerque, New Mexico, ERMS 228740.

Brush, L. H., and Y. Xiong. 2003a. Calculation of Actinide Solubilities for the WIPP Compliance Recertification Application (May 8). Carlsbad, NM: Sandia National Laboratories. ERMS 529131.

Brush, L. H., and Y. Xiong. 2003b. Calculation of Actinide Solubilities for the WIPP Compliance Recertification Application (March 20). Carlsbad, NM: Sandia National Laboratories. AP 098. ERMS 526862.

Brush, L. H., and Y. Xiong. 2003c. Calculation of Actinide Solubilities for the WIPP Compliance Recertification Application (Rev. 1, April 14). Carlsbad, NM: Sandia National Laboratories. AP 098. ERMS 527714.

Brush, L. H., and Y. Xiong. 2003d. Calculation of Organic Ligand Concentrations for the WIPP Compliance Recertification Application (April 14). Carlsbad, NM: Sandia National Laboratories. ERMS 527567.

Brush, L. H. 2005. Results of Calculations of Actinide Solubilities for the WIPP Performance Assessment Baseline Calculations (May 18). Carlsbad, NM: Sandia National Laboratories. ERMS 539800.

Brush, L.H., and J.W. Garner. 2005. Additional Justification of the Insignificant Effect of Np on the Long-Term Performance of the WIPP. Memorandum to D.S. Kessel, February 1, 2005. Carlsbad, NM: Sandia National Laboratories. ERMS 538533.

Brush, L. H., and Y. Xiong, 2005a. Calculation of Actinide Solubilities for the WIPP Performance-Assessment Baseline Calculations (Rev. 0, April 4). Carlsbad, NM: Sandia National Laboratories. AP 120. ERMS 539255.

Brush, L. H., and Y. Xiong, 2005b. Calculation of Organic-Ligand Concentrations for the WIPP Performance-Assessment Baseline Calculations (May 4). Carlsbad, NM: Sandia National Laboratories. ERMS 539635.

Brush, L.H., Y. Xiong, J.W. Garner, A. Ismail, and G.T. Roselle. 2006. Consumption of Carbon Dioxide by Precipitation of Carbonate Minerals Resulting from Dissolution of Sulfate Minerals in the Salado Formation In Response to Microbial Sulfate Reduction in the WIPP. Sandia National Laboratories, Carlsbad, NM. ERMS 544785.

Brush, L. H., Y.-L. Xiong, and J.J. Long. 2009. Results of the Calculations of Actinide Solubilities for the CRA-2009 PABC. Analysis Report, October 7, 2009. Carlsbad, NM: Sandia National Laboratories. ERMS 552201.

Brush, L. H., and P. S. Domski. 2013a. Prediction of Baseline Actinide Solubilities for the WIPP CRA-2014 PA. Analysis Report, January 21, 2013. Carlsbad, NM: Sandia National Laboratories. ERMS 559138.

Brush, L. H., and P. S. Domski. 2013b. Uncertainty Analysis of Actinide Solubilities for the WIPP CRA-2014 PA, (Revision. 1), Supercedes ERMS559278. (Analysis Report, April 5, 2013) Sandia National Laboratories, Carlsbad, New Mexico. ERMS 559712.

Bryson, D. 2015. Letter to Mr. Jonathan D. Edwards, Director, Radiation Protection Division. Subject: Response to the U.S. Environmental Protection Agency Letters Dated February 27, 2015 and June 5, 2015 Regarding the 2014 Compliance Recertification Application. September 5, 2015. Department of Energy, Carlsbad Field Office, Carlsbad, NM.

Buck, E. and D. C. Sassani 2007. Waste Form and In-Drift Colloids-Associated Radionuclide Concentrations: Abstraction and Summary. Sandia National Laboratories, Albuquerque, New Mexico.

Bunyakina, N.V., and D.A. Storozhenko. 2004. $MgSO_4$-$Ln_2(SO_4)_3$-H_2O (Ln = Pr, Nd, Gd) Systems at 25 ºC. Russian Journal of Inorganic Chemistry. Vol. 49, no. 11, 1772-1774.

Bynum, R. V., C. Stockman, Y. Wang, A. Peterson, J. Krumhansl, J. Nowak, J. Cotton, S.J. Patchet, and M.S.Y. Chu. 1996. Implementation of Chemical Controls through a Backfill System for the Waste Isolation Pilot Plant (WIPP). Sandia National Laboratories, Albuquerque, New Mexico. SAND96 2656C.

Choppin, G. R., A. H. Bond, M. Borkowski, M. G. Bronikowski, J. F. Chen, S. Lis, J. Mizera, O. Pokrovsky, N. A. Wall, Y. X. Xia, and R. C. Moore. 2001. Waste Isolation Pilot Plant Actinide Source Term Test Program: Solubility Studies and Development of Modeling Parameters. Albuquerque, NM: Sandia National Laboratories. SAND99 0943. ERMS 518556.

Clayton, D. J. 2008. Memorandum to Larry Brush. Subject: Update to the Calculation of the Minimum Brine Volume for a Direct Brine Release. April 2, 2008. ERMS 548522. Carlsbad, NM: Sandia National Laboratories. ERMS 548522.

Clayton, D. J. 2013. Justification of Chemistry Parameters for Use in BRAGFLO for AP-164, (Revision 1). Carlsbad, NM: Sandia National Laboratories. ERMS 559466.

Colàs, E., M. Grivé, I. Rojo, and L. Duro. 2011. Solubility of $ThO_2.xH_2O$(am) in the Presence of Gluconate. Radiochimica Acta. Vol. 99, no. 5, 269–273.

Cotsworth, E. 2005. Letter to I. Triay. Subject: EPA Letter on Conducting the Performance Assessment Baseline Change (PABC) Verification Test. 4 March 2005. U.S. Environmental Protection Agency, Office of Air and Radiation, Washington, DC. ERMS 538858.

Day, B. 2019. Memo. Subject: Reassessment of Need and Parameter Justification for Modeling Gas Generation due to Radiolysis of Brine and Cellulose/Plastic/Rubber in WIPP for CRA-2019 memo. Carlsbad, NM: Sandia National Laboratories. ERMS 570873.

Deal, D. E., R. J. Abitz, J. Myers, J. B. Case, D. S. Belski, M. L. Martin, and W. M. Roggenthen. 1991. Brine Sampling and Evaluation Program 1990 Report. Carlsbad, NM: U.S. DOE Waste Isolation Pilot Plant Project Office. DOE/WIPP 91 036.

Denbigh, K. 1981. The Principles of Chemical Equilibrium, 4th edition. Cambridge University Press, Cambridge. pg 225.

Derjaguin, B. V., and L. Landau 1941. Theory of stability of strongly charged lyophobic sols and of the adhesion of strongly charged particles in solutions of electrolytes. Acta Physicochim, Vol. 17:633-662.

Domski, P. S. 2015. Memo AP-173, EQ3/6 Database Update: DATA0.FM2. Sandia National Laboratories, Carlsbad, New Mexico. ERMS# 564914.

Domski, P. S., 2018a. Memo. Subject: Recommended Ranges of pcH, Ionic Strength, Total Inorganic Carbon (TIC), and Carbon Dioxide Fugacity for WIPP Baseline Solubility Uncertainty Calculations. June 25, 2018. Sandia National Laboratory, Carlsbad, NM ERMS 570102.

Domski, P. S. 2018b. Memo on the estimation of the solubility product (Log Ksp) for Ca2EDTA.7H2O, and Pitzer parameters for the Na+ / CaEDTA2- pair. Carlsbad, NM: Sandia National Laboratories. ERMS#570202.

Domski, P. S. 2018c. Memo on the estimation of Pitzer parameters for the Mg^{2+} / $CaEDTA^{2-}$, Mg^{2+} / $MgEDTA^{2-}$. Sandia National Laboratories. Carlsbad, NM. ERMS 570855.

Domski, P. S. 2019a. An Update to the EQ3/6 Pitzer Thermodynamic Database DATA0.FM1 with the Creation of DATA0.FM4. Sandia National Laboratories. Carlsbad, New Mexico. ERMS 571052.

Domski, P. S. 2019b. Uncertainty Analysis of Actinide Solubilities for CRA 2019. Sandia National Laboratories, Carlsbad, New Mexico. ERMS 571179.

Domski, P. S. 2019c. Memo. Subject: Technical Aspects of the Baseline Solubility Model for the CRA-2019 PA. Sandia National Laboratories. Carlsbad, New Mexico. ERMS 571535.

Domski, P.S. 2019d. Parameter Problem Report for CRA 2019 Analysis. Material Abbreviated Name: SOLMOD3, Property Abbreviated Name: SOLSOH. April 16, 2019. Sandia National Laboratory. ERMS 572492.

Domski, P. 2019e. Parameter Problem Report for CRA 2019 Analysis. Material Abbreviated Name: SOLMOD3, Property Abbreviated Name: SOLSOH2. April 16, 2019. Sandia National Laboratory. ERMS 572493.

Domski, P. 2019f. Parameter Problem Report for CRA 2019 Analysis. Material Abbreviated Name: SOLMOD3, Property Abbreviated Name: SOLSOH3. April 16, 2019. Sandia National Laboratory. ERMS 572494.

Domski, P. 2019g. Parameter Problem Report for CRA 2019 Analysis. Material Abbreviated Name: SOLMOD3, Property Abbreviated Name: SOLSOH4. April 16, 2019. Sandia National Laboratory. ERMS 572495.

Domski, P. 2019h. Parameter Problem Report for CRA 2019 Analysis. Material Abbreviated Name: SOLMOD3, Property Abbreviated Name: SOLSOH5. April 16, 2019. Sandia National Laboratory. ERMS 572496.

Domski, P. 2019i. Parameter Problem Report for CRA 2019 Analysis. Material Abbreviated Name: SOLMOD3, Property Abbreviated Name: SOLCOH. April 16, 2019. Sandia National Laboratory. ERMS 572497.

Domski, P. 2019j. Parameter Problem Report for CRA 2019 Analysis. Material Abbreviated Name: SOLMOD3, Property Abbreviated Name: SOLSCOH2. April 16, 2019. Sandia National Laboratory. ERMS 572498.

Domski, P. 2019k. Parameter Problem Report for CRA 2019 Analysis. Material Abbreviated Name: SOLMOD3, Property Abbreviated Name: SOLCOH3. April 16, 2019. Sandia National Laboratory. ERMS 572499.

Domski, P. 2019l. Parameter Problem Report for CRA 2019 Analysis. Material Abbreviated Name: SOLMOD3, Property Abbreviated Name: SOLCOH4. April 16, 2019. Sandia National Laboratory. ERMS 572500.

Domski, P. 2019m. Parameter Problem Report for CRA 2019 Analysis. Material Abbreviated Name: SOLMOD3, Property Abbreviated Name: SOLCOH5. April 16, 2019. Sandia National Laboratory. ERMS 572501.

Domski, P. S. and C. Sisk-Scott. 2019. Prediction of Baseline Actinide Solubilities for CRA 2019 with an Updated EQ3/6 Pitzer Thermodynamic Database, DATA0.FM4. Sandia National Laboratories, Carlsbad, New Mexico. ERMS 571178.

Easley, R. A., and R. H. Byrne. 2011. The ionic strength dependence of lead (II) carbonate complexation in perchlorate media. Geochimica et Cosmochimica Acta, Vol. 75: 5638-5647.

Ekberg, C., Y. Albinsson, M. J. Comarmond, and P. L. Brown. 2000. Studies on the Complexation Behavior of Thorium(IV). 1. Hydrolysis Equilibria. Journal of Solution Chemistry, Vol. 29, No. 1.

Evans, N., P. Warwick, T. Lewis, and N. Bryan. 2011. Influence of humic acid on the sorption of uranium (IV) to kaolin, Environmental Chemistry Letters, 9(1):25-30.

Fanghänel, Th., J. I. Kim, P. Paviet, R. Klenze, and W. Hauser. 1994. Thermodynamics of radioactive trace elements in concentrated electrolyte solutions: Hydrolysis of Cm3+ in NaCl-solutions. Radiochimica Acta, Vol. 66/67: 81-87.

Fanghänel, Th., V. Neck, and J. I. Kim. 1995. Thermodynamics of Np(V) in concentrated salt solutions: II. Ion interaction (Pitzer) parameters for Np(V) hydrolysis species and carbonate complexes. Radiochimica Acta, Vol. 69: 169-176.

Fanghänel, Th., and J. I. Kim. 1998. Spectroscopic Evaluation of Thermodynamics of Trivalent Actinides in Brines. Journal of Alloys and Compounds, 271–273: 728–737.

Fanghänel, Th., T. Könnecke, H. Weger, P. Paviet-Hartmann, V. Neck, and J. I. Kim. 1999. Thermodynamics of Cm(III) in concentrated salt solutions: carbonate complexation in NaCl solution at 25 ºC. Journal of Solution Chemistry, Vol. 28: 447-462.

Fellhauer, D., V. Neck, M. Altmaier, J. Lützenkirchen, and T. Fanghänel. 2010. Solubility of Tetravalent Actinides in Alkaline $CaCl_2$ Solutions and Formation of $Ca_4[An(OH)_8]^{4+}$ Complexes: A Study of Np(IV) and Pu(IV) under Reducing Conditions and the Systematic Trend in the An(IV) Series. Radiochimica Acta Vol. 98, nos. 9-11 (Migration 2009), 541–548.

Felmy, A. R., and J. H. Weare. 1986. The prediction of borate mineral equilibria in natural waters: Application to Searles Lake, California. Geochimica et Cosmochimica Acta, Vol. 50: 2771-2783.

Felmy, A. R., D. Rai, and R. W. Fulton. 1990. The solubility of $AmOHCO_3$(c) and the aqueous thermodynamics of the system Na-Am-HCO3-CO3-OH-H2O. Radiochimica Acta, Vol. 50: 193-204.

Felmy, A. R., D. Rai, and M. J. Mason. 1991. The solubility of hydrous thorium (IV) oxide in chloride media: Development of an aqueous ion-interaction model. Radiochimica Acta, Vol. 55: 177-185.

Felmy, A. R., and D. Rai. 1992. An aqueous thermodynamic model for a high valence 4:2 electrolyte Th4+-SO42-in the system Na-K-Li-NH4-Th-SO4-HSO4-H2O to high concentration. Journal of Solution Chemistry, Vol. 21: 407-423.

Felmy, A. R., D. Rai, S. M. Sterner, M. J. Mason, N. Hess, and S. D. Conradson. 1997. Thermodynamic models for highly charged aqueous species: Solubility of Th (IV) hydrous oxide in concentrated NaHCO3 and Na2CO3 solutions. Journal of Solution Chemistry, Vol. 26: 233-248.

Felmy, A. R, and D. Rai, 1999. Application of Pitzer's Equations for Modeling a Review. Journal of Solution Chemistry, Vol. 28:533-553 (SAND99-0340J).

Felmy, A. R., L. M. Onishi, N. S. Foster, J. R. Rustad, D. Rai, M. J. Mason. 2000. An aqueous thermodynamic model for the Pb^{2+} - Na^{+} - K^{+} - Ca^{2+} - Mg^{2+} - H^{+} - Cl^{-} - SO_4^{2-} - H_2O system to high concentration: Application to WIPP brines. Geochimica et Cosmochimica Acta, Vol. 64: 3615-3628.

Felmy, A. R., and M. J. Mason. 2003. An Aqueous Thermodynamic Model for the Complexation of Sodium and Strontium with Organic Chelates Valid to High Ionic Strength. I. Ethylenedinitrilotetraacetic Acid (EDTA). Journal of Solution Chemistry, Vol. 32, No. 4, April 2003.

Felmy, A.R., H. Cho, D. A. Dixon, Y. Xia, N. J. Hess, and Z. Wang. 2006.
The Aqueous Complexation of Thorium with Citrate under Neutral to Basic Conditions. Radiochimica Acta, Vol. 94, 205-212.

Francis, A. J., and J. B. Gillow. 1994. Effects of microbial processes on gas generation under expected Waste Isolation Pilot Plant repository conditions. Sandia National Laboratories, Albuquerque, New Mexico. SAND93-7036.

Francis, A. J., J. B. Gillow, and M. R. Giles. 1997. Microbial gas generation under expected Waste Isolation Pilot Plant repository conditions. Albuquerque, NM: Sandia National Laboratories. SAND96-2582.

Francis, A.J. 1998. Biotransformation of uranium and other actinides in radioactive wastes. Journal of Alloys and Compounds, 271–273: 78–84.

Fuger, J. and F. L. Oetting. 1976. The Chemical Thermodynamics of Actinide Elements and Compounds Part 2. The Actinide Aqueous Ions. Int. Atomic Energy Agency, Vienna, Austria.

Gaona, X., V. Montoya, E. Colas, M. Grive, and L. Duro. 2008. Review of the complexation of tetravalent actinides by ISA and gluconate under alkaline to hyperalkaline conditions. Journal of Contaminant Hydrology, 102(3-4):217-227.

Giambalvo, E. R. 2002. Recommended Parameter Values for Modeling Organic Ligands in WIPP Brines. Carlsbad, NM: Sandia National Laboratories. ERMS 522981.

Giambalvo, E. R. 2002a. Memorandum to L. H. Brush. Subject: Recommended Parameter Values for Modeling An(III) Solubility in WIPP Brines. July 25, 2002. Carlsbad, NM: Sandia National Laboratories. ERMS 522982.

Giambalvo, E. R. 2002b. Memorandum to L. H. Brush. Subject: Recommended Parameter Values for Modeling An(IV) Solubility in WIPP Brines. July 25, 2002. Carlsbad, NM: Sandia National Laboratories. ERMS522986.

Giambalvo, E. R. 2002c. Memorandum to L. H. Brush. Subject: Recommended Parameter Values for Modeling An(V) Solubility in WIPP Brines. July 26, 2002. ERMS 522990. Carlsbad, NM: Sandia National Laboratories. ERMS 522990.

Giambalvo, E. R. 2002d. Memorandum to L.H. Brush. Subject: Recommended μ^o/RT Values for Modeling the Solubility of Oxalate Solids in WIPP Brines, Giambalvo to Brush. July 31, 2002. ERMS 523057.

Giambalvo, E. R. 2003. Release of FMT Database FMT_021120.CHEMDAT. Unpublished memorandum to L.H. Brush, (March 10, 2003). Carlsbad, NM: Sandia National Laboratories. ERMS 526372.

Gillow, J. B., A. J. Francis, C. J. Dodge, R. Harris, T. J. Beveridge, P. V. Brady, and H. W. Papenguth. 1998. Actinide biocolloid formation in brine by halophilic bacteria. 22nd Symposium on Scientific Basis for Nuclear Waste Management held at the 1998 MRS Fall Meeting. Boston, MA, Nov. 30 - Dec 4, 1998.

Gillow J.B., and A.J. Francis. 2006. Microbial gas generation under expected Waste Isolation Pilot Plant Repository Conditions: Final Report. Albuquerque, NM: Sandia National Laboratories. Report BNL 96148 2011 IR.

Gruber, C., A. Legat, M. Pfaffenhuemer, C. Radax, G. Weidler, H. J. Busse, and H. Stan-Lotter. 2004. Halobacterium noricense sp nov., an archaeal isolate from a bore core of an alpine Permian salt deposit, classification of Halobacterium sp NRC-1 as a strain of H-salinarum and emended description of H-salinarum. Extremophiles, Vol. 8(6):431-439.

Haberman, J. H., and D. J. Frydrych. 1988. Corrosion Studies of A216 Grade WCA Steel in Hydrothermal Magnesium-Containing Brines. Materials Research Society Symposium Proceedings: Scientific Basis for Nuclear Waste Management XI Eds. M.J. Apted and R.E. Westerman. Pittsburgh: Materials Research Society. pp. 761-72.

Hansen, C.W., L. H. Brush, M.B. Gross, F. D. Hansen, B. Park, J. S. Stein, and T. W. Thompson. 2003. Effects of Supercompacted Waste and Heterogeneous Waste Emplacement on Repository Performance (Revision 1). Carlsbad, NM: Sandia National Laboratories. ERMS 532475.

Harvie, C. E., N. Møller, and J. H. Weare. 1984. The prediction of mineral solubilities in natural waters: The Na-K-Mg-Ca-H-Cl-SO_4-OH-HCO_3-CO_3-CO_2-H_2O system to high ionic strengths at 25C. Geochimica et Cosmochimica Acta, Vol. 48: 723-751. TIC: 239849.

Helton, J. C., J. E. Bean, J. W. Berglund, F. J. Davis, K. Economy, J. W. Garner, J. D. Johnson, R. J., MacKinnon, J. Miller, D. G. O'Brien, J.L. Ramsey, J. D. Schreiber, A. Shinta, L. N. Smith, D. M. Stoelzel, C. Stockman, and P. Vaughn. 1998. Uncertainty and Sensitivity Analysis Results Obtained in the 1996 Performance Assessment for the Waste Isolation Pilot Plant. Albuquerque, NM: Sandia National Laboratories. SAND98-0365. ERMS 252619.

Hu, J. D., Y. Zevi, X. M. Kou, J. Xiao, X. J. Wang, and Y. Jin. 2010. Effect of dissolved organic matter on the stability of magnetite nanoparticles under different pH and ionic strength conditions. Science of the Total Environment, Vol. 408(16):3477-3489.

Hummel, W., G. Anderegg, I. Puigdomenech, L. Rao, and O. Tochiyama. 2005. Chemical Thermodynamics of Compounds and Complexes of U, Np, Pu, Am, Tc, Zr, Ni and Se with Selected Organic Ligands. OECD Nuclear Energy Agency, Data Bank, Issy-les-Moulineaux, France, Elsevier B.B. Amsterdam, The Netherlands. Chemical Thermodynamics, Vol. 9, p. 1088.

Ismail, A. E., H. Deng, J.-H. Jang, and T. J. Wolery. 2009. Memorandum to Records. Subject: Verification of FMT database and conversion to EQ3/6 format. Carlsbad, NM: Sandia National Laboratories. ERMS 550689.

Jang, J. J. 2017. Solubility Model for the Fe^{+2} - Mg^{+2} - Na^{+} - Ca^{+2} - H^{+} - Cl^{-} - oxalate^{-2} - EDTA^{-4} - citrate^{-3} - H_2O Systems, Sandia National Laboratories, Carlsbad, New Mexico, ERMS 568758.

Jang, J. 2019. Analysis plan for derivation and addition of equilibrium constants and Pitzer interaction parameters to the WIPP Geochemical Thermodynamic Database. AP-182, Revision 0. Sandia National Laboratories. Carlsbad, NM. ERMS 571074.

Janot, N., M. F. Benedetti, and P. E. Reiller. 2013. Influence of solution parameters on europium(III), alpha-Al2O3, and humic acid interactions: Macroscopic and time-resolved laser-induced luminescence data. Geochimica Et Cosmochimica Acta, Vol. 123:35-54.

Johnson, G. L., and L. M. Toth. 1978. Plutonium(IV) and thorium(IV) hydrous polymer chemistry. Oak Ridge National Laboratory, Oak Ridge, Tennessee. ORNL/TM 6365.

Kelly, T. 2010. Untitled letter with enclosure to D. C. Moody with fourth set of CRA comments and requests for additional information, February 22, 2010. U.S. Environmental Protection Agency, Washington, DC.

Khalili, F. I., V. Symeopoulos, J.-F. Chen, and G. R. Choppin. 1994. Solubility of Nd in Brine. Radiochimica Acta, Vol. 66/67, 51-54.

Kim, J. I. 1992. Actinide colloid generation in groundwater. Radiochimica Acta, Vol. 52/53 (pt. 1):71-81.

Kim, J. L. and T. Sekine 1991. Complexation of neptunium(V) with humic acid. Radiochimica Acta, Vol. 55(4):187-192.

Kim, S. S., M. H. Baik, J. W. Choi, H. S. Shin, and J. I. Yun. 2010. The Dissolution of ThO_2(cr) in Carbonate Solutions and a Granitic Groundwater. Journal of Radioanalytical and Nuclear Chemistry, Vol. 286, 91–97.

Kim, S., C. Marrs, M. Nemer, and J-H Jang. 2017. Solubility Model for Ferrous Iron Hydroxide, Hibbingite, Siderite, and Chukanovite in High Saline Solutions of Sodium Chloride, Sodium Sulfate, and Sodium Carbonate. ACS Earth Space Chem., 1, 647−663.

Kirchner, T. B. 2013. Sensitivity of the CRA-2014 Performance Assessment Releases to Parameters. May 17, 2013. Sandia National Laboratories, Carlsbad NM. ERMS 560043.

Kirkes, L. 2019. Lead Inventory Impact on Gas Generation. Sandia National Laboratories. Carlsbad, NM. ERMS# 571255.

Könnecke, Th., Th. Fanghänel, and J. I. Kim, 1997. Thermodynamics of trivalent actinides in concentrated electrolyte solutions: Modelling the chloride complexation of Cm(III). Radiochimica Acta, Vol. 76: 131-135.

Labonne-Wall, N., G. R. Choppin, C. Lopez, and J.-M. Monsallier. 1999. Interaction of uranyl with humic and fulvic acids at high ionic strength. Actinide Speciation in High Ionic Strength Media, edited by Reed, D. T., S. B. Clark, and Linfeng Rao. Plenum Publishers, New York.

Lambert, S. J. 1992. Geochemistry of the Waste Isolation Pilot Plant (WIPP) site, southeastern New Mexico, U.S.A. Applied Geochemistry, 7: 513-531.

Langmuir, D. 1965. Stability constants of carbonates in the system MgO-CO_2-H_2O. The Journal of Geology, Vol. 73: 730-754.

Laszak, I., and G. R. Choppin. 2001. Interaction study between Ca2+ and humic acids in brine media. Radiochimica Acta, Vol. 89(10):653-659.

Lead, J. R., J. Hamiltontaylor, N. Hesketh, M. N. Jones, A. E. Wilkinson, and E. Tipping. 1994. A Comparative-Study of Proton and Alkaline-Earth Metal-Binding by Humic Substances. Analytica Chimica Acta, Vol. 294(3):319-327.

Leigh, C., J. Kanney, L. Brush, J. Garner, R. Kirkes, T. Lowry, M. Nemer, J. Stein, E. Vugrin, S. Wagner, and T. Kirchner. 2005. 2004 Compliance Recertification Application Performance Assessment Baseline Calculation (Revision 0). Carlsbad, NM: Sandia National Laboratories. ERMS 541521.

Lide, D. R. 1991. CRC Handbook of Chemistry and Physics, 72nd ed., CRC Press, Boca Raton, 2486 pgs.

Lide, D. R. 1997. CRC Handbook of Chemistry and Physics, 77th ed., CRC Press, Boca Raton, 2496 pgs.

Lide, D. R. 2006. CRC Handbook of Chemistry and Physics, 87th ed., CRC Press, Boca Raton, 2608 pgs.

Lu, Y. F., and H. E. Allen. 2002. Characterization of copper complexation with natural dissolved organic matter (DOM) - link to acidic moieties of DOM and competition by Ca and Mg. Water Research, Vol. 36(20):5083-5101.

Lucchini, J.-F., M. Borkowski, M. K. Richmann, S. Ballard, and D. T. Reed. 2007. Solubility of Nd^{3+} and UO_2^{2+} in WIPP Brine as Oxidation-State Invariant Analogs for Plutonium. Journal of Alloys and Compounds, Vol. 444–445, 506–511.

Maes, A., J. Debrabandere, and A. Cremers. 1988. A Modified Schubert Method for the Measurement of the Stability of Europium Humic-Acid Complexes in Alkaline Conditions. Radiochimica Acta, Vol. 44-45:51-57.

Maes, A., J. Debrabandere, and A. Cremers. 1991. Complexation of Eu-3+ and Am-3+ with Humic Substances. Radiochimica Acta, Vol. 52-53:41-47.

Makino, H., T. Yajima, H. Yoshikawa, M. Yui, and N. Sasaki. 1993. Nd(III) Hydrolysis Constants and Solubilities of Nd(III) Hydroxide. Nippon Kagaku Kaishi. Vol. 5, 445-450.

Mariner, P. E. 2014. Analysis Plan for the Evaluation of Humic-Actinide Complexation for WIPP Conditions. , Revision 0. Sandia National Laboratories, Carlsbad, New Mexico. AP-167.

Mariner, P. E., and D. C. Sassani. 2014. Analysis report for WIPP colloid model constraints and performance assessment parameters. Sandia National Laboratories, Carlsbad, New Mexico. SAND2014-1961.

Mariner, P. E. 2016. Actinide(IV)-Humic Complexation in the WIPP Performance Assessment. Sandia National Laboratories, Carlsbad, New Mexico. ERMS 567222.

Mariner, P. E. 2018. Actinide(III)-Humic Complexation in the WIPP Performance Assessment. Sandia National Laboratories, Carlsbad, New Mexico. ERMS 569599.

Mariner, P. E. 2019. Memo. Subject: A summary of humic colloid parameter values to be implemented in the CRA-2019 Deferred Performance Assessment Memo. April 15, 2019. Sandia National Laboratories, Carlsbad, New Mexico. ERMS 571250.

McGenity, T. J., R. T. Gemmell, W. D. Grant, and H. Stan-Lotter. 2000. Origins of halophilic microorganisms in ancient salt deposits. Environmental Microbiology, Vol. 2(3):243-250.

Meinrath, D., and J.I. Kim. 1991. Solubility Products of Different Am(III) and Nd(III) Carbonates. European Journal of Solid State and Inorganic Chemistry. Vol. 28, 383-388.

Meinrath, G., and H. Takeishi. 1993. Solid-Liquid Equilibria of Nd^{3+} in Carbonate Solutions. Journal of Alloys and Compounds, Vol. 194, no. 1, 93–99.

Mendenhall, F. T., and W. Gerstle. 1995. WIPP Anhydrite Fracture Modeling, Systems Prioritization Method - Iteration 2 Baseline Position Paper: Disposal Room and Cutting Models. Appendix F: Comparison of Two Geomechanical Analysis Codes for WIPP Disposal Room Modeling: SANCHO and SPECTROM-32. Albuquerque, NM: Sandia National Laboratories. ERMS 239830.

Migdisov, A. A., and A. E. Williams-Jones. 2007. An Experimental Study of the Solubility and Speciation of Neodymium (III) Fluoride in F-Bearing Aqueous Solutions. Geochimica et Cosmochimica Acta, Vol. 71, no. 12, 3056–3079.

Millero, F.J., and R. H. Byrne. 1984. Use of Pitzer equations to determine the media effect on the formation of lead chloro complexes. Geochimica et Cosmochimica Acta, Vol. 48 (5), 1145-1150.

Mizera, J., A. H. Bond, G. R. Choppin, and R. C. Moore. 1999. Dissociation Constants of Carboxylic Acids At High Ionic Strengths In: Reed, D. T., S. B. Clark, L. Rao (eds) Actinide Speciation in High Ionic Strength MediaKluwer Academic I Plenum Publishers, New York, 1999. Pp 113-124.

Molecke, M. A. 1979. Gas Generation From Transuranic Waste Degradation: Data Summary and Interpretation, , Sandia National Laboratories, Albuquerque, New Mexico. SAND79-1245.

Moog, H. C., S. Hagemann, and A. V. Rumyantsev. 2004. Isopiestic investigation of the systems FeCl2-(Na, K, Mg, Ca)Cln-H2O at 298.15 K. ZEITSCHRIFT FUR PHYSIKALISCHE CHEMIE-INTERNATIONAL JOURNAL OF RESEARCH IN PHYSICAL CHEMISTRY & CHEMICAL PHYSICS 218, 1063-1087.

Moore, R. C. 1996. Memo to C.F. Novak. Subject: Final Model Parameters for Deprotonation of Lactic Acid, Citric Acid, Oxalic Acid, and EDTA and Complexation Of Acetate, Lactate, Citrate, Oxalate, and EDTA with NpO_2^+, Am^{3+}, Th^{4+}, and UO_2^{2+} in NaCl media. February 22, 1996. Albuquerque: Sandia National Laboratories. WPO 35307.

Moore, R. C., M. Borkowski, M. G. Bronikowski, J. Chen, O. S. Pokrovsky, Y. Xia, and G. R. Choppin, 1999. Thermodynamic modeling of actinide complexation with acetate and lactate at high ionic strength. Journal of Solution Chemistry, Vol. 28: 521-531.

Moriyama, H., T. Sasaki, T. Kobayashi, and I. Takagi. 2005. Systematics of Hydrolysis Constants of Tetravalent Actinide Ions. Journal of Nuclear Science and Technology, Vol. 42:7, 626-635, DOI: 10.1080/18811248.2004.9726430.

Morss, L. R., and C. W. Williams. 1994. Synthesis of crystalline americium hydroxide, $Am(OH)_3$, and determination of its enthalpy of formation; estimation of the solubility-product constants of actinide (III) hydroxides. Radiochimica Acta, Vol. 66/67; 89-93.

Moser, C., R. Kautenburger, and H. Philipp Beck. 2012. Complexation of europium and uranium by humic acids analyzed by capillary electrophoresis-inductively coupled plasma mass spectrometry. Electrophoresis, Vol. 33(9-10):1482-1487.

Moulin, C., B. Amekraza, S. Hubert, and V. Moulin. 2001. Study of Thorium Hydrolysis Species by Electrospray-Ionization Mass Spectrometry. Analytica Chimica Acta, Vol. 441: 269–79.

Neck, V., Th. Fanghanel, G. Rudolph, and J. I. Kim. 1995. Thermodynamics of Np(V) in concentrated salt solutions: Chloride complexation and ion interaction (Pitzer) parameters for the NpO_2^+ ion. Radiochimica Acta, Vol. 69: 39-47.

Neck, V., and J. I. Kim. 2001. Solubility and hydrolysis of tetravalent actinides. Radiochimica Acta, Vol. 89:1-16.

Neck, V., R. Muller, M. Bouby, M. Altmaier, J. Rothe, M. A. Denecke, and J. I. Kim. 2002. Solubility of amorphous Th(IV) hydroxide - application of LIBD to determine the solubility product and EXAFS for aqueous speciation. Radiochimica Acta, Vol. 90(9-11):485-494.

Neck, V., M. Altmaier, R. Muller, A. Bauer, T. Fanghänel, and J. I. Kim. 2003. Solubility of crystalline thorium dioxide. Radiochimica Acta, Vol. 91(5):253-262.

Neck, V., M. Altmaier, and Th. Fanghänel. 2006. Ion Interaction (SIT) Coefficients for the Th4+ Ion and Trace Activity Coefficients in NaClO4, NaNO3 and NaCl Solution Determined by Solvent Extraction with TBP. Radiochimica Acta, Vol. 94: 501–07.

Neck, V., M. Altmaier, T. Rabung, J. Luetzenkirchen, and T. Fanghänel. 2009. Thermodynamics of Trivalent Actinides and Neodymium in NaCl, $MgCl_2$, and $CaCl_2$ Solutions: Solubility, Hydrolysis, and Ternary Ca-M(III)-OH Complexes. Pure and Applied Chemistry, Vol., 81, no. 9, 1555-1568.

Nemer, M. B., and J. S. Stein. 2005. Analysis Package for BRAGFLO, 2004 Compliance Recertification Application Performance Assessment Baseline Calculation (June 28). Carlsbad, NM: Sandia National Laboratories. ERMS 540527.

Nemer, M. B., J. S. Stein, and W. Zelinski. 2005. Analysis Report for BRAGFLO Preliminary Modeling Results with New Gas Generation Rates Based Upon Recent Experimental Results. Carlsbad, NM: Sandia National Laboratories. ERMS 540527.

Nemer, M., Y. Xiong, A. E. Ismail, and J. Jang. 2011. Solubility of $Fe_2(OH)_3Cl$ (pure-iron end-member of hibbingite) in NaCl and Na_2SO_4 brines. Chemical Geology, Vol. 280: 26-32.

Nitsche, H., K. Roberts, R. C. Gatti, T. Prussin, K. Becraft, S. C. Leung, S. A. Carpenter, and C. F. Novak. 1992. Plutonium Solubility and Speciation Studies in a Simulant of Air Intake Shaft Water from the Culebra Dolomite at the Waste Isolation Pilot Plant. Sandia National Laboratories, Albuquerque, NM. SAND92-0659.

Nitsche, H., K. Roberts, R. Xi, T. Prussin, K. Becraft, I. Al Mahamid, H. B. Silber, S. A. Carpenter, R. C. Gatti, and C. F. Novak. 1994. Long Term Plutonium Solubility and Speciation

Studies in a Synthetic Brine. Radiochimica Acta, Special Issue: Chemistry and Migration Behaviour of Actinides and Fission Products in the Geosphere, Proceedings of the Fourth International Conference, Charleston, SC, December 12-17, 1993. Munich: R. Oldenbourg Verlag. Vol. 66/67, 3-8.

Novak, C. F., 1996a. Development of the FMT chemical transport simulator: coupling aqueous density and mineral volume fraction to phase compositions. Journal of Contaminant Hydrology. 21(1-4). pp. 297-310.

Novak, C. F., 1996b. Memo to E. J. Nowak. Subject: Preliminary inorganic model for thorium solubility in WIPP brines, in database file HMW_3Th5_960119.CHEMDAT. January 19, 1996. Albuquerque, NM: Sandia National Laboratories. ERMS 230930.

Novak, C. F., and R. C. Moore. 1996. Memo to M. Siegel. Subject: Estimates of Dissolved Concentrations for ID, IV, V, and VI Actinides in Salado and Castile Brine Under Anticipated Repository Conditions. Sandia National Laboratories. Albuquerque, NM. WPO 43072.

Novak, C. F., H. Nitsche, H. B. Silber, K. E. Roberts, P. C. Toretto, T. Prussin, K. A. Becraft, S. A. Carpenter, D. E. Hobart, Al Rifai, and I. Al Mahamid. 1996a. Neptunium(V) and Neptunium(VI) solubilities in synthetic brines of interest to the Waste Isolation Pilot Plant (WIPP), SAND96-2472C.

Novak, C. F., R. C. Moore, and R. V. Bynum. 1996b. Prediction of Dissolved Actinide Concentrations in Concentrated Electrolyte Solutions: A Conceptual Model and Model Results for the Waste Isolation Pilot Plant (WIPP), Proceedings of the International Conference on Deep Geological Disposal of Radioactive Waste, Winnipeg, Manitoba, Canada, September 16-19, 1996.

Novak, C. F., I. Al Mahamid, K. A. Becraft, S. A. Carpenter, N. Hakem, and T. Prussin. 1997. Measurement and thermodynamic modeling of Np(V) solubility in aqueous K2CO3 solutions to high concentrations. Journal of Solution Chemistry, Vol. 26: 681-697.

Novak, C.F. 1997. Memorandum to R.V. Bynum Subject: Calculation of Actinide Solubilities in WIPP SPC and ERDA-6 Brines under MgO Backfill Scenarios Containing either Nesquehonite or Hydromagnesite as the Mg-CO3 Solubility-Limiting Phase. April 21, 1997. Albuquerque, NM: Sandia National Laboratories. ERMS 246124.

Nowak, E. J. 2005. Memo to L. Brush. Recommended Change in the FMT Thermodynamic Data Base, Nowak to Brush, 01 April 05, ERMS 539227.

Okamoto, Y., Y. Mochizuki, and S. Tsushima. 2003. Theoretical study of hydrolysis reactions of tetravalent thorium ion. Chemical Physics Letters 373 (2003) 213–217.

Oren, A. 2011. Thermodynamic limits to microbial life at high salt concentrations. Environmental Microbiology, Vol. 13: 1908-1923.

Östhols, E., J. Bruno, and I. Grenthe. 1994. On the Influence of Carbonate on Mineral Dissolution. III. The Solubility of Microcrystalline ThO_2 in CO_2-H_2O Media. Geochimica et Cosmochimica Acta, Vol. 58, 613-623.

Palomino, D., and S. Stoll. 2013. Fulvic acids concentration and pH influence on the stability of hematite nanoparticles in aquatic systems. Journal of Nanoparticle Research, Vol. 15(2).

Papenguth, H. W. 1996. H. W. Papenguth to Christine T. Stockman: Parameter Record Package for Colloidal Actinide Source Term Parameters, Attachment A: Rationale for Definition of Parameter Values for Humic Substances May 7,1996. Sandia National Laboratories, Carlsbad, New Mexico. ERMS 416348.

Papenguth, H. W., and Y. K. Behl. 1996. Test Plan for Evaluation of Colloid-Facilitated Actinide Transport at the Waste Isolation Pilot Plant. Sandia National Laboratories, Carlsbad, New Mexico. Test Plan TP 96 01. ERMS 417319.

Paviet, P., T. Fanghänel, R. Lenze and J.I. Kim, 1996. Thermodynamics of curium (III) in concentrated electrolyte solutions: Formation of sulfate complexes in $NaCl/Na_2SO_4$ solutions. Radiochemica Acta, Vol. 74:99-103.

Peretrukhin, V. F., S. V. Kryutchkov, V. I. Silin, and I. G. Tananaev. 1996. Determination of the Solubility of Np(IV)-(VI), Pu(III)-(VI), Am(III)-(VI), and Tc(IV), (V) Hydroxo Compounds in 0.5-14 M NaOH Solutions (Revision 0). Richland, WA: Westinghouse Hanford Co. WHC-EP 0897.

Pitzer, K. S. 1973. Thermodynamics of electrolytes. I. Theoretical basis and general equations. The Journal of Physical Chemistry, Vol. 77: 268-277.

Pitzer, K. S., and G. Mayorga. 1973. Thermodynamics of electrolytes. II. Activity and osmotic coefficients for strong electrolytes with one or both ions univalent. The Journal of Physical Chemistry, Vol. 77: 2300-2308.

Pitzer, K. S, and J. J. Kim. 1974. Thermodynamics of electrolytes. IV. Activity and osmotic coefficients for mixed electrolytes. Journal of the American Chemical Society, Vol. 96: 5701-5707.

Pitzer, K. S. 1975. Thermodynamics of electrolytes. V. Effects of higher-order electrostatic terms. Journal of Solution Chemistry, Vol. 4: 249-265.

Pitzer, K. S., and L. F. Silvester. 1976. Thermodynamics of electrolytes. VI. Weak electrolytes including H_3PO_4. Journal of Solution Chemistry, Vol. 5: 269-278.

Pitzer, K. S. 1991. Ion interaction approach: theory and data correlation, in Pitzer, K.S., ed. Activity Coefficients in Electrolyte Solutions, 2nd edition, Ch. 3, 75-153, CRC Press, Boca Raton, Florida. TIC: 251799.

Pokrovsky, O., M. G. Bronikowski, R. C. Moore, and G. R. Choppin, 1998. Interaction of neptunyl(V) and uranyl(VI) with EDTA in NaCl media: Experimental study and Pitzer modeling. Radiochimica Acta, Vol. 80: 23-29.

Popielak, R. S., R. L. Beauheim, S. R. Black, W. E. Coons, C. T. Ellingson, and R. L. Olsen. 1983. Brine Reservoirs in the Castile Formation, Waste Isolation Pilot Plant Project, Southeastern New Mexico. Carlsbad, NM: U.S. Department of Energy. TME-3153.

Pourret, O., M. Davranche, G. Gruau, and A. Dia. 2007. Rare earth elements complexation with humic acid. Chemical Geology, Vol. 243(1-2):128-141.

Powell, K. J., P. L. Brown, R. H. Byrne, T. Gajda, G. Hefter, A.-K Luez, S. Sjoberg, and H. Wanner. 2009. Chemical speciation of environmentally significant metals with inorganic ligands. Part 3: the Pb^{2+} + OH^-, Cl^-, CO_3^{2-}, SO_4^{2-}, and PO_4^{3-} systems (IUPAC Technical Report). Pure and Applied Chemistry 81 (12), 2425-2476.

Powell, B. A., Z. R. Dai, M. Zavarin, P. H. Zhao, and A. B. Kersting. 2011. Stabilization of Plutonium Nano-Colloids by Epitaxial Distortion on Mineral Surfaces. Environmental Science & Technology, Vol. 45(7):2698-2703.

Powers, D. W., S. J. Lambert, S. E. Shaffer, I. R. Hill, and W. D. Weart, eds. 1978. Geological Characterization Report, Waste Isolation Pilot Plant (WIPP) Site, Southeastern New Mexico. Albuquerque, NM: Sandia National Laboratories. SAND78-1596. 2vols. ERMS 205448.

Rabung, T., M. Altmaier, V. Neck, and T. Fanghänel. 2008. A TRLFS Study of Cm(III) Hydroxide Complexes in Alkaline CaCl2 Solutions. Radiochimica Acta, Vol. 96, nos. 9-11 (Migration 2007), 551–559.

Rai, D., A. R. Felmy, and R. W. Fulton. 1995a. Nd3+ and Am3+ ion interaction with sulfate ion and their influence on NdPO4(c) solubility. Journal of Solution Chemistry, Vol. 24: 879–95.

Rai, D., A. R. Felmy, D. Moore, and M. J. Mason. 1995b. The Solubility of Th(IV) and U(IV) Hydrous Oxides in Concentrated NaHCO3 and Na2CO3 Solutions, Scientific Basis for Nuclear Waste Management XVIII, Materials Research Society Symposium Proceedings, Symposium Held October 23-27, 1994, Kyoto, Japan. Eds. T. Murakami and R. C. Ewing. Pittsburgh, PA: Materials Research Society. Vol. 353, 1143-1150.

Rai, D., A. R. Felmy, S. M. Sterner, D. A. Moore, M. J. Mason, and C. F. Novak. 1997. The Solubility of Th(IV) and U(IV) Hydrous Oxides in Concentrated NaCl and MgCl2 Solutions. Radiochimica Acta, Vol. 79, 239-247

Rai, D., D. A. Moore, C. S. Oakes, and M. Yui. 2000. Thermodynamic Model for the Solubility of Thorium Dioxide in the Na+-Cl–-OH–-H2O System at 23 °C and 90 °C. Radiochimica Acta. Vol. 88, 297-306.

Rai, D., M. Yui, N. J. Hess, A. R. Felmy, and D. A. Moore. 2005. Thorium Reactions in Borosilicate-Glass/Water Systems. Radiochimica Acta, Vol. 93, no. 8, 443-455.

Rai, D., M. Yui, D. A. Moore, G. J. Lumetta, K. M. Rosso, Y. Xia, A. R. Felmy, and F. N. Skomurski. 2008. Thermodynamic Model for ThO2(am) Solubility in Alkaline Silica Solutions. Journal of Solution Chemistry, Vol. 37, no. 12, 1725-1746.

Rai, D., M. Yui, D. A. Moore, and L. Rao. 2009. Thermodynamic Model for ThO2(am) Solubility in Isosaccharinate Solutions. Journal of Solution Chemistry, Vol. 38, no. 12, 1573-1587.

Rai, D., M. Yui, A. Kitamura, and B. Grambow. 2011. Thermodynamic Approach for Predicting Actinide and Rare Earth Concentrations in Leachates from Radioactive Waste Glasses. Journal of Solution Chemistry, Vol. 40, 1473-1504.

Rand, M. H., F. J. Mompean, J. Perrone, and M. Illemasséne. 2008. Chemical Thermodynamics of Thorium. Paris, France, OECD Pub.

Rao, L., D. Rai, and A. R. Felmy. 1996a. Solubility of Nd(OH)3(c) in 0.1 M NaCl Aqueous Solution at 25 ºC and 90 ºC. Radiochimica Acta, Vol. 72, no. 3, 151–155. ERMS 243171.

Rao, L., D. Rai, A. R. Felmy, R. W. Fulton, and C. F. Novak. 1996b. Solubility of NaNd(CO3)3·6H2O(c) in Concentrated Na2CO3 and NaHCO3 Solutions. Radiochimica Acta, Vol. 75, 141–147.

Rao, L., D. Rai, A. R. Felmy, and C. F. Novak. 1999. Solubility of NaNd(CO3)2·6H2O(c) in Mixed Electrolyte (Na-Cl-CO3-HCO3) and Synthetic Brine Solutions, Actinide Speciation in High Ionic Strength Media: Experimental and Modeling Approaches to Predicting Actinide Speciation and Migration in the Subsurface. Proceedings of an American Chemical Society Symposium on Experimental and Modeling Studies of Actinide Speciation in Non-Ideal Systems, Held August 26-28, 1996, in Orlando, Florida. Eds. D.T. Reed, S.B. Clark, and L. Rao. New York, NY: Kluwer Academic/Plenum Publishers. 153-169.

Reed, D., J. Swanson, J. F. Lucchini, and M. Richmann. 2013a. Intrinsic, mineral and microbial colloid enhancement parameters for the WIPP actinide source term. Los Alamos National Laboratory, Los Alamos, NM. LANL-CO ACRSP/LCO-ACP-18.

Reed, D. T., J. F. Lucchini, M. K. Richmann, and M. Borkowski. 2013b. Long-term plutonium speciation in Fe-dominated high ionic-strength brines. Technical Abstracts of the ABC Salt III Workshop, April 15-17, 2013. Santa Fe, New Mexico.

Reed, D.T., J. Lucchini, M. Morkowski, M. Richmann. 2010. Reduction of Higher-Valent Plutonium by Iron under WIPP-Relevant Conditions: Data Summary and Recommendations. Rev. 0. Los Alamos National Laboratory, Los Alamos, New Mexico. LCO-ACP-09.

Reed, D. T., J. Swanson, and F. Stanley. 2019. LANL/ACRSP Parameter Recommendations for the CRA-2019 Deferred Performance Assessment. Los Alamos National Laboratory, Los Alamos, NM. LANL-CO ACRSP/;CP-ACP-24. LA-UR 19-22787.

Reiller, P., V. Moulin, F. Casanova, and C. Dautel. 2003. On the study of Th(IV)-humic acid interactions by competition sorption studies with silica and determination of global interaction constants. Radiochimica Acta, Vol. 91(9):513-524.

Reiller, P. E., N. D. M. Evans, and G. Szabo. 2008. Complexation parameters for the actinides(IV)-humic acid system: a search for consistency and application to laboratory and field observations. Radiochimica Acta, Vol. 96(6):345-358.

Roberts, R. M., R. L. Beauheim, and P. S. Domski. 1999. Hydraulic Testing of Salado Formation Evaporites at the Waste Isolation Pilot Plant Site: Final Report. Sandia National Laboratories, Albuquerque, NM. SAND 98-2537.

Robie, R. A., and B. S. Hemingway. 1973. The enthalpies of formation of nesquehonite, $MgCO_3 \cdot 3H_2O$, and hydromagnesite, $5MgO \cdot 4CO_2 \cdot 5H_2O$. Journal of Research of the U. S. Geological Survey**,** Vol. 1: 543-547.

Roselle, G. T. 2009. Iron and Lead Corrosion in WIPP-Relevant Conditions: Six Month Results. Milestone Report. Carlsbad, NM: Sandia National Laboratories. October 7, 2009. ERMS 552218.

Roselle, G. T. 2010. Iron and Lead Corrosion in WIPP-Relevant Conditions: 12 Month Results. Milestone report. Carlsbad, NM: Sandia National Laboratories. October 14, 2010. ERMS 554383.

Roselle, G. T. 2011a. Iron and Lead Corrosion in WIPP-Relevant Conditions: 18 Month Results. Milestone report, Carlsbad, NM: Sandia National Laboratories. January 5, 2011. ERMS 554715.

Roselle, G. T. 2011b. Iron and Lead Corrosion in WIPP-Relevant Conditions: 24 Month Results. Milestone report. Carlsbad, NM: Sandia National Laboratories. May 3, 2011. ERMS 555246.

Roselle, G. T. 2011c. Determination of pCH+ Correction Factors in Brines. Milestone Report. Carlsbad, NM: Sandia National Laboratories. December 1, 2011. ERMS 556699.

Roselle, G. T. 2013a. Anoxic corrosion of steel and lead in Na-Cl(+/-)Mg dominated brine. Technical Abstracts of the ABC Salt III Workshop, Santa Fe, New Mexico April 15-17 2013. Page 43. LA-UR-13-21114.

Roselle, G. T. 2013b. Letter from G. Roselle to S. Dunagan. Subject: Summary of colloid parameters to be implemented in the CRA-2014 PA. February 15, 2013. Sandia National Laboratories, Carlsbad, New Mexico. ERMS 559205

Roselle, G. T. 2013c. Determination of Corrosion Rates from Iron/Lead Corrosion Experiments to be used for Gas Generation Calculations (Revision 1). Analysis Report, January 23, 2013. Sandia National Laboratories, Carlsbad, NM. ERMS 559077.

Roy, R. N., K. M. Vogel, C. E. Good, W. B. Davis, L. N. Roy, D. A. Johnson, A. R. Felmy, and K. S. Pitzer. 1992. Activity coefficients in electrolyte mixtures: HCl + ThCl4 + H2O for 5-55 ºC. Journal of Physical Chemistry, Vol. 96: 11065-11072.

Runde, W., G. Meinrath, and J.I. Kim. 1992. A Study of Solid-Liquid Phase Equilibria of Trivalent Lanthanide and Actinide Ions in Carbonate Systems. Radiochimica Acta, Vol. 58/59, 93–100.

Runde, W., and J. I. Kim. 1994. Untersuchungen der Übertragbarkeit von Labordaten natürliche Verhältnisse. Chemisches Verhalten von drei- und fünfwertigem Americium in salinen NaCl-Lösungen. Munich: Institut für Radiochemie, Technische Universität München. (Available from National Technical Information Service, 555 Port Royal Road, Springfield, VA, 22161, 703/487-4650 as DE 95752244.) Report RCM-01094.

Ryan J. L., and D. Rai. 1987. Thorium (IV) hydrous oxide solubility, Inorganic Chemistry, Vol. 26: 4141-4142.

Sakuragi, T., S. Sawa, S. Sato, T. Kozaki, T. Mitsugashira, M. Hara, and Y. Suzuki. 2005. Interaction of americium(III) with humic acid over wide pH region. Journal of Radioanalytical and Nuclear Chemistry, Vol. 265(3):349-353.

Sanchez, L. C., and H. R. Trellue. 1996. Memorandum to T. Hicks. Subject: Estimation of Maximum RH-TRU Thermal Heat Load for WIPP. Albuquerque, NM: Sandia National Laboratories. January 17, 1996. WPO 31165. ERMS 231165.

Sarathi, R., 2019. Memo to R. Camphouse. Subject: Explanation of CAPMIC definition and usage in PA calculations. January 14, 2019. Sandia National Laboratories, Carlsbad, NM. ERMS 570685.

Sassani, D. C. 2011. Analysis Plan for Evaluating Constraints on Colloid Parameters in the WIPP Repository. AP-152. Sandia National Laboratories, Albuquerque, New Mexico. ERMS 555186.

Shi, H., M. Chu, and P. Zhang. 2010. Optical properties of UO2 and PuO2. Journal of Nuclear Materials, Vol. 400:151-156.

Shock, E. L.; D. C. Sassani, M. Willis, and D. A. Sverjensky. 1997. Inorganic Species in Geologic Fluids: Correlations Among Standard Molal Thermodynamic Properties of Aqueous Ions and Hydroxide Complexes. Geochimica et Cosmochimica Acta, Vol. 61 907−950.

Shrader, T. 2016. Response to the U.S. Environmental Protection Agency Letters dated June 5, 2015, July 30, 2015, and February 26, 2016, Regarding the 2014 Compliance Recertification Application.

Silva, R.J. 1982. The Solubilities of Crystalline Neodymium and Americium Trihydroxides. Berkeley, CA: Lawrence Berkeley National Laboratory. LBL-15055.

Silva, R. J., G. Bidoglio, M. H. Rand, P. B. Robouch, H. Wanner, and I. Puigdomenech. 1995. Chemical Thermodynamics of Americium. Chemical Thermodynamics Series 2. New York Elsevier.

Simonnet, M., N. Barre, R. Drot, C. Le Naour, V. Sladkov, and S. Delpech. 2016. Multiparametric Study of Thorium Oxide Dissolution in Aqueous Media. Radiochimica Acta, Vol. 104, Issue 10, Pages 691–700.

Skokan, C. K., M. C. Pfeifer, G. V. Keller, and H. T. Anderses. 1987. Studies of Electrical and Electromagnetic Methods for Characterizing Salt Properties at the WIPP Site, New Mexico. Carlsbad NM: Sandia National Laboratories SAND87-7174.

Snider, A. C. 2003. Verification of the Definition of Generic Weep Brine and the Development of a Recipe for This Brine. Carlsbad, NM: Sandia National Laboratories. ERMS 527505.

Sonke, J. E., and V. J. M. Salters. 2006. Lanthanide-humic substances complexation. I. Experimental evidence for a lanthanide contraction effect. Geochimica Et Cosmochimica Acta, Vol. 70(6):1495-1506.

Stein, J. S. 2005. Memorandum to L. H. Brush. Subject: Estimate of Volume of Brine in Repository that Leads to a Brine Release. Carlsbad, NM: Sandia National Laboratories. 140-4142. April 13, 2005. ERMS 539372.

Stein, E., J. Frederick, G. E. Hammond, J. Bethune. 2018. Update to the PFLOTRAN-BRAGFLO Benchmark Comparison of Test Cases and Simulations in the 2-D Flared Grid, Revision 1. Sandia National Laboratories, Carlsbad, NM. ERMS 570622.

Stern, J. C., J. E. Sonke, and V. J. M. Salters. 2007. A capillary electrophoresis-ICP-MS study of rare earth element complexation by humic acids. Chemical Geology, Vol. 246(3-4):170-180.

Stern, J. C., D. I. Foustoukos, J. E. Sonke, and V. J. M. Salters. 2014. Humic acid complexation of Th, Hf and Zr in ligand competition experiments: Metal loading and pH effects. Chemical Geology, Vol. 363:241-249.

Stumm, W., and J. J. Morgan. 1996 Aquatic Chemistry, 3rd ed.; John Wiley and Sons.

Swanson, J. S., D. T. Reed, D. A. Ams, D. M. Norden, and K. A. Simmons. 2012. Status report on the microbial characterization of halite and groundwater samples from the WIPP. Los Alamos National Laboratory, Los Alamos, New Mexico. LANL/ACRSP Report LCO ACP 12, LA-UR 12-22824.

Swanson, J. S., D. M. Norden, H. M. Khaing, and D. T. Reed. 2013. Degradation of Organic Complexing Agents by Halophilic Microorganisms in Brines. Geomicrobiology Journal, Vol. 30(3):189-198.

Swanson, J. S., and K. Simmons. 2013. Update on microbial characterization of WIPP groundwaters. Los Alamos National Laboratory, Los Alamos, New Mexico. LANL/ACRSP Report LCO ACP 20, LA-UR 13-20623.

Swanson, J. S., and D. T. Reed. 2018 Update on Microbiology Research for the Waste Isolation Pilot Plant. Los Alamos National Laboratory, NM, USA. Los Alamos Report LAUR 18-31313.

Swanson, J., C. Hazelton, F. Stanley, E. Yalcintas, and D. T. Reed. 2019. Review of the Microbial Colloid Contribution to the WIPP Actinide Source Term. Los Alamos National Laboratory, NM, USA. Los Alamos Report LA-UR 19-22310.

Telander, M. R., and R. E. Westerman. 1993. Hydrogen Generation by Metal Corrosion in Simulated Waste Isolation Pilot Plant Environments: Progress Report for the Period November 1989 Through December 1992. Albuquerque, NM: Sandia National Laboratories. SAND92-7347. ERMS 223456.

Telander, M. R., and R. E. Westerman. 1997. Hydrogen Generation by Metal Corrosion in Simulated Waste Isolation Pilot Plant Environments. Albuquerque, NM: Sandia National Laboratories. SAND96-2538.

Tierney, M. 1996. WIPP Data Entry Form 464, Id: 3429, Idmtrl: PHUMOX3, Idpram: PHUMCIM. Sandia National Laboratories, Carlsbad, New Mexico. ERMS 27683

Traexler, K. A., S. Utsunomiya, A. B. Kersting, and R. C. Ewing. 2004. Colloid transport of radionuclides: Yucca Mountain performance assessment. Scientific Basis for Nuclear Waste Management XXVII, Symposium held April 12-16, 2004, San Francisco, CA, USA. Materials Research Society, Warrendale, Pennsylvania. 807, 1-6.

Trovato, E.R. 1997. Letter to G. Dails from E.R. Trovato. Subject: Untitled follow-up letter regarding the EPA review of DOE Compliance Certification Application for the WIPP. April 25, 1997. Washington, DC: U. S. Environmental Protection Agency Office of Radiation and Indoor Air.

U. S. Department of Energy (DOE). 1996. Title 40 CFR Part 191 Compliance Certification Application for the Waste Isolation Pilot Plant (October). 21 vols. Carlsbad, NM: Carlsbad Field Office. DOE/CAO-1996-2184.

U. S. Department of Energy (DOE). 2002. January 31, 2002 Technical baseline Report: Compliance Monitoring and Repository Investigations, Milestone Rll 10. U.S. Department of Energy Waste Isolation Pilot Plant, Carlsbad, NM. ERMS #520467.

U. S. Department of Energy (DOE). 2004. Title 40 CFR Part 191 Compliance Recertification Application for the Waste Isolation Pilot Plant (March). 10 vols. Carlsbad, NM: Carlsbad Field Office. DOE/WIPP 2004-3231.

U. S. Department of Energy (DOE). 2009. Title 40 CFR Part 191 Compliance Recertification Application for the Waste Isolation Pilot. Carlsbad, NM: U.S. Department of Energy Carlsbad Area Office. DOE/WIPP 2009-2434,

U. S. Department of Energy (DOE). 2014. Title 40 CFR Part 191 Compliance Recertification Application for the Waste Isolation Pilot Plant. DOE Waste Isolation Pilot Plant, Carlsbad Field Office. DOE/WIPP 2014-3503.

U. S. Department of Energy (DOE). 2016. Transuranic Waste Acceptance Criteria for the Waste Isolation Pilot Plant. Revision 8.0, July, 2016. DOE/WIPP-02-3122.

U.S. Department of Energy (DOE). 2019. Title 40 CFR Part 191 Subparts B and C. Compliance Recertification Application for the Waste Isolation Pilot Plant (March 26, 2019and December 18, 2019). Carlsbad Field Office, Carlsbad, NM. DOE/WIPP 2019-3609.

U. S. Environmental Protection Agency (EPA). 1998. Technical Support Document for Section 194.24: EPA's Evaluation of DOE's Actinide Source Term, Environmental Protection Agency: Office of Radiation and Indoor Air. Washington DC. Docket A-93-02, Item V-B-17.

U. S. Environmental Protection Agency (EPA). 2006. Technical Support Document for Section 194.24: Evaluation of the Compliance Recertification - Actinide Source Term and Culebra Dolomite Distribution Coefficient Values. Washington, DC: U.S. Environmental Protection Agency, Office of Air and Radiation. EPA Air Docket A 98-49, Item II B1-3.

U. S. Environmental Protection Agency (EPA). 2008. Verification of the Waste Isolation Pilot Plant Chemistry Conceptual Models. Washington, DC: Office of Radiation and Indoor Air.

U. S. Environmental Protection Agency (EPA). 2010. Technical Support Document for Section 194.24: Evaluation of the Compliance Recertification Actinide Source Term, Backfill Efficacy and Culebra Dolomite Distribution. Coefficient Values (Revision 1). Washington DC: Office of Air and Radiation. EPA Air Docket A-98-49, Item II-B1-25.

U. S. Environmental Protection Agency (EPA). 2011. EPA's E-mail on September 17, 2011 to DOE for Approval of EQ3/6 for Its Intended Use at WIPP. Carlsbad, NM: Sandia National Laboratories. ERMS 556219.

U. S. Environmental Protection Agency (EPA). 2015. Edwards, Johnathan Letter to Jose R. Franco. Subject: Third Set of Agency Completeness comments and questions. Jun 5, 2015. ERMS 564435.

U. S. Environmental Protection Agency (EPA). 2016. Reference and Data Selection for the CRA-2014 PABC Actinide Solubility Uncertainty Distributions. U.S. Environmental Protection Agency. September 30, 2016. ERMS 567126.

U. S. Environmental Protection Agency (EPA). 2017. Technical Support Document for Section 194.24: Evaluation of the Compliance Recertification Actinide Source Term, Backfill Efficacy and Culebra Dolomite Distribution Coefficient Values. US Environmental Protection Agency. DOCKET: EPA-HQ-OAR-2014-0609.

U. S. Environmental Protection Agency (EPA). 2018a. EPA's Letter to Mike Brown. Subject: EPA's resolution of four chemistry-related technical issues from the CRA-2014. U.S. Environmental Protection Agency. June 22, 2016. ERMS 570087.

U.S. Environmental Protection Agency (EPA). 2018b. Tom Peake letter to Mike Brown, Accepting resolutions to CRA-2014 issues table. October 9, 2018. ERMS 570585.

Van Soest, G. 2018. Performance Assessment Inventory Report-2018 (PAIR 2018).LANL-CO/Inventory Report, Los Alamos, NM: Los Alamos National Laboratory. INV-PA-18.

Vandenborre, J., A. Abdelouas, and B. Grambow. 2008. Discrepancies in thorium oxide solubility values: a new experimental approach to improve understanding of oxide surface at solid/solution interface. Radiochimica Acta, Vol. 96(9-11): 515-520.

Vandenborre, J., B. Grambow, and A. Abdelouas. 2010. Discrepancies in Thorium Oxide Solubility Values: Study of Attachment/Detachment Processes at the Solid/Solution Interface. Inorganic Chemistry, Vol. 49(19) 8736–8748.

Verwey, E. J. W., and J. T. G. Overbeek. 1948. Theory of the stability of lyophobic colloids. Amsterdam, Elsevier.

Vitorge, P., and P. Tran The. 1991. Solubility Limits of Radionuclides in Interstitial Water: Americium in Cement. Task 3: Characterization of Waste Forms. Luxembourg: Commission of the European Communities. A Series of Final Reports (1985-89): N. 34. EUR 13664.

Wall, N. A., M. Borkowski, J. F. Chen, G. R. Choppin. 2002. Complexation of americium with humic, fulvic and citric acids at high ionic strength. Radiochimica Acta, Vol. 90(9-11):563-568.

Wall, N. A., and G. R. Choppin. 2003. Humic acids coagulation: influence of divalent cations. Applied Geochemistry, Vol. 18(10):1573-1582.

Wall, N. A., and S. A. Mathews. 2003. Humic acids in the WIPP. Presentation at the 2003 Radiochemistry Conference, July 14-16, 2003. Sandia National Laboratories, Carlsbad, New Mexico.

Wall, N. A., and S. A. Mathews. 2005. Sustainability of humic acids in the presence of magnesium oxide. Applied Geochemistry, Vol. 20:1704-1713.

Wang, Y., and L. H. Brush. 1996. Memorandum to M.S. Tierney. Subject: Estimates of Gas-Generation Parameters for the Long-Term WIPP Performance Assessment. January 26, 1996. Carlsbad, NM: Sandia National Laboratories. ERMS 231943.

Wang, Y. 1998. WIPP PA Validation Document for FMT (Version 2.4), Carlsbad, NM: Sandia National Laboratories. Document Version 2.4. ERMS 251587.

Warwick, P., N. Evans, A. Hall, G. Walker, E. Steigleder. 2005. Stability constants of U(VI) and U(IV)-humic acid complexes. Journal of Radioanalytical and Nuclear Chemistry, Vol. 266(2):179-190.

Wilson, C., D. Porter, J. Gibbons, E. Oswald, G. Sjoblom, and F. Caporuscio. 1996. Conceptual Models Supplementary Peer Review Report (December). Carlsbad, NM: Carlsbad Area Office. ERMS 243153.

Wolery, T.J. 2008. Analysis Plan for EQ3/6 Analytical Studies. AP-140, (Revision. 0). May, 15, 2008. Carlsbad, NM: Sandia National Laboratories. ERMS 548930.

Wolery, T.J., and R.L. Jarek. 2003. Software User's Manual: EQ3/6, Version 8.0. Albuquerque, NM: Sandia National Laboratories. Software Document No. 10813-UM-8.0-00. ERMS 548926.

Wolery, T. J., Y.-L. Xiong, and J. J. Long. 2010. Verification and Validation Plan/Validation Document for EQ3/6 Version 8.0a for Actinide Chemistry. Carlsbad, NM: Sandia National Laboratories. Document Version 8.10. ERMS 550239.

Wood, S.A., D.A. Palmer, D.J. Wesolowski, and P. Bénézeth. 2002. The Aqueous Geochemistry of the Rare Earth Elements and Yttrium. Part XI. The Solubility of Nd(OH)3 and Hydrolysis of Nd3+ from 30 to 290 °C at Saturated Water Vapor Pressure with In-Situ pHm Measurement, Water-Rock Interactions, Ore Deposits, and Environmental Geochemistry: A Tribute to David A. Crerar. Eds. R. Hellmann and S.A. Wood. St. Louis, MO: The Geochemical Society, Special Publication N. 7, 229-256.

Wood, S.A. 2005. Understanding the Chemistry of the Actinides in High Level Waste Tank Systems: The Impact of Temperature on Hydrolysis and Complexation with Organics. Washington, DC: U. S. Department of Energy. DOE/ER/14935-3A.

Xia, Y., A. R. Felmy, L. Rao, Z. Wang, and N. J. Hess. 2003. Thermodynamic Model for the Solubility of ThO2(am) in the Aqueous Na+-H+-OH--NO3--H2O-EDTA System. Radiochimica Acta. Vol. 91, 751-760.

Xiong, Y.-L. 2004. A Correction of the Molecular Weight of Oxalate in FMT_021120. CHEMDAT, and Incorporation of Calcium Oxalate Monohydrate (Whewellite) into CHEMDAT with Its Recommended Dimensionless Standard Chemical Potential Value,

Xiong to Brush, June 8, 2004, ERMS 535813.

Xiong, Y.-L. 2005. Release of FMT_050405.CHEMDAT. Carlsbad, NM: Sandia National Laboratories. ERMS 539304.

Xiong, Y.-L, E. J. Nowak, and L. H. Brush. 2005a. Updated Uncertainty Analysis of Actinide Solubilities for the Response to EPA Comment C-23-16 (Supersedes ERMS 538219). Analysis Report, April 29, 2005. Carlsbad, NM: Sandia National Laboratories. ERMS 539595.

Xiong, Y.-L, E.J. Nowak, and L.H. Brush. 2005b. Predicting Actinide Solubilities in Concentrated Brines: The Fracture-Matrix Transport (FMT) code. May 2005. Geochimica et Cosmochimica Acta Supplement, 69;10, A417.

Xiong, Y.-L., and A. C. S. Lord. 2008. Experimental investigations of the reaction path in the MgO–CO2–H2O system in solutions with ionic strengths, and their applications to nuclear waste isolation. Applied Geochemistry, Vol. 23:1634–1659.

Xiong, Y-L. 2009. Release of FMT_090720.CHEMDAT. Carlsbad, NM: Sandia National Laboratories. ERMS 551706.

Xiong, Y.-L, H.-R. Deng, M. Nemer, and S. Johnsen. 2009. Thermodynamic Data for Phase 5 ($Mg_3Cl(OH)_5 \cdot 4H_2O$) Determined from Solubility Experiments. Carlsbad, NM: Sandia National Laboratories. ERMS 551294.

Xiong, Y.-L, H. Deng, M. Nemer, and S. Johnson. 2010a. Experimental Determination of the Solubility Constant for Magnesium Chloride Hydroxide Hydrate (Mg3Cl(OH)5•4H2O, Phase 5) at Room Temperature, and Its Importance to Nuclear Waste Isolation in Geological Repositories in Salt Formations. Geochimica et Cosmochimica Acta, Vol. 74:4605-4611.

Xiong, Y.-L, L. H. Brush, J. W. Garner, and J. J. Long. 2010b. Responses to three EPA comments pertaining to comparisons of measured and predicted dissolved and colloidal Th(IV) and Am(III) concentrations. Analysis Report, May 4, 2010. Sandia National Laboratories, Carlsbad, NM. ERMS 553409.

Xiong, Y.-L. 2011. E-mail to Jennifer Long Subject: Release of EQ3/6 Database DATA0.FM1. March 9, 2011. Carlsbad, NM: Sandia National Laboratories. ERMS 555152.

Xiong, Y.-L, L. H. Brush, P. S. Domski, J. J. Long. 2011. Uncertainty Analysis of Actinide Solubilities for the WIPP CRA-2009 PABC, (Revision 1), Supersedes ERMS 552500. Analysis report, January 24, 2011. Carlsbad, NM: Sandia National Laboratories. ERMS 554875.

Xiong, Y.-L. 2013. Experimental Determination of Solubilities of Crystalline Lead Oxalate, PbC_2O_4(cr), in the NaCl-H_2O system. Carlsbad, NM: Sandia National Laboratories. ERMS 560651.

Xiong, Y.-L. 2014a. Experimental and Thermodynamic Modeling of $PbCit^-$ Interactions in NaCl and Mg_2Cl_2 Solutions. Carlsbad, NM: Sandia National Laboratories. ERMS 562836.

Xiong, Y.-L. 2014b. Experimental and Thermodynamic Modeling of $PbEDTA^{2-}$ Interactions in NaCl and Mg_2Cl_2 Solutions. Carlsbad, NM: Sandia National Laboratories. ERMS 562877.

Xiong, Y.-L. 2015a. Experimental and Thermodynamic Modeling Solubility of Cerussite, PbCO3(s), in the Carbonate System to High Ionic Strengths, (Revision 1), Supersedes ERMS 561917 Carlsbad, NM: Sandia National Laboratories. ERMS 564929.

Xiong, Y.-L. 2015b. Experimental Determination of Solubilities of Lead Oxalate (PbC_2O_4), Di-Calcium Ethlenediamineetetraacetic Acid (Ca_2EDTA(s)) in $MgCl_2$-H_2O System, and Earlandite ($Ca_3[C_3H_5O(COO)_3]_2 \cdot 4H_2O$) in NaCl-$H_2O$ and $MgCl_2$-H_2O Systems, and Their Respective Pitzer Interaction Parameters. (Revision 1), Supersedes ERMS 564844. Analysis Report for AP-154. Carlsbad, NM: Sandia National Laboratories. ERMS 564948.

Xiong, Y.-L., and P. S. Domski. 2016. Memo. Subject: A Sensitivity Analysis of Am(III) Solubilities as a Function of Concentration of Total Reduced Sulfur (Σ HS^-) (and hence Σ Pb2) in the Presence of Galena (PbS) January 21, 2016. Carlsbad, NM: Sandia National Laboratories. ERMS 565376.

Xiong, Y.-L., L. Kirkes, T. Westfall, J. Knox, H. Burton, and C. Marrs. 2017. Absence of Mineral Colloids in High Ionic Strength Solutions Associated with Salt Formations: Experimental Determination and Applications to Nuclear Waste Management, Sandia National Laboratories. Carlsbad, NM. ERMS 568244.

Zeitler, T. R., and C. Hansen. 2015a. Memo. Subject: Cumulative distribution for STEEL:CORRMCO2. November 3, 2015. Sandia National Laboratories, Carlsbad, NM. ERMS 565009.

Zeitler, T. R., and C. Hansen. 2015b. Memo. Subject: Updated calculation of the cumulative distribution for STEEL:HUMCORR. December 8, 2015. Sandia National Laboratories, Carlsbad, NM. ERMS 565108.

Zeitler, T. R. 2018. Memo. Subject: Bounding calculation of the cumulative distribution for STEEL:HUMCORR. April 30, 2018. Sandia National Laboratories, Carlsbad, NM. ERMS 569807.

Zeitler, T. R. 2019. Analysis Package for Parameter Sampling in the 2019 Compliance Recertification Application Performance Assessment (CRA-2019 PA), Rev. 0. June, 2019. Sandia National Laboratories, Carlsbad, NM. ERMS 571367.

Zhang, P.-C., H. L. Anderson, J. W. Kelly, J. L. Krumhansl, H. W. Papenguth. 2000. Kinetics and mechanisms of formation of magnesite from hydromagnesite in brine. Sandia National Laboratories, Albuquerque, New Mexico. Submitted to Applied Geochemistry. SAND99-1946B.

Zhao, P., and S. A. Steward. 1997. Literature review of intrinsic actinide colloids related to spent fuel waste package release rates. Lawrence Livermore National Laboratory, Livermore, California. UCRL-ID-126039.

Zimmerman, T., M. Zavarin, and B. A. Powell. 2014. Influence of humic acid on plutonium sorption to gibbsite: Determination of Pu-humic acid complexation constants and ternary sorption studies. Radiochimica Acta, Vol. 102(7):629-643.